DOCTOR OF PHILOSOPHY

Multiscale modelling of cancer evolution
the role of fibres and macrophages in invasion patterns

Suveges , Szabolcs

Award date:
2021

Multiscale modelling of cancer evolution:

the role of fibres and macrophages in invasion patterns

Szabolcs Bálint Süveges

Mathematics

University of Dundee

This dissertation is submitted for the degree of

Doctor of Philosophy

2021

Contents

List of Figures

List of Tables

Acknowledgements

I would first like to offer my special thanks to both of my supervisors Dr. Dumitru Trucu and Prof. Raluca Eftimie for giving me the possibility to carry out my PhD studies at the University of Dundee. I am also grateful for their guidance, continued support and patience throughout the research project which inspired me to think critically and independently and helped me to gain invaluable knowledge and research experience.

I am thankful to all my family members for the continuous love and support they have given me during my studies.

Last, but not least, I would like to gratefully acknowledge the support of the Engineering and Physical Sciences Research Council (UK) grant number EP/R513192/1.

Declaration

I hereby declare that except where specific reference is made to the work of others, the contents of this dissertation are original and have not been submitted in whole or in part for consideration for any other degree or qualification in this, or any other university. This dissertation is my own work and contains nothing which is the outcome of work done in collaboration with others, except as specified in the text and Acknowledgements. This dissertation contains fewer than 65,000 words including appendices, bibliography, footnotes, tables and equations and has fewer than 150 figures.

Szabolcs Suveges

Certification

This is to certify that Szabolcs Süveges has complied with all the requirements for the submission of this Doctor of Philosophy thesis to the University of Dundee.

Dr. Dumitru Trucu and Prof. Raluca Eftimie

Publications

1. Suveges, S.; Eftimie, R.; Trucu, D. (2020) "Directionality of Macrophages Movement in Tumour Invasion: A Multiscale Moving-Boundary Approach". Bulletin of Mathematical Biology, 82. doi:10.1007/s11538-020-00819-7

2. Suveges, S.; Chamseddine, I.; Rejniak, K. A.; Eftimie, R.; Trucu, D. (2021) "Collective Cell Migration in a Fibrous Environment: A Hybrid Multiscale Modelling Approach". Frontiers in Applied Mathematics and Statistics, 7:680029. doi:10.3389/fams.2021.680029

3. Suveges, S.; Hossain-Ibrahim, K.; Steele, J.D.; Eftimie, R.; Trucu, D. (2021) "Mathematical Modelling of Glioblastomas Invasion within the Brain: A 3D Multi-Scale Moving-Boundary Approach". Mathematics 9.18 (Sept. 2021), p. 2214. doi: 10.3390/math9182214.

4. Suveges, S.; Eftimie, R.; Trucu, D. (2021) "Re-polarisation of Macrophages Within a Multi-Scale Moving Boundary Tumour Invasion Model". arXiv:2103.03384. Submitted

5. Suveges, S.; Hossain-Ibrahim, K.; Steele, J.D.; Eftimie, R.; Trucu, D. "Exploration of Treatment Options for Glioblastomas Using a 3D Multi-scale Moving-Boundary Framework". In preparation

6. Suveges, S.; Eftimie, R.; Trucu, D. "3D Macrophage Dynamics Within a Multi-Scale Moving Boundary Tumour Invasion Model". In preparation

Abstract

The ability to invade its surrounding tissue is one of the acknowledged hallmarks of cancer. This complex multi-scale process is affected by many players of the tumour microenvironment (TME), including the extracellular matrix (ECM) and various stromal cells such as macrophages. One of these key processes is the secretion of matrix degrading enzymes that enables the degradation of the neighbouring ECM and cell-matrix adhesion. By varying the strength of cell-matrix and multiple cell-cell adhesions, cancer cells can spread into the surrounding tissues which combined with an unregulated proliferation results in an uncontrollable, indefinite growth.

This thesis considers a continuous multi-scale moving boundary model for general solid tumours that takes into account the multi-scale interactions between the different cell populations and a two-phase ECM as well as the proteolytic molecular processes taking place along the leading edge of a growing solid tumour. To that end, we investigate how one of the most abundant immune cells in the TME, the macrophages, and their phenotype influence the overall tumour progression, by exploring their multi-scale effects. Moreover, we extend our approach and consider a discrete cell population consisting of individual cancer cells that allows us to further study the complex interaction between the cancer cells and a two-phase ECM as well as the overall shape and migration type of a tumour aggregation. Finally, we apply our general continuous model to a specific type of brain tumour, glioblastomas, using patient-specific brain scans that allows us to investigate the role of brain micro-fibres in a 3-dimensional invading tumour.

Chapter 1

Introduction

Over the last few decades, cancer has gained increased attention due to its diversity and capability to metastasise, one of the leading causes of death. Cancer is also known to be effective at developing drug resistance to current treatment strategies, which further increases the need to understand this complex, deadly disease with the hope of establishing successful treatment protocols. This has been motivating current research interest within many different scientific fields such as biology and mathematics. While biology collects concluding evidence for various possible treatments using experiments, mathematics connects new theories and hypotheses with these experiments, ultimately reducing the cost of novel discoveries that otherwise would be both impractical and expensive.

1.1 Biological Background

The main difference between normal and cancer cells is that while the former one can be controlled and regulated through different signals [77], cancer cells acquired various hallmark capabilities that help them avoid these regulations leading to abnormal cell functions [99, 98]. One of these identified "hallmarks of cancer" is the cancer cells' ability to *invade the surrounding tissues* by altering their local and non-local

interaction to both neighbouring cells (which can either be cancerous or of different types) and extracellular matrix (ECM). Pioneer cells that gain this ability at some point during the tumour development may detach from the primary tumour mass and travel to distant sites where they have a chance to form new secondary colonies. This process is called *metastasis*, which can be especially lethal when cancer cells get into the bloodstream that transports them to a new terrain where, at least at the beginning, they have access to abundant nutrients, and space [161]. Generally speaking, once these distant tumour sites are formed, for example, in bone, liver or brain, the survival rate is drastically decreased and in most cases (90%) eventually leads to death [253].

Tumours are also referred to as *"wounds that never heal"* [78] because most processes associated with wound healing are similar to the ones involved in tumour development, and so the immune system reacts to both of them similarly. However, while for wound healing, such an immune response is necessary and effective, for tumour development, it has an opposite effect, and in most cases, it promotes tumour growth rather than stops it.

1.1.1 The Tumour Micro-environment

In the following, we briefly review some components of the tumour micro-environment (TME) which are the focus of this Thesis.

ECM. The ECM is a complex network of various macromolecules (such as fibrous proteins, water, minerals and proteoglycans) and plays an essential role in any healthy tissue [77]. For instance, it regulates cell behaviour and tissue homeostasis, enables cell migration and communication as well as it provides structural support. It can be split into two major phases, a *fibre ECM* phase, accounting for all significant fibrous proteins (such as collagen and fibronectin) and a *non-fibre ECM* phase that contains every other ECM constituent (such as non-fibrous proteins,

enzymes, polysaccharides and extracellular Ca2+ions). To maintain its functionality, the ECM is subject to continuous remodelling (via synthesis and degradation). However, this carefully orchestrated process is disturbed by the progressing tumour, resulting in drastic changes in the structure of the ECM (*i.e.,* a rearrangement of the ECM micro-fibre constituents). Moreover, in the tumour microenvironment (TME), the excessive degradation of the ECM is related to the over-secretion of several enzymes capable of degrading the ECM, for instance, the matrix metalloproteinases (MMPs). Such enzymes are not explicitly tied to cancer cells, but instead, several other stromal cells within the TME secrete them as well [171].

Macrophages. One of these stromal cell populations is the *macrophages*, which can form up to 50% of the tumour mass [132, 286]. The immune system's response to a tumour's presence is to send white blood cells called monocytes (which are produced by stem cells in the bone marrow) to the tumour sites through the bloodstream, and once they leave the vasculature, they mature into macrophages. The, macrophages are a heterogeneous set of differentiated immune cells that are polarised according to the surrounding stimuli to exhibit different properties and functions. A specific class of these cells present in the TME, is called the *tumour-associated macrophages* (TAMs), and they are in general correlated with poor prognosis in various type of cancers [39, 41, 96, 151, 223, 288, 296, 306, 307, 311]. These activated macrophages are often categorised as the *pro-inflammatory M1-like macrophages* and the *anti-inflammatory M2-like macrophages*, and so while the former expresses anti-tumoral functions, the latter one has pro-tumoral properties. These phenotypes are illustrated in Figure 1.1. Due to their fundamentally different effects on the tumour, the ratio between the M1 and M2 TAMs can significantly affect the prognosis [61, 204, 303, 307, 222]. Because of the plasticity of macrophages phenotypes (*i.e.,* their phenotype can be changed in response to the environment [24, 234]) (a process which is called polarisation and re-polarisation, see Figure 1.1), shifting this ratio

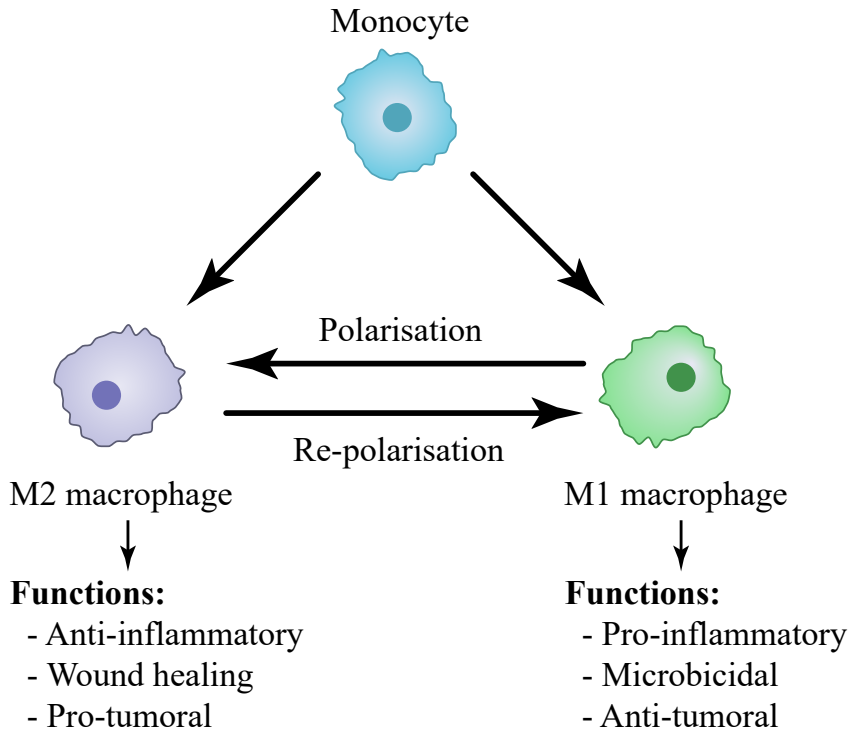

Figure 1.1: *Illustration of the two macrophage phenotype and their primary roles as well as the possible switch (polarisation and re-polarisation) between the two phenotype.*

towards an M1 phenotype has been shown to reduce tumour progression [201, 308].

Nutrients. Nutrients (e.g. oxygen and glucose) are essential for any cells to live and function properly, including cancer cells and macrophages, and so in healthy tissues, a certain level of nutrients is maintained. In order to supply these vital nutrients to every tissue of the body, nutrients are extravasated from the blood flow and diffuse through the ECM. However, the progressing tumour destroys significant parts of the vasculature, excessively influencing the blood flow and, therefore, the level of supplied nutrients. Even though tumours are capable of promoting new blood vessels through the secretion of vascular endothelial growth factors [34, 195, 277], due to their rapid expansion, they outgrow the nutrient supply [250]. Consequently, once they reach a certain size, these blood vessels can no longer fully penetrate the tumour and reach their centre. Therefore, as the advancing tumour over-consumes the nutrient supply, it creates areas where the level of nutrients becomes low, so such areas first become hypoxic and then necrotic. Accordingly, cells situated in necrotic regions are being deprived of nutrients, leading to cell death and ultimately giving rise to a dense *necrotic core*. Quiescent cells that are located within the *hypoxic layer* that surrounds the necrotic core change their behaviour to promote ECM remodelling as well as they become more migratory and metastatic. In the *proliferating rim* where the level of nutrients is still sufficient for typical cell functions, cancer cells directly interacting with the surrounding ECM and stroma, and so they are responsible for the invasion of the local tissue neighbourhood. These three regions are also illustrated in Figure 1.2. Finally, since nutrients are vital for each cell, the reduced levels affecting not only the cancer cell population but also the macrophages in many ways, including proliferation, death and the rate at which TAMs changes their phenotype [98, 130, 273].

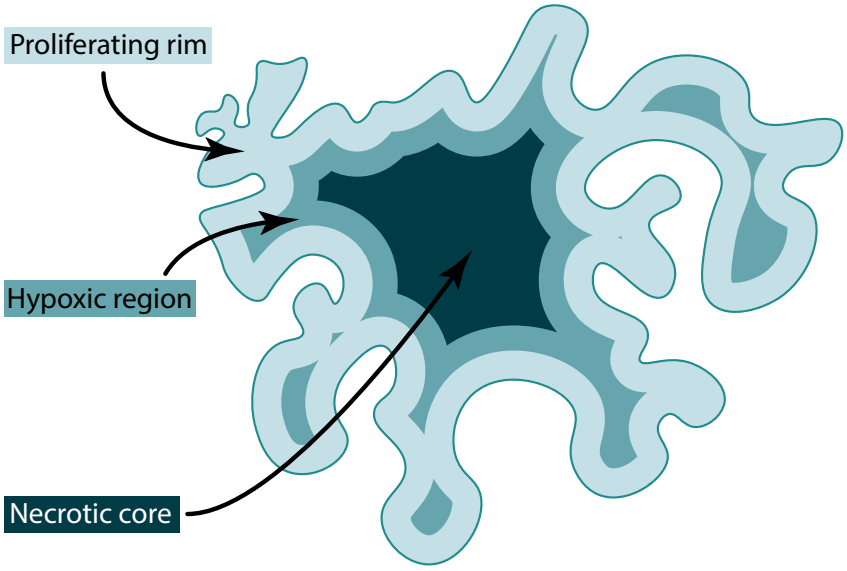

Figure 1.2: *Illustration of a tumour with its three basic layers, namely outer proliferating rim, middle hypoxic/quiescent region and inner necrotic core.*

1.1.2 Local Cancer Invasion

The phenomenon of local cell invasion is a result of multiple crucial underlying *cell-scale* (micro-scale) processes that are often interlinked. Together, they enable cell migration and collective population dynamics, which result in this *tissue-scale* (macro-scale) phenomenon called cell invasion. A recognised hallmark of cancer cells [98] is that they acquire the ability to stimulate themselves with their own growth factors (thus reducing their dependency on growth factors produced by other cells), which leads to tumour growth. Moreover, cancer cells are also capable of secreting various *matrix degrading enzymes* (MDEs) (such as MMPs, a property that, as mentioned before, are not exclusive to them) which travel through the ECM (within a cell-scale neighbourhood) and degrade several ECM components (called proteolysis), resulting in changes in the local surrounding tissue structure. Ultimately, all these processes mutually enable sustainable tumour growth and spread.

Although collective cell migration is present in a healthy environment, it also plays a vital role in tumour development since it allows cells to travel and invade

into the surrounding tissues as a community [25, 26, 129, 276]. This collective cell migration is enabled by different *cell-cell* and *cell-ECM adhesions*. For instance, cancer cells and macrophages can establish adhesive bonds between each other through the secretion of cell adhesion molecules; in addition, individual cells can also initiate adhesive bonds with different ECM constituents, bonds which are regulated by integrins (a calcium-independent cell adhesion molecule that connects the cell's cytoskeleton to the surrounding ECM). Ultimately, cells can vary the strength of these different adhesions, allowing them to develop different migratory patterns. For example, a decrease in cell-cell adhesion combined with an increase in cell-ECM adhesions enables the cancer cells to detach from the primary tumour mass and invade further into the neighbouring tissues, which results in a more invasive tumour behaviour [42].

1.1.3 Glioblastoma Multiforme

An example for a solid tumour and more specifically a brain tumour is the highly invasive and aggressive glioblastoma multiforme which typically has poor patient prognosis [35, 65, 139, 162, 182, 216, 252] (median survival rate is less than 1 year [33]). These tumours arise from abnormal glial cells located in the central nervous system, and shortly after their appearance they invade the surrounding tissues in a heterogeneous fashion. This heterogeneous invasion pattern leads to tumours whose outer edges are difficult or impossible to determine with current imaging technologies, including for instance *magnetic resonance imaging* (MRI) and *diffusion tensor imaging* (DTI), both of which measure the diffusion of water molecules and enable the study of brain structures. For this reason, tumour recurrence is inevitable and complete surgical resection is impossible without greatly damaging also the healthy tissue of the brain [100].

As for other tumour cell types, the glioblastoma cell invasion into the brain extracellular matrix (ECM) is the result of the secretion of proteolic enzymes, as well

as cell-cell and cell-ECM interactions [100]. Glioma cells can navigate along brain structures, such as blood vessels (but they rarely intravasate into blood vessels) [100].

Due to the limited experimental approaches that one can use to study the brain, researchers have started using mathematical models to provide certain biological insights that otherwise would be difficult to obtain experimentally. Such models can help predict how tumours grow for specific patients, aiding clinicians in decision-making, or they can help test and provide new hypotheses about potential anti-tumour treatments.

1.2 Mathematical Modelling of Tumour Development

In spite of the advancements achieved over the years in theoretical and experimental biology, tumour development still poses one of the greatest challenges within the scientific community. It is difficult to accurately predict tumour's behaviour as it involves modelling several interlinked processes occurring on different spatio-temporal scales. Existing techniques are often expensive, and relax the complexity of the problem by constraining it to a single scale,leading to significant information loss and reduced predictive capabilities. Thus, this thesis builds on and extends a multi-scale mathematical/computational model introduced in [279, 245], to further propose new research hypotheses, to narrow down scientific ideas and to predict outcomes.

1.2.1 Continuous and Hybrid Models

In the past few decades, we have seen substantial advances in mathematical and computational modelling approaches that are used for predicting certain outcomes,

exploring potential treatments or just trying to capture the general underlying processes [7, 8, 9, 11, 14, 12, 37, 44, 47, 46, 63, 67, 68, 70, 135, 141, 174, 180, 183, 217, 232, 245, 258, 272, 279, 59]. These modelling approaches can be categorised into two main types, namely *discrete* and *continuous* models and each of these techniques carries its own advantages and disadvantages [239]. To minimise drawbacks, people formulated the so-called *hybrid* methods that combine these two models which can also be used to study tumour development [44].

The continuous approaches

The main advantage of the continuous approaches is that they allow us to model the dynamics on a population scale, and so we do not need to consider and store each individual cell's position and properties. This reduces memory storage as well as speeds up the computation, enabling us to carry out longer computational simulations within a larger space. This is especially important when we would like to study, for example, the effects of drugs or various treatment strategies in the long term. On the other hand, this also impedes us to give different properties to individual cells that may be useful or required in some cases. Moreover, continuous approaches that model cell movement also require the use of appropriate numerical schemes to avoid, for instance, negativity and to keep the conservation of mass property of the partial differential equation (PDE). In some cases, this may be difficult and require additional computations.

It is now widely known that both MDEs (and so the degradation of the ECM [164, 190]) and ECM structure [102, 301] play an important role within the cell migration process and thus they have been incorporated into many mathematical models. On one hand, an important aspect of these proteolytic enzymes is their secretion and transport within a cell-scale neighbourhood, directly impacting the level of ECM degradation in the surrounding tissue [9, 46, 67, 206, 246, 279]. On the other hand, the structure of the underlying ECM and its effect on cell migration,

adhesion, proliferation has also received its own spotlight [14, 17, 29, 48, 81, 203, 245, 280] as well as how the heterogeneity of the ECM affects tumour development [48, 107, 203].

One of the first studies that proposed a continuous modelling approach for the interactions between cancer cells and ECM via MDEs was [11]. There, the movement of cancer cells was split into a diffusion term describing random cell motility, and a haptotaxis term that biases cell movement according to the surrounding ECM. It was concluded, using numerical simulations, that haptotaxis plays a significant role in cancer cell invasion and that it cannot be ignored within mathematical models. Later, a continuous approach for cell-cell adhesion was derived in [17] which describes cell sensing and biding in a *non-local* fashion that ultimately guides cell movement based on cell-cell adhesive forces. This non-local approach was extended to also incorporate cell-matrix adhesions in [81] where a thorough numerical investigation was carried out. Also, the same model was analytically studied in [45] with different adhesion regimes to show how these changes affect the cancer cell population. Furthermore, in recent years, a modelling approach for capturing the underlying ECM structure was proposed in [245] where a multi-scale *two-phase ECM* was considered that introduces further bias for the cancer cell movement. Hence, this model empowers the cancer cells to follow the micro-scale distribution of the fibre ECM phase, which in the meantime is being rearranged by the cancer cell population in a multi-scale manner. Another continuous model that focuses on tissue structure and aims to investigate mesenchymal motion was proposed in [106] and later expanded in [203] where it was shown that contact-guidance and ECM remodelling are adequate for cell invasion.

The other abundant cell population within the TME is the macrophages. Despite the fact that they are present in significant quantities, only a modest number of mathematical models consider their role during tumour development [63, 141, 174, 180, 200, 198, 199, 290]. Since macrophages are indeed immune cells, initial

models [200, 199, 290] were only focusing on their anti-tumoral role and used them within treatment strategies. However, a turning point that escalated the research of macrophages occurred when the dual role of macrophages was discovered within tumours [156, 214] where the positive correlation between TAMs and tumour growth was shown. Consequently, mathematical models started to focus on the plasticity of the macrophages, and the fact that cancer cells are able to *polarise* them into the pro-tumoral M2 phenotype [141, 174]. Hence, these models began studying how M2-like macrophages affected the overall tumour development, which ultimately led to multiple biological research theorising the possibility of *re-polarising* these pro-tumoral M2 TAMs back into the anti-tumoral M1 TAMs and whether this would be an effective treatment strategy [49, 61, 105, 197, 204, 307]. However, due to the novelty of this theory, the number of mathematical models focusing on it has been limited [32, 74, 137, 142, 163, 289].

Due to their essential role, nutrients have been the focus of many mathematical models. As was mentioned before, the depleted level of nutrients emerges a three-layer structure in tumours (necrotic core, hypoxic region of quiescent cells and proliferating rim) which many models have successfully reproduced [13, 15, 36, 124, 126, 168, 169, 177, 244].

The hybrid approaches

Finally, the second class of mathematical models that we consider is the so-called hybrid models. The aim of using them is to combine the advantages of both continuous and discrete models that can ultimately give further insights into some of the underlying processes. One of the advantages of these models is that complex intracellular changes can be modelled and follow for each individual cells (agents) simply by using ordinary differential equations. Moreover, it is possible to trace extracellular factors via partial differential equations without the need to sacrifice the *agent-based* approach. Hence, this approach is well suited for the multi-scale nature

of cancer and can be used to model different processes on various scales [44, 231].

There are various sub-types of discrete models that one can use within a hybrid approach such as cellular automata models [12, 136, 213, 274], cellular potts models [10, 215, 255] and particle-force models [83, 120, 185]. Of particular importance for us are the particle-force models, that allows us to model individual cells in an off-lattice setup, and so the position of a cell does not depend on any predefined grid. The model that we will use and extend was originally introduced in [135] and later extended in several other works [27, 127, 128] to incorporate different aspects of cancer invasion and to investigate different drug delivery strategies. Looking at these hybrid mathematical modelling approaches over the last couple of decades in general, we can see significant advances both in theory and application to a wide variety of cancer related problems [43, 62, 83, 110, 149, 167, 207, 218, 233, 240, 256, 271, 280].

1.2.2 3D Continuous Glioma Models

Although the majority of the above-mentioned models do not restrict themselves to a specific tumour type and rather focus on general tumours, there are some models that focus on the evolution of specific tumour types such as gliomas within the brain [5, 75, 116, 202, 241, 267, 269, 268, 270]. These models are also very important since they help us understand how the different components of a model can affect the overall tumour progression via fitting the model to real-word examples of tumour growths. Recently, models also started to incorporate the structure of the brain, by including MRI and DTI scans [53, 54, 75, 116, 121, 143, 202] which can be thought of as one of the underlying components that can be fit to patient-specific tumours. Even though these images are generated in 3D, most of these models are simulating the tumour growth in 2D and only a few of them are 3D models [53, 260, 302]. Moreover, as mentioned before, the majority of published models focus on tumour progression only on one spatio-temporal scale and neglect the fact that it is characterised by various biological processes occurring on different scales.

Therefore, the literature lack of 3D multi-scale approaches that can appropriately model complex brain tumour behaviour.

1.3 Thesis Outline

The primary aim of this thesis is to gain further insights into the complex tumour development process by investigating the collective migration of cancer cells as well as studying one of the most abundant stromal cells within TME, *i.e.,* the macrophage population. To explore the behaviour and effects of macrophages, we use a fully continuous multi-scale moving boundary model that is expanded upon the initial framework introduced in [279] and later expanded in [245] to account for the micro-scale structure of the ECM. On the other hand, to further investigate both the overall shape of tumour aggregations as well as cell migration and invasion patterns, we develop a hybrid multi-scale model that combines a continuous multi-scale two-phase ECM [245], and a discrete off-lattice agent-based model *MultiCell-LF* for the cancer cells [27, 128, 135]. Furthermore, we apply our continuous multi-scale framework to a specific tumour type, to study tumour growth in a 3D fibrous brain environment.

Specifically, in Chapter 2, we will extend the multi-scale moving boundary model introduced in [245] by including the M2 TAMs population and several of its effects exercised on the rest of the tumour dynamics. Hence, in this model, we consider the tumour dynamics to be given by a mix of two interacting populations, *i.e.,* cancer and M2 TAMs, embedded within a two-phase ECM. To this end, we will study the movement of macrophages and how this affects the overall tumour progression by considering both random and directed movements of these immune cells, where the directed portion incorporates multiple non-local adhesion processes. Moreover, we incorporate a few effects of the M2 TAMs exerted on the cancer cells within the macro-scale dynamics, such as regulation of proliferation and bias of cell migration.

Besides these macro-scale effects, due to their ability to secrete MDEs, M2 TAMs also play an important role in both the proteolytic processes occurring at the leading edge of the tumour and the fibre rearrangement process. Consequently, we capture the effects of M2 TAMs in a multi-scale fashion and examine their extensive effects on the overall tumour invasion process. The extension presented in this chapter will be numerically explored, placing particular focus on the macrophage non-local interactions.

Besides the M2-like macrophages, in Chapter 3, we also include the contribution of M1-like macrophages to the overall tumour dynamics, by considering the impact of these cells to both macro- and micro-scales. We pay special attention to the dynamics of M1 and M2 cells near the tumour interface, and their interactions with the tumour and with the ECM. We also focus on the M1→M2 tumour-induced polarisation (in the presence/absence of nutrients) and on the M2→M1 re-polarisation as induced by various treatment protocols (e.g., the agonist anti-CD40 mAb [23]). In this new extended framework, we also model the potential role of nutrients on the proliferation/death of M1 and M2 macrophages and cancer cells. With the help of this new extended multi-scale model, we aim to investigate the impact of re-polarising the M2 TAMs into the anti-tumoral M1 phenotype and how such a strategy affects the overall tumour progression. In particular, we explore numerically whether an effective macrophage M2→M1 re-polarisation strategy (within a fibrous tissue environment which impacts macrophage dynamics) is spatial and/or temporal dependent. Furthermore, we study how the presence of nutrients influence the overall dynamics and particularly how they affect the re-polarisation based strategy.

Then, in Chapter 4 we derive our hybrid multi-scale modelling framework. The main goal of this chapter is to study further the various aspects that are responsible for the shape of the emerging tumour aggregations. To this end, here, we model the cancer cell population as individual cells (agents) which are embedded within

a two-phase ECM, also used in Chapters 2 and 3. Although many experimental studies discussed the role of ECM in individual and collective cell migration, there are still unanswered questions about the impact of non-local cell sensing of other cells on the overall shape of tumour aggregation and its migration type. Moreover, cell migration and tumour spread occurring at the boundary between different tissues with diverse collagen fibre orientation poses further unresolved challenges. To that end, we use numerical simulations to investigate these questions and conclude that multiple properties of the ECM fibres heavily impact the movement of tumour aggregations.

Finally in Chapter 5, we extend our 2D multi-scale moving boundary framework to 3D and use it to numerically simulate the growth of a specific *brain tumour* type, namely the *glioblastoma multiforme*. Since brain-related experiments are usually limited by nature, mathematical models such as the one that we developed, can be used to generate and test new biological hypotheses. Hence, in this chapter, we use our model to capture the complex multi-scale tumour invasion patterns in 3D brains where we pay special focus on the role of brain micro-fibres. Moreover, we utilise T1 weighted and DTI scans as initial conditions and to parametrise our model. To that end, we use numerical simulations to investigate the role of an anisotropic diffusion term and the effects of brain micro-fibres.

Chapter 2

The Role and Directionality of M2 Macrophages within a Multi-Scale Moving Boundary Tumour Invasion Model

Aims and Novelty: In this chapter, we open up the possibility to investigate tumour invasion in the context of a heterogeneous microenvironment, using a multi-scale moving boundary framework, that was initially formulated in [279] and later extended in [245]. Hence, we investigate how the various types of M2 TAMs adhesions affect the overall tumour progression and morphology within a fibrous environment, including macrophage-macrophage, macrophage-cancer cell and macrophage-fibres adhesions.

2.1 Introduction

During the last few decades, mathematical models have mainly focused on a few key players of tumour invasion, namely cancer cells, ECM and MDEs. Moreover,

most of these models do not account for the multi-scale nature of the tumour invasion process, for instance, although tumours themselves can be modelled on tissue scale, MDEs, which are secreted by several tumour constituents, interact with the surrounding ECM on the molecular scale. To account for such interactions, a multi-scale moving boundary model was proposed in [279] which was later expanded in [245] also to incorporate the multi-scale nature of the ECM.

Furthermore, besides these three primary players, there are other significant constituents within the TME, such as macrophages which are one of the most abundant stromal cells, and they can form up to 50% of tumour mass [132, 286]. Although these macrophages are usually categorised into two extreme phenotypes, namely the classically-activated anti-tumour M1 and the alternatively-activated pro-tumour M2 phenotype [176, 249], advanced (detectable) tumours contain mostly M2-like macrophages [155]. Hence, we propose a (multi-scale moving boundary) model that expands upon the one formulated in [245] and takes into consideration the M2-like macrophages and their role in the tumour invasion process.

Therefore, in this chapter, we study the directional interactions of macrophages with the surrounding directional/random ECM and how this affects tumour spread. The content of Sections 2.3-2.7 has been thoroughly discussed and presented in our recent publication [265].

2.2 Modelling Part 1: A Brief Overview of the Existing Multiscale Moving Boundary Model of Tumour Dynamics within a Fibrous ECM

As the work that we developed in this chapter builds on the multi-scale modelling developed in [245, 279], in this section we focus on giving a brief overview of the key features of the existing framework.

2.2.1 Macro-Scale Dynamics of the Existing Model

Hence, at macro-scale, we explore the cancer invasion process occurring within a maximal tissue cube $Y \in \mathbb{R}^N$ for $N = 2, 3$, where the expanding tumour region denoted by $\Omega(t)$ progresses over the time interval $[0, T]$ (*i.e.,* $\Omega(t) \subset Y$, $\forall\, t \in [0, T]$). We adopt the same simplified context as in [279, 206, 245, 246, 247] where aside from the tumour cells population $c(x, t)$ that is defied within the tumour region $\Omega(t)$, the rest of the tumour microenvironment and surrounding tissue is represented here simply by a generic ECM. To that end, while we acknowledge that, besides the tumour cells, some of the tumour microenvironment components are not ECM constituents and are rather only supported by the usual ECM, in this framework we still regard all those constituents (such as VEGF, FGF, TGF-beta, and ions such as Ca^{2+}) as being part of and represented by this extended concept of ECM. Furthermore, due to the biologically established importance played within cell migration by the major ECM fibres, namely collagen and fibronectin, as considered also in [246, 247, 245], we regard this ECM as two-phase matter, consisting of an ECM fibre phase and an ECM non-fibre phase. Specifically, on one hand the ECM fibres phase accounts exclusively for all major fibres components such as collagen and fibronectin (notably characterised by their insolubility properties [117]), and its amount distributed at (x, t) is denoted here by $F(x, t)$. On the other hand, besides the major fibres components, the ECM contains also an entire host of other soluble constituents, such as calcium ions Ca^{2+} [28, 109], as well as other small proteins and soluble peptides that beyond a certain concentration threshold lead to the formation of insoluble amyloid fibrils [227], which notably have been found to support support cell adhesion [84, 90, 91, 119]. Thus, here all these ECM constituents that are not major fibres (i.e., these are neither collagen nor fibronectin) are bundled into a second ECM phase, and to immediately distinguish these from the ECM fibres, we simply refer to this phase as the *non-fibre ECM phase*. The spatio-temporal distribution of the non-fibre ECM phase at (x, t) is denoted by $l(x, t)$. Since ECM

is present in the body naturally, both fibre ECM phase $F(x,t)$ and non-fibre ECM phase $l(x,t)$ are defined within the maximal tissue cube Y.

Finally, for a compact notation, we denote by $\tilde{\boldsymbol{u}}$ the global three-dimensional tumour vector given by

$$\tilde{\boldsymbol{u}}(x,t) := (c(x,t), F(x,t), l(x,t))^T, \tag{2.1}$$

and $\rho(\tilde{\boldsymbol{u}})$ represents the total space occupied at position x, *i.e.*,

$$\rho(\tilde{\boldsymbol{u}}) = c(x,t) + F(x,t) + l(x,t), \tag{2.2}$$

for all $t \in [0,T]$ and all $x \in Y$.

Tumour cells population dynamics of the existing model

First, the cancer cell population $c(x,t)$ exercises not only random movement (captured here through diffusion), but their spatial transport of the cell population is further amended and biased by a directional movement induced by the cell-adhesion processes [115, 210, 292, 297]. Hence, assuming a logistic type growth (see [145, 146, 275]) with constant rate $\mu_c > 0$, the spatio-temporal dynamics of the cancer cell population can be expressed mathematically as:

$$\frac{\partial c}{\partial t} = \nabla \cdot \Big[D_c \nabla c - c\mathcal{A}_c(x,t,\tilde{\boldsymbol{u}},\theta_f) \Big] + \mu_c c(1-\rho(\tilde{\boldsymbol{u}})), \tag{2.3}$$

where $D_c > 0$ is a constant diffusion coefficient, and $\mathcal{A}_c(x,t,\tilde{\boldsymbol{u}},\theta_f)$ describes the cell-adhesion processes that bias the cancer cell population movement in accordance to the spatial heterogeneous distribution of the surrounding cancer cells and ECM components including the oriented ECM fibres. Hence, as in [245, 246, 247], here, we explore the adhesive interactions of the cells distributed at $x \in \Omega(t)$ with the other cancer cells as well as with the distribution of non-fibres ECM phase [84, 90, 91, 119]

and the oriented ECM fibres phase [294, 295] within a sensing region $\mathbf{B}(x,R)$ of radius $R>0$. Ultimately, such interactions can be mathematically expressed with the following non-local flux term:

$$\mathcal{A}_c(x,t,\tilde{\boldsymbol{u}},\theta_f) := \frac{1}{R}\int\limits_{\mathbf{B}(0,R)} \mathcal{K}(y)\Big[n(y)\big(\mathbf{S}_{cc}c(x+y,t)+\mathbf{S}_{cl}l(x+y,t)\big) + \widehat{n}(y,\theta_f(x+y,t))\mathbf{S}_{cF}F(x+y,t)\Big]\big[1-\rho(\tilde{\boldsymbol{u}}(x+y,t))\big]^{+}, \tag{2.4}$$

with the involved terms being detailed as follows. First, existing biological evidence [94, 109] (revealing the positive correlation between the availability of the extracellular Ca^{+2} ions within the ECM and the strength of the adhesion bonds that the cancer cells are able to establish between themselves) enables us to assume that the cell-cell adhesion strength $\mathbf{S}_{cc}$ depends on the non-fibre ECM density. Hence, proceeding here as in [245, 246, 247], we take $\mathbf{S}_{cc}$ to be of the form

$$\mathbf{S}_{cc}(x,t) := \mathbf{S}_{min} + (\mathbf{S}_{max}-\mathbf{S}_{min})\exp\left[1-\frac{1}{1-(1-l(x,t))^2}\right],$$

which smoothly explores a full range of cell-cell cancer self-adhesion strengths, from its maximum level $\mathbf{S}_{max}>0$ that corresponds to the Ca^{+2}-saturation level to its minimum values $\mathbf{S}_{min}>0$ that corresponds to the minimum level of Ca^{+2}. Finally, the cell-matrix adhesion manifests itself in this context both through adhesion between the cell and the ECM fibres [294, 295] and adhesion between the cells and non-ECM fibre phase (which includes for instance densities of amyloid fibrils that have been proved experimentally to support cell-adhesion [84, 90, 91, 119]). The adhesion strength between cancer cells and non-fibre ECM as well as the adhesion strength between cancer cells and fibre ECM, denoted here by $\mathbf{S}_{cl}$ and $\mathbf{S}_{cF}$, respectively, are considered to be positive constants. Furthermore, $n(\cdot)$ represents here

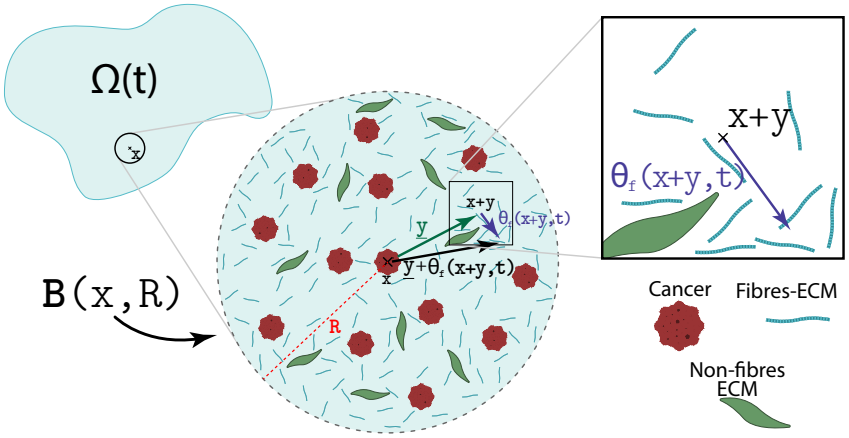

Figure 2.1: *Schematics of the cell-fibre adhesion that is biassed by the orientation of the fibres.*

the unit radial vector given by

$$n(y) := \begin{cases} \dfrac{y}{\parallel y \parallel} & \text{if } y \in \mathbf{B}(0,R) \setminus \{0\}, \\ 0 & \text{if } y = 0, \end{cases}$$

and $\widehat{n}(\cdot,\cdot)$ is the unit vector that is biased by the fibre orientations, i.e.,

$$\widehat{n}(y,\theta_f(x+y,t)) := \begin{cases} \dfrac{y+\theta_f(x+y,t)}{\parallel y+\theta_f(x+y,t) \parallel} & \text{if } y \in \mathbf{B}(0,R) \setminus \{0\}, \\ 0 & \text{if } y = 0 \text{ or } y = \theta_f(x+y,t), \end{cases} \tag{2.5}$$

where $\theta_f(x,t)$ is the orientation of the fibres at macro-scale that was derived and introduced for the first time in [245], being derived by exploring the structural micro-scale mass distribution of their constituent micro-fibres and characterising the spatial bias of the ECM fibres distributed at the macro-scale location $x \in Y$, see for details Section2.2.2. Figure 2.1 shows one of the biased vectors $y+\theta_f(x+y,t)$, with $y \in \mathbf{B}(0,R)$, that are involved in (2.5), illustrating the way in which the orientation of the ECM fibres bias the direction of vector y, crucially influencing the cell-fibre adhesion process.

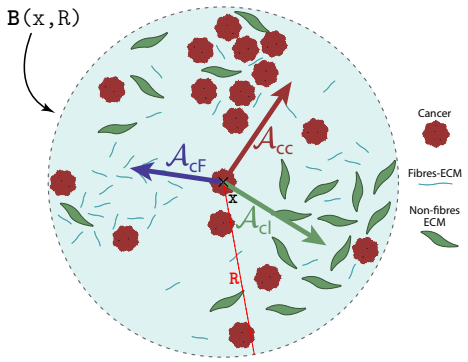

Figure 2.2: *Schematics of adhesion process inside the sensing region* $\mathbf{B}(x, R)$. *In order to illustrate this process, the adhesion term* $\mathcal{A}_c(\cdot, \cdot, \cdot, \cdot)$ *given in* (2.4) *is appropriately given as the sum of three main constituents, namely* $\mathcal{A}_{cc}$, $\mathcal{A}_{cl}$ *and* $\mathcal{A}_{cF}$ *that correspond to cell-cell, cell-non ECM fibres and cell-ECM fibres adhesions, respectively. Here we envisaged three regions inside the sensing region* $\mathbf{B}(x, R)$ *where one of the tumour components (i.e., either cancer cells, or ECM fibres or ECM non-fibres) is predominant and forms a local majority in terms of their spatial distribution versus the other two. In this context, the vector* $\mathcal{A}_{cl}$ *is pointing from the centre of the sensing region towards the non-fibre group because the non-local bonds are the strongest towards that direction. We see a similar behaviour for* $\mathcal{A}_{cc}$ *and* $\mathcal{A}_{cF}$. *However, the fibre adhesion is biased by the orientation of the fibres, and so the vector points towards a biased direction; see Figure 2.1. On the other hand, since* $\mathbf{S}_{cc}$ *depends on the density of non-fibre ECM, we observe that* $\mathcal{A}_{cc}$ *is aided by the position of the region where we have the grouping of the non-fibre component. Adding these elements together yields* $\mathcal{A}_c(x, t, \tilde{\boldsymbol{u}}, \theta_f)$ *that is given by* (2.4) *and so we expect the mass of tumour cells distributed at position* x *to move towards this direction.*

To account in (2.4) also for the gradual weakening of the adhesion between cancer cells and macrophages as well as of the adhesive bonds between the cancer cells at $x \in \Omega(t_0)$ and the cells and ECM fibre and non-fibre phases as we move away from the location x within $\mathbf{B}(x, R)$, we use a radially symmetric $\mathcal{K}(\cdot)$ that is given here by

$$\mathcal{K}(y) = \psi(\frac{y}{R}), \qquad \forall y \in \mathbf{B}(0, R), \tag{2.6}$$

where $\psi(\cdot)$ is the standard mollifier defined in Appendix A.2. Here, we can notice that due to the smoothness of the kernel $\mathcal{K}(\cdot)$, the adhesion integral A_c, defined in (2.4), is a smooth C^∞ function. Finally in (2.4), $(1 - \rho(\tilde{\boldsymbol{u}}))^+ = \max(0, 1 - \rho(\tilde{\boldsymbol{u}}))$ ensures that overcrowded tumour sites do not contribute to the migration of the cancer cells. To conclude, Figure 2.2 illustrates the way the adhesion flux $\mathcal{A}_c(x, t, \tilde{\boldsymbol{u}}, \theta_f)$ emerges, as this can be regarded as a sum of three different adhesion contributors, namely: $\mathcal{A}_{cc}$ for cell-cell cancer self-adhesion, $\mathcal{A}_{cl}$ for cell-non-fibre adhesion, and $\mathcal{A}_{cF}$ for cell-fibre adhesion, which are given by:

$$\begin{aligned}
\mathcal{A}_{cc}(x, t, \tilde{\boldsymbol{u}}, \theta_f) &:= \frac{1}{R} \int\limits_{\mathbf{B}(0,R)} \mathcal{K}(y) n(y) \big(\mathbf{S}_{cc} c(x + y, t)\big) \big[1 - \rho(\tilde{\boldsymbol{u}}(x + y, t))\big]^+, \\
\mathcal{A}_{cl}(x, t, \tilde{\boldsymbol{u}}, \theta_f) &:= \frac{1}{R} \int\limits_{\mathbf{B}(0,R)} \mathcal{K}(y) n(y) \big(\mathbf{S}_{cl} l(x + y, t)\big) \big[1 - \rho(\tilde{\boldsymbol{u}}(x + y, t))\big]^+, \\
\mathcal{A}_{cF}(x, t, \tilde{\boldsymbol{u}}, \theta_f) &:= \frac{1}{R} \int\limits_{\mathbf{B}(0,R)} \mathcal{K}(y) \widehat{n}(y) \big(\mathbf{S}_{cF} F(x + y, t)\big) \big[1 - \rho(\tilde{\boldsymbol{u}}(x + y, t))\big]^+.
\end{aligned}$$

Macro-scale dynamics of the fibres and non-fibre ECM phases of the existing model

Based on biological evidence that the components of non-fibre ECM phase (e.g., the amyloid fibrils) are degraded by several classes of matrix metalloproteinases [257, 153], here we follow [245, 246, 247] and consider the case when the non-fibre

ECM phase is getting degraded and remodelled by the tumour cells. Hence, the dynamics of the non-fibre component $l(x,t)$ is described by

$$\frac{\partial l}{\partial t} = -\lambda_{lc} c l + \alpha_1 (1 - \rho(\tilde{\boldsymbol{u}})), \tag{2.7}$$

where $\lambda_{lc} > 0$ denotes the rate of degradation and $\alpha_1 > 0$ is the remodelling rate.

Finally, the macroscopic ECM fibres $F(x,t)$ are also getting degraded by the cancer cell population (through the secretion of MDEs), and so their macro-scale dynamics can be mathematically formalised as

$$\frac{\partial F}{\partial t} = -\gamma_{Fc} c F, \tag{2.8}$$

where $\gamma_{Fc} > 0$ is the ECM fibres degradation rate caused by the cancer cells.

Summary of the existing macro-dynamics

In summary, using (2.3), (2.7) and (2.8) the coupled PDEs system that describes the existing macro-scale cancer invasion dynamics is given by

$$\frac{\partial c}{\partial t} = \nabla \cdot \Big[D_c \nabla c - c \boldsymbol{\mathcal{A}}(x,t,\tilde{\boldsymbol{u}},\theta_f) \Big] + \mu_c c (1 - \rho(\tilde{\boldsymbol{u}})), \tag{2.9a}$$

$$\frac{\partial F}{\partial t} = -\gamma_{Fc} c F, \tag{2.9b}$$

$$\frac{\partial l}{\partial t} = -\lambda_{lc} c l + \alpha_1 (1 - \rho(\tilde{\boldsymbol{u}})), \tag{2.9c}$$

with zero-flux boundary conditions. Finally in Table 2.1, we summarize the adhesion effects between the different constituents that were considered throughout this section.

	Cancer cells	Non-fibre ECM	Fibre ECM
Cancer cells	$\mathbf{S}_{cc}$	$\mathbf{S}_{cl}$	$\mathbf{S}_{cF}$
Non-fibre ECM	0	0	0
Fibre ECM	0	0	0

Table 2.1: *Summary of all adhesion processes that we consider in the existing macro-scale dynamics* (2.9).

2.2.2 Processes on the Micro-Scales and their Links to Macro-Scale within the Existing Model

The macro-scale cancer invasion process is accompanied by several closely linked micro-dynamic processes [293]. Particularly important are those micro-processes concerning the cell-scale spatial re-distribution of the ECM fibres micro-constituents caused by the interaction with the cancer cell population, and the cell-scale proteolytic processes occurring at the leading edge of the tumour. While different in nature, both of these micro-processes are intrinsically linked to the same macro-process, and in the following will explore the details of these micro-dynamics together with the associated double feedback links that connects them to the invasive tumour macro-dynamics.

Fibres: their micro-scale structure and macro-scale representation

As discussed in detail in [245], it is important to observe that the macroscopic ECM fibres are not only represented through their amount $F(x,t)$ distributed at $(x,t) \in \Omega(t) \times [0,T]$, but also through their naturally emerging spatial bias to withstand incoming cell fluxes and forces. This spatial bias is induced by their micro-scale distribution of micro-fibres $f(z,t)$ on a cell-scale micro-domain $\delta Y(x) := x + \delta Y$ of appropriate micro-scale size $\delta > 0$. Indeed, as derived and formalised in [245], these two important characteristics of the ECM fibres (i.e., the amount of distributed ECM fibres, and their associated spatial bias at (x,t)) can be captured simultaneously through a vector field representation of the ECM fibres, $\theta_f(x,t)$, that

is mathematically expressed as

$$\theta_f(x,t) := \frac{1}{\lambda(\delta Y(x))} \int\limits_{\delta Y(x)} f(z,t)\, dz \frac{\theta_{f,\delta Y(x)}(x,t)}{\parallel \theta_{f,\delta Y(x)}(x,t) \parallel_2}. \tag{2.10}$$

Here, λ is the Lebesgue measure in $\mathbb{R}^N$, $\parallel \cdot \parallel_2$ denoted the Euclidean norm (*i.e.* for an arbitrary vector $\boldsymbol{x} \in \mathbb{R}^N$ we define it as $\parallel \boldsymbol{x} \parallel_2 := (x_1^2 + \cdots + x_N^2)^{1/2}$ with $N = 2$) and $\theta_{f,\delta Y(x)}(x,t)$ is the revolving barycentral orientation with respect to the measure $f(z,t)\lambda(\cdot)$ that is induced and uniquely defined by the mass distribution of micro-fibres on the cell-scale micro-domain $\delta Y(x)$. This is given by the Bochner-mean-value [304] of the *barycentral vector-valued function* $\delta Y(x) \ni z \mapsto z - x \in \mathbb{R}^N$, namely

$$\theta_{f,\delta Y(x)}(x,t) := \frac{\int\limits_{\delta Y(x)} f(z,t)(z-x)\, dz}{\int\limits_{\delta Y(x)} f(z,t)\, dz}. \tag{2.11}$$

Finally, the magnitude of the ECM fibres is given by the Euclidean norm of $\theta_f(x,t)$, i.e.,

$$F(x,t) := \parallel \theta_f(x,t) \parallel_2,$$

and represents the mean-value of micro-fibres distributed on $\delta Y(x)$ at time $t \in [0,T]$.

Fibre rearrangement in the presence of cancer cells

Under the incidence of the macro-scale spatial flux generated by the tumour macro-dynamics, the rearrangement of the ECM fibres takes place on each micro-domain $\delta Y(x)$ through the spatial re-distribution of its micro-fibres constituents. As considered in [245], this process is instigated by the emerging macro-scale cancer cell flux $\mathcal{F}_c$, that is defined by:

$$\mathcal{F}_c(x,t) := D_c \nabla c(x,t) - c(x,t)\mathcal{A}_c(x,t,\tilde{\boldsymbol{u}},\theta_f), \tag{2.12}$$

Therefore, at any spatio-temporal node (x,t), the spatial flux $\mathcal{F}_c(x,t)$ that acts uniformly upon the fibres distributed on the micro-domain $\delta Y(x)$ results in the emergence of a *micro-fibres rearrangement vector* $r(\delta Y(x),t)$ given by

$$r(\delta Y(x),t) := \omega_c(x,t)\mathcal{F}_c(x,t) + (1-\omega_c)(x,t)\theta_f(x,t). \tag{2.13}$$

where the weight ω_c is defined by

$$\omega_c(x,t) := \frac{c(x,t)}{c(x,t)+F(x,t)}.$$

Then this rearrangement vector $r(\cdot,\cdot)$ acts upon the mass distribution of the micro-fibres $f(z,t)$ on $\delta Y(x)$, causing these to be spatially redistributed both on $\delta Y(x)$ and on the neighbouring micro-domains. Following [245], we use this naturally emerging macro-scale rearrangement vector $r(\delta Y(x),t)$, defined in (2.13), to construct the so-called *relocation vector* $\nu_{\delta Y(z)}$ (defined for each z on the micro-scale) that accounts not only for the rearrangement vector $r(\delta Y(x),t)$, but also upon the degree of alignment between the barycentral position vector $x_{dir}(z) := z - x$ and the acting rearrangement vector $r(\delta Y(x),t)$ as well as both the level of fibres saturation at z and the level of occupancy at the target position z^*. Thus, the relocation vector $\nu_{\delta Y(z)}(z,t)$ is mathematically formulated as:

$$\nu_{\delta Y(x)}(z,t) := \big[x_{dir}(z) + r(\delta Y(x),t)\big]\frac{f(z,t)[f_{max}-f(z,t)]}{f^{*}+ \parallel r(\delta Y(x),t) - x_{dir}(z) \parallel_2}\chi_{\{f(\cdot,t)>0\}},$$

with f_{max} being the maximum level of fibres at any micro-location $\zeta \in \delta Y(x)$, $f^* = f(z,t)/f_{max}$ being the micro-fibres level of saturation, and $\chi_{\{f(\cdot,t)>0\}}$ representing the characteristic function of the micro-fibres support. Ultimately such relocation vector $\nu_{\delta Y(z)}$ allows us to compute the new position z^* of each micro-point z as

$$z^* := z + \nu_{\delta Y(z)}(z,t).$$

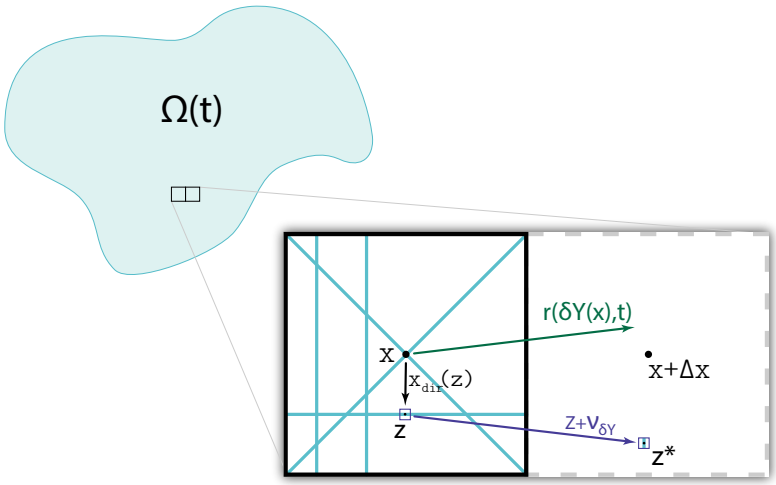

Figure 2.3: *Sketch of the micro-fibre reallocation to the neighbouring fibres micro-domain and the vectors required for the process.*

To highlight the role of each of these vectors in the micro-scale process, we refer the reader to Figure 2.3, where we consider a typical example of $x_{dir}(z)$, $r(\delta Y(x), t)$ and $\nu_{\delta Y(x)}(z, t)$.

Finally, the amount of fibres distributed at z that will be moved to the new micro position z^* is controlled by a movement probability $p_{_{move}}$ that explores the fibre capacity available at the new location, and so this is given as

$$p_{_{move}} := \max\left(0, \frac{f_{_{max}} - f(z^*)}{f_{_{max}}}\right),$$

and the amount of fibres moving to z^* being given by $p_{move} \cdot f(z, t)$ and the rest of the fibres $(1 - p_{move}) \cdot f(z, t)$ remaining at position z.

The existing boundary micro-scale dynamics

The second type of micro-dynamics that we consider here is that exercised by the proteolytic molecular processes occurring along the invasive edge of the tumour due to the cancer cells' ability to secrete various matrix-degrading enzymes (MDEs),

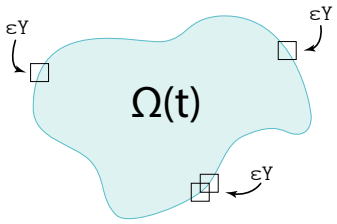

Figure 2.4: *Schematics of the overlapping ϵ-cubes that covers the boundary $\partial\Omega(t_0)$.*

which are essential for tumour progression. Secreted by the cancer cells within the outer proliferating rim of the tumour, these molecules exercise a cross-interface transport within a cell-scale neighbourhood of the tumour interface, leading to degradation of the ECM in the peritumoural region, ultimately resulting in changes of the tumour boundary morphology and subsequent further tumour progression.

To explore this emerging proteolytic micro-dynamics, we adopt the approach initially developed and introduced in [279]. Specifically, we denote by $m(\cdot,\cdot)$ the spatio-temporal distribution of MDEs that are transported within a cell-scale neighbourhood of $\partial\Omega(t)$. This neighbourhood is represented by the union of an appropriately constructed covering bundle of overlapping micro-domains $\{\epsilon Y\}_{\epsilon Y\in\mathcal{P}(t)}$ illustrated in Figure 2.4, which enable us to decompose the overall boundary dynamics into a union of proteolytic micro-dynamics taking place on each ϵY. Thus, for any macroscopic time $t_0 \in [0,T]$ on any boundary micro-domain ϵY, at any spatio-temporal location $(y,\tau) \in (\epsilon Y \cap \Omega(t_0)) \times [t_0, t_0+\Delta t]$, a source $h(\cdot,\cdot)$ of MDEs arise as a collective contribution of the cancer cells distributed within the tumour's outer proliferating rim within a distance $\gamma > 0$ from y. This source can be mathematically formulated as:

$$\begin{aligned} h(y,\tau) =& \frac{\int\limits_{\mathbf{B}(y,\gamma)\cap\Omega(t_0)} c(x,t_0+\tau)dx}{\lambda(\mathbf{B}(y,\gamma)\cap\Omega(t_0))}, \qquad y \in \epsilon Y \cap \Omega(t_0), \\ h(y,\tau) =& 0, \qquad y \notin \epsilon Y \setminus (\Omega(t_0) + \{z \in Y \mid \|z\|_2 < \rho\}), \end{aligned} \tag{2.14}$$

where $\mathbf{B}(y,\tau) := \{z \in Y \mid \|y-z\|_\infty \leq \gamma\}$ denotes the $\|\cdot\|_\infty$ ball with appropriately

chosen radius $\gamma > 0$ where the source of MDEs is accumulated, and $0 < \rho < \gamma$ is a small mollification range that smooths out the source $h(\cdot, \cdot)$ along the tumour interface. Also, the infinity norm is defined for an arbitrary vector $\boldsymbol{x} \in \mathbb{R}^N$ as $\| \boldsymbol{x} \|_\infty := \max(|x_1|, |x_2)$.

Finally, the source $h(\cdot, \cdot)$ defined in (2.14) allows us to formulate the MDE micro-dynamics

$$\begin{aligned} \frac{\partial m}{\partial \tau} &= D_m \Delta m + h(y, \tau), \\ m(y, 0) &= 0, \\ \frac{\partial m}{\partial n}\Big|_{\partial \epsilon Y} &= 0, \end{aligned} \tag{2.15}$$

which ultimately enables us to determine the movement of this interface. Hence, using the solution of (2.15), we adopt the technique developed in [279] to determine the relocation of the boundary. To that end, as described in [279], we select an appropriate dyadic decomposition $\{\mathcal{D}_k\}_{k \in \mathcal{J}}$ of the boundary micro-domain $\epsilon Y(x) \in \mathcal{P}(t)$. Furthermore, we denote by y_k the barycentre of each $\mathcal{D}_k$ and we further select a subfamily of dyadic cubes $\{\mathcal{D}_k\}_{\mathcal{J}^*}$ that are furthest away from x and are outside of $\Omega(t_0)$ with the property that they still support a level of MDEs that exceeds the mean of MDEs distributed on $\epsilon Y(x)$. Then, the transitional measure of movement that was introduced in [279] (assessing the likelihood of the boundary to migrate based on the amount of MDEs transported in the peritumoural region) is given by

$$q(x) := \frac{\int\limits_{\epsilon Y(x) \setminus \Omega(t_0)} m(y, \tau_f)\, dy}{\int\limits_{\epsilon Y(x)} m(y, \tau_f)\, dy}. \tag{2.16}$$

and is used to evaluate whether the boundary point x will be moved to a new location or will stay at the same position. This assessment is carried out by comparing the likelihood for invasion given by the transitional measure of movement with re-

spect to the significant level of peritumoural ECM degradation that is explored by a tissue parameter $\beta \in (0,1)$, as defined in [279]. This tissue parameter β explores the necessary level of significant (but not complete) ECM degradation for the tumour to progress, and captures the tissue conditions for invasion through the tissue thresholds $\omega : (0,1) \times \epsilon Y(x_B) \to [0,1]$ given by

$$\omega(\beta, \epsilon Y(x)) := \begin{cases} \sin\left[\dfrac{\pi}{2}\left(1 - \dfrac{\alpha(x)}{\beta}\right)\right] & \text{if } \alpha(x) \leq \beta, \\ \sin\left[\dfrac{\pi(\alpha(x)-\beta)}{2(1-\beta)}\right] & \text{if } \alpha(x) > \beta, \end{cases} \tag{2.17}$$

where $\alpha(x)$ is defined by

$$\alpha(x) := \frac{l(x, t+\Delta t) + F(x, t+\Delta t)}{\sup\limits_{\xi \in \partial\Omega(t_0)} \left[l(\xi, t+\Delta t) + F(\xi, t+\Delta t)\right]}.$$

Provided that sufficient degradation but not total destruction of the ECM has taken place over the time interval $[t_0, t_0 + \Delta t]$, situation that is explored by the condition

$$q(x) > \omega(\beta, \epsilon Y(x_B)),$$

Then the predicted tumour boundary movement is exercised in the direction $\eta_{\epsilon Y(x)}$ and magnitude $\xi_{\epsilon Y(x)}$ obtained from the boundary micro-dynamics (as described in [279]), given by

$$\begin{aligned} \eta_{\epsilon Y(x)} &:= x + \nu \sum_{l \in \mathcal{J}^*} \left(\int_{\mathcal{D}_l} m(y, \tau_f)\, dy \right) \Big(y_l - x \Big), \qquad \nu \in [0, \infty), \\ \xi_{\epsilon Y(x)} &:= \sum_{l \in \mathcal{J}^*} \frac{\int_{\mathcal{D}_l} m(y, \tau_f)\, dy}{\sum_{l \in \mathcal{J}^*} \int_{\mathcal{D}_l} m(y, \tau_f)\, dy} \parallel \overrightarrow{xy_l} \parallel_2 . \end{aligned} \tag{2.18}$$

On the other hand, when the ECM condition is not satisfied, *i.e.,* when $q(x) \not> $

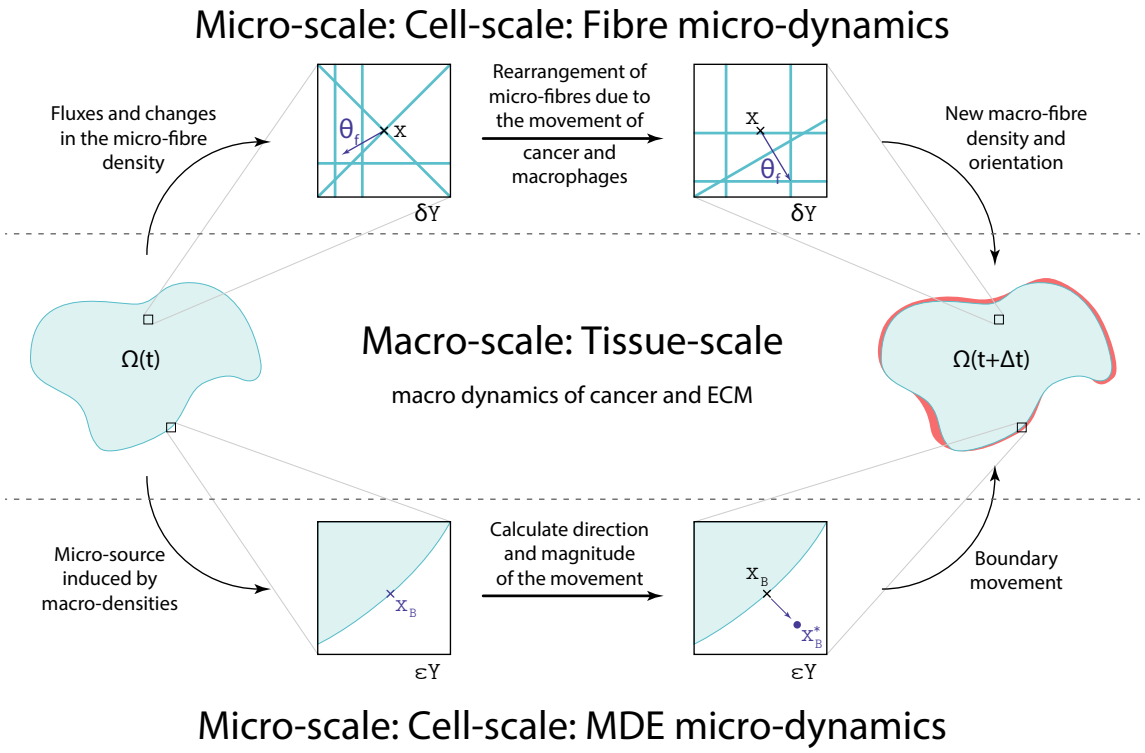

Figure 2.5: *Links between the scales, and how the scales affect each other, in particular, the link between boundary-micro and macro scales as well as fibre-micro and macro scales.*

$\omega(\beta, \epsilon Y(x_B))$ and so the ECM is either degraded too much or not enough, the boundary point x_B stays at the same position (or equivalently its movement magnitude is zero: $\xi_{\epsilon Y(x)} = 0$). This way, over the time interval $[t_0, t_0 + \Delta t]$, the macroscopic tumour $\Omega(t_0)$ will be progressed into a newly expanded invasive tumour domain $\Omega(t_0 + \Delta t)$.

2.2.3 Summary of the Links Between the Scales

In summary, both micro-scales have their unique link to the macro-scale and vice versa. First, we recall that the spatial flux defined in (2.12) result in a vector field induced by the movement of the cancer cells. This spatial flux interacts in a weighted manner with the oriented fibres (represented here again as a vector field),

ultimately enabling the rearrangement of distribution of the micro-scale constituents of the fibres (referred to as micro-fibres), resulting in a changed spatial orientation of the ECM fibres. This establishes a *fibres top-down* link and it is illustrated in Figure 2.5. On the other hand, the freshly rearranged micro-fibre density translate into a change of density as well as the orientation of the ECM fibres observed at the macro-scale, as detailed in Section 2.2.2, which in turn have a major impact upon the macro-scale dynamics (2.9). This establishes now a *fibres bottom-up* link, that connects the fibre-micro-scale to the macro-dynamics.

Shifting our focus to the relation between the boundary micro-dynamics and the macro-dynamics, the source of the MDEs (2.14) on the micro-scale is induced by the macro-scale population of cancer cells. Under the presence of this source, the micro-dynamics (2.15) takes place within a cell-scale neighbourhood enabled by a covering bundle of overlapping boundary micro-domains $\{\epsilon Y\}_{\epsilon Y \in \mathcal{P}(t)}$, and their solution on each of ϵY ultimately enables us to determine a direction and magnitude for the movement of the tumour boundary captured by ϵY. The local expansion of the tumour domain in the direction and by the magnitude determined from the proteolytic boundary micro-dynamics is finally exercised provided that a significant but not complete level of ECM degradation within the peritumoural tissue neghbourhood is realised. A quantification of this significant but not complete level of peritumoural degradation (which translates in the most favourable tissue conditions for invasion) is explored through a tissue parameter $\beta \in (0, 1)$ that has been introduced and formalised in [279], and also described in Section 2.2.2, but for full details, we refer the reader to this initial reference. Thus, this connection between the boundary micro-dynamics and macro-dynamics are again connected through a *top-down – bottom-up* double feedback loop that is illustrated in the bottom half of Figure 2.5.

2.3 Modelling Part 2: Novel Multiscale Modelling of Tumour and Macrophages Interacting Dynamics within Fibrous ECM

Building on the multiscale moving boundary modelling approaches proposed for cancer invasion in [245, 279] and described in Section 2.2, in this work we extend and advance this modelling platform by exploring further the macro- and micro-scale dynamics of the tumour invasion process. Specifically, in contrast to the situation addressed in [245, 279] and Section 2.2, we expand now the biological context by exploring the multiscale process of cancer cells invasion in the presence of M2 TAMs. This will extend the modelling presented in [245] and Section 2.2 by incorporating here the dynamics of M2 TAMs population and the impact of its directional motility on the overall tumour progression.

2.3.1 Macro-Scale Tumour-Macrophages Interacting Dynamics

Along with the macro-scale constituents considered in 2.2, *i.e.,* cancer cells $c(x,t)$, fibre $F(x,t)$ and non-fibre ECM $l(x,t)$ phases, here, we also consider the presence of a population of M2-like TAMs, denoted by $M_2(x,t)$ within the tumour domain $\Omega(t)$. Furthermore, M2 TAMs infiltrate the tumour as an immune response though the outer boundary that we denote by $\partial\Omega_o(t) \subset \partial\Omega(t)$, which is mathematically defined in Appendix A.1 and is illustrated schematically in Figure 2.6. Hence, here, we denote by $\partial\Omega(t)$ the boundary of the tumour in the usual sense and we denote by $\partial\Omega_o(t)$ a subset of the whole tumour boundary that for instance do not include the boundary of the "islands" located within the tumour, as illustrated in Figure 2.6. Finally, for a compact notation, we denote by $\mathbf{u}$ the global four-dimensional tumour

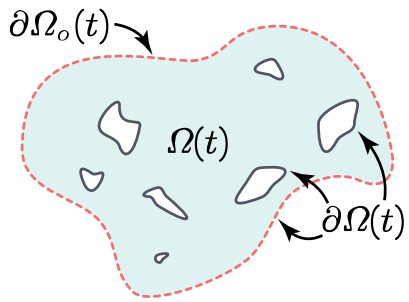

Figure 2.6: *Illustration of the outer boundary* $\partial\Omega_o(t)$ *that is highlighted with the* dashed red *line.*

vector given by

$$\mathbf{u}(x,t) := (c(x,t), F(x,t), l(x,t), M_2(x,t))^T, \tag{2.19}$$

and $\rho(\mathbf{u})$ represents the total space occupied at position x, *i.e.*,

$$\rho(\mathbf{u}) = c(x,t) + F(x,t) + l(x,t) + M_2(x,t), \tag{2.20}$$

for all $t \in [0,T]$ and all $x \in Y$.

Tumour cells population dynamics in the presence of M2 TAMs

Recent biological evidence shows that M2 TAMs macrophages enhance the cancer cell proliferation process [89]. Hence, assuming logistic type growth for the cancer cell population as in Section 2.2, this enhancement brought in by the macrophages leads to an augmented proliferation for the cancer cells, which can be captured mathematically as:

$$P_c(\mathbf{u}) := \mu_c c(1 + \mu_{cM} M_2)(1 - \rho(\mathbf{u}))^+, \tag{2.21}$$

where $\mu_c > 0$ is the baseline proliferation rate and $\mu_{cM} > 0$ is the cancer proliferation enhancement rate due to the presence of M2 TAMs. Furthermore, as in Section 2.2, we model the movement of the cancer cell population by both random and direc-

tional movement induced by the cell-adhesion processes [115, 210, 292, 297]. In this context, the spatio-temporal dynamics of the cancer cell population can therefore be expressed mathematically as:

$$\frac{\partial c}{\partial t} = \nabla \cdot \Big[D_c \nabla c - c\mathcal{A}_c(x,t,\mathbf{u},\theta_f) \Big] + P_c(\mathbf{u}), \tag{2.22}$$

where $D_c > 0$ is the constant diffusion coefficient, and $\mathcal{A}_c(x,t,\mathbf{u},\theta_f)$ describes the various cell-adhesion processes. Specifically, in addition to the situation considered in Section 2.2, here the flux term $\mathcal{A}_c(x,t,\mathbf{u},\theta_f)$ explores the key biological evidence underlining the contribution of the macrophages to the directional movement of the tumour cells. Indeed, this explores not only the fact that cancer cells bind themselves to TAMs [49], but also accounts for the experimental evidence detailed in [55, 92, 291, 300] that underscores the existence of a cross-talk between tumour cells and macrophages which is mediated through various chemokines. Further, while we do not model here explicitly the involved chemokine activities, mathematically we account for this cross-talk through the following non-local flux term:

$$\begin{aligned}\mathcal{A}_c(x,t,\mathbf{u},\theta_f) := \frac{1}{R} \int\limits_{\mathbf{B}(0,R)} \mathcal{K}(y) \Big[n(y) \big(\mathbf{S}_{cc} c(x+y,t) \\ + \mathbf{S}_{cM} M_2(x+y,t) + \mathbf{S}_{cl} l(x+y,t) \big) \\ + \widehat{n}(y, \theta_f(x+y,t)) \mathbf{S}_{cF} F(x+y,t) \Big] \big[1 - \rho(\mathbf{u}(x+y,t)) \big]^+,\end{aligned} \tag{2.23}$$

where $\mathbf{S}_{cc}$, $\mathbf{S}_{cl}$ and $\mathbf{S}_{cF}$ are the adhesion strengths of the cancer-cancer, cancer-non-fibre ECM and cancer-fibre ECM adhesions, R is the radius of the sensing region $\mathbf{B}(x,t)$, $n(\cdot)$ is the unit radial vector, $\widehat{n}(\cdot,\cdot)$ denotes the unit radial vector biased by the fibre orientations, $\mathcal{K}(y)$ accounts for the gradual weakening of the various adhesion bonds and $(1-\rho(\mathbf{u}))^+$ ensures that overcrowded tumour sites do not contribute to the migration of the cancer cells. All these components have

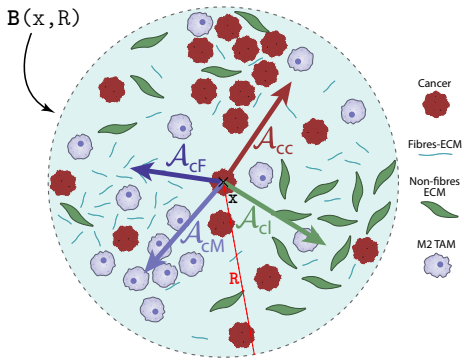

Figure 2.7: *Schematics of adhesion process inside the sensing region* $\mathbf{B}(x, R)$. *In order to illustrate this process, the adhesion term* $\mathcal{A}_c(\cdot, \cdot, \cdot, \cdot)$ *given in* (2.23) *is appropriately given as the sum of four main constituents, namely* $\mathcal{A}_{cc}$, $\mathcal{A}_{cl}$, $\mathcal{A}_{cF}$ *and* $\mathcal{A}_{cM}$ *that correspond to cell-cell, cell-non ECM fibres, cell-ECM fibres adhesions and cell-macrophage adhesion contributions, respectively. Here we envisaged four regions inside the sensing region* $\mathbf{B}(x, R)$ *where one of the tumour components (i.e., either cancer cells, or ECM fibres or ECM non-fibres or M2 TAMs) is predominant and forms a local majority in terms of their spatial distribution versus the other three. In this context, the vector* $\mathcal{A}_{cl}$ *is pointing from the centre of the sensing region towards the non-fibre group because the non-local bonds are the strongest towards that direction. We see a similar behaviour for* $\mathcal{A}_{cc}$, $\mathcal{A}_{cF}$ *and* $\mathcal{A}_{cM}$. *However, the fibre adhesion is biased by the orientation of the fibres, and so the vector points towards a biased direction; see Figure 2.1. On the other hand, since* $\mathbf{S}_{cc}$ *depends on the density of non-fibre ECM, we observe that* $\mathcal{A}_{cc}$ *is aided by the position of the region where we have the grouping of the non-fibre component. Finally,* $\mathcal{A}_{cM}$ *points from the centre point* x *towards the groupings of M2 TAMs due to adhesion. Adding these elements together yields* $\mathcal{A}_c(x, t, \mathbf{u}, \theta_f)$ *that is given by* (2.23) *and so we expect the mass of tumour cells distributed at position* x *to move towards this direction.*

already been introduced and defined in Section 2.2.1 except that here we plug in the tumour vector that contains also the macrophages $\mathbf{u}$ instead of $\tilde{\boldsymbol{u}}$ (which did not include the macrophages). However, with (2.23), we also account for a cancer-macrophage adhesion with strength $\mathbf{S}_{cM} > 0$.

In Figure 2.7, we illustrate the way the adhesion flux $\mathcal{A}_c(x, t, \mathbf{u}, \theta_f)$ emerges. As before, we note that this can be considered as the sum of all the different adhesion contributors, namely: $\mathcal{A}_{cc}$ for cell-cell cancer self-adhesion, $\mathcal{A}_{cM}$ for cell-macrophage adhesion, $\mathcal{A}_{cl}$ for cell-non-fibre adhesion, and $\mathcal{A}_{cF}$ for cell-fibre adhesion, that are

defined as:

$$\mathcal{A}_{cc}(x,t,\mathbf{u},\theta_f) := \frac{1}{R}\int\limits_{\mathbf{B}(0,R)} \mathcal{K}(y)n(y)\big(\mathbf{S}_{cc}c(x+y,t)\big)\big[1-\rho(\mathbf{u}(x+y,t))\big]^+,$$

$$\mathcal{A}_{cM}(x,t,\mathbf{u},\theta_f) := \frac{1}{R}\int\limits_{\mathbf{B}(0,R)} \mathcal{K}(y)n(y)\big(\mathbf{S}_{cM}M_2(x+y,t)\big)\big[1-\rho(\mathbf{u}(x+y,t))\big]^+,$$

$$\mathcal{A}_{cl}(x,t,\mathbf{u},\theta_f) := \frac{1}{R}\int\limits_{\mathbf{B}(0,R)} \mathcal{K}(y)n(y)\big(\mathbf{S}_{cl}l(x+y,t)\big)\big[1-\rho(\mathbf{u}(x+y,t))\big]^+,$$

$$\mathcal{A}_{cF}(x,t,\mathbf{u},\theta_f) := \frac{1}{R}\int\limits_{\mathbf{B}(0,R)} \mathcal{K}(y)\widehat{n}(y)\big(\mathbf{S}_{cF}F(x+y,t)\big)\big[1-\rho(\mathbf{u}(x+y,t))\big]^+.$$

Macro-scale dynamics of the fibres and non-fibre ECM phases in the presence of M2 TAMs

Here, we extend the context considered in [245, 246, 247] and Section 2.2, where the non-fibre ECM degradation was considered to be caused only by the MMPs secreted by the cancer cells. So now we consider not only the contribution of cancer cells but also that of the macrophages to the secretion of the various classes of matrix metalloproteinases [16, 114]. Hence, the degradation of the non-fibre ECM phase is caused indirectly (through the secretion of MMPs) not only by the tumour cells, at rate $\lambda_{lc} > 0$, but also by the M2 TAMs, at rate $\lambda_{lM} > 0$. Furthermore, while depending on the free space available, the remodelling of the ECM is also enhanced by the presence of the macrophages [3, 89, 254]. Hence, the dynamics of the non-fibre component $l(x,t)$ is described by

$$\frac{\partial l}{\partial t} = -l(\lambda_{lc}c + \lambda_{lM}M_2) + (\alpha_1 + \alpha_2 M_2)(1-\rho(\mathbf{u})), \tag{2.24}$$

where α_1 is the remodelling rate in the absence of M_2, and α_2 represents the remodelling enhancement rate enabled by the presence of M_2.

Moreover, at macro-scale the ECM fibres $F(x,t)$ are also degraded both by the cancer cells and by the macrophages (with collagen-endocytosing TAMs being one of the main contributors towards the degradation of collagen in tumours, according to [173]). Thus, their dynamics can be mathematically formalised as

$$\frac{\partial F}{\partial t} = -F(\gamma_{Fc}c + \gamma_{FM}M_2), \tag{2.25}$$

where γ_{Fc} and γ_{FM} are the ECM fibres degradation rates associated with cancer cells and macrophages, respectively.

M2 macrophage

The last macro-scale tumour constituent that we consider in this work is the family of M2 TAMs macrophages $M_2(x,t)$. To describe the macrophages dynamics we note that the experimental study in [229] showed that: (i) the number of peritumoral macrophages increased during oncogeny, (ii) the macrophages entering the circulation from the bone marrow (to reach the tumour site) already had a M2-phenotype, likely due to tumour-derived biochemical signals [229]. Moreover, the experimental study in [92] showed that TAMs localise at the invasive area of the tumour, where they secrete cytokines and proteases that contribute to tumour invasion. Therefore, in this study we assume that the M2-like macrophages enter the tumour through blood vessels at the tumour boundary, at a constant influx density M_0. Denoting the tumour boundary by $\Omega_o(t)$, we define the M2 influx term as follows:

$$M_I(x,t) := M_0(\chi_{\partial\Omega_o(t)} * \psi_\rho)(x). \tag{2.26}$$

Here, $\chi_{\partial\Omega_o(t)}$ represents the characteristic function of the outer boundary $\partial\Omega_o(t)$ (defined in Appendix A.1), $\psi_\rho(\cdot)$ denotes the standard mollifier given by $\psi_\rho(x) := \frac{1}{\rho^N}\psi(x)$ with a small cell-scale mollification range $\rho > 0$ and "$*$" is the convolution operator [64].

Regarding macrophages proliferation, on one hand biological evidence [40, 52, 122] shows that cancer cells trigger this proliferative process through the production of survival and proliferation factors. On the other hand, the ECM stiffness was also shown to enhance macrophages proliferation [2]. Furthermore, based on the biological evidence presented in [220], where it was demonstrated experimentally that increased collagen matrix density increases matrix stiffness (a fact that was further confirmed in [184, 298]), there exists a direct correlation between the ECM stiffness and the ECM fibre phase density. Hence, this direct correlation enables us to assume here not only that the ECM stiffness is directly proportional to the ECM fibre phase density, but in fact that the ECM stiffness is actually given directly by $F(x,t)$ (*i.e.*, the proportionality constant is considered here to be 1). Thus, the proliferation law of the macrophages can therefore be mathematically formulated as

$$P_M(\mathbf{u}) := \mu_M M_2 c(1+\mu_{MF}F)(1-\rho(\mathbf{u}))^+,$$

where $\mu_M > 0$ is the baseline proliferation rate, $\mu_{MF} > 0$ is the enhancement rate of the fibres and $(1-\rho(\mathbf{u}))^+$ ensures that there is no overcrowding.

Similar to the cancer cells, macrophages exercises not only random movement but also directed migration. Hence, we account for the random movement part via diffusion with a coefficient $D_M > 0$ (which for the time being is considered constant), while their directed movement is captured through an *adhesion* term that is similar to the one that we used for the cancer cell population in (2.23). Specifically, we consider here a cell-cell M2 TAMs self-adhesion with constant strength $\mathbf{S}_{MM} > 0$ and a macrophage-cancer cell adhesion with strength $\mathbf{S}_{Mc} > 0$ (we have already mentioned in Section 2.3.1 that cancer cells can bind themselves to TAMs, in addition to attracting TAMs, as shown in [55, 72, 299]). Finally, since we aim to explore the various factors that may affect macrophage movement, we also consider macrophage-fibre ECM adhesion with strength $\mathbf{S}_{MF} > 0$. Hence, the macrophage

adhesion term $\mathcal{A}_M(x,t,\mathbf{u},\cdot)$ is given by

$$\mathcal{A}_M(x,t,\mathbf{u},\theta_f) := \frac{1}{R}\int\limits_{\mathbf{B}(0,R)} \mathcal{K}(y)\Big[n(y)\big(\mathbf{S}_{MM}M_2(x+y,t)+\mathbf{S}_{Mc}c(x+y,t)\big) + \widehat{n}(y,\theta_f(x+y,t))\mathbf{S}_{MF}F(x+y,t)\Big]\big[1-\rho(\mathbf{u}(x+y,t))\big]^+. \tag{2.27}$$

We note here that the rest of the terms have already been introduced and defined in Section 2.2.1. Due to the similarities between the structure of the two adhesion fluxes, *i.e.*, $\mathcal{A}_c(x,t,\mathbf{u},\theta_f)$ given in (2.23) and $\mathcal{A}_M(x,t,\mathbf{u},\theta_f)$ given in (2.27), we refer the reader to Figure 2.1 and Figure 2.7 for illustration of the macrophage adhesion term (2.27).

Therefore, the dynamics of the M2-like macrophages $M_2(x,t)$ is given by

$$\frac{\partial M_2}{\partial t} = \nabla\cdot[D_M\nabla M_2 - M_2\mathcal{A}_M(x,t,\mathbf{u},\theta_f)] - d_M M_2 + M_I + P_M(\mathbf{u}), \tag{2.28}$$

where $d_M > 0$ represents the macrophages natural macrophages death rate.

Remark. *Since various experimental studies discuss the distribution of M2 TAMs macrophages inside tumour tissue and its prognostic value [158, 261], here we focus exclusively on the tumour-macrophage interactions on the tumour domain, rather than considering these mixed within the ECM further afield outside the tumour. This is another reason for which our modelling assumptions assume a macrophage influx through tumour boundary (see equation (2.26)).*

Summary of the macro-dynamics

In summary, using (2.22), (2.24), (2.25) and (2.28) the coupled system of PDEs that characterise this extended macro-scale cancer invasion dynamics is given by

$$\frac{\partial c}{\partial t} = \nabla \cdot \Big[D_c \nabla c - c\mathcal{A}(x,t,\mathbf{u},\theta_f) \Big] + P_c(\mathbf{u}), \tag{2.29a}$$

$$\frac{\partial F}{\partial t} = -F(\gamma_{Fc} c + \gamma_{FM} M_2), \tag{2.29b}$$

$$\frac{\partial l}{\partial t} = -l(\lambda_{lc} c + \lambda_{lM} M_2) + (\alpha_1 + \alpha_2 M_2)(1 - \rho(\mathbf{u})), \tag{2.29c}$$

$$\frac{\partial M_2}{\partial t} = \nabla \cdot [D_M \nabla M_2 - M_2 \mathcal{A}_M(x,t,\mathbf{u},\theta_f)] - d_M M_2 + M_I + P_M(\mathbf{u}), \tag{2.29d}$$

with zero-flux boundary conditions. Finally, in Table 2.2 we also summarise all the different adhesion effects/strengths that occurs between the various components of this extended model.

	Cancer cells	M2 TAMs	Non-fibre ECM	Fibre ECM
Cancer cells	$\mathbf{S}_{cc}$	$\mathbf{S}_{cM}$	$\mathbf{S}_{cl}$	$\mathbf{S}_{cF}$
M2 TAMs	$\mathbf{S}_{Mc}$	$\mathbf{S}_{MM}$	0	$\mathbf{S}_{MF}$
Non-fibre ECM	0	0	0	0
Fibre ECM	0	0	0	0

Table 2.2: *Summary of all adhesion processes that we consider in our macro-scale dynamics* (2.29).

2.3.2 Processes on the Micro-Scales and their Links to Macro-Scale in the presence of M2 TAMs

In this section, we detail the how the presence of M2 TAMs extends both micro-scale processes. However, we first note that the representation of fibres on the macro-scale does not change, and so to avoid repetition, we omit the details of the fibres bottom-up link.

Fibre rearrangement in the presence of both cancer cells and macrophages populations

As in Section 2.2, the rearrangement of the ECM fibres takes place on each micro-domain $\delta Y(x)$ due to the cell movements occurring at macro-scale. However, since M2 TAMs also secrete MDEs, this process is induced not only by the emerging macro-scale cancer cell flux $\mathcal{F}_c$ (as considered in Section 2.2), but also by the spatial flux of migrating M2 TAMs macrophages $\mathcal{F}_M$, these being defined by:

$$\begin{aligned} \mathcal{F}_c(x,t) :=& D_c \nabla c(x,t) - c(x,t)\mathcal{A}_c(x,t,\mathbf{u},\theta_f), \\ \mathcal{F}_M(x,t) :=& D_M \nabla M_2(x,t) - M_2(x,t)\mathcal{A}_M(x,t,\mathbf{u},\theta_f). \end{aligned} \tag{2.30}$$

Hence, now the emergence of the micro-fibres rearrangement vector $r(\delta Y(x),t)$ is due to the combined spatial flux $\mathcal{F}_c(x,t) + \mathcal{F}_M(x,t)$, and so is given by

$$r(\delta Y(x),t) := \omega_c(x,t)\mathcal{F}_c(x,t) + \omega_M(x,t)\mathcal{F}_M(x,t) + \omega_F(x,t)\theta_f(x,t). \tag{2.31}$$

where the weights are appropriately given by the associated mass fractions of cancer cells, macrophages, and ECM fibres distributed at at (x,t), namely:

$$\omega_c(x,t) := \tfrac{c(x,t)}{c(x,t)+F(x,t)+M_2(x,t)}, \quad \omega_M(x,t) := \tfrac{M_2(x,t)}{c(x,t)+F(x,t)+M_2(x,t)},$$
$$\omega_F(x,t) := \tfrac{F(x,t)}{c(x,t)+F(x,t)+M_2(x,t)}.$$

Then using this new extended rearrangement vector $r(\delta Y(x),t)$ (2.31), we can follow the same process as in Section 2.2 to construct the relocation vector $\nu_{\delta Y(z)}$ and ultimately determine both the new positions z^* of each micro-points z and the appropriate amount of fibres that will be moved to these new positions.

Boundary micro-scale in the presence of M2 TAMs

To account for the second micro-dynamics, *i.e.,* the proteolytic processes occurring along the tumour interface, we follow the same procedure as in Section 2.2. However, biological evidence suggest that besides cancer cells, TAMs also produce matrix-degrading enzymes (MDEs), such as matrix-metalloproteinases (MMP) of both type 2 (MMP-2) and of type 9 (MMP-9) molecules [89], which are essential for tumour progression. Thus, at any spatio-temporal location $(y, \tau) \in (\epsilon Y \cap \Omega(t_0)) \times [t_0, t_0 + \Delta t]$, the source $h(\cdot, \cdot)$ of MDEs now arise as a collective contribution of both the cancer cells and the macrophages distributed within a small neighbourhood of the tumour's invasive edge. Thus, we extend the source term by also considering the contribution of the M2 TAMs, and so we formulate $h(\cdot, \cdot)$ as:

$$\begin{aligned} h(y,\tau) =& \frac{\int\limits_{\mathbf{B}(y,\gamma)\cap\Omega(t_0)} \alpha_c c(x, t_0+\tau) + \alpha_M M_2(x, t_0+\tau) dx}{\lambda(\mathbf{B}(y,\gamma) \cap \Omega(t_0))}, \qquad y \in \epsilon Y \cap \Omega(t_0), \\ h(y,\tau) =& 0, \qquad y \notin \epsilon Y \setminus (\Omega(t_0) + \{z \in Y \mid \|z\|_2 < \rho\}), \end{aligned} \tag{2.32}$$

where α_c and α_M are the MDE secreting rate of the cancer and the M2 TAMs, respectively (and the rest of the terms remain the same as before in Section 2.2). Furthermore, since we do not have to modify the micro-dynamics of the MDEs defined in (2.15), the MDE bottom-up remains the same and to avoid repetition we omit the details of it and for further details we refer the reader to Section 2.2.

2.4 Numerical Approach

To describe our numerical approach, let us introduce some basic notation that will be used throughout the whole section. Let L be the length of Y and $h_L = \Delta x = \Delta y$ to be the spatial step size, that is uniform in both direction. The uniform discretisation

of the maximal tissue cube Y is represented through the set of discretised macro-spatial locations $\{(x_i, y_j)\}_{i,j=1...N}$, with $N = L/h_L + 1$.

To numerically solve the macro-dynamics (2.29) we adopt the non-local predictor-corrector scheme introduced in [245] (involving the Euler method as predictor, and a non-local Trapezoidal rule as corrector with uniform step size Δt) as well as we follow [70, 81, 82] to construct a flux limiter method for the spatial derivatives. Also, to evaluate the adhesion terms $\mathcal{A}_c$ and $\mathcal{A}_M$ defined in (2.23) and (2.27), respectively, we aim to use a fast convolution-driven approach. Finally, we detail the MDE-micro-scale calculations.

2.4.1 Macro-Scale Dynamics

In this section we focus on deriving the numerical scheme for model (2.29). Hence, in (2.29), we have two distinct spatial operators, namely a diffusion and an adhesion term. Since the form of both of these terms are similar for cancer cells and M2 TAMs, in the following we will focus only on describing the scheme that we derive for the cancer cell population.

Focusing now on the discretisation of the spatial operator in (2.29), which can be expressed as

$$\nabla \cdot \mathcal{F}_c := \nabla \cdot [(D_c \nabla c) - c\mathcal{A}_c],$$

let us start by addressing first the diffusion part, $\nabla \cdot (D_c \nabla c)$, and only afterwards will formulate the computational approach for the adhesion part $\nabla \cdot c\mathcal{A}_c$.

Discretisation of the diffusion operator $\nabla \cdot (D_c \nabla c)$

Since in this model we consider the diffusion coefficient D_c to be described by a positive constant, we can denote for convenience the gradient flux of the cancer cells by

$$\mathcal{F}_{c,D} := D_c \nabla c,$$

this diffusion part of the spatial operator $\nabla \cdot \mathcal{F}_{c,D}$ can therefore be rewritten as $\nabla \cdot (D_c \nabla c) = \nabla \cdot \mathcal{F}_{c,D}$, and to discretise this we simply use a second order central difference scheme with the usual 5 point stencil.

During the computations, we detect our expanding tumour domain $\Omega(t_0)$ via an indicator function denoted by $\mathcal{I}(\cdot,\cdot) : X \times Y \to \{0,1\}$, with $X = Y = \{1,...,N\}$, and defined by

$$\mathcal{I}(i,j) := \begin{cases} 1 & \text{if } (x_i, y_j) \in \Omega(t_0), \\ 0 & \text{otherwise.} \end{cases} \tag{2.33}$$

which enables us to determine whether a spatial node is inside or outside the tumour domain. Further, we construct a similar indicator function for the boundary nodes. Hence, let us denote this by $\mathcal{I}_B(\cdot,\cdot) : X \times Y \to \{0,1\}$ and define it as

$$\mathcal{I}_B(i,j) := \begin{cases} 1 & \text{if } (x_i, y_j) \in \partial\Omega(t_0), \\ 0 & \text{if } (x_i, y_j) \notin \partial\Omega(t_0), \end{cases} \tag{2.34}$$

where $\partial\Omega(t_0)$ denotes the boundary of the domain $\Omega(t_0)$. These two functions allow us to split the macro-scale dynamics computation into two parts, i.e., strictly inside the tumour and on the tumour boundary. The motivation behind this is that, given the complexity of our multiscale algorithm (where *"on-the-fly"* rearrangements of micro-fibres are required), to reduce the computational time, we aim to apply some appropriately constructed universal discrete macro-scale numerical operators that would enable us to deal with the approximation of the right-hand side spatial operators at as many macro-nodes as possible at once, ultimately resulting in a macro-scale computational techniques that is faster than the one proposed in [245]. However, due to the continuously changing tumour domain $\Omega(t)$ (resulting in an irregular tumour shape) and the presence of zero-flux boundary conditions for the tumour macro-dynamics, we cannot derive one global numerical approach for the dynamics at all the tumour macro-points, and rather we need to split the

computation in these two parts (i.e., inside the tumour and tumour boundary) and deal with them separately.

For convenience, we also define the indicator function for the interior of $\Omega(t_0)$ by $\mathcal{I}_I(\cdot,\cdot) = \mathcal{I}(\cdot,\cdot) - \mathcal{I}_B(\cdot,\cdot)$ as

$$\mathcal{I}_{In}(i,j) := \begin{cases} 1 & \text{if } (x_i, y_j) \in \Omega(t_0) \text{ and } (x_i, y_j) \notin \partial\Omega(t_0), \\ 0 & \text{else,} \end{cases} \tag{2.35}$$

Then using these two indicator functions (2.34) and (2.35) we also define two sets of points Λ_B and Λ_{In}, containing the boundary and interior nodes, respectively,

$$\begin{aligned} \Lambda_B &:= \{(i,j) \in X \times Y |\, \mathcal{I}_B(i,j) = 1\}, \\ \Lambda_{In} &:= \{(i,j) \in X \times Y |\, \mathcal{I}_{In}(i,j) = 1\}. \end{aligned} \tag{2.36}$$

Since, aiming to reduce computational cost, our goal is to partition the problem into two main computational components, it is therefore indispensable to split appropriately the numerical approximation of the diffusion part of the spatial operator, namely of $\nabla \cdot \mathcal{F}_{c,D}$. For this, let us notice that at any spatial node $(x_i, x_j) \in \Omega(t_0) \subset Y$, the discretisation of $\nabla \cdot \mathcal{F}_{c,D}$ can actually be represented as follows

$$\nabla \cdot \mathcal{F}_{c,D}(i,j) = \begin{cases} \nabla \cdot \mathcal{F}^{In}_{c,D}(i,j) & \text{if } (i,j) \in \Lambda_I, \\ \nabla \cdot \mathcal{F}^{B}_{c,D}(i,j) & \text{if } (i,j) \in \Lambda_B, \\ 0 & \text{else.} \end{cases} \tag{2.37}$$

Further, considering now the *three-row* matrices $\{T_i\}_{i=2,N-1}$

$$T_i := [\underbrace{\mathbf{0} \ldots \mathbf{0}}_{i-2}, \mathbf{I}_3, \underbrace{\mathbf{0} \ldots \mathbf{0}}_{N-i-1}] \tag{2.38}$$

where $\mathbf{0}$ represents an $3-$dimensional zero column vector and $\mathbf{I}_3$ is the 3×3 identity

matrix, for any $(i,j) \in \{2,\ldots,N-1\}$, we extract the 3×3 sub-matrices centred at (i,j) that contain the values at (i,j) and its corresponding 8 neighbouring locations for the various constituents of the coupled dynamics. Thus, these sub-matrices are given by

$$[c^n_{i,j}] = T_i\ c^n\ T_j^{\intercal}, \tag{2.39}$$

where c^n is the corresponding discretised values for the cell population at the mesh points $\{(x_i,y_j)\}_{i,j=1\ldots N}$, at time step n. With this notation (detailed in (2.39)), we will be able to represent finite difference approach for $\nabla\cdot\mathcal{F}_{c,D}$ in terms of matrix operations.

In this context, our scheme for spatial flux $\nabla\cdot\mathcal{F}_{c,D}(\cdot,\cdot)$ can be written down explicitly using central differences and midpoint approximations. Thus, for $\nabla\cdot\mathcal{F}^{In}_{c,D}(\cdot,\cdot)$, using the Hadamard product "$\circ$" (defined for completion in Appendix A.3 while for further details we refer the reader to [111]), $\forall(i,j)\in\Lambda_{In}$ and for any time-step n, we have that

$$\left(\nabla\cdot\mathcal{F}^{In}_{c,D}\right)^n_{i,j} = \frac{D_c}{\Delta x^2}\sum_{k=1}^{2}\left[\sum\left([c^n_{i,j}]\circ\mathcal{K}^k_F\right) - \sum\left([c^n_{i,j}]\circ\mathcal{K}^k_B\right)\right], \tag{2.40}$$

Here, $\sum$ denotes the Frobenius inner product [87], which, for completion, is also defined in the Appendix A.3. Furthermore, in (2.40) $\mathcal{K}^k_F$ and $\mathcal{K}^k_B$ denote the 3×3 matrices induced by the forward and backward differences at each $(i,j)\in\Lambda_I$, respectively. Hence, in both direction i (if $k=1$) and direction j (if $k=2$), these are given by:

$$\mathcal{K}^1_F = \begin{bmatrix}0&0&0\\1&-1&0\\0&0&0\end{bmatrix},\ \mathcal{K}^1_B = \begin{bmatrix}0&0&0\\0&1&-1\\0&0&0\end{bmatrix},\ \mathcal{K}^2_F = \begin{bmatrix}0&1&0\\0&-1&0\\0&0&0\end{bmatrix},\ \mathcal{K}^2_B = \begin{bmatrix}0&0&0\\0&1&0\\0&-1&0\end{bmatrix}. \tag{2.41}$$

Finally, we can observe that at the interior nodes of $\Omega(t_0)$, equation (2.40) can be

equivalently expressed via discrete convolutions, and so we can write this as

$$\left(\nabla \cdot \mathcal{F}^{In}_{c,D}\right)^n = \frac{D_c}{\Delta x^2} \sum_{k=1}^{2} \left[\left(c^n * \widetilde{\mathcal{K}}^k_F \right) - \left(c^n * \widetilde{\mathcal{K}}^k_B \right) \right], \tag{2.42}$$

where $*$ is the discrete convolution operator [64] for the discretised tumour dynamic constituents. Furthermore, due to the definition of discrete convolution, the $\widetilde{\mathcal{K}}$s used in (2.42) are appropriately derived from $\mathcal{K}$s (defined in (2.41)) and are given as

$$\widetilde{\mathcal{K}} := J_3 \mathcal{K} J_3,$$

where J_3 is the anti-diagonal identity matrix, *i.e.,*

$$J_3 = \begin{bmatrix} 0 & 0 & 1 \\ 0 & 1 & 0 \\ 1 & 0 & 0 \end{bmatrix}. \tag{2.43}$$

However, for the boundary nodes, the discretisation formulated in (2.42) could not be applicable directly, and so for this we revisit (2.40) by taking into account now the zero-flux boundary conditions. These boundary conditions are accounted for through a new family of 3×3 sub-matrices that are defined as follows:

$$[c^n_{i,j}]^B := [c^n_{i,j}] \circ [\mathcal{I}^n_{i,j}] + (J_3 [c^n_{i,j}] J_3) \circ \left(\mathbb{1} - [\mathcal{I}^n_{i,j}] \right) \tag{2.44}$$

where $\mathbb{1}$ is a 3×3 matrix of ones, J_3 is the anti-diagonal identity matrix defined in (2.43), while the 3×3 matrices $[\mathcal{I}^n_{i,j}]$ are given at each (i, j) by

$$[\mathcal{I}^n_{i,j}] := T_i \, \mathcal{I}^n \, T_j^{\intercal}.$$

Therefore, using (2.44) we separate these boundary-sub-matrices into two parts, *i.e.,* a part that is inside the tumour and to another part that is outside the tumour

(determined by the indicator function $\mathcal{I}$). Hence, in these 3×3 boundary-submatrices the distribution at the nodes that are inside the tumour are the same as the one defined in (2.39), but we appropriately provide values on the neighbouring nodes, captured by $[\mathcal{I}^n_{i,j}]$, outside the tumour so that we could implement the zero-flux boundary condition. Hence, at any time t_n, our scheme at any boundary node $(i,j) \in \Lambda_B$ is given by

$$\left(\nabla \cdot \mathcal{F}^B_{c,D}\right)^n_{i,j} = \frac{D_c}{\Delta x^2} \sum_{k=1}^{2} \left[\sum \left([c^n_{i,j}]^B \circ \mathcal{K}^k_F \right) - \sum \left([c^n_{i,j}]^B \circ \mathcal{K}^k_B \right) \right], \tag{2.45}$$

where the "$\mathcal{K}$" matrices involved here are the non-convolutional ones that we already defined in (2.41).

Discretisation of the *adhesion* operator $\nabla \cdot c\mathcal{A}_c$

Now we shift our attention to the cancer cell adhesion term $\nabla \cdot c\mathcal{A}_c$. Postponing for the moment, the spatial discretisation of the adhesion vector field $\mathcal{A}_c$ at time t_n, which we denote by $\mathcal{A}^n_c$, whose details will be discussed in Section 2.4.2, in the following we will focus on addressing the overall discretisation of the adhesion operator $\nabla \cdot c\mathcal{A}_c$, for which we will propose a flux limiter approach.

Although also here we will split the discretised spatial tumour domain into two regions, these will be slightly different from the interior and boundary parts mentioned in the previous section. Further, since we aim here is to use a flux limiter, such approach requires the usage of *"ghost" outside nodes* that are further away from the boundary nodes than their immediate neighbours (for instance the ghost point $(i+2, j)$ if $(i,j) \in \Lambda_B$). Thus, we appropriately split $\Omega(t_0)$ into two regions that we refer to as the *"layer"* and *"inside"* parts.

Focusing first on the *inside* part, this is determined by the requirements of the flux limiter (detailed below), which, for calculations at position (i,j), demands availabilities for the values of the quantities involved on a region that includes the

four neighbours (in both i and j direction) of the four neighbouring locations with respect to (i, j). Therefore, the *inside* part contains the discretised spatial region given by the macro-nodes of the domain $\Omega(t_0)$ that are at least two macro-nodes "distance" away from the boundary, hence this consists of all the points that are neither boundary points nor immediate neighbours of any boundary point. Thus, we can determine the *inside* part mathematically by considering the following indicator function denoted by $\mathcal{I}_I(\cdot,\cdot) : X \times Y \to \{0, 1\}$ and define by

$$\mathcal{I}_I(i,j) := \begin{cases} 1 & \text{if } (\mathcal{I} * \mathcal{K}_{in})_{i,j} = 1, \\ 0 & \text{if } (\mathcal{I} * \mathcal{K}_{in})_{i,j} = 0, \end{cases} \tag{2.46}$$

where $*$ is the discrete convolution operator, $\mathcal{I}$ is defined in (2.33) and $\mathcal{K}_{in}$ is defined by

$$\mathcal{K}_{in} = \frac{1}{13} \begin{bmatrix} 0 & 0 & 1 & 0 & 0 \\ 0 & 1 & 1 & 1 & 0 \\ 1 & 1 & 1 & 1 & 1 \\ 0 & 1 & 1 & 1 & 0 \\ 0 & 0 & 1 & 0 & 0 \end{bmatrix},$$

which is based on the stencil induced by the flux limiter scheme.

Turning now our attention to the *layer* part, the macro-nodes that are considered to be in this region of the discretised tumour domain $\Omega(t_0)$ are the ones that are either classified as boundary nodes or their immediate neighbours. The motivation behind this is again to treat nodes that use values at ghost/outside points differently than the ones that do not require such values during the approximation and would this way enable a reduction in the computational cost. Thus, the points in the *layer*

region are simply given by the difference indicator function $\mathcal{I}_L := \mathcal{I} - \mathcal{I}_I$, *i.e.*,

$$\mathcal{I}_L(i,j) := \begin{cases} 1 & \text{if } \mathcal{I}(i,j) - \mathcal{I}_I(i,j) = 1, \\ 0 & \text{if } \mathcal{I}(i,j) - \mathcal{I}_I(i,j) = 0. \end{cases} \tag{2.47}$$

Therefore, using (2.46) and (2.47), we obtain that the discretised *inside* and *layer* parts of $\Omega(t_0)$, denoted here by Λ_I and Λ_L, are given by the preimages $\Lambda_I := \mathcal{I}_I^{-1}(\{1\})$ and $\Lambda_L := \mathcal{I}_L^{-1}(\{1\})$, respectively, *i.e.,*

$$\begin{aligned} \Lambda_I &:= \{(i,j) \in X \times Y |\, \mathcal{I}_I(i,j) = 1\}, \\ \Lambda_L &:= \{(i,j) \in X \times Y |\, \mathcal{I}_L(i,j) = 1\}. \end{aligned}$$

Focusing now on computations on the *inside* region of $\Omega(t_0)$, at any time t_n and any inside node $(i,j) \in \Lambda_I$, the cancer cell adhesion discretisation is defined by

$$\nabla \cdot (c\mathcal{A}_c)^n_{i,j} := \frac{1}{\Delta x}\Big((H^x)^n_{i,j} - (H^x)^n_{i-1,j}\Big) + \frac{1}{\Delta y}\Big((H^y)^n_{i,j} - (H^y)^n_{i,j-1}\Big) \tag{2.48}$$

where $H^x_{i,j}$ and $H^y_{i,j}$ are defined as

$$\begin{aligned} (H^x)^n_{i,j} &:= \max\{0, \operatorname{sgn}[(\mathcal{F}^y_{c,\mathcal{A}})^n_{i,j}]\}(L^+_x)^n_{i,j} + \min\{0, \operatorname{sgn}[(\mathcal{F}^x_{c,\mathcal{A}})^n_{i,j}]\}(L^-_x)^n_{i,j}, \\ (H^y)^n_{i,j} &:= \max\{0, \operatorname{sgn}[(\mathcal{F}^y_{c,\mathcal{A}})^n_{i,j}]\}(L^+_y)^n_{i,j} + \min\{0, \operatorname{sgn}[(\mathcal{F}^y_{c,\mathcal{A}})^n_{i,j}]\}(L^-_y)^n_{i,j}. \end{aligned} \tag{2.49}$$

Here, for a compact notation, $(\mathcal{F}^x_{c,\mathcal{A}})^n_{i,j}$ and $(\mathcal{F}^y_{c,\mathcal{A}})^n_{i,j}$ denote the cancer cell adhesion fluxes and they are given by

$$\begin{aligned} (\mathcal{F}^x_{c,\mathcal{A}})^n_{i,j} &:= c^n_{i,j}\mathcal{A}^x_c(t_n, \mathbf{u}^n_{i,j}, (\theta_f)^n_{i,j}), \\ (\mathcal{F}^y_{c,\mathcal{A}})^n_{i,j} &:= c^n_{i,j}\mathcal{A}^y_c(t_n, \mathbf{u}^n_{i,j}, (\theta_f)^n_{i,j}), \end{aligned} \tag{2.50}$$

where $\mathbf{u}^n_{i,j} = (c^n_{i,j}, F^n_{i,j}, l^n_{i,j}, M^n_{i,j})^T$ (defined in (2.19)) with the matrices c^n, F^n, l^n, M^n_2 and $(\theta_f)^n$ represent the discrete values at the grid points of the cancer cells, fibres

ECM, non-fibres ECM, M2 TAMs, and oriented ECM fibres, respectively. Also, in (2.50) $\mathcal{A}_c^x$ and $\mathcal{A}_c^y$ denote the x and y components of the adhesion vector field $\mathcal{A}_c$, respectively.

Furthermore, in equations (2.49), the terms $(L_x^+)_{i,j}^n$, $(L_x^-)_{i,j}^n$, $(L_y^+)_{i,j}^n$ and $(L_y^-)_{i,j}^n$ are usually referred to as *state interpolants*, and to construct these we involve the so-called *limiter function* $\phi(r)$, which ultimately enables us to use second order approximation when the solution is smooth and a first order approximation near sharp gradients. Hence, these state interpolants at time t_n and any inside node $(i,j) \in \Lambda_I$ are defined by

$$\begin{aligned}
(L_x^+)_{i,j}^n :=& (\mathcal{F}_c^x)_{i,j}^n + \frac{1}{2}\phi(r_{i,j}^x)\Big((\mathcal{F}_c^x)_{i,j}^n - (\mathcal{F}_c^x)_{i-1,j}^n\Big),\\
(L_x^-)_{i,j}^n :=& (\mathcal{F}_c^x)_{i+1,j}^n + \frac{1}{2}\phi\left(\frac{1}{r_{i+1,j}^x}\right)\Big((\mathcal{F}_c^x)_{i+1,j}^n - (\mathcal{F}_c^x)_{i+2,j}^n\Big),\\
(L_y^+)_{i,j}^n :=& (\mathcal{F}_c^y)_{i,j}^n + \frac{1}{2}\phi(r_{i,j}^y)\Big((\mathcal{F}_c^y)_{i,j}^n - (\mathcal{F}_c^y)_{i,j-1}^n\Big),\\
(L_y^-)_{i,j}^n :=& (\mathcal{F}_c^y)_{i,j+1}^n + \frac{1}{2}\phi\left(\frac{1}{r_{i,j+1}^y}\right)\Big((\mathcal{F}_c^y)_{i,j+1}^n - (\mathcal{F}_c^y)_{i,j+2}^n\Big),
\end{aligned} \tag{2.51}$$

where $r_{i,j}^x$ and $r_{i,j}^y$ are the *smoothness monitor functions* in x and y directions, respectively, *i.e.*, they are given by

$$r_{i,j}^x := \begin{cases} \dfrac{(\mathcal{F}_c^x)_{i+1,j}^n - (\mathcal{F}_c^x)_{i,j}^n}{(\mathcal{F}_c^x)_{i,j}^n - (\mathcal{F}_c^x)_{i-1,j}^n} & \text{if } (\mathcal{F}_c^x)_{i,j}^n \neq (\mathcal{F}_c^x)_{i-1,j}^n \\ & \text{and } (\mathcal{F}_c^x)_{i+1,j}^n \neq (\mathcal{F}_c^x)_{i,j}^n, \\ 0 & \text{otherwise,} \end{cases} \tag{2.52a}$$

$$r_{i,j}^y := \begin{cases} \dfrac{(\mathcal{F}_c^y)_{i,j+1}^n - (\mathcal{F}_c^y)_{i,j}^n}{(\mathcal{F}_c^y)_{i,j}^n - (\mathcal{F}_c^y)_{i,j-1}^n} & \text{if } (\mathcal{F}_c^y)_{i,j}^n \neq (\mathcal{F}_c^y)_{i,j-1}^n \\ & \text{and } (\mathcal{F}_c^y)_{i,j+1}^n \neq (\mathcal{F}_c^y)_{i,j}^n, \\ 0 & \text{otherwise.} \end{cases} \tag{2.52b}$$

In all of our numerical simulations (presented Section 2.6) we use the so-called

"UMIST limiter function" [154] (although there are more limiter functions available [144]) that is given by

$$\phi(r) := \max[0, \min(2r, 0.25 + 0.75r, 0.75 + 0.25r, 2)],$$

which completes the flux limiter part of the scheme for any inside node $(i, j) \in \Lambda_I$ at time t_n.

Finally, we turn our attention to the computations on the *layer* part Λ_L of the discretised tumour domain $\Omega(t_0)$. To approximate the cancer cell adhesion term $\nabla \cdot c\mathcal{A}_c$ in this region, we use a first order upwind scheme, which we obtain by choosing $\phi \equiv 0$ in (2.51). Hence, with $\phi \equiv 0$, we can now use directly the method derived in (2.48)-(2.52) for any node that are a layer point, but not a boundary point, *i.e.*, at all spatial nodes $(i, j) \in \Lambda_L \setminus \Lambda_B$. This leaves us with only the boundary nodes where we still need to address the computation. Since at these points we also aim to use the unwinding scheme, we need to appropriately approximate the value of any ghost point. To that end, we involve a first order approximation of the cancer cell zero-flux boundary condition which then enables us to appropriately estimate the values at the required ghost/outside point. Finally, this allows us to use the method derived in (2.48)-(2.52), for any boundary node $(i, j) \in \Lambda_B$ at any time-step n, with $\phi \equiv 0$. Therefore, we have fully defined our numerical scheme for the spatial transport of the cancer cell population *i.e.* for $\nabla \cdot \mathcal{F}_c$. To avoid repetition, we did not include here also the details of the derivation of the numerical scheme for the M2 TAM macrophages, as, due to the similarity in the structures of the spatial operators (involved in the transport of M2 TAMs), the numerical treatment is identical to the one outlined for the cancer cell equation. Hence, the scheme derived in this Section is straightforward to implement for the M2 TAMs as well, or in fact for any other population with the same spatial operators and so we do not pay special attention for this procedure.

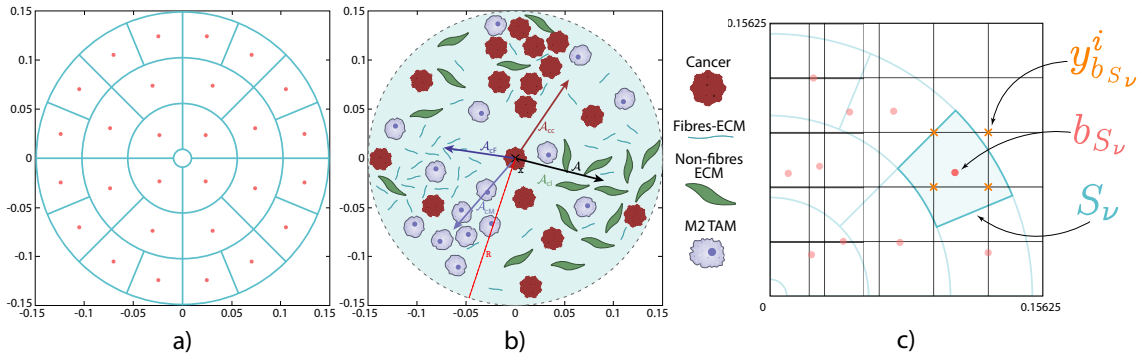

Figure 2.8: *The sensing region $B(0,R)$. a) Decomposition of the region using annulus sectors S_ν with barycentres b_{S_ν}, highlighted with red dots. b) Illustration of the vector valued $\mathcal{A}_c(x,y)$, influenced by the surrounding components and the strength of these bonds. c) Highlight of an annulus sector S_ν with its barycentre b_{S_ν} as well as the four neighbouring on-grid points $\{y^i_{b_{S_\nu}}\}_{i=1,4}$.*

2.4.2 Adhesion Terms

Focusing now our attention to the sensing region $x+\mathbf{B}(0,R)$, where the cell-adhesion processes cell-fibres ECM adhesion and cell-non-fibres ECM adhesion, as well as cell-cell self-adhesion and cell-cell adhesion for both cancer cells and M2 TAMs macrophages populations (modelled in (2.23) and (2.27)) are exercised, we adopt the partitioning of this region from [245] as illustrated in Figure 2.8. Furthermore, as the computational procedure is identical for both adhesion operators $\mathcal{A}_c$ (that is associated with cancer cell) and A_M (that is associated M2 TAMs macrophages), let us detail this approach simultaneously, *i.e.,* for the adhesion operator $\mathcal{A} \in \{\mathcal{A}_c, \mathcal{A}_M\}$.

Thus, let us denote the number of annulus sectors in this partitioning by N_s, and since this determined by the intersection of each of the s annuli centred at x with a number of uniformly distributed sectors $2^{m+(k-1)}$ (which is dyadic-ally increasing as k progresses from the first and inner most annulus to that last and biggest one), $k \in \{1,\ldots,s\}$, we have that

$$N_s := \sum_{k=1}^{s} 2^{m+(k-1)},$$

Then, denoting these annulus sectors by S_ν, with $\nu = 1, \ldots, N_s$, this enables us to approximate the adhesion integral (2.23) the integral of the step function associated with these sectors, whose value on each S_ν is appropriately constructed as a linear combination of the mean-values on S_ν of the cancer cell-populations, M2 TAMs macrophages, and ECM components involved in the adhesion processes described by (2.23) and (2.27).

Hence, to calculate these mean-values, on each S_ν, we first need to integrate the cancer and M2 TAM macrophages populations, the non-fibres ECM, the fibres ECM as well as the fibres orientation on S_ν. For this, we denote the off-grid barycentres of each annulus sector by b_{S_ν} and observe first that each b_{S_ν} belongs to the rectangle defined by its four immediately surrounding on-grid macro-mesh neighbouring nodes $\{y^i_{b_{S_\nu}}\}_{i=1,4}$, as illustrated in Figure 2.8 c), namely

$$b_{S_\nu} \in [y^1_{b_{S_\nu}}, y^3_{b_{S_\nu}}] \times [y^2_{b_{S_\nu}}, y^4_{b_{S_\nu}}],$$

Then, we use bi-linear shape functions to obtain the values of cancer population, M2 TAMs macrophages, the non-fibres ECM, the fibres ECM as well as the fibres orientation on S_ν at b_{S_ν} as a convex combination with uniquely determined weights β^k_ν, $k = 1, \ldots, 4$ of the values these quantities carry at the neighbouring on-grid points $\{y^i_{b_{S_\nu}}\}_{i=1,4}$.

Finally, since we seek to use again convolutions for our calculation, N_s different matrices are constructed (one for each barycentre) that we denote here by $\mathcal{K}^{S_\nu}_{\mathcal{A}}$. For this, considering an arbitrary annulus k and a sector j that defines S_ν, the associated

$\mathcal{K}_{\mathcal{A}}^{S_\nu}$ is given by

$$\mathcal{K}_{\mathcal{A}}^{S_\nu} = \begin{bmatrix} 0 & \dots & \dots & \dots & \dots & 0 \\ \vdots & & \ddots & & & \\ 0 & \dots & \beta_\nu^1 & \beta_\nu^3 & \dots & 0 \\ 0 & \dots & \beta_\nu^2 & \beta_\nu^4 & \dots & 0 \\ \vdots & & & \ddots & & \\ 0 & \dots & \dots & \dots & \dots & 0 \end{bmatrix},$$

which is a $P \times P-$ matrix (with $P := (\lceil 2R/\Delta x \rceil + 1)$) that corresponds to the on-grid minimal squared regions of macro-mesh points $\{y_x^i\}_{i=1,P^2}$ that cover the sensing region $\mathbf{B}(x, R)$, and that is nonzero only on the four positions corresponding to the barycentre b_{S_ν} neighbouring locations where this is given by the weights β_ν^k, $k = 1, \dots, 4$.

Therefore, at each instance of time t_n, the approximation of the adhesion integral $\mathcal{A} \in \{\mathcal{A}_c, \mathcal{A}_M\}$ is given by

$$\mathcal{A}^n = \sum_{\nu=1}^{N_s} \mathcal{A}_{S_\nu}^n,$$

where the expression of $\mathcal{A}_{S_\nu}^n$ for each of the two adhesion operators in $\{\mathcal{A}_c, \mathcal{A}_M\}$ are as follows:

– for $\mathcal{A} := \mathcal{A}_c$, we have

$$(\mathcal{A}_c)_{S_\nu}^n = \frac{K(b_{S_\nu})}{R}\Bigg[\left(n_\nu \widetilde{\mathcal{K}}_{\mathcal{A}}^{S_\nu}\right) * \left((\mathbf{S}_{cc}c^n + \mathbf{S}_{cl}l^n + \mathbf{S}_{cM}M_2^n) \circ (1 - \rho(\mathbf{u}^n))^+\right) + \left(\widehat{n}_\nu \widetilde{\mathcal{K}}_{\mathcal{A}}^{S_\nu}\right) * \left((\mathbf{S}_{cF}F^n) \circ (1 - \rho(\mathbf{u}^n))^+\right)\Bigg].$$

– for $\mathcal{A} := \mathcal{A}_M$, we have

$$(\mathcal{A}_M)_{S_\nu}^n = \frac{K(b_{S_\nu})}{R}\Bigg[\left(n_\nu \widetilde{\mathcal{K}}_{\mathcal{A}}^{S_\nu}\right) * \left((\mathbf{S}_{MM}M_2^n + \mathbf{S}_{Mc}c^n) \circ (1 - \rho(\mathbf{u}^n))^+\right) + \left(\widehat{n}_\nu \widetilde{\mathcal{K}}_{\mathcal{A}}^{S_\nu}\right) * \left((\mathbf{S}_{MF}F^n) \circ (1 - \rho(\mathbf{u}^n))^+\right)\Bigg].$$

with $\widetilde{\mathcal{K}}_{\mathcal{A}}^{S_\nu}$ being the flipped matrix associated with $\mathcal{K}_{\mathcal{A}}^{S_\nu}$ obtained with the help of the J_3 anti-diagonal identity matrix defined in (2.43), *i.e.,*

$$\widetilde{\mathcal{K}}_{\mathcal{A}}^{S_\nu} := J_3 \mathcal{K}_{\mathcal{A}}^{S_\nu} J_3.$$

2.4.3 Boundary Micro-Scale Dynamics

To calculate the source term $h(\cdot,\cdot)$ defined in (2.32) which is used in the MDE micro-scale equation (2.15), we need to integrate the cancer and M2 TAMs densities. For any such integral we can use discrete convolutions with an appropriately chosen matrix $\mathcal{K}_I$ that will be detailed below. As before, we split the source into two parts

$$h(i,j) = \begin{cases} h_I(i,j) & \text{if } (i,j) \in \Lambda_{In} \cup \Lambda_B, \\ 0 & \text{else.} \end{cases}$$

Hence, at time t_n the source inside the tumour domain is given by

$$h_I^n = 4\gamma^2 \frac{(N_f-1)^2}{\mathcal{I} * \mathbb{1}} \circ \Big[\big(\alpha_c c^n + \alpha_M M_2^n \big) * \mathcal{K}_I \Big], \tag{2.53}$$

where, $\mathcal{I}$ was defined in (2.33), $\mathbb{1}$ is a matrix of ones with size being the same as $\mathcal{K}_I$ that is a $[2\gamma/\Delta x + 1] \times [2\gamma/\Delta x + 1]$ matrix with γ defined in (2.32). Equation (2.53) is simply the measure of the boundary domain ϵY multiplied by the ratio of the nodes that lie inside the tumour times the integral. For our calculations, we construct $\mathcal{K}_I$ via the trapezoidal method, and so this is given by

$$\mathcal{K}_I = \begin{bmatrix} 1 & 2 & \dots & 2 & 1 \\ 2 & 4 & \dots & 4 & 2 \\ \vdots & \vdots & \ddots & \vdots & \vdots \\ 2 & 4 & \dots & 4 & 2 \\ 1 & 2 & \dots & 2 & 1 \end{bmatrix}.$$

At this point, we need to note that besides the usual error that the trapezoidal method gives due to the discontinuity we have in $B(y,\gamma) \cap \Omega(t)$ using a universal matrix for the integration has its drawbacks. This is because when we use the same matrix $\mathcal{K}_I$ for each $B(y,\gamma) \cap \Omega(t)$, then essentially we ignore that the function is discontinuous, resulting in an increase in the coefficients of the boundary nodes. On the other hand, by constructing unique kernels, we also run into difficulties in some cases; therefore, a universal matrix $\mathcal{K}_I$ was chosen to calculate the integral.

Since both cancer and macrophage densities are on the macro-scale, and we need to solve the MDE equation defined in (2.15) on the micro-scale, the source needs to be approximated on each micro point y. To do this, we adopt the technique described in [279], *i.e.,* involving bilinear shape functions on a square micro-mesh. Finally, due to the simplicity of the equation, we involve the Method of Lines, where the time-marching is carried out via the backward Euler method, while the space discretisation is based on central differences.

2.5 Parameter Values

In Table 2.3 we present the baseline set of parameters that we will use in the upcoming section.

Table 2.3: *Parameter set used for the numerical simulations in this chapter. If we could not find any references for some of our parameters then we "Estimated" them (i.e., we chose an arbitrary value for the simulations).*

Variable	Value	Description	Reference
D_c	10^{-4}	Diffusion coeff. for the cancer cell population c	[70]
D_M	5×10^{-5}	Diffusion coeff. for the M2	Est. using [101]

Continued on next page

Table 2.3 – continued from previous page

Variable	Value	Description	Reference
		TAM population M_2	
D_m	2.5×10^{-3}	Diffusion coeff. for MDEs	[206]
$\mathbf{S}_{max}$	0.5	Cell-cell adhesion coeff.	[245]
$\mathbf{S}_{min}$	0.01	Minimum level of cell-cell adhesion	Estimated
$\mathbf{S}_{cl}$	0.01	Cell-non-fibre adhesion coeff.	[245]
$\mathbf{S}_{cM}$	0.125	Cell-macrophage adhesion coeff.	Estimated
$\mathbf{S}_{cF}$	0.3	Cell-fibre adhesion coeff.	[70]
$\mathbf{S}_{MM}$	0.175	Macrophage self adhesion coeff.	Estimated
$\mathbf{S}_{Mc}$	0.125	Macrophage-cancer adhesion coeff.	Estimated
$\mathbf{S}_{MF}$	0.3	Macrophage-fibre adhesion coeff.	Estimated
μ_c	0.25	Proliferation coeff. for cancer cell population c	[70]
μ_{cM}	1.4	Coeff. for the M2 TAMs dependence in the cancer cell proliferation	Est. using [113]
M_0	0.05	Influx of the M2 TAMs	Estimated
μ_M	0.1	Inside tissue proliferation rate of M2 TAMs	Estimated
μMF	2.4	Coeff. for the ECM stiffness dependence in the M2 TAMs proliferation	Est. using [101]

Continued on next page

Table 2.3 – continued from previous page

Variable	Value	Description	Reference
d_M	0.03	Decay rate of M_2	Est. using [259]
λ_{lc}	1.0	Degradation coeff. for non-fibre ECM due to the tumour	Estimated
λ_{lM}	1.0	Degradation coeff. for non-fibre ECM due to the M2 TAMs	Estimated
γ_{Fc}	0.75	Degradation coeff. for fibre ECM due to the tumour	Estimated
γ_{FM}	0.75	Degradation coeff. for fibre ECM due to the M2 TAMs	Estimated
α_1	0	Baseline remodelling	Estimated
α_2	0	Remodelling of the non-fibre ECM due to the M2 TAMs	Estimated
α_c	1	MDE secreting rate by the cancer cells	Estimated
α_M	1	MDE secreting rate by the M2 TAMs	Estimated
R	0.15	Sensing radius	[245]
r	0.0016	Width of micro-fibres	[245]
f_{max}	0.6360	Maximum of micro-fibre density at any point	[245]
p	0.2	Percentage of non-fibre ECM	[245]

Continued on next page

Table 2.3 – continued from previous page

Variable	Value	Description	Reference
h_L	0.03125	Macro-scale spatial step-size	[279]
ϵ	0.0625	Size of the boundary micro-domain $\epsilon Y(\mathbf{x})$	[279]
δ	0.03125	Size of the fibre micro-domain $\delta Y(\mathbf{x})$	[245]
Δt	10^{-3}	Macro-scale temporal step size	Estimated
$\Delta \tau$	10^{-4}	MDE micro-scale temporal step size	Estimated

2.6 Computational Simulations

For the numerical simulations we consider a spatial domain $Y = [0, 4] \times [0, 4]$. We start with the following initial conditions

$$\begin{aligned} c(x,0) &= 0.2 \cdot \chi_{\mathbf{B}((2,2),0.25)}(x), \\ l(x,0) &= \min\left(\frac{1}{2} + \frac{1}{4}\sin(7\pi x_1 x_2)^3 \cdot \sin\left(7\pi \frac{x_2}{x_1}\right), 1 - c(x,0)\right), \\ M_2(x,0) &= \frac{1}{2} \cdot c(x,0), \end{aligned} \tag{2.54}$$

where, for consistency, we take the form of the non-fibre phase from previous works [245, 246, 247].

These macro-scale initial conditions can be seen in Figure 2.9 a). Here, the white curves indicate the boundary of the tumour. In Figure 2.9 b) we show the initial condition for one micro-scale fibre domain $\delta Y(x)$, which is repeated for all macro-scale points. Note that the pattern of the fibres on the micro-scale is not visible on the macro-scale because in order to get the density of the fibres at any macro-point

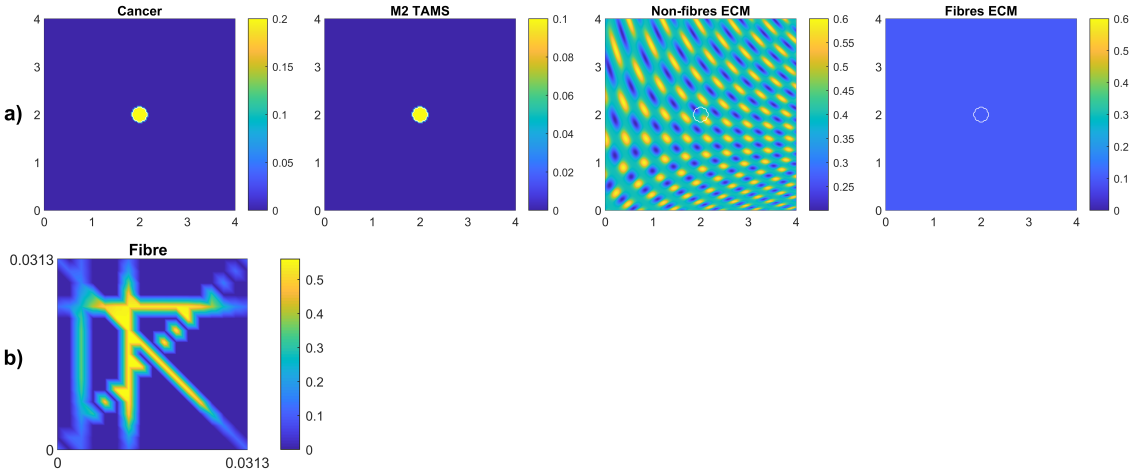

Figure 2.9: *a) Initial conditions for the macro scale densities i.e. for cancer, non-fibre ECM and fibres ECM defined in* (2.54)*. b) The initial condition of one micro-fibre domain which is repeated for every point on the macro scale.*

x we integrate the corresponding fibre-micro domain $\delta Y(x)$ seen in Figure 2.9 b). We note here that the ratio between the fibres and non-fibres components of ECM is assumed to be $20\% : 80\%$, a choice which is based on previous works [245, 246, 247].

In this section, we present all of our simulations at time $50\Delta t$, using the parameter values from the set $\mathcal{S}$ described in Table 2.3 which we regard as baseline, and any departure from these values will be stated accordingly.

We note here that any small differences in the model outcomes will be exclusively the result of changes in the parameter values, and not of any model stochasticity, as all equations and initial conditions are deterministic.

2.6.1 Simulation Results

In this section we investigate numerically the dynamics of the macro-scale model (2.29), where both cancer and macrophage diffusions are constants.

Baseline dynamics. In Figure 2.10 we show the distribution of macroscopic variables at time $50\Delta t$, when we assume that all macrophage adhesion terms are zero:

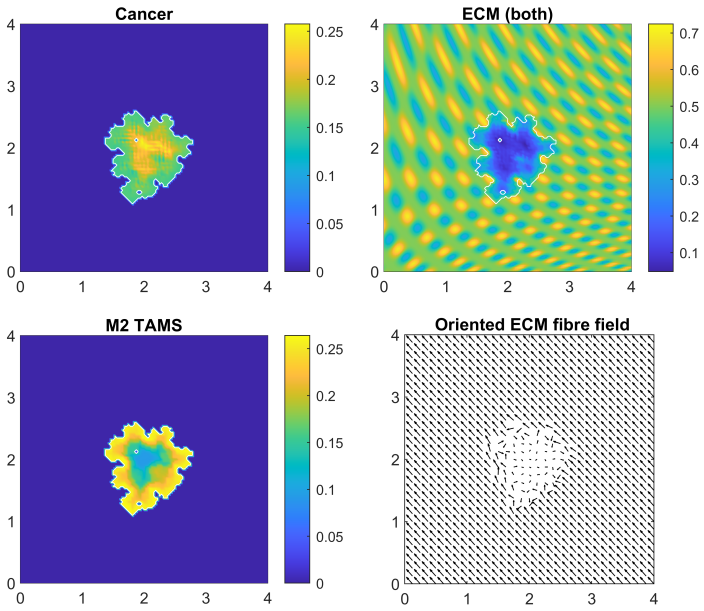

Figure 2.10: *Baseline simulation at time* $50\Delta t$ *where none of the newly introduced adhesions are present* i.e., *we set* $\mathbf{S}_{cM} = 0$, $\mathbf{S}_{MM} = 0$, $\mathbf{S}_{Mc} = 0$ *and* $\mathbf{S}_{MF} = 0$.

$\mathbf{S}_{cM} = 0$, $\mathbf{S}_{MM} = 0$, $\mathbf{S}_{Mc} = 0$ and $\mathbf{S}_{MF} = 0$ (while all other parameters are as in Table 2.3). We observe that in this case the M2 TAMs are located near the outer boundary of the tumour. This is the result of the assumptions that macrophages infiltrate the tumour though the outer boundary (see Eq. (2.26)), and that macrophages diffuse with constant coefficient. Further, we observe that the initial homogeneous cancer cell density becomes heterogeneous due to the many cancer cell adhesion precesses, highly influenced by the rearranged and degraded ECM (caused by both cancer cells and TAMs). On the other hand, in peritumoral regions, the ECM degradation creates free space for the tumour to expand and spread to the neighbouring tissues resulting in some *tumour fingering*, which gives an irregular tumour domain (that mainly follows the ECM pattern). This effect is complemented by the rearrangement of the micro-fibres that ultimately induces new a fibre structure. For illustrative purposes, in Figure 2.10 we coarsen four-fold the ECM fibre field.

The impact of macrophage interactions on tumour dynamics. In Figure 2.11 we investigate the effect of each individual adhesion interaction that we introduced in this paper *i.e.*, cancer-M2, M2-M2, M2-cancer and M2-fibres interactions. For comparison purposes, Figure 2.11a) shows again the baseline cancer and TAM dynamics (as copied from Figure 2.10).

In Figure 2.11b) we show the effect of cancer-M2 adhesion interaction (i.e., $\mathbf{S}_{cM} = 0.125$, while $\mathbf{S}_{MM} = \mathbf{S}_{Mc} = \mathbf{S}_{MF} = 0$). Interestingly, we do not see much difference compared to Figure 2.11a) (baseline simulation). This may indicate that this particular interaction is overwhelmed by the many other cancer cell-cell and cell-ECM adhesive interactions, and thus the cancer-M2 adhesion alone is not powerful enough to lead to a distinct tumour invasion pattern.

In Figure 2.11c) we show the effect of M2 TAMs self-adhesion (i.e., $\mathbf{S}_{MM} = 0.175$ and $\mathbf{S}_{cM} = \mathbf{S}_{Mc} = \mathbf{S}_{MF} = 0$). Compared to the baseline simulations, here the density of M2 TAMs becomes higher in the peripheral tumour region. As expected, when macrophages infiltrate the tumour, they prefer not to migrate but to stay together (due to $\mathbf{S}_{MM} > 0$).

In Figure 2.11d) we consider the M2-cancer adhesion process (i.e., $S_{Mc} = 0.125$, and $\mathbf{S}_{cM} = \mathbf{S}_{MM} = \mathbf{S}_{MF} = 0$). We notice here a more aggressive tumour fingering morphology compared to the baseline result. Moreover, the minimum of the M2 TAMs density inside the tumour domain is also decreased. To understand the reason behind this we refer to the M2-cancer adhesion part of (2.27), where we note that this process does not only depend on the cancer cell density but also on the free space available (accounted for via $(1 - \rho(\mathbf{u}))^+$). Therefore, M2 TAMs prefer areas of the tumour domain where the density of the cancer cells is high yet not too high, so that there is some free space available. Hence, this process could be one of the mechanisms responsible for accumulating and keeping M2 TAMs in the peripheral region.

In Figure 2.11e) we consider the effect of M2-fibre adhesion (to explore the

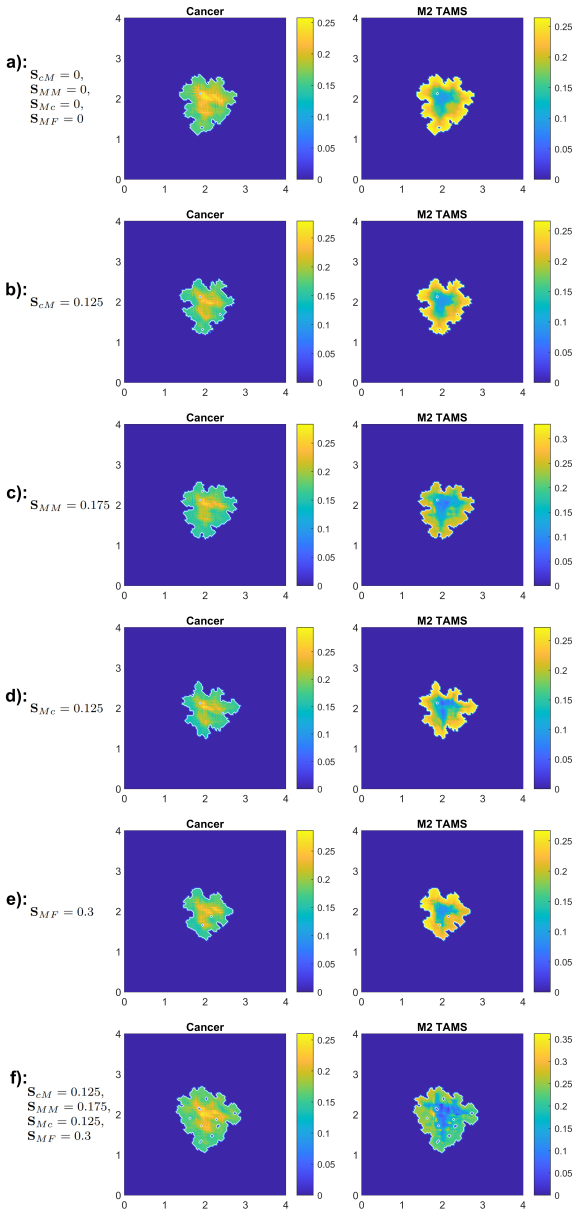

Figure 2.11: *Simulations illustrating the effects of each freshly introduced adhesion separately. Hence, a) corresponds to the baseline solution (also seen in Figure 2.10), and b)-e) represent the effect of each strength* $\mathbf{S}_{cM}$, $\mathbf{S}_{MM}$, $\mathbf{S}_{Mc}$ *and* $\mathbf{S}_{MF}$, *respectively. Finally, f) corresponds to their combined effects* (i.e., *we take* $\mathbf{S}_{cM}$, $\mathbf{S}_{MM}$, $\mathbf{S}_{Mc}$ *and* $\mathbf{S}_{MF}$ *from the parameter set* $\mathcal{S}$ *in Table 2.3). Each simulation presented in this figure uses the initial conditions from* (2.54) *and Figure 2.9 as well as corresponds to* $50\Delta t$.

possibility that M2 TAMs movement depends also on the oriented ECM fibres). To this end we set $\mathbf{S}_{MF} = 0.3$ (and $\mathbf{S}_{cM} = \mathbf{S}_{MM} = \mathbf{S}_{Mc} = 0$). Comparing this simulation result with the baseline result shown in Figure 2.11a), we can see that the M2 TAMs follow the fibre orientations. Since we assumed aligned ECM fibres (*i.e.*, induced by the oriented ECM fibre density shown in Figure 2.9b)), the M2 TAM density in the peripheral region is higher in the direction of the oriented ECM fibres (as the initial ECM fibres have all the same top-left orientations on the macro-scale), and so at the top-left region of the tumour the M2 TAMs macrophages density is higher. This indicates that M2 TAMs accumulations may also depend on the oriented ECM fibre distribution.

Finally, in Figure 2.11f), we combine all these adhesion processes (i.e., we use the values from the parameter set $\mathcal{S}$ in Table 2.3 for $\mathbf{S}_{cM}$, $\mathbf{S}_{MM}$, $\mathbf{S}_{Mc}$ and $\mathbf{S}_{MF}$). Until this point, we have not emphasised the fact that by considering each of these processes separately, we observed a slightly smaller tumour spread compared to the baseline simulation. However, as shown in Figure 2.11f), by combining all these adhesion processes, we see an increase in tumour spread. This suggests that it may not be enough to focus only on one aspect of macrophages and rather we need to focus on these processes as a whole in order to stop the pro-tumoural behaviour of the M2 TAMs. Hence, these different adhesion processes may work with and magnify each other in an underlying fashion that creates a favourable environment for tumour development.

The impact of ECM fibre structure and fibre-adhesion strengths on tumour dynamics. Next, we explore how the fibrous composition of ECM and the corresponding fibre-adhesion strengths affect the evolution of the solid tumour. In Figure 2.12, we investigate the effect of changing (i) the ECM fibre percentage (compared to the non-fibre ECM), and (ii) the M2-fibre and cancer-fibre adhesion strengths, for the particular case where we have only M2-fibre adhesion (i.e.,

$\mathbf{S}_{cM} = 0$, $\mathbf{S}_{MM} = 0$, $\mathbf{S}_{Mc} = 0$). For comparison purposes, in Figure 2.12a) we present again the M2-fibre adhesion case (*i.e.*, the one shown in Figure 2.11e), where $\mathbf{S}_{MF} = 0.3$, and $\mathbf{S}_{cF} = 0.3$.

In Figure 2.12b) we decrease the fibre magnitude and take the ratio between the fibre and non-fibre ECM to be $10\% : 90\%$. In this case we see both more tumour fingers, as well as an increase in the tumour spread. This is expected since by decreasing the fibre percentage, we also decrease the fibre adhesions. Moreover, the accumulation of fibres at tumour boundary becomes less dense, allowing the tumour to spread further, more efficiently.

In Figure 2.12c), we consider again the baseline ECM fibre percentage (20%) but we decrease the M2-fibre adhesion strength to $\mathbf{S}_{MF} = 0.1$ (while keeping the cancer-fibre adhesion strength $\mathbf{S}_{MF} = 0.3$). We observe here that due to the changes within the oriented ECM fibres distribution (caused by the fibres rearrangement at the micro-scale induced by the macro-scale spatial flux of cancer cells and M2 TAMs), the macrophages cannot move efficiently within the tumour microenvironment, and within the assumed conditions of low macrophages-fibre adhesion strength, the effect of the macrophages diffusion increases. Comparing these simulation results with those in Figure 2.12a), we see a considerable increase in tumour spread. This suggests that the decrease in the M2-fibres adhesion leads to a diffusion-dominated macrophage movement, which likely helps tumour spread indirectly via the degradation of ECM.

In Figure 2.12d), we present the simulation results when we decrease the fibre percentage to 10% and keep a low small M2-fibre adhesion strength ($\mathbf{S}_{MF} = 0.1$; as in Figure 2.12c). Compared to the situation addressed in Figure 2.12b), where we had larger macrophage-fibre adhesion strength, we note here an increase in the tumour spread. However comparing now the results in row four to the ones in Figure 2.12c) (where we had identical adhesion strength, but with increased level of ECM fibres to 20% was considered) we observe a decrease in the tumour spread. Hence, the de-

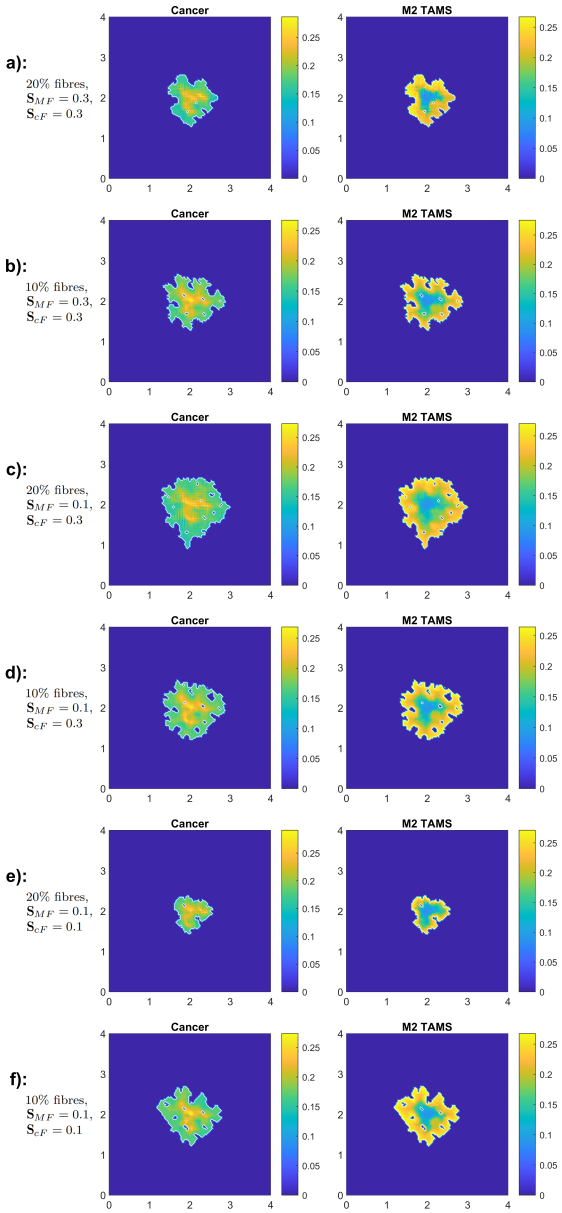

Figure 2.12: *Simulations when only M2-fibre adhesion is present (*i.e., *we set* $\mathbf{S}_{cM} = 0$, $\mathbf{S}_{MM} = 0$, $\mathbf{S}_{Mc} = 0$*) at time* $50\Delta t$*: a) baseline for this figure and so it is identical to Figure 2.11e) with* 20% *fibres (*80% *non-fibre ECM) and* $\mathbf{S}_{cF} = 0.3$, $\mathbf{S}_{MF} = 0.3$*; b) same fibre-adhesion strengths but with only* 10% *fibres (*90% *non-fibre ECM); c)* 20% *fibres with decreased M2-fibre adhesion* $\mathbf{S}_{MF} = 0.1$*; d)* 10% *fibres with decreased M2-fibre adhesion* $\mathbf{S}_{MF} = 0.1$*; e)* 20% *fibres and both cancer and M2-fibre adhesion strengths are reduced* $\mathbf{S}_{cF} = 0.1$ *and* $\mathbf{S}_{MF} = 0.1$*; f)* 10% *fibres with the reduced fibre adhesion strengths* $\mathbf{S}_{cF} = 0.1$ *and* $\mathbf{S}_{MF} = 0.1$.

creased level of macrophages-fibres adhesion strength (considered in simulations on rows three and four) reverse the observation concerning tumour spread that emerged by comparing Figures 2.12a) and b) (with a higher level of macrophages-fibres adhesion strength, $\mathbf{S}_{MF} = 0.3$). Hence, macrophages-fibres mediated movement exert a level of control on the tumour spread and the evolution of its morphology, by monotonically reducing tumour diffusive spread and at the same time stimulating lobular cancer invasion patterns.

In Figures 2.12e) and f), we investigate the effects of weak M2-fibre adhesion combined with weak cancer-fibre adhesion (i.e., $\mathbf{S}_{cF} = 0.1$, $\mathbf{S}_{MF} = 0.1$). Comparing the simulation results in Figure 2.12e) with those in Figure 2.12c), we conclude that by reducing the cancer-fibre adhesion strength we decrease significantly the tumour spread. However, if we reduce also the amount of fibres to 10% (see rows five and six), we see an increase in tumour spread (likely due to larger cell-non-fibre adhesions).

Next, in contrast to Figure 2.12, where no macrophage-macrophage self-adhesion nor cancer-macrophage or macrophage-cancer adhesion relations were considered, we address the case in which these processes are present, namely $\mathbf{S}_{cM} > 0$, $\mathbf{S}_{MM} > 0$ and $\mathbf{S}_{Mc} > 0$ (with the baseline values given in Table 2.3, used also in Figure 2.11f)). Furthermore, as before, we vary the values of cell-fibres and macrophages-fibre adhesion, $\mathbf{S}_{cF}$ and $\mathbf{S}_{MF}$. In these conditions, in Figure 2.13, we explore the importance of the M2-fibre adhesion compared to the the rest of the adhesion terms. Again, for comparison purposes, in Figure 2.13a) we show the baseline dynamics of this case, as copied from Figure 2.11f).

In these new conditions, Figures 2.13a)-d) show that changes in macrophage-fibre adhesion at ECM fibres regimes of both 20% and 10% do not have a significant impact on the tumour spread (although a smaller cancer spread is noticed when lower S_{MF} is considered).

However, as shown in the ECM regime with 20% fibres levels, the comparison of

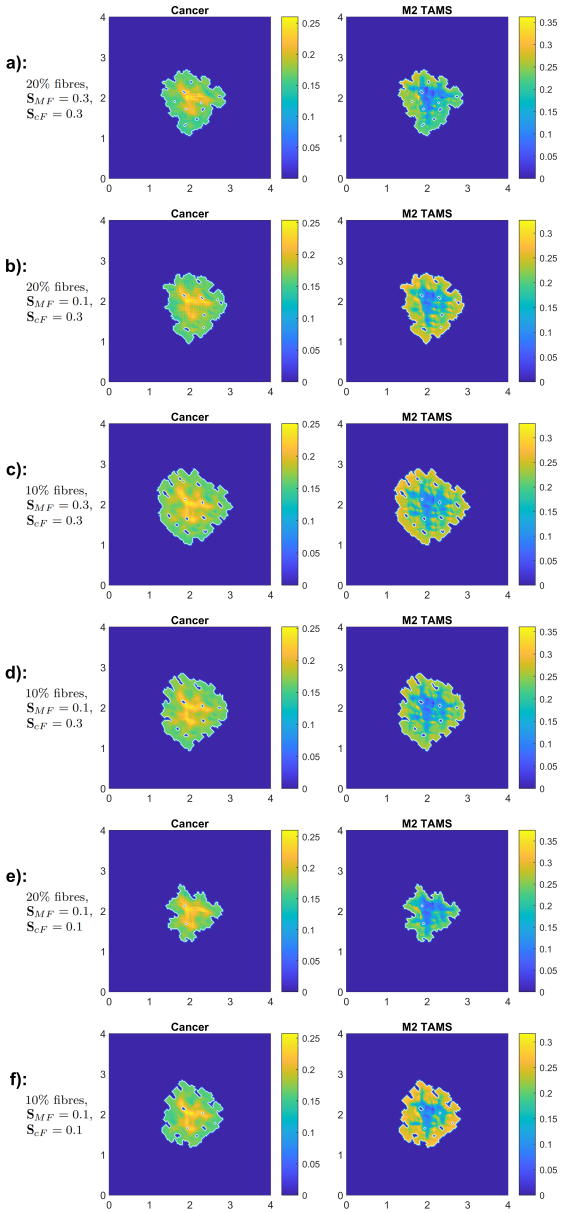

Figure 2.13: *Simulations at time* $50\Delta t$ *when all new M2 TAM adhesions are present:* i.e., *using the values from the parameter set* $\mathcal{S}$ *(see Table 2.3, for* $\mathbf{S}_{cM}$, $\mathbf{S}_{MM}$, $\mathbf{S}_{Mc}$*) while altering* $\mathbf{S}_{cF}$ *and* $\mathbf{S}_{MF}$*: a) the baseline for this figure that is identical to Figure 2.11f); b) decreased M2-fibre adhesion* $\mathbf{S}_{MF} = 0.1$ *with* 20% *fibres; c)* 10% *fibres with* $\mathbf{S}_{MF} = 0.3$*; d)* 10% *fibres with decreased M2-fibre adhesion* $\mathbf{S}_{MF} = 0.1$*; e)* 20% *fibres and both cancer and M2-fibre adhesion strengths are reduced* $\mathbf{S}_{cF} = 0.1$ *and* $\mathbf{S}_{MF} = 0.1$*; f)* 10% *fibres with the reduced fibre adhesion strengths* $\mathbf{S}_{cF} = 0.1$ *and* $\mathbf{S}_{MF} = 0.1$.

the results from row five (where low cancer-fibre adhesion $\mathbf{S}_{cF} = 0.1$ is considered) with those in row two highlight the importance of cancer-fibres adhesion within the invasion, as we record higher tumour spread for higher values of $\mathbf{S}_{cF}$. The same behaviour is observed through the comparison of row four and row six, where the same variation of $\mathbf{S}_{cF}$ when we consider a lower level of ECM fibres and of macrophage-fibre adhesion, $\mathbf{S}_{MF} = 0.1$.

Finally, by comparing Figures 2.13a), b) and e) we observe that it is the cell-fibres rather than the macrophages-fibre adhesion that plays the dominant role at higher level fibres (20%) within the ECM. However, the comparison between rows three, four and six of Figure 2.13 shows that in regimes with lower levels of fibres (10%) within the ECM, the influence of the macrophages-fibres adhesion on the overall cancer invasion is still important.

The effect of random micro-fibre distribution. In all our previous numerical simulations we used the micro-fibre structure described in Figure 2.9b) that we repeated for each micro-fibre domain $\delta Y(x)$, thus inducing the same fibre orientation at each macro-scale node (top-left orientation seen in Figure 2.10). Now we consider random mass distributions of micro-fibres for each micro-domain $\delta Y(x_i, y_j)$, (i.e., we draw five random straight lines in each δY rather than use the five-line configuration presented in Figure 2.9b)).

In Figure 2.14, we present three simulations with randomised mass distributions of micro-fibres on each $\delta Y(x_i, y_j)$, $i, j \in \{1, \dots, n\}$ (where the same random distribution is used for all three simulations as an initial condition). Here we focus on the case when all of the adhesion terms are present (i.e., $\mathbf{S}_{cM}$, $\mathbf{S}_{MM}$, $\mathbf{S}_{Mc}$, $\mathbf{S}_{MF}$, $\mathbf{S}_{cF} > 0$, as given in Table 2.3).

In Figure 2.14a) we use 20% fibres, and we observe that due to the random fibres, the tumour spread is reduced (by $\approx 25\%$) compared to Figure 2.11f). This is not surprising as we moved from aligned fibres to a random oriented fibres, where the

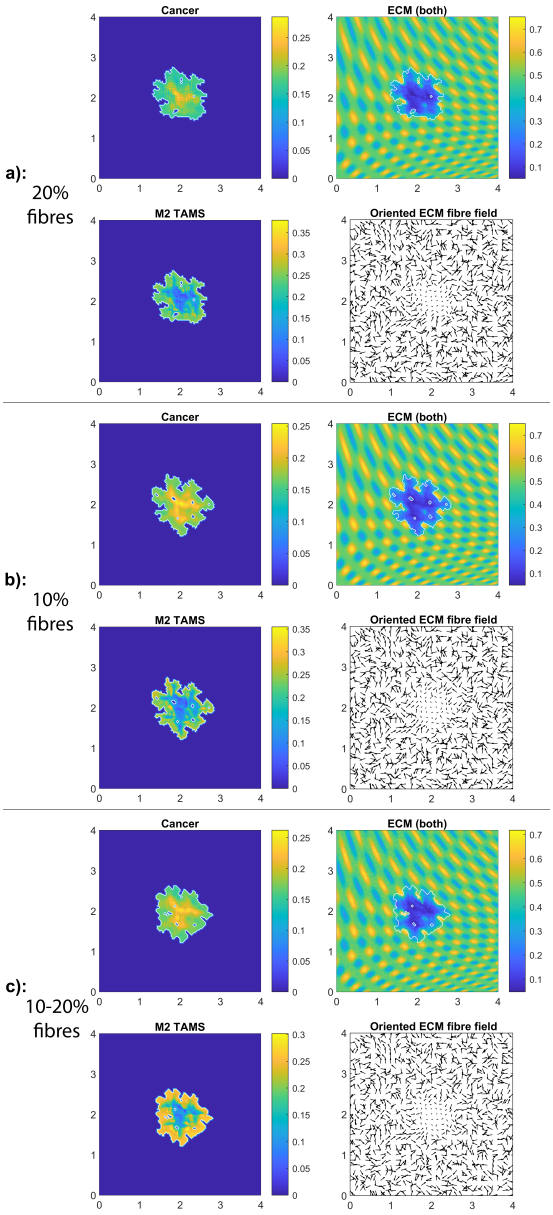

Figure 2.14: *Simulations with random fibre structures for each micro-fibre domain δY combined with every adhesion terms (*i.e., *using $\mathbf{S}_{cM}$, $\mathbf{S}_{MM}$, $\mathbf{S}_{Mc}$, $\mathbf{S}_{MF}$ and $\mathbf{S}_{cF}$ from the parameter set $\mathcal{S}$ Table 2.3) at time $50\Delta t$: a) (first two rows) represent the result of random micro-fibre structure, but their macro-scale magnitude is still considered to be a constant 20%; b) (third and fourth rows) presents the result of 10% fibres with random structures; c) (last two rows) also uses random structure but also uses random macro-scale magnitude for each micro-domain δY between 10% and 20%.*

movement is expected to be slower.

In Figure 2.14b) we reduce the fibres to 10%, and we observe an even greater tumour reduction compared to the aligned fibre case in Figure 2.12b) (approximately 43% reduction in tumour area). Also, as before, we see an increase in the tumour spread when we decrease the fibres from 20% to 10%.

In Figure 2.14c) we consider not only random micro-fibre structures but also use random macro-fibre magnitudes (i.e., at each macro-node, we now have a random level of fibres between 10% and 20%). For this case we see that tumour spread is slightly greater than for the 20% fibre case, but slightly smaller than for the 10% case. We can conclude from here that using random fibres may considerably reduce tumour spread, but it does not introduce new tumour morphology.

2.6.2 Different Tissue Conditions

Based on biological knowledge [99, 293], given the complex and naturally multi-scale cancer invasion process, a solid cancer progresses further within the surrounding tissue provided that significant but not complete tumour peritumoural ECM degradation will have been achieved, *i.e.*, favourable tissue conditions for invasion are met. In all the simulation that we carried out so far in this work, these tissue conditions for tumour progression have been explored within the framework defined in [279], where these were captured through a tissue parameter $\beta \in (0, 1)$, which characterises the relative level of significant degradation of the peritumoural ECM. For all the results presented in Figures 2.10-12, this parameter was set to the level of $\beta := 0.65$, which corresponds to relatively mild conditions for invasion. However, as we wish to explore our modelling also for more demanding tissue conditions for tumour invasion, that requires more elevated levels of significant peritumoural ECM degradation, we now vary the parameter β by increasing its value.

To illustrate our results in new tissue conditions favourable for tumour progression induced by elevated values of β, in Figure 2.15a) we show the result for our

model without the new adhesion processes and tissue conditions induced by $\beta = 0.8$. Here we observe a pronounced lobular formation and increased fingering within the tumour morphology where the number and size of the islands inside tumour are also increased. Then, the results in Figure 2.15b) show that, by increasing further the tissue parameter $\beta = 0.825$ (while keeping the same diffusion and adhesion regime), we obtain an even more aggressive tumour fingering and lobular formation, and a rather decreased tumour area compared to Figure 2.15a). Finally, in Figure 2.15c) we show the results that we obtain when we re-introduce the adhesion processes (*i.e.,* we take $\mathbf{S}_{cM}$, $\mathbf{S}_{MM}$, $\mathbf{S}_{Mc}$ and $\mathbf{S}_{MF}$ from the Parameter set $\mathcal{S}$ in Table 2.3) which results in further decrease in the tumour area while maintaining a significant tumour fingering and lobular behaviour.

2.7 Discussion

In this study, we further developed the multi-scale moving boundary framework for tumour invasion introduced in [245, 279], by including also a tumour-associated macrophage cell population, with the goal of investigating the interactions between macrophages directional movement and the directionality of ECM fibres on the overall tumour spread. We focused on the M2-like macrophages since various experimental and clinical studies have shown that these cells are not only one of the most abundant immune cell populations that infiltrate the tumour mass [132, 286], but they are also involved in the degradation of ECM [69, 172, 194, 228] thus helping tumour invasion. We considered this modelling and computational approach since in the experimental literature there is still little knowledge about the directional interactions of macrophages with the directional/random ECM architecture, and how this affects tumour spread.

To address this lack of knowledge and to propose new hypotheses on these interactions, we started with the modelling framework in [245] that focused on the

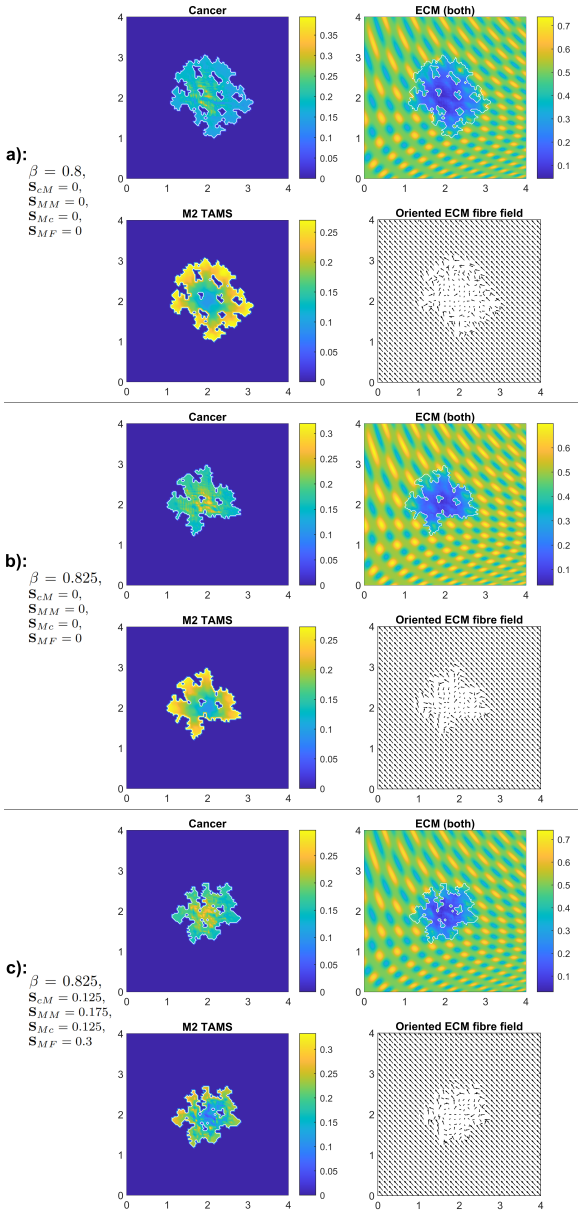

Figure 2.15: *Simulations, at time* $50\Delta t$*, with the extended model* (2.29) *for different tissue conditions* (β)*, while we consider* 20% *fibres. a) simulation with zero-macrophage adhesion coefficients* (i.e., $\mathbf{S}_{cM} = 0$, $\mathbf{S}_{MM} = 0$, $\mathbf{S}_{Mc} = 0$ *and* $\mathbf{S}_{MF} = 0$) *and an increased* $\beta = 0.8$*; b) the tissue parameter is further increased to* $\beta = 0.825$ *without considering any macrophage adhesion processes* (i.e., $\mathbf{S}_{cM} = 0$, $\mathbf{S}_{MM} = 0$, $\mathbf{S}_{Mc} = 0$ *and* $\mathbf{S}_{MF} = 0$)*; c) simulation with* $\beta = 0.825$ *where we take the values for* $\mathbf{S}_{cM}$, $\mathbf{S}_{MM}$, $\mathbf{S}_{Mc}$ *and* $\mathbf{S}_{MF}$ *from the Parameter set* $\mathcal{S}$ *in Table 2.3.*

dynamics of tumour cells and extracellular matrix at both micro- and macro-scales, and introduced a new macro-scale equation for the pro-tumour M2 cells. In this new equation, we considered the M2 TAMs movement to be both random and directed, with the directed movement being the result of self-adhesion and fibre-adhesions, as well as M2-cancer adhesion. The rest of the M2 TAMs dynamics included a linear death term, a proliferation term and an influx term where we assumed a constant influx of M2 TAMs on the outer tumour boundary. Since the M2 TAMs secrete MDEs, the degradation of both ECM components is not only influenced by the density of the cancer cells but also by the density of M2 TAMs. Therefore, the macrophages have a direct contribution to the source for the proteolytic micro-dynamics of MDEs occuring at the invasive edge of the tumour, which ultimately determines the way the tumour boundary is relocated during invasion. Furthermore, as macrophages are moving, they influence the re-arrangement of the micro-fibres through the flux that they induce. Thus, the M2 macrophages are involved in both the *top-down* and *bottom-up* links of the two interconnected multiscale subsystems that take place both at leading edge and on the bulk of an invading tumour (which are schematically summarised in Figure 2.5).

While the genuine heterogeneous and multiphase structure of the ECM has been acknowledged by the entire experimental and biological community [99, 117], the two-phase ECM modelling perspective proposed in this current work (as well as in [245, 246, 247]) not only that was naturally motivated, but the insights that this brings (through the possibility of exploring in detail the multiscale and complex adhesive interaction between the cells and macrophages on one hand and both the non-fibres ECM phase [84, 90, 91, 119] and the oriented ECM fibre phase [294, 295]) open the way for a deeper understanding of both directed and undirected tumour cell population movement in the presence of M2 TAMs macrophages. This will have direct implication in the planned future works on drug and chemotherapy delivery which naturally follows the non-fibres ECM phase, rather than the ECM fibres

phase.

We used this new extended multi-scale moving boundary mathematical model to explore some biological hypotheses regarding the role of M2 cells on tumour spread. First we investigated the individual effects of the cancer-M2 and M2-cancer adhesions, as well as the M2-self and M2-fibre adhesions, and we concluded that individually these interactions do not lead to a significant increase in tumour spread. However, they do change the tumour morphology, by leading to various accumulation sites for the M2 TAMs (see Figure 2.11). We also showed that combining all these different adhesion terms leads to an increase in tumour spread. Then we explored how the fibrous component of the ECM and the corresponding fibre adhesion strengths could affect tumour development (see Figures 2.12 and 2.13). The simulations showed that decreasing the fibre density could be helpful to reduce tumour spread; but this depended also on the M2 TAMs directed movement via fibre adhesion. We also investigated the importance of M2-fibre adhesion compared to the rest of the adhesions. In our model, this suggested that the M2-fibre adhesion play a minor role and do not significantly affect tumour development. Moreover, we considered an unstructured, random micro-fibre structure that revealed that although it does not introduce new properties, it can reduce the spread quite dramatically.

We note here that all these numerical results were obtained with a low β value (to be consistent with the studies in [245, 246, 247]), which means that even if the ECM was not significantly degraded the tumour was still able to invade the surrounding tissue. Therefore, changes in the various parameter values considered in Figures 2.11-2.14 did not lead to huge differences in tumour invasion patterns. However, in Figure 2.15 we presented some simulations for the tumour dynamics , as we varied the tissue environment parameter β. We have seen that for higher β, changes in cell-cell and cell-matrix adhesion strengths lead to completely different tumour invasion patterns, with more tumour fingering, and clear uni-directional movement towards the direction of ECM fibres.

All these numerical results indicate that the combined effects of macrophage-tumour-ECM interactions (via different cell-cell and cell-fibre adhesions) are important for tumour development. Moreover, these results allow us to conclude that it is difficult to ascertain at a macroscopic level the specific molecular (i.e., adhesion) mechanisms that could be responsible for the observed macroscopic patterns of tumour spread and/or accumulation.

The complexity of the interaction between tumour cell and macrophages exceeds the context captured in this work through the mutual adhesion terms involved in the macroscopic model equations. For example, this approach does not capture explicitly the complex cross-talk between tumour cells and macrophages via chemokines. Such aspects will be investigated in future studies. Further, due to the complexity of the multi-scale moving-boundary framework and the numerical simulations of these equations, in this work we focused only on the dynamics of the tumour and the immune cells infiltrating it. For this reason, we assumed that macrophages enter the tumour though tumour boundary. In the future, we will extend this modelling approach to account also for the dynamics of macrophages outside the tumour (which are attracted to the tumour site via chemokines secreted by the tumour cells [92]).

Finally, another aspect that will be addressed in future work is the analysis of the complex multi-scale numerical framework proposed in this study. As this computational framework is new, this is an open problem that requires a proper independent investigation.

Chapter 3

Re-Polarisation of Macrophages within a Multi-Scale Moving Boundary Tumour Invasion Model

Aims and Novelty: In this chapter, we aim to expand further upon the multi-scale moving boundary framework introduced in Chapter 2 by incorporating not only the M1-like macrophages but the nutrients as well. Ultimately, this allows us to explore how different scenarios could affect a potential re-polarisation (M2→M1) based treatment strategy.

3.1 Introduction

The last few decades have seen a shift in the focus of cancer research: from research that was focused on individual tumour cells to research that is now focused on the TME and the interactions between different types of cells inside the TME [104]. In Chapter 2 we have acknowledged the fact that macrophages are one of the most abundant stromal cell populations within the TME [132, 286]. However, we focused on the pro-tumoral M2 TAMs alone and did not consider the presence

of the anti-tumoral M1 TAMs since the majority of macrophages are polarised into the M2 phenotype in advanced (detectable) tumours [155]. Due to their plasticity, macrophages can switch their phenotype (M1↔M2), and over the last decades, experimental and clinical studies have shown that re-educating TAMs to exhibit anti-tumour responses by switching their cell phenotype from M2-like to M1-like cells can lead to successful anti-cancer treatment protocols [155]. An example of such a treatment protocol involving macrophage re-polarisation, which was shown to be successful in human pancreatic cancer, involved the use of agonist anti-CD40 mAb [23].

Besides cancer cells, macrophages and the ECM, the tumour's vasculature also plays a crucially important role within the TME since it is responsible for the supply of nutrients (e.g. oxygen and glucose) that are vital for any cells to live and function properly, including cancer cells and macrophages. In avascular solid tumours, nutrients are extravasated from the blood flow and diffuse through the ECM into the tumour through the tumour boundary, and therefore tumour progression leads to the formation of regions inside the tumours with very low nutrient levels. These regions first become hypoxic and then necrotic, and cells in these regions undergo cell death due to deprivation of nutrients. Moreover, these hypoxic conditions can also modify the polarisation of macrophages and influence the malignant behaviour of some cancer cells [130].

Therefore, in this chapter, we explore how the re-polarisation of TAMs (M2→M1) affects the overall tumour progression (mass and spread) and whether a re-polarisation based treatment strategy is space-time dependent. On the other hand, we also study how the introduction of nutrients within this multi-scale moving boundary approach influence tumour behaviour and whether it has a meaningful effect on a re-polarisation based treatment. The content of this chapter has also been explored and discussed in full detail in our recent publication [264].

3.2 Multi-Scale Modelling of the Tumour Dynamics

Using the multi-scale moving boundary framework described in Chapter 2 where we only considered the presence of the M2 phenotype (besides the cancer cell population and a two-phase ECM), here, we further extend this modelling platform by introducing the M1-like macrophages. Hence, we assess the impact of this anti-tumoral phenotype within the interlinked tissue-scale (macro-scale) and cell-scale (micro-scale) tumour dynamics. Moreover, the biological context of the tumour macro-dynamics is further broadened by considering the presence of the nutrients, which include components such as glucose and oxygen that are crucial constituents of the tumour microenvironment and play an essential role within overall tumour progression.

3.2.1 Macro-Scale Dynamics

Since the model described in this chapter extends the one outlined in Chapter 2, we have the same underlying multi-scale features that for clarity, we briefly discuss here again. Hence, on the macro-scale we focus on the expanding tumour region $\Omega(t)$ that progresses within a maximal tissue cube $Y \subset \mathbb{R}^N$, for $N = 2$ and over the time interval $[0, T]$ (*i.e.*, $\Omega(t) \subset Y, \forall t \in [0, T]$). In this context, at at any macro-scale spatio-temporal point $(x, t) \in \Omega(t) \times [0, T]$, we consider a mixed cell population consisting of distributions of: (a) cancer cells $c(x, t)$; (b) M1-like macrophages, $M_1(x, t)$, briefly addressed here as M1 TAM; and (c) M2-like macrophages, $M_2(x, t)$, which are briefly referred to as M2 TAM. This mixture of cancer cells and macrophages exercise their naturally multi-scale dynamics within a two-phase ECM, which as in Chapter 2 and in [245, 246, 247], is regarded as consisting of two major phases, namely a fibrous and a non-fibrous one. Thus, as before, the fibre ECM phase accounts for all major fibrous proteins (such as collagen and fibronectin), whose

spatio-temporal distribution at the macro-scale point (x,t) is described by a vector field $\theta_f(x,t)$, where $\theta_f(\cdot,t):\mathbb{R}^N\to\mathbb{R}^N$, with its Euclidean norm $F(x,t):=\|\theta_f(x,t)\|_2$ representing the amount of fibres at (x,t) and for further details we refer the reader to Section 2.2.2. On the other hand, as in Chapter 2 we bundle together the rest of the ECM constituents (such as non-fibrous proteins, enzymes, polysaccharides and extracellular Ca^{2+} ions) and refer to it as the non-fibre ECM phase, whose distribution at each (x,t) is denoted by $l(x,t)$. Similarly to Chapter 2, here we also define all cell populations ($c(x,t)$, $M_1(x,t)$ and $M_2(x,t)$) within the tumour domain $\Omega(t)$ and the two ECM phases ($F(x,t)$ and $l(x,t)$) within the tissue cube Y. Therefore, to also include the density of M1 TAMs, in this chapter we define the global tumour vector $\mathbf{u}$ as

$$\mathbf{u}:=(c(x,t),M_1(x,t),M_2(x,t),l(x,t),F(x,t))^\intercal, \tag{3.1}$$

as well as we define the total space occupied at (x,t) as

$$\rho(\mathbf{u}):=c(x,t)+F(x,t)+l(x,t)+M_1(x,t)+M_2(x,t), \tag{3.2}$$

for all $(x,t)\in Y\times[0,T]$. Furthermore, the last component of the macro-scale dynamics is the nutrients density $\sigma(x,t)$, whose level within the tumour microenvironment is depleted by the invading cancer.

Finally, we consider the macrophages to infiltrate the tumour through the same *outer boundary* $\partial\Omega_o(t)\subset\partial\Omega(t)$ that we used previously in Chapter 2 and which is defined in Appendix A.1 (see Figure 2.6 for illustration).

Nutrient

In this chapter we focus on an avascular tumour mass, whose growth is supported by an influx of nutrients that diffuse through the outer boundary of the tumour. To incorporate this aspect into our mathematical model, we consider the overall influx of a generic nutrient through the outer tumour boundary $\partial\Omega_o(t)$ by using

Dirichlet boundary conditions. Hence, here, we consider a nutrient field that is only affected within the tumour, and so outside of the tumour its level is assumed to be unaffected/normal. Although different cell types uptake the supplied nutrients at different rates, for simplicity here we assume that all present cell populations (cancer cells, M1 and M2 TAMs) uptake nutrients at the same constant rate $d_\sigma > 0$. The spatial transport of the nutrients is modelled by a diffusion term with constant coefficient $D_\sigma > 0$. Since this diffusion occurs more rapidly than cell diffusion (i.e., cell random walk), we use a quasi steady state reaction-diffusion equation (similar to the one for instance in [169]) for the generic nutrients $\sigma(x,t)$:

$$0 = D_\sigma \Delta\sigma - d_\sigma(c + M_1 + M_2)\sigma, \tag{3.3a}$$

$$\sigma(x,t) = \sigma_{nor}, \qquad \forall x \in \partial\Omega_o(t), \forall t \in [0,T]. \tag{3.3b}$$

Here, σ_{nor} is the normal level of nutrients along the tumour interface, which is considered to be a constant.

Since cells require nutrients to function properly, here we introduce four smooth bounded *effect-functions* that we use to model the effects of the nutrients on the different cell functions that considers the following critical nutrients levels:

- the necrotic minimal threshold $\sigma_n > 0$ (i.e., if $\sigma \leq \sigma_n$ this leads to necrotic tumour cell death in that area [148];
- the intrinsic nutrient level sufficient for cells to function properly: $\sigma_p > 0$;
- the normal level of nutrients: σ_{nor} (threshold value that is used also as the Dirichlet boundary condition in (3.3)).

Hence, we have the following relationship between these three values, namely: $\sigma_{nor} > \sigma_p > \sigma_n$.

Starting with the effect of nutrients on cell proliferation, we first assume that this effect is relatively similar for cancer cells and both macrophage populations, in

the sense that very low nutrient level impedes cell proliferation and extremely high nutrient level cannot increase cell proliferation rate above a certain maximum. We consider a maximal proliferation enhancement rate $\Psi_{p,max} > 0$ which corresponds to nutrient levels $\sigma \geq \sigma_p$. Also, we assume no proliferation in the necrotic regions. Thus, we define the proliferation effect-function:

$$\Psi_p(\sigma) := \begin{cases} 0 & \text{if } \sigma \leq \sigma_n, \\ \Psi_{p,max} & \text{if } \sigma \geq \sigma_p, \\ \Phi(\sigma, \Psi_{p,max}, 0, \sigma_p - \sigma_n) & \text{otherwise,} \end{cases} \tag{3.4}$$

where $\Phi(\sigma, \cdot, \cdot, \cdot)$ is a generic cosine function that describes a smooth transition between the two extrema, *i.e.,* for any level $\sigma_n < \sigma < \sigma_p$. Thus, $\Phi(\sigma, \cdot, \cdot, \cdot)$ is defined by

$$\Phi(\sigma, \Phi_{max}, \Phi_{min}, \Phi_L) := \frac{\Phi_{max} - \Phi_{min}}{2} \left(\cos\left(\frac{\pi(\sigma - \sigma_n - \Phi_L)}{\sigma_p - \sigma_n} \right) + 1 \right) + \Phi_{min}, \tag{3.5}$$

where Φ_{min} is the minimum, Φ_{max} is the maximum and Φ_L controls the phase shift of the cosine function. We illustrate the proliferation effect-function, defined in (3.4) in Figure 3.1.

As opposed to cell proliferation, we distinguish between the death of cancer cells and death of macrophages, since cancer cells resist death [98, 99] while macrophages do not. Moreover, experimental studies have shown that macrophages can die in the absence of nutrients [238]. Also, it is known that following hypoxia-induced chemo-attractant signals, macrophages position themselves into pre-necrotic regions to clear out dead cells in the necrotic regions [181]. Therefore, we consider a maximal enhancement death rate $\Psi_{d,max} > 0$ in necrotic regions for both populations, and while we assume no death for cancer cells, we consider a minimal level of macrophage enhancement death rate $\Psi_{dM,min} > 0$ in regions where the nutrient level is $\sigma \geq \sigma_p$.

Hence, cancer cell death and macrophage death effect-functions are defined as (using the transition function (3.5)):

$$\Psi_{dc}(\sigma) := \begin{cases} \Psi_{d,max} & \text{if } \sigma \leq \sigma_n, \\ 0 & \text{if } \sigma \geq \sigma_p, \\ \Phi(\sigma, \Psi_{dc,max}, 0, 0) & \text{otherwise,} \end{cases} \tag{3.6a}$$

$$\Psi_{dM}(\sigma) := \begin{cases} \Psi_{d,max} & \text{if } \sigma \leq \sigma_n, \\ \Psi_{dM,min} & \text{if } \sigma \geq \sigma_p, \\ \Phi(\sigma, \Psi_{dM,max}, \Psi_{dM,min}, 0) & \text{otherwise.} \end{cases} \tag{3.6b}$$

These death effect-functions are illustrated in Figure 3.1.

Finally, it was shown experimentally [273] that the nutrient level affects the macrophages polarisation rate, and so here we consider also a polarisation effect-function. Thus, we consider a maximal enhancement rate $\Psi_{M,max} > 0$ in necrotic regions and a minimal enhancement rate $\Psi_{M,min} > 0$ in regions with normal nutrient levels. Using the smooth transition function (3.5), we define the polarisation effect-function $\Psi_M(\sigma)$ by

$$\Psi_M(\sigma) := \begin{cases} \Psi_{M,max} & \text{if } \sigma \leq \sigma_n, \\ \Psi_{M,min} & \text{if } \sigma \geq \sigma_{nor}, \\ \Phi(\sigma, \Psi_{M,max}, \Psi_{M,min}, 0) & \text{otherwise.} \end{cases} \tag{3.7}$$

This function is illustrated in Figure 3.1.

Dynamics of both M1 and M2 TAMs

Focusing now on the macrophage population, specifically to the two extreme phenotypes, M1 and M2 TAMs, in this chapter, we focus on the dynamics of the two

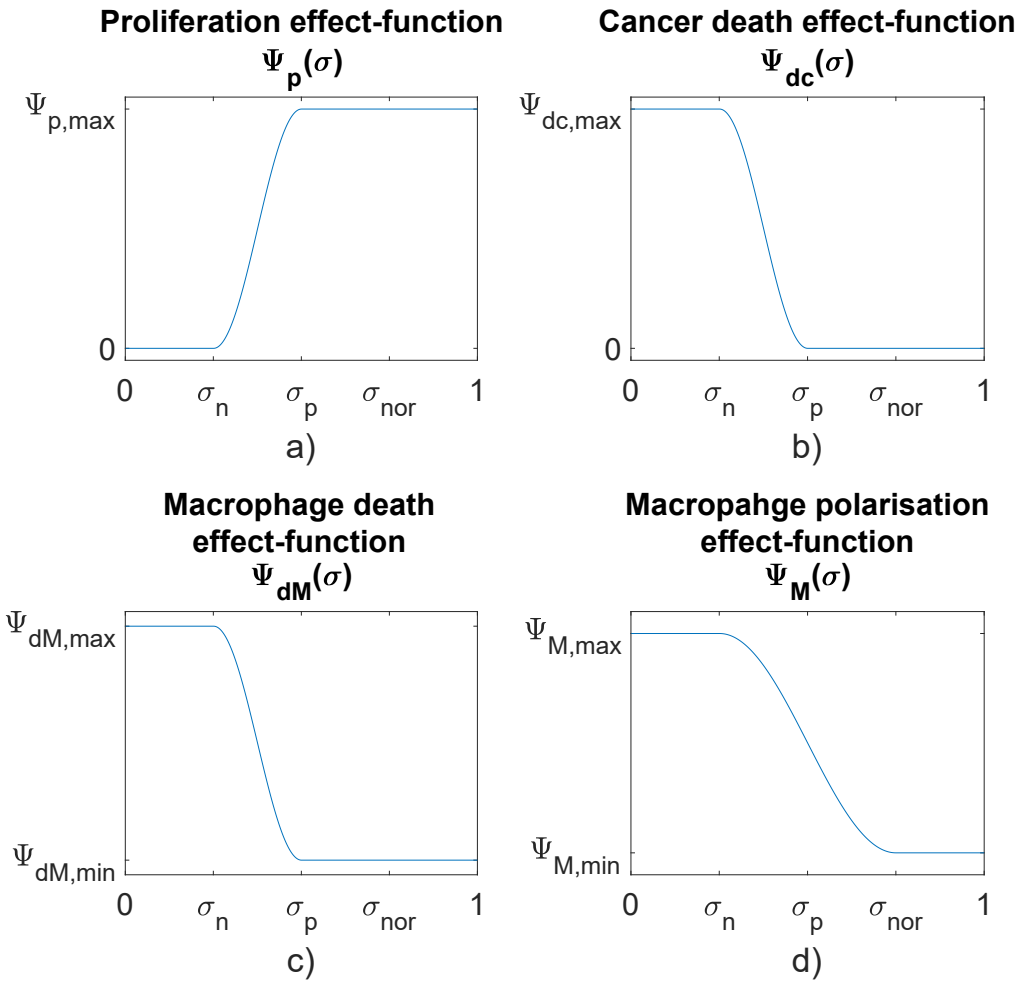

Figure 3.1: *Schematic plots of the four nutrients effect-functions a)* $\Psi_p(\sigma)$*, b)* $\Psi_{dc}(\sigma)$*, c)* $\Psi_{dM}(\sigma)$ *and d)* $\Psi_M(\sigma)$ *defined in* (3.4)*,* (3.6)*, and* (3.7)*, respectively.*

TAMs populations exclusively inside the tumour domain $\Omega(t)$, the evolution of the macrophages distribution in the surrounding tumour stroma being beyond the scope of this current work. Hence, since macrophages are recruited to tumour sites as an immune response through the peritumoral vasculature, here this influx is represented by a source of M1 TAMs that is localised along the outer tumour boundary $\partial\Omega_o(t)$, which is enabled by the immediate activation of macrophages into M1 TAMs as they enter the tumour [265]. As in Chapter 2, for simplicity, we assume that both profile and maximal magnitude $M_0 > 0$ of this source are identical along the tumour interface, and so this influx term is given by

$$M_I := M_0(\chi_{\partial\Omega_o(t)} * \psi_\rho)(x). \tag{3.8}$$

Here, ψ_ρ is the standard mollifier with appropriately chosen range $\rho > 0$, " $*$ " is the convolution operator [64] and $\chi_{\partial\Omega_o(t)}$ is the characteristic function of the outer boundary $\partial\Omega_o(t)$.

Experimental studies have shown that resident macrophages can proliferate in situ, which can lead to the accumulation of tumour-associated macrophages inside various tumours [281]. Moreover, as in Chapter 2 and [265], we recognise that the stiffness of the ECM plays a role in the proliferation of the macrophages [101] and that according to several biological studies [40, 52, 122], cancer cells trigger the proliferation of macrophages by producing survival and proliferation factors. Hence, we denote by $\mu_{MF} > 0$ the macrophages proliferation enhancement rate due to the fibres while the proliferation effect-function $\Psi_p(\sigma)$ defined in (3.4) accounts for the effect of nutrients on the macrophage proliferation. For simplicity, both the fibre enhancement rate and the effect-function are assumed to remain unchanged for both phenotypes. Thus, we formulate the proliferation laws for the M1 and M2 TAMs as

$$P_{M_1}(\mathbf{u}) := \mu_M \Psi_p(\sigma)(1 + \mu_{MF} F) M_1 c (1 - \rho(\mathbf{u}))^+, \tag{3.9a}$$

$$P_{M_2}(\mathbf{u}) := \mu_M \Psi_p(\sigma)(1 + \mu_{MF} F) M_2 c (1 - \rho(\mathbf{u}))^+, \tag{3.9b}$$

respectively. In (3.9), μ_M is the positive baseline proliferation rate while the term $(1 - \rho(\mathbf{u}))^+ := \max(0, 1 - \rho(\mathbf{u}))$ ensures that there is no overcrowding.

Experimental studies have shown that macrophages' death can be induced by nutritional starvation [238]. Thus, for both M1 and M2 TAMs, we consider a natural death rate $d_M > 0$ that is regulated by the available nutrients through the death effect-function $\Psi_{dM}(\sigma)$ introduced in (3.6b), and so the death terms are defined by

$$Q_{M_1}(\mathbf{u}) := d_M \Psi_{dM}(\sigma) M_1, \tag{3.10a}$$

$$Q_{M_2}(\mathbf{u}) := d_M \Psi_{dM}(\sigma) M_2, \tag{3.10b}$$

for the M1 and M2 TAMs populations, respectively.

Due to the versatility of the macrophages, their phenotype can be switched from one to another [24, 234]. In the present work, we focus on two factors that drive the polarisation of M1 TAMs into M2 TAMs, which are detailed as follows. On the one hand, cytokines secreted by the cancer cells were shown [205, 248] to trigger the polarisation process. On the other hand, the nutrient level was also shown [273] to affect this process. As a consequence, we describe the polarisation of M1 TAMs to M2 TAMs by

$$T_{12}(\mathbf{u}) := p_{12} \Psi_M(\sigma) c M_1, \tag{3.11}$$

where $p_{12} > 0$ is a constant proliferation rate, and Ψ_M is the polarisation effect-function defined in (3.7). Furthermore, in vitro, it has been demonstrated [66] that the M2-like macrophages can be re-polarised back into the M1 phenotype which may be a viable strategy against tumour development. To that end, we explore

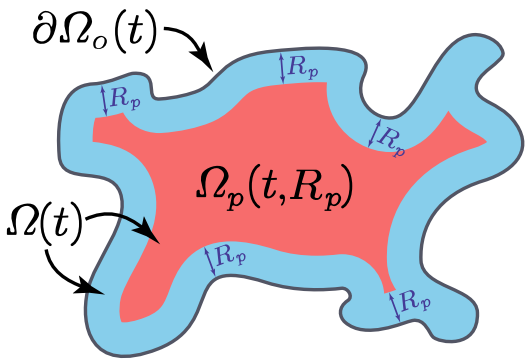

Figure 3.2: *Schematic of the re-polarisation domain $\Omega_p(t, R_p)$ that is highlighted with red.*

here mathematically the possibilities of the re-polarisation strategy through a re-polarisation term of the form

$$T_{21}(\mathbf{u}) := \begin{cases} 0 & \text{if } t < t_p, \\ p_{21} M_2(\chi_{\Omega_p(t,R_p)} * \psi_\rho)(x) & \text{if } t \geq t_p. \end{cases} \tag{3.12}$$

Here, $p_{21} > 0$ is the constant re-polarisation rate, $t_p > 0$ is the activation time and $\chi_{\Omega_p(t,R_p)}$ is the characteristic function of the re-polarisation domain $\Omega_p(t, R_p)$ that is defined in Appendix A.4 and illustrated in Figure 3.2. This re-polarisation term (3.12) allows us to examine whether or not we would need to account for spatio-temporal dependencies through the domain $\Omega_p(t, R_p)$ and activation times $t_p > 0$ in order to obtain an effective re-polarisation strategy.

The motility of both macrophages phenotypes is driven both by random and directed movement. Based on recent biological evidence [101], increased stiffness of the substrate leads to an increase in macrophages' speed, aspect explored in our modelling through a diffusion enhancement that corresponds to with the level of ECM fibres. To that end, we consider a stiffness-dependent macrophage diffusion

coefficient $D^M(\mathbf{u})$ of the form

$$D^M(\mathbf{u}) := D_M(1 + D_{MF}F), \tag{3.13}$$

where $D_M > 0$ is the baseline macrophage diffusion rate, and $D_{MF} > 0$ is the diffusion enhancement rate due to the presence of fibres. On the other hand, besides random movement, macrophages also exercise directed migration due to a both adhesive interactions with the surrounding cells and the ECM as well as an underlying cross-talk between themselves and the cancer cells. A similar *"non-local flux term"* to the one introduced in Chapter 2 and in [265] is used here to explore the complex interactions of the cells distributed at $x \in \Omega(t_0)$ with other cells within a sensing region $\mathbf{B}(0, R)$, and this accounts for: (1) cell-cell TAMs self-adhesion [60]; (2) nutrients level mediated movement[188]; and (3) the contribution of the cancer cells to the directional movement of the macrophages [49, 55, 72, 299]. Specifically, the contribution of the cancer cells to the directional movement of the macrophages account not only for the biological evidence that cancer cells can bind themselves to TAMs [49] but also for the fact that cancer cells can attract TAMs [55, 72, 299] by secreting various chemokines. Although we neither model explicitly the involved chemokine activities within this cross-talk nor the chemo-attractant activities involved with the nutrients, here we appropriately account for both of them through the following non-local flux term:

$$\begin{aligned}\mathcal{A}_M(x, t, \mathbf{u}, \mathbf{S}_{MM}) := \frac{1}{R} \int\limits_{\mathbf{B}(0,R)} \mathcal{K}(y)n(y)\Big[S_{M\sigma}\big(1 - \sigma(x + y, t)\big) \\ + \mathbf{S}_{MM}\big(M_1(x + y, t) + M_2(x + y, t)\big) \\ + \mathbf{S}_{Mc}c(x + y, t)\Big]\big[1 - \rho(\mathbf{u}(x + y, t))\big]^+,\end{aligned} \tag{3.14}$$

where R represents the radius of the sensing region $\mathbf{B}(0, R)$. Further, $\mathbf{S}_{Mc} > 0$ is the combined strength of the macrophage-cancer adhesion, and $\mathbf{S}_{M\sigma} > 0$ denotes

strength of the macrophage-nutrient relationship, with both $\mathbf{S}_{Mc}$ and $\mathbf{S}_{M\sigma}$ being assumed to maintain their individual values unchanged when considering the cases of M1 and M2 TAMs populations. Furthermore, $\mathbf{S}_{MM}$ denotes the self-adhesion strength that differs for M1 and M2 TAMs [60], *i.e.*,

- for M1 TAMs $\mathbf{S}_{MM} = \mathbf{S}_{M_1M} > 0$, and
- for M2 TAMs $\mathbf{S}_{MM} = \mathbf{S}_{M_2M} > 0$,

with $\mathbf{S}_{M_1M} \neq \mathbf{S}_{M_2M}$. As in Chapter 2, to account in (3.14) for the gradual weakening of these different adhesions as we move away from the centre x within $\mathbf{B}(x, R)$, we use a radially symmetric kernel $\mathcal{K}(\cdot)$ that is given by

$$\mathcal{K}(y) = \psi\Big(\frac{y}{R}\Big), \qquad \forall y \in \mathbf{B}(0, R),$$

where $\psi(\cdot)$ is the standard mollifier. Moreover, in (3.14), $[1 - \rho(\mathbf{u})]^+$ ensures that overcrowded tumour regions do not contribute to macrophage migration and $n(\cdot)$ is the unit radial vector given by

$$n(y) := \begin{cases} \dfrac{y}{\| y \|_2} & \text{if } y \in \mathbf{B}(0, R) \setminus \{0\}, \\ 0 & \text{if } y = 0. \end{cases} \tag{3.15}$$

Thus, aggregating now all these different aspects of macrophages explored in (3.8) - (3.14), the dynamics of the two distinct macrophages phenotypes are mathematically formulated as

$$\begin{aligned} \frac{\partial M_1}{\partial t} =& \nabla \cdot [D^M(\mathbf{u}) \nabla M_1 - M_1 \mathcal{A}_M(x, t, \mathbf{u}, \mathbf{S}_{M_1M})] + P_{M_1}(\mathbf{u}) - Q_{M_1}(\mathbf{u}) \\ & - T_{12}(\mathbf{u}) + T_{21}(\mathbf{u}) + M_I, \end{aligned} \tag{3.16a}$$

$$\begin{aligned} \frac{\partial M_2}{\partial t} =& \nabla \cdot [D^M(\mathbf{u}) \nabla M_2 - M_2 \mathcal{A}_M(x, t, \mathbf{u}, \mathbf{S}_{M_2M})] + P_{M_2}(\mathbf{u}) - Q_{M_2}(\mathbf{u}), \\ & + T_{12}(\mathbf{u}) - T_{21}(\mathbf{u}), \end{aligned} \tag{3.16b}$$

where $\mathbf{S}_{M_1M} > 0$ and $\mathbf{S}_{M_2M} > 0$ are the self-adhesion strengths of M1 and M2 TAMs, respectively.

Dynamics of the cancer cell population

The third cell population that we consider at the macro-scale is the cancer cell population. Crucially important for cancer development and invasion, cancer cell proliferation is a complex process regulated by several processes involving nutrients and macrophages. From the modelling perspective, while we consider the proliferation process as being of logistic type [145, 146, 275] analogously to Chapter 2, we explore the influence of nutrients and macrophages as follows. On the one hand, similar to both TAMs populations, we consider the proliferation effect-function $\Psi_p(\sigma)$ defined in (3.4) to explore the influence of the available nutrients on the rate of cancer cell proliferation. On the other hand, biological evidence shows that while M2 TAMs promote cancer cell proliferation [113], M1 TAMs inhibits this [157]. Thus, here we expand the proliferation law introduced in Chapter 2 and [265] by accounting for the negative effect of M1 TAMs, leading to the following proliferation law:

$$P_c(\mathbf{u}) := \mu_c \Psi_p(\sigma)(1 - \mu_{cM_1} M_1 + \mu_{cM_2} M_2) c(1 - \rho(\mathbf{u}))^+, \tag{3.17}$$

where $\mu_c > 0$ is a baseline proliferation rate that is being regulated by the available nutrients, being enhanced by the M2 TAMs at a rate $\mu_{cM_2} > 0$ and at the same time weakened by the presence of the M1 TAMs at a rate $\mu_{cM_1} > 0$. Again, here the term $(1 - \rho(\mathbf{u}))^+$ ensures that there is no overcrowding.

Besides proliferation, it is well known that cancer cells resist death [98, 99]. However, due to the peritumoral vasculature as well as the excessive degradation of the ECM, the efficiency of the nutrients delivery significantly reduces inside the tumour, leading to necrosis [309]. In addition, numerous studies have shown [30, 147, 170, 179, 192] that classically activated M1-like macrophages can produce significant

amounts of pro-inflammatory cytokines and thereby have the ability to kill cancer cells. To that end, we assume here a baseline death rate $d_c > 0$ that is regulated not only by the cancer cell death effect-function $\Psi_{dc}(\sigma)$ introduced in (3.6a), but also by the M1 TAMs at a rate $d_{cM_1} > 0$. This results in the following mathematical representation of the cancer cell death process, namely

$$Q_c(\mathbf{u}) := d_c(\Psi_{dc}(\sigma) + d_{cM_1}M_1)c. \tag{3.18}$$

Similar to the macrophages, for the cancer cell population, we also account for the diffusion enhancement that the spatial distribution of ECM fibres enables [6, 50, 73, 118, 160, 224, 230, 237, 278]. Furthermore, the random movement of the cell population is also affected by the presence of both macrophage populations. While in general, the M2 TAMs were shown to promote cancer cell motility, [3] recent biological evidence [150, 157] indicates that the M1 phenotype has a negative effect on the cancer cell motility. Therefore, the diffusion coefficient for the random movement of the cancer cells can be formulated mathematically as

$$D^c(\mathbf{u}) := D_c(1 + D_{cM_2}M_2 + D_{cF}F - D_{cM_1}M_1). \tag{3.19}$$

where $D_c > 0$ is a baseline diffusion rate, $D_{cF} > 0$ is the ECM fibres enhancement coefficient, $D_{cM_1} > 0$ represents the weakening effect due to the presence of M1 TAM, and $D_{cM_2} > 0$ accounts for the positive motility effect due to the presence of M2 TAM.

Besides random motility, the directed movement of the cancer cells induced by various adhesion mediated processes [49, 55, 115, 210, 292, 297] is a central player in cancer invasion within the oriented fibrous environment. To that end, extending here on the modelling approach proposed in Chapter 2 and [265] to include the interactions of cancer cells with both families of macrophages, *i.e.,* M1 and M2 TAM, we have that the non-local spatial flux that drives the directed movement is

given in this case as:

$$\mathcal{A}_c(x,t,\mathbf{u},\theta_f) := \frac{1}{R}\int\limits_{\mathbf{B}(0,R)} \mathcal{K}(y)\Big[n(y)\big(\mathbf{S}_{cc}c(x+y,t)+\mathbf{S}_{cl}l(x+y,t) \\ +\mathbf{S}_{cM}(M_1(x+y,t)+M_2(x+y,t))\big) \\ +\widehat{n}(y,\theta_f(x+y,t))\mathbf{S}_{cF}F(x+y,t)\Big]\big[1-\rho(\mathbf{u}(x+y,t))\big]^+, \tag{3.20}$$

where R, $n(\cdot)$ and $\mathcal{K}(\cdot)$ are the same as in (3.14). Further, in (3.20) $\widehat{n}(\cdot,\cdot)$ is the unit radial vector biased by the orientation of the fibres, *i.e.,*

$$\widehat{n}(y,\theta_f(x+y)) := \begin{cases} \dfrac{y+\theta_f(x+y,t)}{\parallel y+\theta_f(x+y,t)\parallel_2} & \text{if } y\in\mathbf{B}(0,R)\setminus\{0\}, \\ 0 & \text{if } y=0 \text{ or } y=\theta_f(x+y,t). \end{cases} \tag{3.21}$$

Since (3.20) is built on the same concept as the non-local adhesion term in Chapter 2, for illustration we refer the reader to Figures 2.1 and 2.7. Moreover, in (3.20) $\mathbf{S}_{cM}>0$ represents the strength of the adhesion relationship between the cancer cells and M1 and M2 TAMs, $S_{cF}>0$ is the strength of the cell-fibre ECM adhesion [295] and $S_{cl}>0$ corresponds to strength of adhesion between the cancer cells and the non-fibre ECM phase (that includes for instance amyloid fibrils, which can support cell-adhesion processes [90, 91]). Furthermore, as high level of extracellular Ca^{+2} ions (which form one of the constituents of the non-fibre ECM phase) are necessary for cell-cell adhesion [94, 109], proceeding as in Chapter 2 and in [245, 246, 247, 265] the cancer cells self-adhesion coefficient $\mathbf{S}_{cc}$ is taken here as

$$\mathbf{S}_{cc}(x,t) := \mathbf{S}_{min}+(\mathbf{S}_{max}-\mathbf{S}_{min})\exp\left(1-\frac{1}{1-(1-l(x,t))^2}\right),$$

where $\mathbf{S}_{max}>0$ and $\mathbf{S}_{min}>0$ correspond to maximum and minimum levels of Ca^{+2} ions. Therefore, $\mathbf{S}_{cc}$ smoothly increases from a minimal to a maximum value in order

to fully explore the varying strengths of cell-cell adhesion.

Thus, using (3.17) to (3.20) the spatio-temporal dynamics of the cancer population $c(x,t)$ is expressed as

$$\frac{\partial c}{\partial t} = \nabla \cdot [D^c(\mathbf{u})\nabla c - c\mathcal{A}_c(x,t,\mathbf{u},\theta_f)] + P_c(\mathbf{u}) - Q_c(\mathbf{u}). \tag{3.22}$$

Two-phase ECM macro-scale dynamics

Besides the cancer cells, both macrophage phenotypes contribute to the degradation of the ECM by secreting proteolytic enzymes [69, 89, 173, 194, 228] (e.g., various classes of matrix metalloproteinases). To that end, we extend the dynamics of the fibre, and non-fibre ECM components used in Chapter 2 and [265] by incorporating the effects of the M1 phenotype. Thus, the dynamics of the non-fibre $l(x,t)$ as well as the fibre ECM $F(x,t)$ are formalized as

$$\frac{\partial l}{\partial t} = -l(\beta_{lc}c + \beta_{lM_1}M_1 + \beta_{lM_2}M_2) + (\gamma_0 + \gamma_{M_2}M_2)(1-\rho(\mathbf{u}))^+, \tag{3.23a}$$

$$\frac{\partial F}{\partial t} = -F(\beta_{Fc}c + \beta_{FM_1}M_1 + \beta_{FM_2}M_2), \tag{3.23b}$$

where β_{lc}, β_{lM_1}, β_{lM_2} are the positive degradation rates of the non-fibre ECM phase due to the cancer cells, M1 and M2 TAMs, respectively. Similarly, β_{Fc}, β_{FM_1}, β_{FM_2} are all positive and describe the degradation rates of the fibre component of the ECM due to the cancer cells, M1 and M2 TAMs, respectively. Finally, in (3.23) $\gamma_0 > 0$ represents the constant rate of remodelling and $\gamma_{M_2} > 0$ is the remodelling enhancement rate induced by the M2 TAM population [3, 89, 254].

The full macro-scale dynamics

In summary, using (3.3), (3.16), (3.22) and (3.23) the non-dimensional macro-scale dynamics is given by the following coupled PDEs

$$\frac{\partial c}{\partial t} = \nabla \cdot [D^c(\mathbf{u})\nabla c - c\mathcal{A}_c(x,t,\mathbf{u},\theta_f)] + P_c(\mathbf{u}) - Q_c(\mathbf{u}), \tag{3.24a}$$

$$\begin{aligned}\frac{\partial M_1}{\partial t} =& \nabla \cdot [D^M(\mathbf{u})\nabla M_1 - M_1\mathcal{A}_M(x,t,\mathbf{u},\mathbf{S}_{M_1M})] + P_{M_1}(\mathbf{u}) - Q_{M_1}(\mathbf{u}) \\ & - T_{12}(\mathbf{u}) + T_{21}(\mathbf{u}) + M_I,\end{aligned} \tag{3.24b}$$

$$\begin{aligned}\frac{\partial M_2}{\partial t} =& \nabla \cdot [D^M(\mathbf{u})\nabla M_2 - M_2\mathcal{A}_M(x,t,\mathbf{u},\mathbf{S}_{M_2M})] + P_{M_2}(\mathbf{u}) - Q_{M_2}(\mathbf{u}) \\ & + T_{12}(\mathbf{u}) - T_{21}(\mathbf{u}),\end{aligned} \tag{3.24c}$$

$$\frac{\partial l}{\partial t} = -\, l(\beta_{lc}c + \beta_{lM_1}M_1 + \beta_{lM_2}M_2) + (\gamma_0 + \gamma_{M_2}M_2)(1-\rho(\mathbf{u})), \tag{3.24d}$$

$$\frac{\partial F}{\partial t} = -\, F(\beta_{Fc}c + \beta_{FM_1}M_1 + \beta_{FM_2}M_2), \tag{3.24e}$$

$$0 = D_\sigma \Delta\sigma - d_\sigma(c + M_1 + M_2), \tag{3.24f}$$

in the presence of appropriate initial conditions (such as those specified in (3.51)) with zero-flux boundary conditions for c, M_1, M_2, l and F, as well as Dirichlet boundary condition (3.3) for the nutrients σ.

3.2.2 Processes on the Micro-Scales and Links Between the Scales

As the process of cancer invasion is truly a multi-scale phenomenon [293], the macro-scale dynamics are tightly linked together with several micro-scale processes. Analogously to Chapter 2, among these micro-scale processes, of primary interest for us are the micro-scale rearrangement of ECM fibre micro-constituents as well as the cell-scale proteolytic processes that take place at the leading edge of the tumour. In

the following, we outline how these micro-scale processes, detailed in Section 2.2.2, change for this new extended model.

Fibres on the micro-scale and their bottom-up and top-down links to macro-dynamics

First, since we do not modify the naturally emerging *fibres bottom-up* link from the one described in Section 2.2.2, we utilise the micro-fibres distribution $f(x,t)$ the same exact way to represent the ECM fibres through their amount $F(x,t)$ and their spatial bias $\theta_f(x,t)$.

On the other hand, within the micro-fibres rearrangement process, *i.e.,* in the *fibre top-bottom* link, we need to account for the fact that M1 TAMs are also capable of secreting MDEs. Indeed, the collective migration of the cancer cells, M1 TAMS, and M2 TAMs lead naturally to the emergence of the associated spatial fluxes $\mathcal{F}_c$, $\mathcal{F}_{M_1}$, and $\mathcal{F}_{M_2}$ given by

$$\begin{aligned}
\mathcal{F}_c(x,t) :=& D^c(M_1,M_2,F)\nabla c - c\mathcal{A}_c(x,t,\mathbf{u},\theta_f),\\
\mathcal{F}_{M_1}(x,t) :=& D^M(F)\nabla M_1 - M_1\mathcal{A}_M(x,t,\mathbf{u},\mathbf{S}_{M_1M}),\\
\mathcal{F}_{M_2}(x,t) :=& D^M(F)\nabla M_2 - M_2\mathcal{A}_M(x,t,\mathbf{u},\mathbf{S}_{M_2M}),
\end{aligned}$$

respectively. The combined action of these fluxes upon the ECM fibres distributed at $(x,t)\in\Omega_t\times[0,T]$ is felt uniformly by its constituent micro-fibres $f(z,t)$ distributed on the associated micro-domain $\delta Y(x)$, consequently inducing a *micro-fibres rearrangement vector* similar to the ones proposed in Section 2.3.2 and in [245, 265] of the form

$$\begin{aligned}
r(\delta Y(x),t) :=& \omega_c(x,t)\mathcal{F}_c(x,t) + \omega_{M_1}(x,t)\mathcal{F}_{M_1}(x,t)\\
&+ \omega_{M_2}(x,t)\mathcal{F}_{M_2}(x,t) + \omega_F(x,t)\theta_f(x,t),
\end{aligned} \tag{3.25}$$

which triggers a spatial redistribution of the micro-fibres in $\delta Y(x)$. In (3.25), the

non-linear weights ω_c, ω_{M_1}, ω_{M_2} and ω_F are the associated mass factions of cancer cells, M1 TAMs, M2 TAMs, and ECM fibres at (x,t), and so these are given by

$$\begin{aligned}
\omega_c(x,t) :=& \frac{c(x,t)}{c(x,t)+M_1(x,t)+M_2(x,t)+F(x,t)},\\
\omega_{M_1}(x,t) :=& \frac{M_1(x,t)}{c(x,t)+M_1(x,t)+M_2(x,t)+F(x,t)},\\
\omega_{M_2}(x,t) :=& \frac{M_2(x,t)}{c(x,t)+M_1(x,t)+M_2(x,t)+F(x,t)},\\
\omega_F(x,t) :=& \frac{F(x,t)}{c(x,t)+M_1(x,t)+M_2(x,t)+F(x,t)},
\end{aligned}$$

respectively. Ultimately, as in Section 2.2.2, the rearrangement vector (3.25) induces a *relocation vector* $\nu_{\delta Y(x)}(z,t)$, and as a result we can appropriately calculate the new positions z^* of any micro-scale node $z \in \delta Y(x)$.

Finally, since the rest of the dynamics based is on the exact same approach as in Section 2.2.2, for further details on the process as well as for illustrations on the rearrangement process and the two links between the macro-scale and the fibre micro-scale, we refer the reader to Section 2.2.2 and Figures 2.3 and 2.5.

MDE boundary micro-dynamics and its connections to macro-dynamics

Analogously to Chapter 2, the second micro-process that we consider is the proteolytic molecular processes which are driven by the secretion of *matrix-degrading enzymes* (MDEs) (such as matrix-metalloproteinases) and takes place along the leading edge of the tumour. Indeed, all three cell populations (cancer cells, M1 TAMs and M2 TAMs) secrete MDEs [69, 89, 173, 194, 228] within the proliferating outer rim of the tumour, and so this way, the tissue-scale dynamics induces a source for cell-scale proteolytic activity. Thus, following here the approach introduced in Section 2.2.2 and [279], we explore the emerging spatio-temporal molecular MDEs micro-dynamics $m(y,\tau)$ on an appropriate cell-scale neighbourhood of the tumour

interface $\partial\Omega(t)$ enabled by the union of a covering bundle of cubic micro-domains $\{\epsilon Y\}_{\epsilon Y \in \mathcal{P}(t)}$, with each ϵY being of micro-scale size $\epsilon > 0$.

Therefore, at any spatio-temporal point $(y, \tau) \in (\epsilon Y \cap \Omega(t_0)) \times [0, \Delta t]$, a source of MDEs arises as a collective contribution of the cancer cell and now both macrophage populations from the outer proliferating rim of the tumour that are situated within a distance $\gamma_h > 0$ from $y \in \epsilon Y$. Hence, in this case, the M1-like macrophages also contribute to the micro-scale MDE source $h(y, \tau)$ term that is now given by

$$h(y,\tau) = \begin{cases} \dfrac{\displaystyle\int_{\mathbf{B}(y,\gamma_h)\cap\Omega(t_0)} h_\Sigma(x,\tau)\, dx}{\lambda(\mathbf{B}(y,\gamma_h)\cap\Omega(t_0))} & y \in \epsilon Y \cap \Omega(t_0), \\ 0 & y \notin \epsilon Y \setminus (\Omega(t_0) + \{z \in Y \mid \|z\|_2 < \rho\}), \end{cases} \tag{3.26}$$

where $\lambda(\cdot)$ is the Lebesgue measure in $\mathbb{R}^N$, $\mathbf{B}(y, \gamma_h)$ denotes the $\|\cdot\|_\infty$ ball with appropriately chosen radius $\gamma_h > 0$ and $0 < \rho < \gamma_h$ is a small mollification range which smooths out the source function $h(\cdot, \cdot)$. Further, in (3.26) h_Σ is given by

$$h_\Sigma(x,\tau) := \alpha_c c(x, t_0 + \tau) + \alpha_{M_1} M_1(x, t_0 + \tau) + \alpha_{M_2} M_2(x, t_0 + \tau),$$

where $\alpha_c > 0$, $\alpha_{M_1} > 0$ and $\alpha_{M_2} > 0$ are constant secretion rates of the MDEs by the cancer cells, M1 and M2 TAMs respectively. As before, since this source term $h(y, \tau)$ is naturally induced by the macro-scale, this establishes a *MDE top-down* link between the tumour macro-dynamics and MDE-micro-dynamics occurring at the tumour interface.

Then, to describe the MDE micro-dynamics we use the same form as in Sec-

tion 2.2.2

$$\begin{aligned} \frac{\partial m}{\partial \tau} &= D_m \Delta m + h(y,\tau), \\ m(y,0) &= 0, \\ \frac{\partial m}{\partial n}\Big|_{\partial \epsilon Y} &= 0, \end{aligned} \tag{3.27}$$

where $D_m > 0$ is the constant diffusion coefficient and n is the outward normal vector. Similarly to Section 2.2.2, this enables us to capture the changes in tumour morphology by determining the direction of movement $\eta_{\epsilon Y(x)}$ and magnitude of the displacement $\xi_{\epsilon Y(x)}$ of invading cancer in the surrounding tissue [279]. To further details on this micro-process as well as illustration of the overlapping ϵ-cubes and the two-links that connects the macro-scale to the MDE micro-scale, we refer the reader to Section 2.2.2 and Figures 2.4 and 2.5.

3.3 Numerical Approaches

In this section, we describe the numerical approach developed to solve the tumour macro-scale dynamics (3.24). First, to solve the quasi-steady nutrients σ equation (3.24f), we use the usual successive over-relaxation method with relaxation parameter $\omega = 0.5$ and tolerance of 10^{-5}. For the rest of the dynamics (3.24a)-(3.24e), we use the method of lines approach to discretise the system (3.24) first in space and then for the resulting ODEs we use a non-local predictor-corrector scheme [245]. In this context, we carry out an accurate approximation of the two distinct spatial operators, namely the diffusion and adhesion operators, by using fast convolution-driven approaches. Specifically, while for the diffusion, we construct a convolution-based second-order central difference scheme [265], for the adhesion operators, we formulate a convolution-driven *fifth-order weighted essentially non-oscillatory* (WENO5) finite difference scheme.

Furthermore, to approximate the adhesion integrals (3.14) and (3.20), we adopt the numerical approach used in Section 2.4.1 and [265]. Here, we omit the technical details of this method since it follows identical steps, the sole difference being that within the formulas, we use the total macrophage population, *i.e.,* M1 + M2 TAMs instead of only the M2 TAMs population. For the same rationale, we also skip the details of the numerical method used in the MDE micro-scale, and for further details, we refer the reader to Section 2.4.1 and [265].

To facilitate the description of the numerical approaches, let us first introduce some basic notations. As in Chapter 2, we discretise the maximal tissue cube $Y \in \mathbb{R}^2$ uniformly in each direction with spatial step size $\Delta x = \Delta y$. Therefore, the discretisation of Y can be represented through the macro-spatial locations $\{(x_i, y_j)\}_{i,j=1..N}$, with $N = L/h_L + 1$. Then the discretised global tumour vector at any time-step n is denoted by $\mathbf{u}^n = [c^n, M_1^n, M_2^n, l^n, F^n]^\intercal$, while the discretised nutrient field is denoted by σ^n. Further, we denote the diffusion coefficient functions and adhesion integrals for cancer cell and TAMs by $(D^c)^n$, $(D^M)^n$, $(\mathcal{A}_c)^n$ and $(\mathcal{A}_M)^n$, respectively. Finally, with these notations, we are able to rewrite the macro-scale dynamics (3.24) in the following convenient form

$$\begin{aligned} \frac{\partial \mathbf{u}}{\partial t} =& \nabla \cdot [\mathcal{D}(\mathbf{u}) \nabla \mathbf{u}] - \nabla \cdot \mathcal{F}(\mathbf{u}) + \mathcal{S}(\mathbf{u}), \\ 0 =& D_\sigma \Delta \sigma - d_\sigma (c + M_1 + M_2), \end{aligned} \tag{3.28}$$

where

$$\mathcal{D}(\mathbf{u}) := \begin{bmatrix} D^c(\mathbf{u}) \\ D^M(\mathbf{u}) \\ D^M(\mathbf{u}) \\ 0 \\ 0 \end{bmatrix}, \qquad \mathcal{F}(\mathbf{u}) := \begin{bmatrix} c\mathcal{A}_c(x,t,\mathbf{u},\theta_f) \\ M_1\mathcal{A}_M(x,t,\mathbf{u},\mathbf{S}_{M_1M}) \\ M_2\mathcal{A}_M(x,t,\mathbf{u},\mathbf{S}_{M_2M}) \\ 0 \\ 0 \end{bmatrix},$$

$$\mathcal{S}(\mathbf{u}) := \begin{bmatrix} P_c(\mathbf{u}) - Q_c(\mathbf{u}) \\ P_{M_1}(\mathbf{u}) - Q_{M_1}(\mathbf{u}) - T_{12}(\mathbf{u}) + T_{21}(\mathbf{u}) + M_I \\ P_{M_2}(\mathbf{u}) - Q_{M_2}(\mathbf{u}) + T_{12}(\mathbf{u}) - T_{21}(\mathbf{u}) \\ -l(\beta_{lc}c + \beta_{lM_1}M_1 + \beta_{lM_2}M_2) + (\gamma_0 + \gamma_{M_2}M_2)(1-\rho(\mathbf{u})) \\ -F(\beta_{Fc}c + \beta_{FM_1}M_1 + \beta_{FM_2}M_2) \end{bmatrix}.$$

3.3.1 Diffusion Operators: $\nabla \cdot [\mathcal{D}(\mathbf{u})\nabla\mathbf{u}]$

Starting with the discretisation of the diffusion operators $\nabla \cdot [\mathcal{D}(\mathbf{u})\nabla\mathbf{u}]$ in (3.28), during the computations, we first detect, as in Section 2.4.1, whether a spatial node (i,j) is inside or outside the expanding tumour domain $\Omega(t_0)$ via an indicator function $\mathcal{I}(\cdot,\cdot) : X \times X \to \{0,1\}$, with $X = \{1,...,M\}$ that is defined by

$$\mathcal{I}(i,j) := \begin{cases} 1 & \text{if } (x_i, x_j) \in \Omega(t_0), \\ 0 & \text{otherwise.} \end{cases} \tag{3.29}$$

Similarly, we detect any boundary nodes using a boundary indicator function defined by

$$\mathcal{I}_B(i,j) := \begin{cases} 1 & \text{if } (x_i, x_j) \in \partial\Omega(t_0), \\ 0 & \text{otherwise,} \end{cases} \tag{3.30}$$

where $\partial\Omega(t_0)$ is boundary of $\Omega(t_0)$, and for convenience we also define the interior indicator function by

$$\mathcal{I}_{In}(i,j) := \begin{cases} 1 & \text{if } (x_i, x_j) \in \Omega(t_0) \setminus \partial\Omega(t_0). \\ 0 & \text{otherwise.} \end{cases} \tag{3.31}$$

These two functions, given in (3.30) and (3.31), enable us to split the domain into two parts, namely to boundary and strictly inside parts. The motivation behind this is the same as before, namely to use two different computational techniques on these parts which eventually reduces the computational cost. Hence, while for any interior node we can use the same discrete universal numerical operator (convolution), for a boundary point we need to apply unique operators due to the zero-flux boundary condition and the continuously changing tumour domain (that may result in an irregular tumour shape). Therefore, to achieve the reduction in computational cost, we accordingly split the spatial operators $\nabla \cdot [\mathcal{D}(\mathbf{u})\nabla\mathbf{u}]$ into two components as well, and so at any spatial node $(x_i, y_j) \in \Omega(t_0) \subset Y$, the diffusion operators can be represented as

$$\nabla \cdot [\mathcal{D}(\mathbf{u})\nabla\mathbf{u}](i,j) := \begin{cases} \nabla \cdot [\mathcal{D}(\mathbf{u})\nabla\mathbf{u}]^{In}(i,j) & \text{if } \mathcal{I}_{In}(i,j) = 1, \\ \nabla \cdot [\mathcal{D}(\mathbf{u})\nabla\mathbf{u}]^{B}(i,j) & \text{if } \mathcal{I}_{B}(i,j) = 1, \\ 0 & \text{otherwise.} \end{cases} \tag{3.32}$$

In this context, the usual two dimensional second-order central difference scheme for a non-constant diffusion operator is given by

$$\begin{aligned}\big(\nabla\cdot[\mathcal{D}(\mathbf{u})\nabla\mathbf{u}]\big)^n_{i,j} = \\ \frac{1}{\Delta x^2}\Bigg(&\frac{\mathcal{D}(\mathbf{u}^n_{i+1,j})+\mathcal{D}(\mathbf{u}^n_{i,j})}{2}\big(\mathbf{u}^n_{i+1,j}-\mathbf{u}^n_{i,j}\big)-\frac{\mathcal{D}(\mathbf{u}^n_{i,j})+\mathcal{D}(\mathbf{u}^n_{i-1,j})}{2}\big(\mathbf{u}^n_{i,j}-\mathbf{u}^n_{i-1,j}\big)\\ &+\frac{\mathcal{D}(\mathbf{u}^n_{i,j+1})+\mathcal{D}(\mathbf{u}^n_{i,j})}{2}\big(\mathbf{u}^n_{i,j+1}-\mathbf{u}^n_{i,j}\big)-\frac{\mathcal{D}(\mathbf{u}^n_{i,j})+\mathcal{D}(\mathbf{u}^n_{i,j-1})}{2}\big(\mathbf{u}^n_{i,j}-\mathbf{u}^n_{i,j-1}\big)\Bigg),\end{aligned} \tag{3.33}$$

where $\mathbf{u}^n_{i,j} = [c^n_{i,j}, M^n_{1_{i,j}}, M^n_{2_{i,j}}, l^n_{i,j}, F^n_{i,j}]^\intercal$. Further, we observe that (3.33) can be equivalently expressed by sum of discrete convolutions and so for all interior nodes (x_i, y_j) the scheme is given by

$$\begin{aligned}\big(\nabla\cdot[\mathcal{D}(\mathbf{u})\nabla\mathbf{u}]^{In}\big)^n = \frac{1}{\Delta x^2}\sum_{k=1}^{2}\Bigg(&\Big(\widetilde{\mathcal{K}}^{2k-1}_A * \mathcal{D}(\mathbf{u}^n)\Big)\circ\Big(\widetilde{\mathcal{K}}^k_F * \mathbf{u}^n\Big)\\ &-\Big(\widetilde{\mathcal{K}}^{2k}_A * \mathcal{D}(\mathbf{u}^n)\Big)\circ\Big(\widetilde{\mathcal{K}}^k_B * \mathbf{u}^n\Big)\Bigg),\end{aligned} \tag{3.34}$$

where $*$ is the discrete convolution and $\circ$ is the Hadamard product, that is defined in A.3 (and for further details we refer the reader to [87]). Also, in (3.34) each $\widetilde{\mathcal{K}}^k_A$, with $k = 1\ldots4$ describe the average between the point (i, j) and one of its immediate neighbour and so they are defined by

$$\widetilde{\mathcal{K}}^1_A = [0, 0.5, 0.5], \quad \widetilde{\mathcal{K}}^2_A = [0.5, 0.5, 0], \quad \widetilde{\mathcal{K}}^3_A = \big(\widetilde{\mathcal{K}}^1_A\big)^\intercal, \quad \widetilde{\mathcal{K}}^4_A = \big(\widetilde{\mathcal{K}}^2_A\big)^\intercal. \tag{3.35}$$

Moreover, in (3.34) $\widetilde{\mathcal{K}}^k_F$ and $\widetilde{\mathcal{K}}^k_B$ with $k = 1, 2$ are induced by the forward and backward differences, respectively. Hence, they are defined in both direction i (if $k = 1$) as well as in direction j (if $k = 2$) by

$$\widetilde{\mathcal{K}}^1_F = [0, -1, 1], \quad \widetilde{\mathcal{K}}^1_B = [-1, 1, 0], \quad \widetilde{\mathcal{K}}^2_F = \big(\widetilde{\mathcal{K}}^1_F\big)^\intercal, \quad \widetilde{\mathcal{K}}^2_B = \big(\widetilde{\mathcal{K}}^1_B\big)^\intercal. \tag{3.36}$$

However, for boundary nodes, we cannot use the form (3.34) due to the imposed zero-flux boundary condition and the continuously changing tumour domain. This is because the calculation of the diffusion operators at the boundary nodes involves the approximation of the values at any node that does not belong to the tumour domain, *i.e.,* for any node $(x_i, y_j) \notin \Omega(t_0)$. In some cases, due to the irregular domain, such values may not be uniquely defined because multiple nodes can require the value of the same ghost/outside node, however, with different values. Consequently, for any boundary node, instead of the convolutional form (3.34), we instead use the usual form (3.33) and symmetrically reflect the values of the interior nodes to the ghost/outside nodes in a node by node fashion.

3.3.2 Adhesion Operators: $\nabla \cdot \mathcal{F}(\mathbf{u})$

The other spatial operators that contribute to the motility are the adhesion operators $\nabla \cdot \mathcal{F}(\mathbf{u})$ in (3.28). The procedure to approximate these differential operators is based on the standard WENO5 scheme proposed in [123, 159]. However, it was shown [310] that these standard WENO5 schemes suffer from slight post-shock oscillations. As a consequence, we adopt here the modified WENO5 scheme proposed in [310], which uses modified smoothness indicators and is referred to as the ZSWENO scheme.

Similarly to the diffusion operator case, here we split the domain into two parts as well. However, ZSWENO schemes induce larger stencils compared to the second-order central difference scheme and so, we need to split the domain $\Omega(t_0)$ into two parts differently. We refer these two parts as the *inside* and *layer* parts. First, the former one is detected by using an inside indicator function $\mathcal{I}_I(i, j)$ that we define by

$$\mathcal{I}_I(i,j) := \begin{cases} 1 & \text{if } (\mathcal{I} * \mathcal{K}_I)_{i,j} = 1, \\ 0 & \text{otherwise,} \end{cases} \tag{3.37}$$

where $\mathcal{I}$ is defined in (3.29) and $\mathcal{K}_I$ is given by

$$\mathcal{K}_{in} = \frac{1}{13}\begin{bmatrix} 0 & 0 & 0 & 1 & 0 & 0 & 0 \\ 0 & 0 & 0 & 1 & 0 & 0 & 0 \\ 0 & 0 & 0 & 1 & 0 & 0 & 0 \\ 1 & 1 & 1 & 1 & 1 & 1 & 1 \\ 0 & 0 & 0 & 1 & 0 & 0 & 0 \\ 0 & 0 & 0 & 1 & 0 & 0 & 0 \\ 0 & 0 & 0 & 1 & 0 & 0 & 0 \end{bmatrix},$$

which is induced by the fifth-order ZSWENO stencils. Then the layer part of the domain is detected by a layer indicator function formulated as

$$\mathcal{I}_L(i,j) := \begin{cases} 1 & \text{if } \mathcal{I}(i,j) - \mathcal{I}_I(i,j) = 1, \\ 0 & \text{otherwise.} \end{cases} \tag{3.38}$$

Similarly to the diffusion, using these indicator functions (3.37) and (3.38), we split the adhesion operator into two parts and so at any spatial node $(x_i, y_j) \in \Omega(t_0)$ this operator is represented as

$$\nabla \cdot \mathcal{F}(\mathbf{u})(i,j) := \begin{cases} \nabla \cdot \mathcal{F}(\mathbf{u})^I(i,j) & \text{if } \mathcal{I}_I(i,j) = 1, \\ \nabla \cdot \mathcal{F}(\mathbf{u})^L(i,j) & \text{if } \mathcal{I}_L(i,j) = 1, \\ 0 & \text{otherwise.} \end{cases} \tag{3.39}$$

Therefore, for the inside operator $\nabla \cdot \mathcal{F}(\mathbf{u})^I$, we use the usual conservative form

$$\nabla \cdot \mathcal{F}(\mathbf{u})^I = \frac{1}{\Delta x}\Big(\hat{F}_{i+\frac{1}{2},j} - \hat{F}_{i-\frac{1}{2},j} + \hat{G}_{i,j+\frac{1}{2}} - \hat{G}_{i,j-\frac{1}{2}}\Big), \tag{3.40}$$

where $\hat{F}_{i+\frac{1}{2},j}$, $\hat{F}_{i-\frac{1}{2},j}$, $\hat{G}_{i,j+\frac{1}{2}}$ and $\hat{G}_{i,j-\frac{1}{2}}$ are the numerical fluxes at $(x_{i+\frac{1}{2}}, y_j)$, $(x_{i-\frac{1}{2}}, y_j)$, $(x_i, y_{j+\frac{1}{2}})$ and $(x_i, y_{j-\frac{1}{2}})$, respectively. Also in (3.40), for compact notation, $\hat{F}$ and

$\hat{G}$ denotes the x and y components of the vector field $\mathcal{F}(\cdot)$, respectively.

For brevity, we will only focus on defining $\hat{F}_{i+\frac{1}{2},j}$ and $\hat{F}_{i-\frac{1}{2},j}$, and note that corresponding calculations for $\hat{G}_{i,j+\frac{1}{2}}$ and $\hat{G}_{i,j-\frac{1}{2}}$ follows identical steps. In this context, we split the x component of $\mathcal{F}(\cdot)$ into two parts

$$\hat{F}(\mathbf{u}) = \hat{F}^{+}(\mathbf{u}) + \hat{F}^{-}(\mathbf{u}),$$

where $d\hat{F}^{+}(\mathbf{u})/d\mathbf{u} > 0$ and $d\hat{F}^{-}(\mathbf{u})/d\mathbf{u} \leq 0$. Then, we define these parts by using the popular Rusanov-type flux splitting method [236] that is given by

$$\hat{F}^{\pm}(\mathbf{u}) = \frac{1}{2}\Big(\hat{F}(\mathbf{u}) \pm \alpha\mathbf{u}\Big), \tag{3.41}$$

where we approximate $\alpha := \max|d\hat{F}(\mathbf{u})/d\mathbf{u}|$, *i.e.,* the spectral radius of the Jacobian generated by $\hat{F}(\cdot)$ in a Jacobian-free manner, detailed in Section 3.3.3. To this end, let us denote by $\hat{F}^{+}_{i\pm\frac{1}{2},j}$ and $\hat{F}^{-}_{i\pm\frac{1}{2},j}$ the numerical fluxes obtained by splitting $\hat{F}(\cdot)$ into the positive and negative parts, respectively. Then these numerical fluxes used in (3.40) are given by the sum of their associated parts

$$\hat{F}_{i\pm\frac{1}{2},j} = \hat{F}^{+}_{i\pm\frac{1}{2},j} + \hat{F}^{-}_{i\pm\frac{1}{2},j},$$

where following the standard ZSWENO procedure, $\hat{F}^{+}_{i\pm\frac{1}{2},j}$ and $\hat{F}^{-}_{i\pm\frac{1}{2},j}$ are given by the weighted combination of the three third-order *essentially non-oscillatory* (ENO) approximations [123, 134, 159, 310]. Hence, they are given by

$$\hat{F}^{\pm}_{i+\frac{1}{2},j} = \sum_{k=0}^{2} \omega^{\pm}_{k,i+\frac{1}{2},j}\hat{F}^{\pm}_{k,+}, \qquad \hat{F}^{\pm}_{i-\frac{1}{2},j} = \sum_{k=0}^{2} \omega^{\pm}_{k,i-\frac{1}{2},j}\hat{F}^{\pm}_{k,-}, \tag{3.42}$$

where $\omega^{\pm}_{k,i\pm\frac{1}{2},j}$ are the non-linear weights that we will define later, $\hat{F}^{\pm}_{k,+}$ are the ENO

approximations given by

$$\begin{aligned}
\hat{F}^{+}_{0,+} =& \frac{1}{3}\hat{F}^{+}(\mathbf{u}_{i-2,j}) - \frac{7}{6}\hat{F}^{+}(\mathbf{u}_{i-1,j}) + \frac{11}{6}\hat{F}^{+}(\mathbf{u}_{i,j}),\\
\hat{F}^{+}_{1,+} =& -\frac{1}{6}\hat{F}^{+}(\mathbf{u}_{i-1,j}) + \frac{5}{6}\hat{F}^{+}(\mathbf{u}_{i,j}) + \frac{1}{3}\hat{F}^{+}(\mathbf{u}_{i+1,j}),\\
\hat{F}^{+}_{2,+} =& \frac{1}{3}\hat{F}^{+}(\mathbf{u}_{i,j}) + \frac{5}{6}\hat{F}^{+}(\mathbf{u}_{i+1,j}) - \frac{1}{6}\hat{F}^{+}(\mathbf{u}_{i+2,j}),\\
\hat{F}^{-}_{0,+} =& \frac{1}{3}\hat{F}^{-}(\mathbf{u}_{i+3,j}) - \frac{7}{6}\hat{F}^{-}(\mathbf{u}_{i+2,j}) + \frac{11}{6}\hat{F}^{-}(\mathbf{u}_{i+1,j}),\\
\hat{F}^{-}_{1,+} =& -\frac{1}{6}\hat{F}^{-}(\mathbf{u}_{i+2,j}) + \frac{5}{6}\hat{F}^{-}(\mathbf{u}_{i+1,j}) + \frac{1}{3}\hat{F}^{-}(\mathbf{u}_{i,j}),\\
\hat{F}^{-}_{2,+} =& \frac{1}{3}\hat{F}^{-}(\mathbf{u}_{i+1,j}) - \frac{5}{6}\hat{F}^{-}(\mathbf{u}_{i,j}) + \frac{1}{6}\hat{F}^{-}(\mathbf{u}_{i-1,j}),
\end{aligned} \tag{3.43}$$

and similarly, $\hat{F}^{\pm}_{k,-}$ are defined by

$$\begin{aligned}
\hat{F}^{+}_{0,-} =& \frac{1}{3}\hat{F}^{+}(\mathbf{u}_{i-3,j}) - \frac{7}{6}\hat{F}^{+}(\mathbf{u}_{i-2,j}) + \frac{11}{6}\hat{F}^{+}(\mathbf{u}_{i-1,j}),\\
\hat{F}^{+}_{1,-} =& -\frac{1}{6}\hat{F}^{+}(\mathbf{u}_{i-2,j}) + \frac{5}{6}\hat{F}^{+}(\mathbf{u}_{i-1,j}) + \frac{1}{3}\hat{F}^{+}(\mathbf{u}_{i,j}),\\
\hat{F}^{+}_{2,-} =& \frac{1}{3}\hat{F}^{+}(\mathbf{u}_{i-1,j}) + \frac{5}{6}\hat{F}^{+}(\mathbf{u}_{i,j}) - \frac{1}{6}\hat{F}^{+}(\mathbf{u}_{i+1,j}),\\
\hat{F}^{-}_{0,-} =& \frac{1}{3}\hat{F}^{-}(\mathbf{u}_{i+2,j}) - \frac{7}{6}\hat{F}^{-}(\mathbf{u}_{i+1,j}) + \frac{11}{6}\hat{F}^{-}(\mathbf{u}_{i,j}),\\
\hat{F}^{-}_{1,-} =& -\frac{1}{6}\hat{F}^{-}(\mathbf{u}_{i+1,j}) + \frac{5}{6}\hat{F}^{-}(\mathbf{u}_{i,j}) + \frac{1}{3}\hat{F}^{-}(\mathbf{u}_{i-1,j}),\\
\hat{F}^{-}_{2,-} =& \frac{1}{3}\hat{F}^{-}(\mathbf{u}_{i,j}) + \frac{5}{6}\hat{F}^{-}(\mathbf{u}_{i-1,j}) - \frac{1}{6}\hat{F}^{-}(\mathbf{u}_{i-2,j}).
\end{aligned} \tag{3.44}$$

Finally, in (3.43) and (3.44) $\hat{F}^{\pm}(\mathbf{u})$ are given by the Rusanov-type flux splitting method defined in (3.41).

Since our aim is to reduce the computational cost and so for this we seek to use convolution, we observe that indeed these ENO fluxes (3.43) and (3.44) can be equivalently represented by discrete convolutions, *i.e.,*

$$\hat{F}^{\pm}_{k,+} = \widetilde{\mathcal{K}}^{\pm}_{k,+} * \mathcal{F}^{\pm}(\mathbf{u}), \qquad \hat{F}^{\pm}_{k,-} = \widetilde{\mathcal{K}}^{\pm}_{k,-} * \mathcal{F}^{\pm}(\mathbf{u}), \tag{3.45}$$

where $\widetilde{\mathcal{K}}^{\pm}_{k,+}$ and $\widetilde{\mathcal{K}}^{\pm}_{k,-}$ are the induced vectors from (3.43) and (3.44), and for completeness they are defined in Appendix A.5.

Let us now shift our attention to the non-linear weights $\omega^{\pm}_{k,i\pm\frac{1}{2},j}$ that we used to construct the ZSWENO approximation in (3.42). Following again the usual procedure [159], we define these weights as

$$\begin{aligned}
\omega^{\pm}_{k,i+\frac{1}{2},j} &:= \frac{\alpha^{\pm}_{k,i+\frac{1}{2},j}}{\sum_{k=0}^{2}\alpha^{\pm}_{k,i+\frac{1}{2},j}}, \qquad \alpha^{\pm}_{k,i+\frac{1}{2},j} := \frac{\omega^{o}_{k,+}}{\Big(\epsilon_{_W} + IS^{\pm}_{k,i+\frac{1}{2},j}\Big)^{p}},\\
\omega^{\pm}_{k,i-\frac{1}{2},j} &:= \frac{\alpha^{\pm}_{k,i-\frac{1}{2},j}}{\sum_{k=0}^{2}\alpha^{\pm}_{k,i-\frac{1}{2},j}}, \qquad \alpha^{\pm}_{k,i-\frac{1}{2},j} := \frac{\omega^{o}_{k,-}}{\Big(\epsilon_{_W} + IS^{\pm}_{k,i-\frac{1}{2},j}\Big)^{p}},
\end{aligned} \tag{3.46}$$

where we take the usual $p = 2$, $\epsilon_{_W} = 10^{-6}$ values [123], and define the optimal weights $\omega^{o}_{k,+}$ and $\omega^{o}_{k,-}$ as: $\omega^{o}_{0,+} = 0.1$, $\omega^{o}_{1,+} = 0.6$, $\omega^{o}_{2,+} = 0.3$ and $\omega^{o}_{0,-} = 0.3$, $\omega^{o}_{1,-} = 0.6$, $\omega^{o}_{2,-} = 0.1$. Furthermore, in (3.46) $IS^{\pm}_{k,i\pm\frac{1}{2},j}$ are the ZSWENO smoothness indicators [310], and the explicit formulae first for $IS^{\pm}_{k,i+\frac{1}{2},j}$ are given by

$$\begin{aligned}
IS^{+}_{0,i+\frac{1}{2},j} =& \big(\hat{F}^{+}(\mathbf{u}_{i-2,j}) - 4\hat{F}^{+}(\mathbf{u}_{i-1,j}) + 3\hat{F}^{+}(\mathbf{u}_{i,j})\big)^2,\\
IS^{+}_{1,i+\frac{1}{2},j} =& \big(\hat{F}^{+}(\mathbf{u}_{i-1,j}) - \hat{F}^{+}(\mathbf{u}_{i+1,j})\big)^2,\\
IS^{+}_{2,i+\frac{1}{2},j} =& \big(3\hat{F}^{+}(\mathbf{u}_{i,j}) - 4\hat{F}^{+}(\mathbf{u}_{i+1,j}) + \hat{F}^{+}(\mathbf{u}_{i+2,j})\big)^2,\\
IS^{-}_{0,i+\frac{1}{2},j} =& \big(\hat{F}^{-}(\mathbf{u}_{i+3,j}) - 4\hat{F}^{-}(\mathbf{u}_{i+2,j}) + 3\hat{F}^{-}(\mathbf{u}_{i+1,j})\big)^2,\\
IS^{-}_{1,i+\frac{1}{2},j} =& \big(\hat{F}^{-}(\mathbf{u}_{i+2,j}) - \hat{F}^{-}(\mathbf{u}_{i,j})\big)^2,\\
IS^{-}_{2,i+\frac{1}{2},j} =& \big(3\hat{F}^{-}(\mathbf{u}_{i+1,j}) - 4\hat{F}^{-}(\mathbf{u}_{i,j}) + \hat{F}^{-}(\mathbf{u}_{i-1,j})\big)^2,
\end{aligned} \tag{3.47}$$

and then for $IS^{\pm}_{k,i-\frac{1}{2},j}$, we have

$$\begin{aligned}
IS^{+}_{0,i-\frac{1}{2},j} =& \big(\hat{F}^{+}(\mathbf{u}_{i-3,j}) - 4\hat{F}^{+}(\mathbf{u}_{i-2,j}) + 3\hat{F}^{+}(\mathbf{u}_{i-1,j})\big)^2,\\
IS^{+}_{1,i-\frac{1}{2},j} =& \big(\hat{F}^{+}(\mathbf{u}_{i-2,j}) - \hat{F}^{+}(\mathbf{u}_{i,j})\big)^2,\\
IS^{+}_{2,i-\frac{1}{2},j} =& \big(3\hat{F}^{+}(\mathbf{u}_{i-1,j}) - 4\hat{F}^{+}(\mathbf{u}_{i,j}) + \hat{F}^{+}(\mathbf{u}_{i-1,j})\big)^2,\\
IS^{-}_{0,i-\frac{1}{2},j} =& \big(\hat{F}^{-}(\mathbf{u}_{i+2,j}) - 4\hat{F}^{-}(\mathbf{u}_{i+1,j}) + 3\hat{F}^{-}(\mathbf{u}_{i,j})\big)^2,\\
IS^{-}_{1,i-\frac{1}{2},j} =& \big(\hat{F}^{-}(\mathbf{u}_{i+1,j}) - \hat{F}^{-}(\mathbf{u}_{i-1,j})\big)^2,\\
IS^{-}_{2,i-\frac{1}{2},j} =& \big(3\hat{F}^{-}(\mathbf{u}_{i,j}) - 4\hat{F}^{-}(\mathbf{u}_{i-1,j}) + \hat{F}^{-}(\mathbf{u}_{i-2,j})\big)^2.
\end{aligned} \tag{3.48}$$

Once again, in (3.47) and (3.48) the positive $\hat{F}^{+}(\mathbf{u})$ and negative $\hat{F}^{-}(\mathbf{u})$ parts are defined by using the Rusanov flux splitting (3.41). Furthermore, we can observe that these smoothness indicators (3.47) and (3.48) can be equivalently expressed in terms of discrete convolutions, *i.e.,*

$$IS^{\pm}_{k,i+\frac{1}{2},j} = \big(\overline{\mathcal{K}}^{\pm}_{k,+} * \mathcal{F}^{\pm}(\mathbf{u})\big)^2, \qquad IS^{\pm}_{k,i-\frac{1}{2},j} = \big(\overline{\mathcal{K}}^{\pm}_{k,-} * \mathcal{F}^{\pm}(\mathbf{u})\big)^2, \tag{3.49}$$

where the appropriately induced vectors $\overline{\mathcal{K}}^{\pm}_{k,+}$ and $\overline{\mathcal{K}}^{\pm}_{k,-}$ are defined in A.5. This completes the description of the convolution-driven ZSWENO scheme for the inside differential operators $\nabla \cdot \mathcal{F}(\mathbf{u})^I$, *i.e.,* the approximation of $\nabla \cdot \mathcal{F}(\mathbf{u})$ for all inside nodes.

However, since the adhesion operators $\nabla \cdot \mathcal{F}(\mathbf{u})$ were split into two parts in (3.39), it remains to describe the ZSWENO scheme for the layer operator $\nabla \cdot \mathcal{F}(\mathbf{u})^L$, accounting for all nodes that are considered to be in the layer part of the domain. As in Section 3.3.1 for the boundary diffusion operators, here we also need to appropriately approximate the value of any point that is located outside of the tumour domain $\Omega(t_0)$. To this end, we symmetrically reflect the values of the interior nodes to the ghost nodes in a node by node fashion due to the irregular tumour domain.

This ultimately enables us to use the standard non-convolutional ZSWENO scheme (3.43), (3.44), (3.47) and (3.48) instead of the convolutional forms (3.45) and (3.49) to approximate the layer operators $\nabla \cdot \mathcal{F}(\mathbf{u})^L$.

3.3.3 Approximation of the Propagation Speed α

Due to the complexity of $\mathcal{F}(\cdot)$, calculating its Jacobian $d\hat{F}(\mathbf{u})/d\mathbf{u}$ is extremely time consuming. Hence, to find the largest eigenvalue α, we rather skip the exact evaluation of the Jacobian and choose to approximate the propagation speed in a Jacobian-free manner. For this, let us first define the eigenvalue problem by

$$Jv = \lambda v, \tag{3.50}$$

where $J = d\mathcal{F}(\mathbf{u})/d\mathbf{u}$ is the Jacobian, v is an eigenvector, and λ is an eigenvalue of J. Then in order to find the largest eigenvalue α, we solve (3.50) iteratively with convergence tolerance of 10^{-14} and with a random initial guess for v. Hence, similarly to, for instance, a Jacobian-free Newton-Krylov method [131, 140], to find λv in (3.50) we evaluate the Jacobian-vector product Jv instead of J, which is proved to be a significantly less time-consuming task. To that end, the approximation of Jv is carried out via the first-order Taylor series expansion, and so it is given by

$$Jv \approx \frac{\mathcal{F}(\mathbf{u} + \epsilon_p v) - \mathcal{F}(\mathbf{u})}{\epsilon_p},$$

where ϵ_p is a small perturbation parameter. Since the precision is limited in the evaluation of the flux $\mathcal{F}(\cdot)$, a good choice to evaluate this small parameter ϵ_p is given by [140]

$$\epsilon_p = \frac{\sqrt{(1+ \parallel \mathbf{u} \parallel)\epsilon_{mach}}}{\parallel v \parallel},$$

where $\epsilon_{mach} > 0$ is the machine precision.

3.4 Parameter Values

In Table 3.1, we summarise the parameter values that we will use in the upcoming result section.

Table 3.1: *Parameter set used for the numerical simulations in this chapter. If we could not find any references for some of our parameters then we "Estimated" them (i.e., we chose an arbitrary value for the simulations).*

Variable	Value	Description	Reference
D_c	10^{-4}	Diffusion coeff. for the cancer cell population c	[31, 70]
D_{cM_1}	4.5	Coeff. of the M2 TAMs dependence in the cancer diffusion	Est. using [150, 157]
D_{cM_2}	1.8	Coeff. of the M2 TAMs dependence in the cancer diffusion	[112]
D_{cF}	8	Coeff. of the fibres dependence in the cancer diffusion	Estimated
D_{M_1}	5×10^{-5}	Diffusion coeff. for the M1 TAM population	[101]
D_{M_1F}	16	Coeff. of the ECM stiffness dependence in the M1 TAMs diffusion	[101]
D_{M_2}	5×10^{-5}	Diffusion coeff. for the M2 TAM population M	[101]
D_{M_2F}	16	Coeff. of the ECM stiffness dependence in the M2 TAMs diffusion	[101]
D_σ	1	Diffusion coeff. for the nutrients	[169]
D_m	2.5×10^{-3}	Diffusion coeff. for MDEs	[206]
$\mathbf{S}_{max}$	0.5	Cell-cell adhesion coeff.	[245]
$\mathbf{S}_{min}$	0.01	Minimum level of cell-cell adhesion	[265]

Continued on next page

Table 3.1 – continued from previous page

Variable	Value	Description	Reference
$\mathbf{S}_{cl}$	0.01	Cell-non-fibre adhesion coeff.	[245]
$\mathbf{S}_{cF}$	0.3	Cell-fibre adhesion coeff.	[70]
$\mathbf{S}_{cM}$	0.125	Cell-macrophage adhesion coeff.	[265]
$\mathbf{S}_{M_1M}$	0.175	M1 TAMs self adhesion coeff.	[60]
$\mathbf{S}_{M_2M}$	0.05	M2 TAMs self adhesion coeff.	[60]
$\mathbf{S}_{Mc}$	0.125	Macrophage-cancer adhesion coeff.	[265]
$\mathbf{S}_{M\sigma}$	0.1	Strength of the Macrophage-nutrients relationship	Estimated
μ_c	0.25	Proliferation coeff. for cancer cell population c	[70]
μ_{cM_1}	4.0	Coeff. for the M1 TAMs dependence in the cancer cell proliferation	Estimated
μ_{cM_2}	1.4	Coeff. for the M2 TAMs dependence in the cancer cell proliferation	[113]
M_0	0.05	Influx of the M1 TAMs	Estimated
μ_M	0.2	Inside tissue proliferation rate of M1 and M2 TAMs	Estimated
μ_{MF}	1.8	Coeff. for the ECM stiffness dependence in the M1 and M2 TAMs prolifs.	[101]
d_c	0.1	Decay rate of the cancer cells	Estimated
d_{cM_1}	50.0	M1 TAMs killing rate of the cancer cells	Estimated
d_M	0.03	Decay rate of M1 and M2 TAMs	[259]
d_σ	80.0	Nutrients uptake rate	Estimated

Continued on next page

Table 3.1 – continued from previous page

Variable	Value	Description	Reference
β_{lc}	3.0	Degradation coeff. for non-fibre ECM due to the tumour	Estimated
β_{lM_1}	3.84	Degradation coeff. for non-fibre ECM due to the M1 TAMs	Estimated
β_{lM_2}	0.96	Degradation coeff. for non-fibre ECM due to the M2 TAMs	Estimated
β_{Fc}	1.5	Degradation coeff. for fibre ECM due to the tumour	[245]
β_{FM_1}	1.92	Degradation coeff. for fibre ECM due to the M1 TAMs	Estimated
β_{FM_2}	0.48	Degradation coeff. for fibre ECM due to the M2 TAMs	Estimated
γ_0	0	Baseline remodelling	[265]
γ_{M_2}	0	Remodelling of the non-fibre ECM due to the M2 TAMs	[265]
p_{12}	14.0	Baseline polarisation rate	Estimated
p_{21}	6.0	Baseline re-polarisation rate	Estimated
t_p	0	Re-polarisation staring time	Estimated
R_p	0	Radius of the re-polarisation domain	Estimated
σ_{nor}	0.4	Normal level of nutrients	[169]
σ_p	0.35	Maximal level of nutrients that is still sufficient	Est. using [169]
σ_n	0.2	Necrotic threshold for the nutrients level	Est. using [169]
$\Psi_{p,max}$	1.0	Maximal proliferation enhancement rate	Estimated

Continued on next page

Table 3.1 – continued from previous page

Variable	Value	Description	Reference
$\Psi_{d,max}$	5.0	Maximal death enhancement rate	Estimated
$\Psi_{dM,min}$	1.0	Minimal death enhancement rate	Estimated
$\Psi_{M,max}$	2.0	Maximal polarisation enhancement rate	Estimated
$\Psi_{M,min}$	1.0	Minimal polarisation enhancement rate	Estimated
α_c	0.625	MDE secreting rate by the cancer cells	Est. using [103]
α_{M_1}	0.8	MDE secreting rate by the M1 TAMs	Est. using [103]
α_{M_2}	0.2	MDE secreting rate by the M2 TAMs	Est. using [103]
β	0.75	Optimal level/tissue environment controller of the ECM density	[279]
R	0.15	Sensing radius	[245]
r	0.0016	Width of micro-fibres	[245]
f_{max}	0.636	Maximum of micro-fibre density at any point	[245]
h_L	0.03125	Macro-scale spatial step-size	[279]
ϵ	0.0625	Size of the boundary micro-domain $\epsilon Y(\mathbf{x})$	[279]
δ	0.03125	Size of the fibre micro-domain $\delta Y(\mathbf{x})$	[245]
Δt	10^{-3}	Macro-scale temporal step size	Estimated
$\Delta\tau$	10^{-4}	MDE micro-scale temporal step size	Estimated

3.5 Numerical Results

In this section, we present the numerical results for our multi-scale model. Hence, for the simulations let us consider a tissue domain $Y = [0, 4] \times [0, 4]$ and the following initial conditions:

$$\begin{aligned} c(x,0) =& \frac{1}{2}\exp\left(\frac{-\parallel x \parallel_2^2}{0.02}\right)\cdot \chi_{\mathbf{B}((2,2),0.25)}, \\ M_1(x,0) =& 10^{-2}\cdot \chi_{\mathbf{B}((2,2),0.25)}, \\ M_2(x,0) =& 10^{-2}\cdot \chi_{\mathbf{B}((2,2),0.25)}, \\ l(x,0) =& \min\left(\frac{1}{2}+\frac{1}{4}\sin(7\pi x_1 x_2)^3\cdot\sin\left(7\pi\frac{x_2}{x_1}\right), 1-c(x,0)\right), \\ \sigma(x,0) =& 0.4; \end{aligned} \tag{3.51}$$

which are illustrated in Figure 3.3a). Here the white curves indicate the boundary of the tumour domain $\partial\Omega(0)$. Besides these macro-scale initial conditions, we also illustrate the initial state of one micro-scale fibre domain $\delta Y(x)$ in Figure 3.3b), which is repeated for all macro-scale points. Also, the ratio between the fibre and non-fibre ECM phases are assumed to be $20\% : 80\%$ for all simulations.

Finally, all presented simulations correspond to time $50\Delta t$. The baseline parameters values are provided in Appendix 3.4, and any alteration from these values will be stated accordingly.

3.5.1 Spatial Dependency of the Re-polarisation

First, we investigate numerically the effects of changing the re-polarisation domain $\Omega_p(t, R_p)$ used in (3.12), defined in Appendix A.4 and illustrated in Figure 3.2. Hence, here we study whether the success of a M2→M1 re-polarisation strategy against the tumour is dependent on the spatial domain $\Omega_p(t, R_p)$, specifically on R_p=the distance from the outer boundary $\partial\Omega_o(t)$. For this let us use the radii $R_p \in \{0, \Delta x, 2\Delta x, 3\Delta x, 4\Delta x\}$ for the re-polarisation domain $\Omega_p(t, R_p)$, as well as let

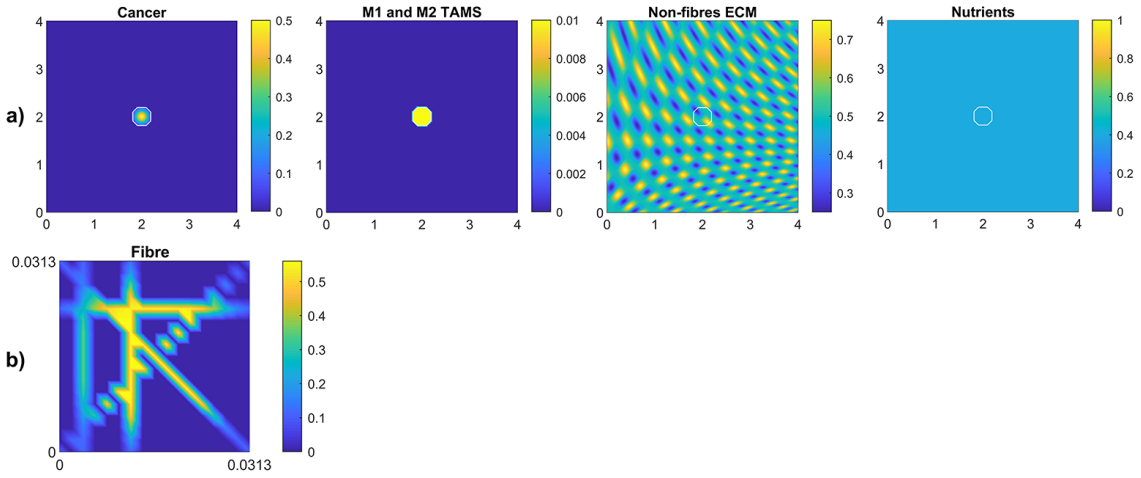

Figure 3.3: *a) Initial conditions of the cancer cells, both M1 and M2 TAMs, non-fibre ECM and the nutrients, respectively. b) Initial condition of the micro-fibres on $\delta Y(x)$, which is repeated for all x.*

us start the process at time 0, *i.e.,* we take $t_p = 0$ in (3.12). To further study these spatial effects, we also consider multiple tissue conditions by changing the tissue environment controller $\beta \in \{0.75, 0.7875, 0.825\}$ (see [279]).

To compare the resulting tumours, we measure the overall tumour mass and spread at final time $50\Delta t$, using the total density of the cancer cells as well as the area of the tumour. Ultimately, this enables us to quantify the changes resulting from the modification of the re-polarisation domain $\Omega_p(t, R_p)$. Specifically, the overall tumour mass is measured by integrating the cancer cell density $c(x, 50\Delta t)$ and the overall tumour spread as given by the area of the tumour domain $\Omega(50\Delta t)$.

Baseline cases: In Figure 3.4 we present the numerical results for the baseline case characterised by the absence of M2→M1 re-polarisation. Specifically, in Figure 3.4 a)-c) we investigate the no-repolarisation case in the context of different tissue environment controllers: a) $\beta = 0.75$, b) $\beta = 0.7875$, and c) $\beta = 0.825$. As we can see, at time $50\Delta t$, the tumour is enlarged and has invaded some of its surroundings, and within the tumour domain $\Omega(50\Delta t)$ we observed heterogeneity in all three cell populations (cancer cell, M1 and M2 TAMs). We also notice that near M2

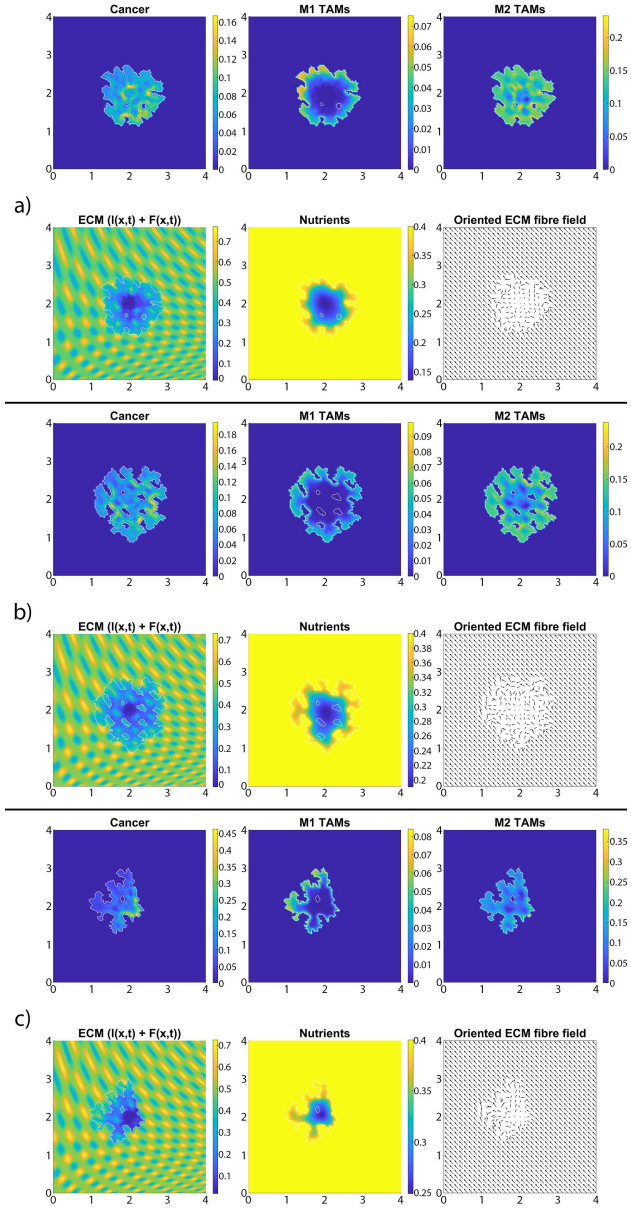

Figure 3.4: *Baseline simulation with no macrophage re-polarisation (*i.e., *we set* $R_p = 0$*) at final time* $50\Delta t$*. a)* $\beta = 0.75$*, b)* $\beta = 0.7875$*, c)* $\beta = 0.825$*.*

TAMs accumulations sites, the density of cancer cells also seems to be higher. In contrast, higher M1 TAMs density usually corresponds to both low M2 TAMs as well as low cancer cell populations. Moreover, the movement and spatial distribution of tumour and immune cells are influenced directly and indirectly by the ECM fibres. For illustrative purposes, the rearranged fibre structure is portrayed by a four-fold coarsened oriented ECM fibres field in Figure 3.4. Furthermore, the peritumoral degradation of the two-phase ECM (caused by the cancer cells and both TAMs) allows the tumour to expand and spread to the neighbouring tissues, resulting in some tumour fingering patterns that vary with the controller β: higher β leads to more tumour fingering. This induces an irregular tumour domain, as well as the formation of "islands" inside the tumour, which corresponds to areas of initially low ECM density, *i.e.,* the ECM level was too low in such areas to support tumour movement. Finally, in Figure 3.4, we also present the level of available nutrients. Hence, we can see that since the nutrients are only supplied through the outer boundary $\Omega_o(t)$, the initial normal level of nutrients is significantly depleted (by the three cell populations) inside the tumour. This can lead to hypoxia and then eventually create a necrotic core (not modelled explicitly in this study).

The impact of M2→M1 re-polarisation: In Figure 3.5 a)-c), we introduce the re-polarisation of the M2 TAMs to M1 TAMs within the domain $\Omega_p(t, \Delta x)$ (*i.e.,* $R_p = \Delta x$), and again we investigate the role of three controller values: a) $\beta = 0.75$, b) $\beta = 0.7875$, c) $\beta = 0.825$. While in Figure 3.4 the M1 TAMs mainly accumulated near the tumour boundary, in Figure 3.5 we see that the re-polarisation of M2 TAMs leads to an increase in the M1 TAMs population inside the tumour, leading to several accumulation sites located further away from the leading edge. In contrast, the presence of M2 TAMs inside of the tumour is decreased compared to Figure 3.4, and these immune cells now accumulate only in a small neighbourhood of the boundary (because we do not re-polarise M2 TAMs into M1 TAMs in a

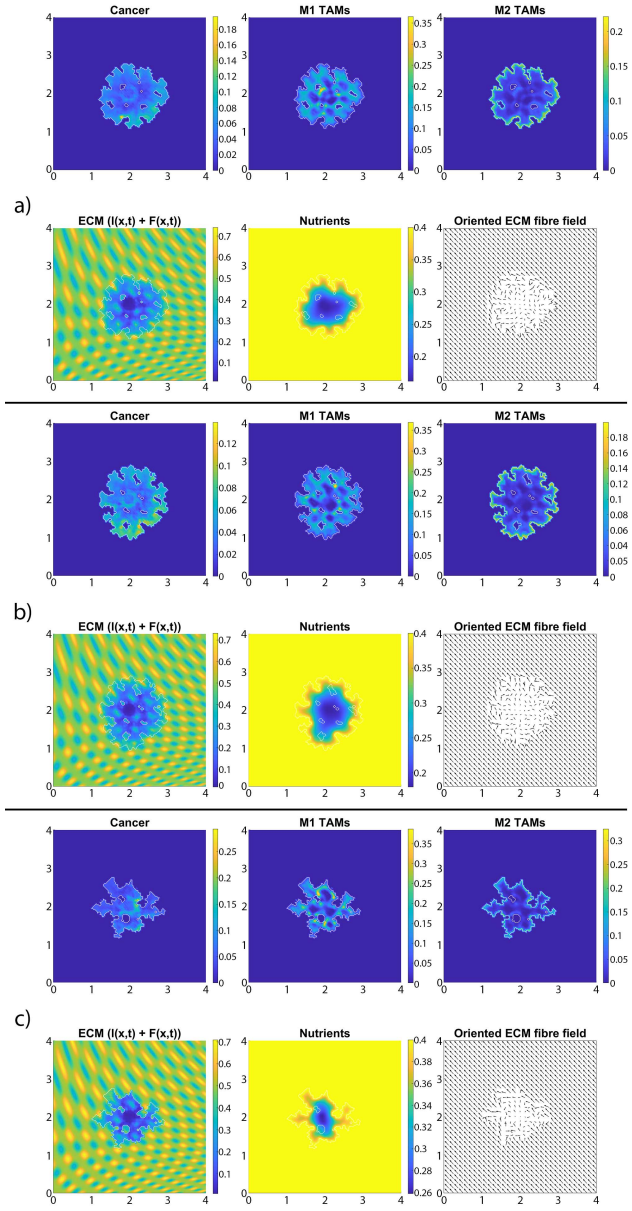

Figure 3.5: *Simulation with re-polarisation domain* $\Omega_p(t, \Delta x)$ *and with starting time* $t_p = 0$ *at the final time* $50\Delta t$*. a)* $\beta = 0.75$*, b)* $\beta = 0.7875$*, c)* $\beta = 0.825$*.*

$R_p = \Delta x$ neighbourhood of the boundary; see Fig 3.2). Since both macrophage populations interact with the cancer cells, we also see some differences in the cancer cell population, and these differences depend on the degradation level of ECM as controlled by the value of β. Using two measures (spread and mass), we first focus on the $\beta = 0.75$ case and compare Figures 3.4 a) and 3.5 a): re-polarisation leads to an $\approx 11\%$ increase in tumour spread as well as an $\approx 20\%$ decrease in tumour mass. Then for $\beta = 0.7875$ (Figures 3.4 b) and 3.5 b)) we observe an $\approx 5\%$ reduction in spread and an $\approx 34\%$ decrease in mass. Finally, for $\beta = 0.825$ (Figures 3.4 c) and 3.5 c)), the tumour spread is increased by $\approx 15\%$ and the tumour mass is reduced by $\approx 31\%$. Hence, although re-polarising M2 TAMs into M1 TAMs does not show an overall improvement in terms of tumour spread, it significantly impeded the migration of the cancer cell mass from hypoxic regions to the proliferating rim as well as helped to reduce the mass by killing the cancer cells. However, since $R_p = \Delta x$, the M2 TAMs are able to accumulate in a Δx neighbourhood of the interface, and so we can still observe a moderate density of cancer cells near the boundary.

Tumour spread/mass changes with respect to R_p: In Figure 3.6 we vary R_p and present the changes in the dimensionless tumour area (spread) and mass resulted by changing the radius R_p. Specifically, in Figure 3.6 a)-c) we again consider the three previously used environment controllers $\beta = 0.75$, $\beta = 0.7875$, $\beta = 0.825$. Moreover, since various types of cancers secrete MMPs at different rates [86], here we also consider high, medium and low MDE secretion rates. Finally, we vary the radii for the re-polarisation domain, $R_p \in \{0, \Delta x, 2\Delta x, 3\Delta x, 4\Delta x\}$, while we assume that the re-polarisation process starts at time 0, *i.e.,* we take $t_p = 0$. The left panels of Figure 3.6 show the changes in the dimensionless variable for tumour areas/spreads with respect to R_p, while the right panels show the changes in the dimensionless variables for tumour mass with respect to R_p. Here, the blue circles correspond to

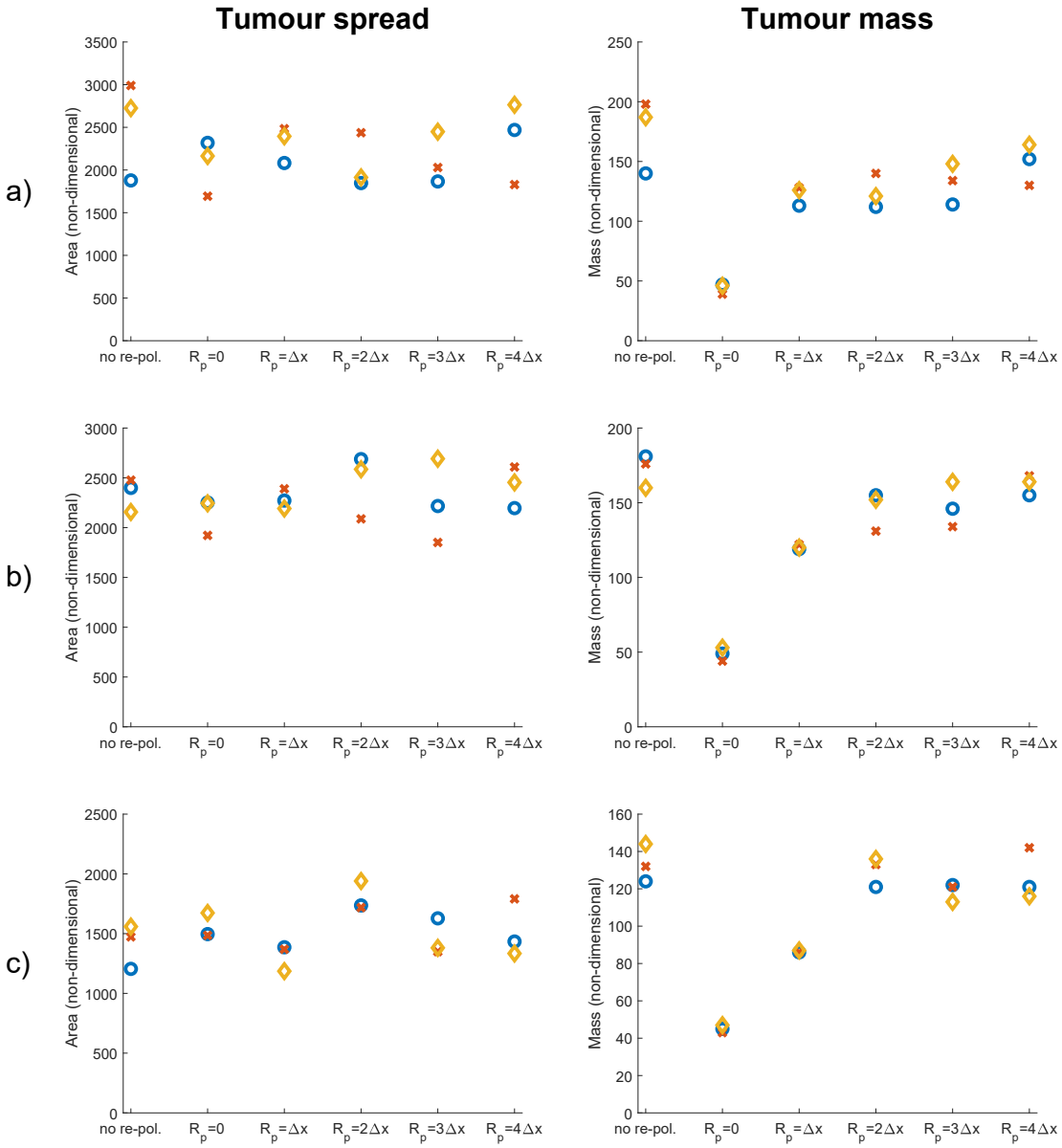

Figure 3.6: *Results of varying the radius of the re-polarisation domain* $R_p \in \{0, \Delta x, 2\Delta x, 3\Delta x, 4\Delta x\}$ *with starting time* $t_p = 0$. *Left panel shows the change in the tumour spread and the right panel shows the change in tumour mass with respect to* R_p. *Here the blue circles correspond to a high ECM degradation rate by cancer cells (*$\beta_{lc} = 3.0$, $\beta_{Fc} = 1.5$, $\alpha_c = 0.625$*), the orange diamonds to a medium ECM degradation rate (*$\beta_{lc} = 2.0$, $\beta_{Fc} = 1.0$, $\alpha_c = 0.42$*) and the red crosses to a low degradation rate (*$\beta_{lc} = 1.0$, $\beta_{Fc} = 0.5$, $\alpha_c = 0.21$*). The environment controller* β *is set to a)* $\beta = 0.75$, *b)* $\beta = 0.7875$, *c)* $\beta = 0.825$.

high ECM degradation rates ($\beta_{lc} = 3.0$, $\beta_{Fc} = 1.5$, $\alpha_c = 0.625$), the orange diamonds correspond to medium degradation rates ($\beta_{lc} = 2.0$, $\beta_{Fc} = 1.0$, $\alpha_c = 0.42$), and the red crosses correspond to low degradation rates ($\beta_{lc} = 1.0$, $\beta_{Fc} = 0.5$, $\alpha_c = 0.21$). Comparing first the changes due to varying the tissue controller β, we can see a clear overall decrease in both tumour spread and mass as we increase β. This was seen also in Figures3.4 and 3.5, where a more prominent tumour fingering pattern was present as we increased β which resulted in a decrease in tumour spread. Furthermore, in Figure 3.6 a)-c) the overall behaviour of the tumour spread does not change significantly as we vary the radius of the re-polarisation domain R_p. Hence, even though the proteolytic molecular processes at the leading tumour edge change (via the MDE source (3.26)) following the M2→M1 re-polarisation, we cannot see a clear trend in tumour spread. This might be because of the complex interactions between tumour and infiltrating immune cell populations: although we see an increase in the M1 TAMs populations near the boundary (that also secrete more MDEs than the M2 cells [103]), the overall proteolytic molecular processes at the leading edge of the tumour might not change too much, which would mean similar tumour spread. Second, the rearrangement of the micro-fibre distribution also affects tumour spread since the amount of fibres being re-located near the leading edge depends on the fluxes generated by the different cell populations. Therefore, our model suggests that merely re-polarising the M2 TAMs into the anti-tumoral M1 phenotype might not be enough to stop tumour spread.

On the other hand, in Figure 3.6 a)-c) we see that the tumour mass is greatly reduced in all of the presented cases. These results also show that for the largest reduction we need to re-polarise the M2 TAMs inside the whole tumour domain (*i.e.,* $R_p = 0$, which means that the re-polarisation domain is $\Omega_p(t, 0) = \Omega(t)$). Hence, the presence of M2 TAMs in the proliferating rim may be enough to maintain the tumour mass and induce tumour spread by leading to a moderate presence of cancer cells in the proliferating rim. In conclusion, the results in Figure 3.6 suggest that

re-polarising M2-like macrophages to the M1 phenotype have the ability to reduce tumour mass, but we may need a supplementary strategy primarily focusing on tumour spread or tumour stroma in order to restrain tumour development.

3.5.2 Temporal Dependency of the Re-polarisation

Let us now concentrate on the temporal aspects of a possible re-polarisation strategy. Since in the previous section, we have shown that the M2→M1 re-polarisation impacts predominantly tumour mass, and since this effect was the strongest when $R_p = 0$, here we investigate the effect of changing t_p on tumour mass when we re-polarise the M2 TAMs within the whole tumour domain. Thus, by varying t_p used in (3.12) we aim to investigate the effectiveness of such strategy when we introduce the re-polarisation of M2 TAMs at time $t_p > 0$. This is crucial since tumours are only detectable above a certain size, and so a potential treatment that uses re-polarisation cannot be started at time $t_p = 0$. To this end, in Figure 3.7 we present the change in the dimensionless tumour mass with respect to the re-polarisation start time t_p. As before, Figure 3.7 a) corresponds to $\beta = 0.75$, Figure 3.7 b) to $\beta = 0.8785$ and Figure 3.7 c) to $\beta = 0.825$. The blue circle corresponds to high ECM degradation rates by cancer cells, the orange diamond to medium degradation rates, and the red cross to low degradation rates for each of these sub-cases. The results in Figure 3.7 suggest that the lowest tumour mass can be achieved by starting the re-polarisation as soon as possible, as one would expect. However, even at moderate times, for instance, at $25\Delta t$, the tumour mass can be controlled at relatively low values. All these tumour values obtained following re-polarisation at different times t_p are smaller than the tumour value obtained for no re-polarisation (see the last point on the horizontal axis in Figure 3.7). This indicates that a re-polarisation based strategy is not only viable when it is introduced at a very early stage, but it could also be effective even against a more advanced and larger tumour.

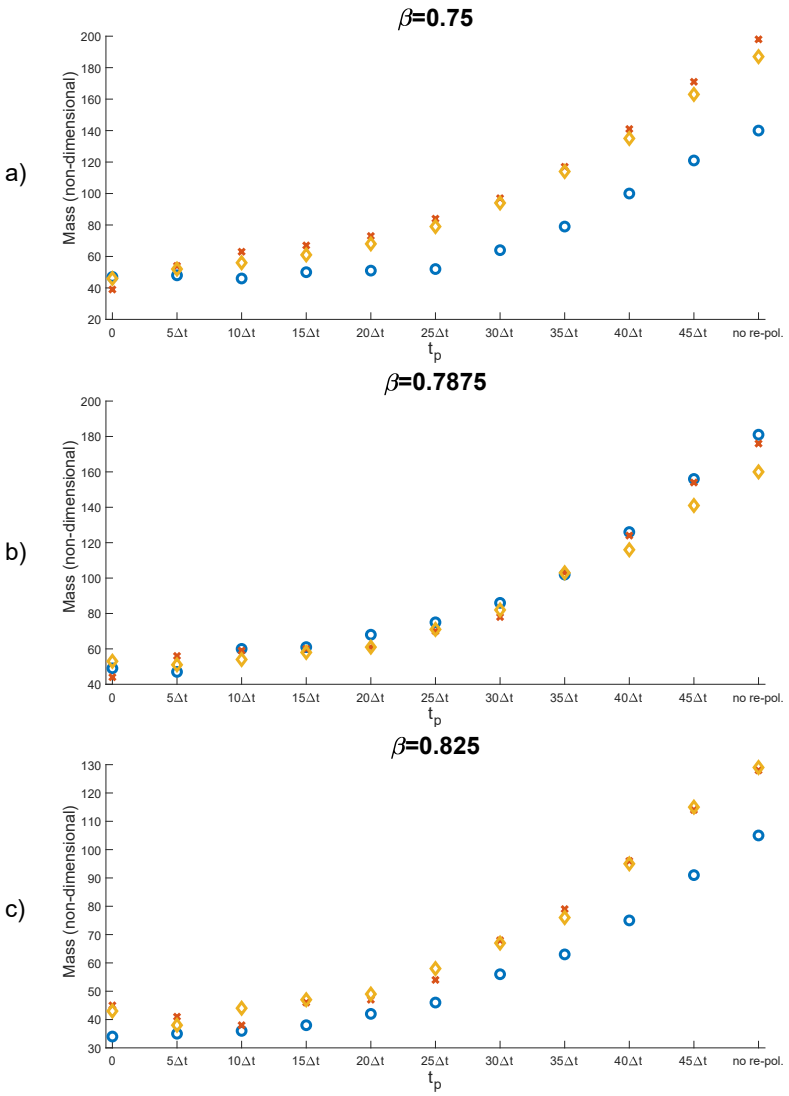

Figure 3.7: *Results of varying the re-polarisation start time* $t_p \in \{0, 5\Delta t, \ldots, 45\Delta t, 50\Delta t\}$. *The blue circles correspond to a high ECM degradation rates by cancer cells* ($\beta_{lc} = 3.0$, $\beta_{Fc} = 1.5$, $\alpha_c = 0.625$), *the orange diamonds to medium ECM degradation rates* ($\beta_{lc} = 2.0$, $\beta_{Fc} = 1.0$, $\alpha_c = 0.42$) *and the red crosses to low ECM degradation rates* ($\beta_{lc} = 1.0$, $\beta_{Fc} = 0.5$, $\alpha_c = 0.21$). *The environment controller* β *is set to a)* $\beta = 0.75$, *b)* $\beta = 0.7875$, *c)* $\beta = 0.825$.

3.5.3 In the Absence of Nutrients

So far, we have considered the presence of nutrients and the related effect-functions within the macro-scale dynamics (3.24). However, here, we also investigate how the absence of these components influence the overall tumour dynamics. Hence, for the rest of this section, we take $\sigma(x,t) \equiv 0$, $\forall (x,t) \in Y \times [0,T]$ and $\Psi_p(\sigma) \equiv 1$, $\Psi_{dc}(\sigma) \equiv 1$, $\Psi_{dM}(\sigma) \equiv 1$ and $\Psi_M(\sigma) \equiv 1$, $\forall \sigma$ and $S_{M\sigma} = 0$. For reasons of comparability, we use the same scenarios as before, and so first, in Figure 3.8, we present the case of no re-polarisation and no nutrients. Although comparing Figures 3.4 and 3.8 we can observe some expected tumour morphology changes, the main difference that we would like to emphasise is that in the absence of nutrients, all three cell populations form a more homogeneous distribution. For example, while in Figure 3.8 there is only one cancer cell accumulation region (about $(2,2)$ where we centred our initial condition), in Figure 3.4 this is not the case, and rather cancer cells are more heterogeneously distributed throughout the tumour domain $\Omega(50\Delta t)$ creating various accumulation regions. Furthermore, we can also see an M2 TAMs population that penetrate the tumour deeper in the presence of nutrients. This is because in this case in Figure 3.8 there are no nutrients mediated movement (since $S_{M\sigma} = 0$), and so the combination of macrophage-macrophage and macrophage-cancer adhesions is not adequate to guide the M2-like macrophages away from the boundaries in most cases. Hence, these results suggest that the nutrient mediated movement play an important, non-negligible role in guiding macrophages towards necrotic regions, which is consistent with biological experiments [188]. Moreover, in Figure 3.9, we introduce M2→M1 re-polarisation (with $\Omega_p(t, \Delta x)$ and $t_p = 0$), and so we can compare it to the results of Figure 3.5 where we presented the same scenario but in the presence of nutrients. By comparing these results, we can observe more homogeneous cell populations (cancer, M1 and M2 TAMs) as well as the same phenomena as before but with the M1 TAMs population (due to the re-polarisation), *i.e.,* in the absence of macrophage-nutrient relationship (since $S_{M\sigma} = 0$) M1-like macrophages

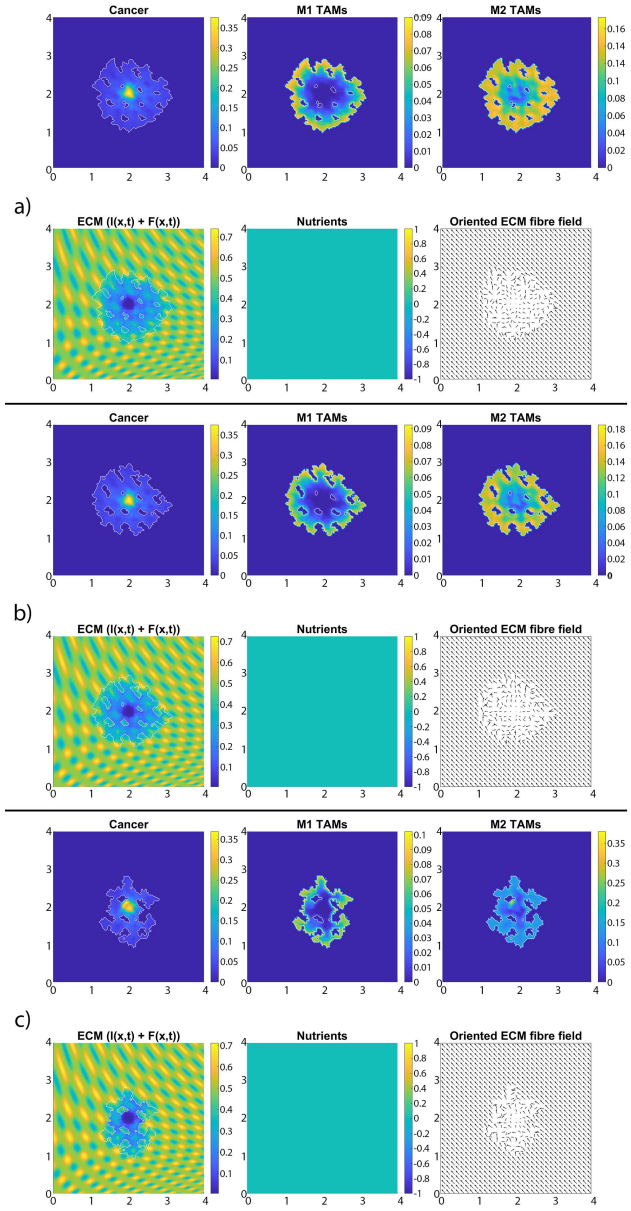

Figure 3.8: *Baseline simulation with no macrophage re-polarisation and no nutrients* (i.e., $\sigma(x,t) \equiv 0$, $\forall (x,t) \in Y \times [0,T]$ *and* $\Psi_p(\sigma) \equiv 1$, $\Psi_{dc}(\sigma) \equiv 1$, $\Psi_{dM}(\sigma) \equiv 1$ *and* $\Psi_M(\sigma) \equiv 1$, $\forall \sigma$ *and* $S_{M\sigma} = 0$) *at final time* $50\Delta t$. *a)* $\beta = 0.75$, *b)* $\beta = 0.7875$, *c)* $\beta = 0.825$.

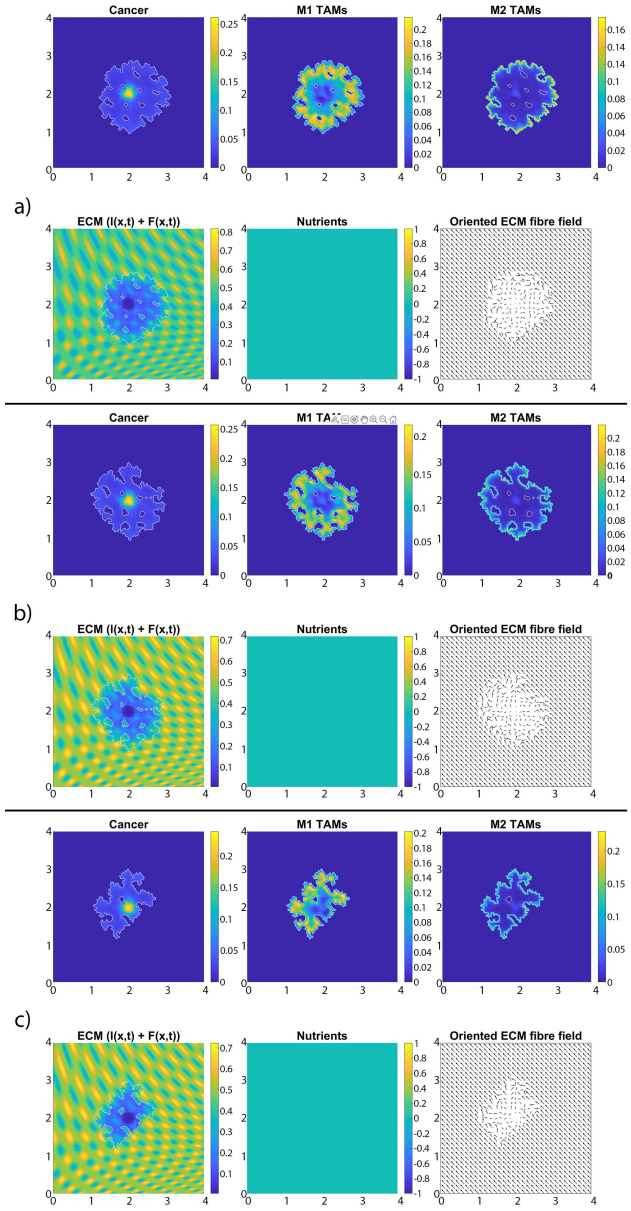

Figure 3.9: *Simulation with re-polarisation domain* $\Omega_p(t, \Delta x)$*, starting time* $t_p = 0$ *and with no nutrients (*i.e., $\sigma(x,t) \equiv 0$, $\forall (x,t) \in Y \times [0,T]$ *and* $\Psi_p(\sigma) \equiv 1$, $\Psi_{dc}(\sigma) \equiv 1$, $\Psi_{dM}(\sigma) \equiv 1$ *and* $\Psi_M(\sigma) \equiv 1$, $\forall \sigma$ *and* $S_{M\sigma} = 0$*) at the final time* $50\Delta t$*. a)* $\beta = 0.75$*, b)* $\beta = 0.7875$*, c)* $\beta = 0.825$*.*

are accumulated closer to the boundary and are less efficient in penetrating the tumour. This may be of particular interest for future mathematical models due to recent advances regarding macrophage-mediated drug delivery [152], an approach that can be used not only for tumours but for other diseases as well.

To investigate the effects of nutrients on the tumour spread and mass behaviour that we have seen in Figure 3.6, here for comparability, we also present the same scenarios but in the absence of nutrients in Figure 3.10. Hence, we consider the three previously used environment controllers $\beta = 0.75$, $\beta = 0.7875$, $\beta = 0.825$ with the three ECM degradation rates (high, medium and low) and present both the tumour spread and mass for each case. Although with some expected changes in the values, in Figure 3.10 we detect a similar behaviour as in Figure 3.6 that the proteolytic molecular processes at the leading edge of the tumour do not change drastically, *i.e.,* varying the radius of the re-polarisation domain R_p does not affect tumour spread substantially. Furthermore, we find consistent results for tumour mass as well, since we achieve the greatest reduction in the case of $R_p = 0$ and then as we increase the radius R_p, tumour mass also increases. Therefore, our results suggest that although nutrients play an important role in the movement of both macrophage phenotype, it does not affect the features and properties of the spatial dependency of the re-polarisation, *i.e.,* both in the presence and in the absence of nutrients the tumour spread and mass react to changes in the re-polarisation radius R_p in a similar fashion.

3.6 Discussion

In this chapter, we have further developed and extended a multi-scale moving boundary framework for cancer invasion, introduced in Chapter 2 and [245, 265, 279] by also considering the dynamics of the anti-tumoral M1 TAMs as well as the nutrients. On the one hand, we took into account the nutrients since every cell requires them

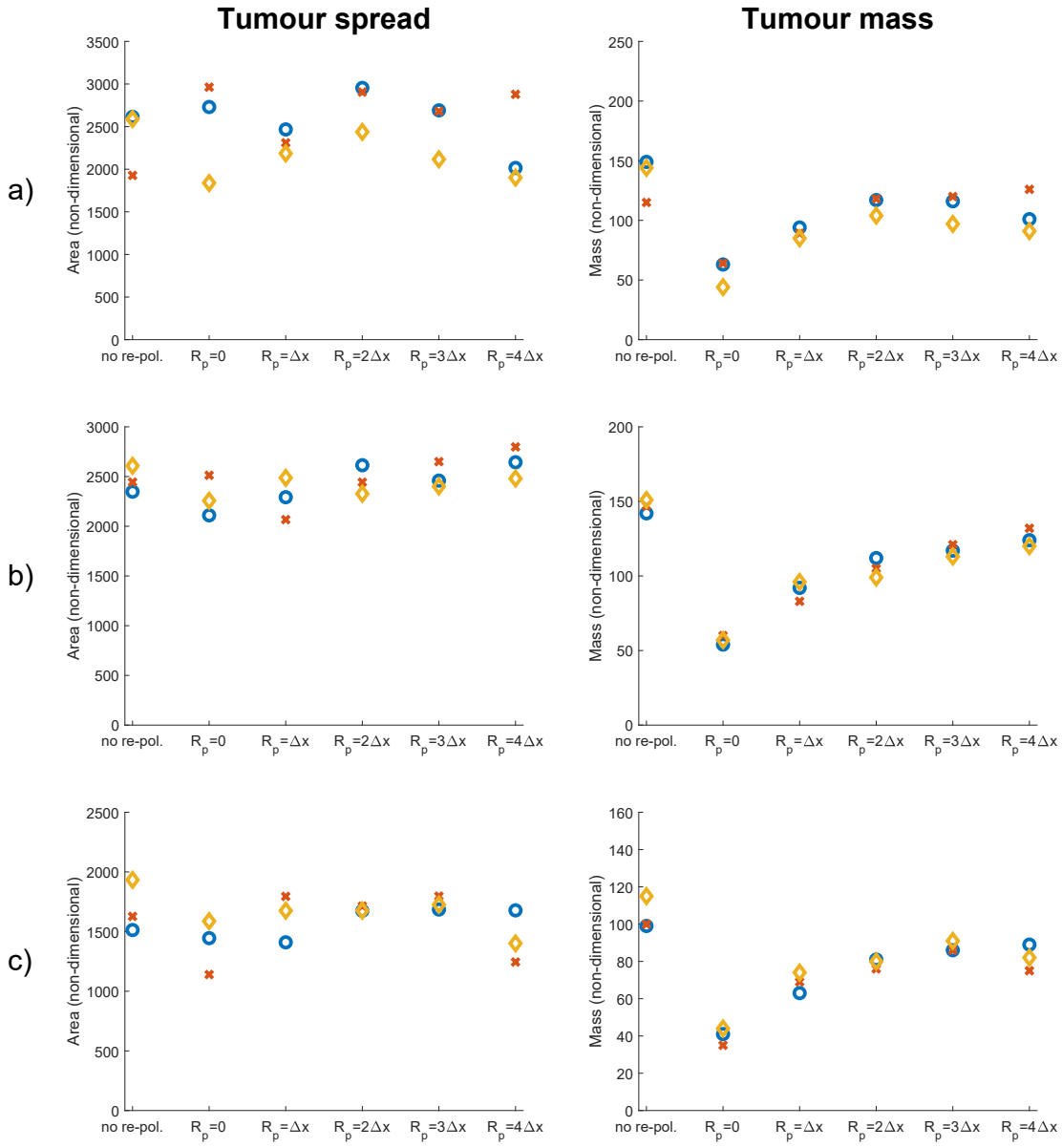

Figure 3.10: *Results of varying the radius of the re-polarisation domain* $R_p \in \{0, \Delta x, 2\Delta x, 3\Delta x, 4\Delta x\}$ *with starting time* $t_p = 0$ *in the absence of nutrients (*i.e., $\sigma(x,t) \equiv 0$, $\forall (x,t) \in Y \times [0,T]$ *and* $\Psi_p(\sigma) \equiv 1$, $\Psi_{dc}(\sigma) \equiv 1$, $\Psi_{dM}(\sigma) \equiv 1$ *and* $\Psi_M(\sigma) \equiv 1$, $\forall \sigma$ *and* $S_{M\sigma} = 0$*). Left panel shows the change in the tumour spread and the right panel shows the change in tumour mass with respect to* R_p*. Here the blue circles correspond to high ECM degradation rates by cancer cells (*$\beta_{lc} = 3.0$, $\beta_{Fc} = 1.5$, $\alpha_c = 0.625$*), the orange diamonds to medium degradation rates (*$\beta_{lc} = 2.0$, $\beta_{Fc} = 1.0$, $\alpha_c = 0.42$*) and the red crosses to low degradation rates (*$\beta_{lc} = 1.0$, $\beta_{Fc} = 0.5$, $\alpha_c = 0.21$*). The environment controller* β *is set to a)* $\beta = 0.75$*, b)* $\beta = 0.7875$*, c)* $\beta = 0.825$*.*

to live and function properly, so their presence is indispensable. On the other hand, we focused on the classically activated M1-like macrophages since they are known to be capable of killing cancer cells. Moreover, since macrophages are one of the most abundant immune cells in the tumour microenvironment and their plasticity enables them to switch phenotypes, they are prime candidates to assist in the fight against cancer. To this end, we investigated how the re-polarisation of the M2 TAMs into M1 TAMs can affect cancer development by focusing especially on the macrophage populations near the leading edge of the tumour. Specifically, we studied the spatial aspect of the M2→M1 re-polarisation through the definition of a re-polarisation domain $\Omega_p(t, R_p)$, and the temporal aspect via the starting re-polarisation time t_p used in (3.12). Finally, while in this work we considered the death of macrophages induced through nutritional starvation, this is only one aspect in the wider picture concerning the death and survival of macrophages within the necrotic region, which so far has not been fully explored experimentally. Future mathematical modelling studies will explore other death and survival aspects involved concerning macrophages in necrotic regions.

To propose new hypotheses, we first introduced a macro-scale quasi-steady reaction-diffusion equation for the nutrients where we considered the spatial transport to be described by diffusion with constant-coefficient as well as a linear uptake rate. Then, to account for the effect of nutrients on the different cell functions, we defined four effect-functions that we used for the rest of tumour dynamics. Furthermore, we introduced another macro-scale equation, describing the behaviour of the M1 TAMs where the motility of the M1 phenotype is represented both by random and directed movements. The rest of the equation involves an influx term, nutrient-dependent proliferation and death laws, as well as nutrient-dependent polarisation and re-polarisation terms that describe the switch between the two phenotypes. Similarly to the M2 TAMs, the M1 phenotype also secrete MDEs that can degrade the ECM. Therefore, this M1 phenotype directly contributes to the re-arrangement

of the micro-fibres constituents and serves as a source of MDEs for the proteolytic processes that occur on the invasive edge of the tumour.

We used this extended model to explore the possibilities of macrophage re-polarisation to depend on the spatial domain as well as on time. First, in Figures 3.4, 3.5 and 3.6 we presented the result of the spatial dependency by varying the re-polarisation domain $\Omega_p(t, R_p)$. We concluded that even though the tumour spread does not seem to be affected much by the M2→M1 re-polarisation (which may be expected as biological studies [103, 165, 197] have shown that M1 TAMs located in the stoma can promote cancer progression), the tumour mass can be reduced significantly. Therefore, even though we may need additional strategies directly targeting tumour spread, the tumour mass can potentially be reduced by the re-polarisation of M2 TAMs to M1 TAMs.

Finally, since tumours are only detectable above a certain size and therefore the M2→M1 re-polarisation is usually applied at later stages in tumour development, in Figure 3.7 we investigated the temporal dependency of M2→M1 re-polarisation. There, we showed that while the smallest tumour mass can be obtained when the re-polarisation starts as soon as possible, in some cases, it is possible to keep the tumour under control even when we re-polarise at later times. For example, in Figure 3.7a), for high ECM degradation levels, tumour mass did not change when $t_p \leq 25\Delta t$. However, tumour mass slowly increased as we delayed the re-polarisation time for medium and low ECM degradation. All these theoretical results suggest that macrophages re-polarisation protocols (through various immunotherapies, such as the use of agonist anti-CD40 mAb [23]) might have to be adapted to the tumour environment and the degradation levels of the ECM.

We emphasise that due to the complexity of this modelling framework, which forced us to work with a nondimensionalised model, the results in this chapter are only qualitative. Nevertheless, they provide new theoretical hypotheses regarding the possible roles of macrophage re-polarisation (within specific regions of the solid

tumours and within specific time scales) in the context of immunotherapies for cancer.

To conclude, we suggest that in addition to the re-polarisation of M2 TAMs, we also need additional strategies targeting tumour spread or tumour stroma in order to stop the tumour from advancing entirely.

Chapter 4

Collective Cell Migration in a Fibrous Environment: a Hybrid Multi-Scale Modelling Approach

Aims and Novelty: In this chapter, we further extend our multi-scale framework to construct a hybrid tumour model where we use our continuous model to capture the two-phase ECM (introduced in Chapter 2) and we use a discrete, agent-based model for the cancer cells. Therefore, this enables us to further study the interaction between the individual cancer cell and ECM fibres and investigate how varying the different adhesion strengths and fibre structure affect the overall tumour shape and invasiveness.

4.1 Introduction

As we have mentioned before, one of the key underlying micro-scale processes involves the micro-scale degradation and redistribution of the ECM fibres. The resulting change in the structure of the ECM is of great importance since the structural component (such as collagen) enables and regularises the movement of cancer cells.

A mathematical model that accounts for such multi-scale nature of the ECM was introduced in [245], which we also used in both Chapter 2 and 3. However, here the cancer cells were modelled as densities in a continuous setting which may not be ideal [239]. On the other hand, fully discrete mathematical models also have their drawbacks and in some cases they are not fitted for a certain task [239]. This motivates the formulation of hybrid models which aim to bring out the best from both modelling frameworks.

Hence, we formulate a hybrid mathematical model that uses a continuous two-phase ECM (that we used in Chapter 2 and 3) and a discrete agent-based cancer cell population [27, 128, 135]. Similarly to Chapter 2, here we concentrate on investigating cell migration patters. However, while in Chapter 2 we focused on the movement of the M2-like macrophages, in this chapter we will exclusively focus on the collective cell migration of the discrete cancer cell population in the absence of any macrophages. The content of this chapter has been discussed in full details in our recent publication [263].

4.2 The Multi-scale Hybrid Model

There are two main types of models that are often used to capture the dynamics of tumour development, namely discrete and continuous models (such as the ones given in Chapter 2 and 3). Both have advantages and drawbacks over the other [239] and to minimise these disadvantages, recent extensive efforts have been made to combine these models into hybrid ones [44].

In this chapter, we employ a hybrid modelling framework [44] that combines the off-lattice agent based model *MultiCell-LF* [27, 128, 135] to represent the cells, and a multi-scale continuous framework (from Chapter 2 and 3 or [246, 247, 245, 265, 264]) to represent the microenvironment. To facilitate the description of this multi-scale hybrid model, let us first introduce some useful notations from both frameworks.

As in Chapter 2 and 3, the model is defined within a maximal tissue cube $Y \in \mathbb{R}^N$ with $N = 2$ and time interval $[0, T]$. The state of an arbitrary individual cell is described by $C_i(t) = \{\mathbf{X}_i(t), C_i^{\text{rad}}(t), C_i^{\text{age}}(t), C_i^{\text{mat}}, C_i^{\text{neigh}}(t)\}$, where $\mathbf{X}_i(t)$ denotes the position of the cell center, $C_i^{\text{rad}}(t)$ the cell radius, $C_i^{\text{age}}(t)$ the current cell age, C_i^{mat} the cell maturation age (*i.e.,* the age when the cell is ready for division which is assigned at birth and so it is independent of time) and $C_i^{\text{neigh}}(t)$ denotes the number of neighbouring cancer cells at time t. Here, $i \in \{1, \ldots, M(t)\}$ where $M(t)$ is the number of cancer cells at time $t \in [0, T]$.

To connect the discrete model to the continuous one, we first need to generate a cancer cell density by using the individual cell properties. For this, let us first observe that such density can be determined by using the fraction of unit space that is occupied by the cancer cells. Therefore, at any macro-scale spatio-temporal position $(x, t) \in Y \times [0, T]$ the density of the cancer cell population in a square neighbourhood $\mathbf{B}(x, \gamma_{\Delta x})$ is given by

$$c(x,t) := \frac{\int\limits_{\mathbf{B}(x,\gamma_{\Delta x})} \mathcal{I}_P(z)\, dz}{\lambda\big(\mathbf{B}(x, \gamma_{\Delta x})\big)}, \qquad \text{with } P := \left\{ \bigcup_{i=1}^{M(t)} \mathbf{B}_{\|\cdot\|_2}\big(X_i(t), C_i^{\text{rad}}(t)\big) \right\} \tag{4.1}$$

where $\lambda(\cdot)$ is the Lebesgue measure in $\mathbb{R}^N$, $\mathcal{I}_{(\cdot)}(\cdot)$ is the usual indicator function, and $\mathbf{B}_{\|\cdot\|_2}\big(X_i(t), C_i^{\text{rad}}(t)\big) := \{z \in Y | \ \| \ X_i - z \ \|_2 \leq \ C_i^{\text{rad}}\}$ describes the spatial region occupied by the body of an individual cell C_i within the neighbourhood $\mathbf{B}(x, \gamma_{\Delta x}) := \{z \in Y | \ \| \ x - z \ \|_\infty \leq \ \gamma_{\Delta x}\}$ that is given by a $\| \cdot \|_\infty$ −ball of an appropriately chosen radius $\gamma_{\Delta x} > 0$ (which is proportional to the spatial step-size of the discretised computational domain Y).

Besides the discrete cancer cell population, here, also we consider the dynamics of a continuous multi-scale two-phase ECM. Specifically, we use our continuous multi-scale two-phase ECM, described in Chapter 2, and so we consider a non-fibre ECM phase denoted by $l(x, t)$ and a fibre ECM phase whose macro-scale density and spatial bias are denoted by $F(x, t)$ and $\theta_f(x, t)$, respectively.

Since in this chapter we do not take into consideration the tumour associated macrophages (*i.e.,* we only account for the cancer cells and the two-phase ECM), the global tumour vector is given here by

$$\mathbf{u} := (c(x,t), F(x,t), l(x,t))^{\intercal},$$

and the total space occupied at position x by

$$\rho(\mathbf{u}) := c(x,t) + F(x,t) + l(x,t).$$

4.2.1 The MultiCell-LF Model

For each single cell in the *MultiCell-LF* (Multi-Cell Lattice-Free) model, several individually-regulated life processes are included, such as cell ageing, cell growth, cell division, cell-cell and cell-ECM interactions, and cell contact inhibition.

The cell cycle

The lifespan of each cell is traced with the current cell age $C_i^{\text{age}}(t)$ that progresses at the same rate as time, and cell maturation age C_i^{mat} that is assigned at the cell birth and varies slightly between the cells to avoid synchronization of cell divisions. The cell cycle is divided into the usual four phases [4]: the G1 phase (gap 1) during which the cells are growing in size, the S phase (synthesis) when biological cells replicate their DNA, the G2 phase (gap 2) in which cells complete the growth and replication processes in preparation for the M phase (mitosis) in which cells physically divide into two daughter cells. Following ours and others previous work, the length of the cell cycle is divided as follows: G1 (45% of the whole cell cycle), S (35%), G2 (15%), and M (5%), respectively [135, 128, 282]. Within the figures, we indicate the phase of an individual cell by different colours, *i.e.,* we use white for the G1 phase, yellow for the S phase, orange for the G2 phase, red for the M phase and black for cells

that are both in M phase and contact inhibited.

Cell growth and division

The radius $C_i^{\text{rad}}(t)$ of a growing cell is increasing linearly until it reaches the size of the mature cell R_{max}. The radius increment has been chosen to assure that the process of cell growth is completed before the M phase. Once the cell current age reaches its division age (*i.e.,* $C_i^{\text{age}}(t) = C_i^{\text{mat}}$), it will divide into two daughter cells that are placed symmetrically around the mother cell's nucleus $\mathbf{X}_i$(t) within a distance equal to the half of the cell maximal radius [135, 128]:

$$\begin{aligned} \mathbf{X}_{i_1}(t) =& \mathbf{X}_i(t) + \frac{1}{2} R_{\max}(\cos(\phi), \sin(\phi)), \\ \mathbf{X}_{i_2}(t) =& \mathbf{X}_i(t) - \frac{1}{2} R_{\max}(\cos(\phi), \sin(\phi)), \end{aligned} \tag{4.2}$$

where ϕ is a uniform random angle on $[0, 2\pi]$, $\mathbf{X}_i(t)$ is the position of the mother cell, and $R_{\max}$ is the maximal cell radius. The initial ages of the two new cells are set to zero ($C_{i_1}^{\text{age}}(t) = C_{i_2}^{\text{age}}(t) = 0$), and their respective maturation ages $C_{i_1}^{\text{mat}}$ and $C_{i_2}^{\text{mat}}$ are inherited from the mother cell maturation age with a small noise term ϵ_{mat} to avoid cell cycle synchronisation between the cells [128, 208]:

$$\begin{aligned} C_{i_1}^{\text{mat}} =& C_i^{\text{mat}}(1 + \epsilon_{\text{mat}}), \\ C_{i_2}^{\text{mat}} =& C_i^{\text{mat}}(1 + \epsilon_{\text{mat}}), \end{aligned}$$

where ϵ_{mat} is a small uniform random variable on $[-0.05, 0.05]$ and C_i^{mat} is the division age of the mother cell. Finally, both initial radii of the daughter cells are set to $0.65R_{\max}$ (*i.e.,* $C_{i1}^{\text{rad}}(t) = C_{i2}^{\text{rad}}(t) = 0.65R_{\max}$) and as a result initially the two daughter cells are overlapping (4.2). Therefore, right after the cell division, both daughter cells experience repulsive forces between each other, as well as with other nearby cells. These forces will push the cells apart until they reach an equilibrium and are no longer overlapping (see Section 4.2.2).

Cell contact inhibition

Once the whole cell colony grows in size, individual cells may become overcrowded and growth-arrested due to the contact inhibition signals from the neighbouring cells. The overcrowding condition is modelled by counting the number of cells $C_i^{\text{neigh}}(t)$ in the specified neighbourhood of radius $R_{neigh} = 4.5R_{max}$ [128]:

$$C_i^{\text{neigh}}(t) = \sum_{j=1}^{M(t)} \mathcal{I}_{\mathcal{S}_i}(\mathbf{X}_j(t)),$$

where $\mathcal{I}_{(\cdot)}(\cdot)$ again denotes the indicator function and $\mathcal{S}_i$ is the set of all cancer cells that are close to the cell $C_i(t)$, *i.e.,*

$$\mathcal{S}_i = \left\{\mathbf{X} \in \{\mathbf{X}_k(t)\}_{k=1,\ldots,M(t)} | \parallel \mathbf{X} - \mathbf{X}_i(t) \parallel_2 \leq R_{\text{neigh}}\right\} \setminus \{\mathbf{X}_i(t)\}.$$

When the number of neighbouring cells reaches a specified threshold N_{neigh} (*i.e.,* $C_i^{\text{neigh}}(t) \geq N_{\text{neigh}}$), the cell C_i(t) is considered overcrowded and growth-arrested. However, such an arrested cell remains metabolically active [57], and can resume its active cell cycle when the contact inhibition conditions change. The time spent in the growth-arrested state does count toward the length of the active cell cycle.

4.2.2 The Hybrid Cell Movement

To model cancer cell passive relocation (due to cell-cell interactions) and active migration (due to cell-ECM interactions), we combine both discrete and continuous approaches. While for cell-cell interactions (both repulsive and adhesive forces) we use the agent-based approach, the cell-ECM (both fibre-based and non-fibre adhesions) are modelled by using a continuous technique, described in Chapter 2. Ultimately, these forces collectively influence the direction of motion of each individual cell, leading to complex tumour dynamics and to the emergence of various tumour morphologies.

Discrete cell-cell repulsive interactions

The repulsive forces between nearby cells are introduced to maintain cell volume and to avoid cell overlapping during its movement or division (see Section 4.2.1). Following previous works [128, 27], these forces are modelled as linear Hookean springs. Hence, considering two arbitrary but distinct cells $C_i(t)$ and $C_j(t)$ (with $i \neq j$), the repulsive force between them is given by

$$\mathbf{F}_{i,j}^{\text{rep}} = \begin{cases} F^{\text{rep}}\Big(\big(C_i^{\text{rad}}(t) + C_j^{\text{rad}}(t)\big) - \parallel \mathbf{X}_{i,j}^{\text{dis}}(t) \parallel_2 \Big) \dfrac{\mathbf{X}_{i,j}^{\text{dis}}(t)}{\parallel \mathbf{X}_{i,j}^{\text{dis}}(t) \parallel_2}, & \text{if } \parallel \mathbf{X}_{i,j}^{\text{dis}}(t) \parallel_2 < \\ & C_i^{\text{rad}}(t) + C_j^{\text{rad}}(t), \\ 0, & \text{otherwise,} \end{cases}$$

where $\mathbf{X}_{i,j}^{\text{dis}}(t) := \mathbf{X}_i(t) - \mathbf{X}_j(t)$, $F^{\text{rep}} > 0$ is the constant spring stiffness and the spring resting length is set be equal to the sum of the two cells' radii, *i.e.,* to $C_i^{\text{rad}}(t) + C_j^{\text{rad}}(t)$. Taking into consideration now the whole cancer cell population, the overall repulsive force that acts on the cell $C_i(t)$ is given by the sum of all repulsive forces between the cell $C_i(t)$ and any other overlapping cell $C_j(t)$, with $j \in \{1, \ldots, M(t)\} \setminus \{i\}$. This cumulative force is given by

$$\mathcal{F}_i^{\text{rep}} := \sum_j \mathbf{F}_{i,j}^{\text{rep}}, \qquad j \in \{1, \ldots, M(t)\} \setminus \{i\}. \tag{4.3}$$

Discrete cell-cell adhesive interactions

The adhesive forces are activated between non-overlapping but nearby cells in order to keep the cell cluster compact. These forces are modelled using Hooke's law with a constant spring stiffness $F^{\text{adh}} > 0$ and resting length of $2R_{\max}$ [128]. Hence, such forces are activated between cells separated by the distance larger than $2R_{\max}$, but not exceeding $2.25R_{\max}$. This prevents from over-activation of the cell-cell adhesion between cells that are located far off each other. Therefore, considering two arbitrary

cells $C_i(t)$ and $C_j(t)$ (with $i \neq j$), the cell-cell adhesion force acting between them is given by

$$\mathbf{F}_{i,j}^{\text{adh}} := \begin{cases} F^{\text{adh}}\Big(2R_{\max} - \parallel \mathbf{X}_{i,j}^{\text{dis}}(t) \parallel_2 \Big) \dfrac{\mathbf{X}_{i,j}^{\text{dis}}(t)}{\parallel \mathbf{X}_{i,j}^{\text{dis}}(t) \parallel_2}, & \text{if } 2 < \dfrac{\parallel \mathbf{X}_{i,j}^{\text{dis}}(t) \parallel_2}{R_{\max}} < 2.25 \\ 0, & \text{otherwise,} \end{cases}$$

where $\mathbf{X}_{i,j}^{\text{dis}}(t) := \mathbf{X}_i(t) - \mathbf{X}_j(t)$. Similarly to the repulsive forces, each cell can be subjected to multiple adhesive forces, thus the cumulative adhesive force which acts on cell $C_i(t)$ is given by

$$\mathcal{F}_i^{\text{adh}} := \sum_j \mathbf{F}_{i,j}^{\text{adh}}, \qquad j \in \{1, \dots, M(t)\} \setminus \{i\}. \tag{4.4}$$

Continuous cell-ECM adhesive interactions

Besides the cell-cell interactions described above, of particular importance, are the cell-ECM adhesions [115, 210, 292, 297] that we explore here through a cell-non-fibre ECM adhesion [84, 90, 91, 119] as well as a cell-fibre ECM adhesion [294, 295]. This type of interaction is usually modelled by a non-local adhesion integral with a *sensing region* $\mathbf{B}(0, R)$ of radius R, see Chapter 2 or the existing literature [17, 81, 70, 71, 206, 245, 246, 247, 265, 264] for further details. Since in our hybrid model the two phase ECM is modelled in a continuous manner using densities, we can adopt this approach to describe the present cell-ECM interactions. To this end, let us define the *cell-ECM adhesion force/velocity* for an arbitrary cell C_i as

$$\begin{aligned} \mathcal{F}_i^{\text{ECM}} := \frac{1}{R} \int\limits_{\mathbf{B}(0,R)} \mathcal{K}(\parallel y \parallel_2) \Big[& n(y) \mathbf{S}_{cl} l(X_i + y, t) \\ & + \widehat{n}(y, \theta_f(X_i + y, t)) \mathbf{S}_{cF} F(X_i + y, t) \Big] \cdot [1 - \rho(\mathbf{u})]^+ dy, \end{aligned} \tag{4.5}$$

which has the same form as its continuous counterpart defined for example in (2.23), the only difference being that we replaced the continuous variable x by the discrete cell positions X_i, *i.e.,* instead of calculating the integral for each macro-scale point x we only calculate it for the discrete cell centres X_i. Hence, each component $\mathbf{B}(0, R)$ with $R > 0$, $S_{cl} > 0$, $S_{cF} > 0$, $n(\cdot)$, $\widehat{n}(\cdot, \cdot)$ and $\mathcal{K}(\cdot)$ has already been defined in Section 2.3.1.

Due to the minimal discrepancy between the continuous (2.23) and discrete (4.5) integrals, we can use the same numerical approach as in Section 2.4.2. Although here we cannot use convolutions, we can still divide the sensing region $\mathbf{B}(0, R)$ into N_s annulus sectors and use simple bi-linear shape functions, on each annulus sector S_ν. Hence, we can approximate the mean-values of the non-fibres ECM, the fibres ECM, as well as their associated macro-scale orientations which enables us to appropriately construct the integral of the step functions associated with each annulus sector S_ν whose value is given by a linear combination of the mean-values. Finally, these mean values are used to obtain the numerical approximation for $\mathcal{F}_i^{\text{ECM}}$ by following the numerical steps fully described in Section 2.4.2 or in [245, 265, 264].

The overall direction of cell movement

Ultimately, the overall movement direction of a cell $C_i(t)$ depends on each of the forces discussed above (repulsion, cell-cell adhesion and cell-ECM adhesion). To this end, the spatial dynamics of a cell $C_i(t)$ is based on Newton's second law of motion where we assume that each cell returns to its equilibrium without oscillations. Further, the overall force acting on a cell $C_i(t)$ is assumed to be proportional to the velocity of the cell and so the dynamics is given by [135, 128, 27]

$$\eta \frac{dX_i}{dt} = \mathcal{F}_i^{\text{rep}} + \mathcal{F}_i^{\text{adh}} + \mathcal{F}_i^{\text{ECM}}, \tag{4.6}$$

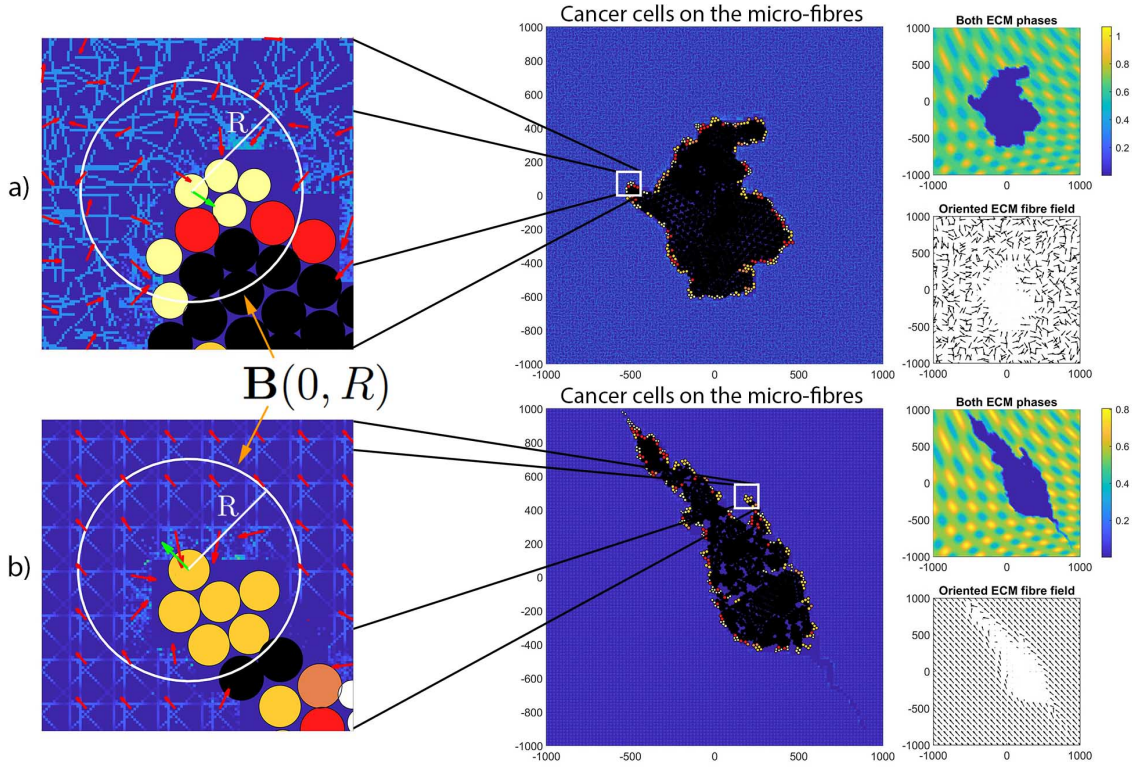

Figure 4.1: *Illustration of the sensing region* $\mathbf{B}(0,R)$ *of radius* R *around a cancer cell, highlighted by the white circle. Within the zoomed-in areas (on the left), the red arrows show the oriented ECM fibre field and the green arrow on the central cancer cell shows the overall travelling direction of that particular cancer cell which is the solution of* (4.6)*. On the right, we show the individual cancer cells with the micro-fibres, the non-fibre ECM densities and the oriented ECM fibre fields (for illustrative purposes these are coarsened four-fold). a) Cancer cell placed within a random fibre environment, identical to Figure 4.7c). b) Cancer cell placed within an aligned fibre environment, identical to Figure 4.7a')*

where η is the damping coefficient and $\mathcal{F}_i^{\text{rep}}$, $\mathcal{F}_i^{\text{adh}}$ and $\mathcal{F}_i^{\text{ECM}}$ are defined in (4.3), (4.4) and (4.5), respectively. To solve the the spatial dynamics (4.6) of the cell $C_i(t)$, we use the classical forward Euler method. We illustrate the overall travelling direction of a cell in Figure 4.1.

4.2.3 The Continuous Multi-Scale ECM

As mentioned before, tumour development is a complex and multi-scale phenomenon where the macro-scale events are accompanied by several related micro-scale processes. One of the most important of these processes is the re-distribution of the fibres ECM micro-constituents triggered by various cell-generated forces. Hence, here we first describe the macro-scale dynamics of the continuous two-phase ECM and then we briefly detail its micro-scale dynamics.

Similarly to the cancer cell density, to achieve connection between the discrete and continuous parts of the model, we first need to appropriately approximate the generated cell forces ($\mathcal{F}_i^{\text{rep}}$, $\mathcal{F}_i^{\text{adh}}$ and $\mathcal{F}_i^{\text{ECM}}$ defined in (4.3), (4.4) and (4.5), respectively) on the macro-scale. For this, let us use the average of the collective contribution of all cell generated forces within a $\gamma_{\Delta x}$ neighbourhood of the macro-node x. This leads to the following continuous cancer cell flux:

$$\mathcal{F}(x,t) := \frac{\int\limits_{\mathbf{B}(x,\gamma_{\Delta x})} \sum\limits_{X_i \in \mathbf{B}(x,\gamma_{\Delta x})} \big(\mathcal{F}_i^{\text{rep}} + \mathcal{F}_i^{\text{adh}} + \mathcal{F}_i^{\text{ECM}}\big)\mathcal{I}_{\mathbf{B}(X_i,C_i^{\text{rad}})}(z)\, dz}{\lambda\big(\mathbf{B}(x,\gamma_{\Delta x})\big) \sum\limits_{i=1}^{M(t)} \mathcal{I}_{\mathbf{B}(x,\gamma_{\Delta x})}(X_i)}, \tag{4.7}$$

where again $\lambda(\cdot)$ is the Lebesgue measure in $\mathbb{R}^N$, $\mathbf{B}(x,\gamma_{\Delta x})$ is the $\|\cdot\|_\infty$ ball used also in (4.1), $\mathcal{I}_{(\cdot)}(\cdot)$ denotes the indicator function.

The two-phase ECM

As opposed to Chapter 2 or 3, here, we only have the cancer cells that degrade the surrounding two-phase ECM via the secretion of MMPs [99, 153, 191, 257, 287, 293]. Consequently, denoting the constant non-fibre ECM degradation rate by $\beta_l > 0$ and the fibre ECM degradation rate by $\beta_F > 0$, the non-dimensional macro-scale

dynamics of both fibre and non-fibre ECM phases are mathematically formalised as

$$\begin{aligned} \frac{\partial F}{\partial t} &= -\beta_F c F, \\ \frac{\partial l}{\partial t} &= -\beta_l c l. \end{aligned} \tag{4.8}$$

Here, we used the macro-scale density of the cancer cell population $c(x,t)$ (see (4.1)), which was derived using the properties of the individual cells provided by the agent-based part of our hybrid model.

Fibre representation and rearrangement

Since we use our multi-scale continuous framework, described in Chapter 2, to model the two-phase ECM, the representation of the macro-scale fibres remained the same as well as the rearrangement process. Hence, the micro-fibre distribution $f(x,t)$ induces both macro-scale quantities, namely the amount $F(x,t)$ and spatial bias $\theta_f(x,t)$ which we referred to as the fibre bottom-up link, illustrated in Figure 2.5 and fully described in Section 2.2.2.

Similarly, the rearrangement process that we refer to as the top-down link, is adopted from Section 2.3.2. However, since in this discrete model we do not consider the presence of macrophages, we consider this complex process to be initiated only by the spatial flux of the cancer cell population $\mathcal{F}(x,t)$ that was defined in (4.7). Consequently, this flux alone is responsible for the emerging of the micro-fibres rearrangement vector which here is defined as

$$r(\delta Y(x),t) := \omega(x,t)\mathcal{F}(x,t) + (1-\omega(x,t))\theta_f(x,t), \tag{4.9}$$

where the weight $\omega(x,t)$ is the appropriate mass fraction of the cancer cells and fibres ECM given by

$$\omega(x,t) := \frac{c(x,t)}{c(x,t)+F(x,t)}.$$

Ultimately, following the steps described in Section 2.3.2, we are able to calculate the new positions z^* of each micro-fibre point z which leads to a rearranged micro-fibre distribution $f(z,t)$. For more details, we refer the reader to Section 2.3.2 or [245].

4.3 Parameter Set

In Table 4.1 we summarise the parameter values (and parameter ranges) used throughout the numerical simulations performed in the next section.

Table 4.1: *Parameter set used for the numerical simulations in this chapter. If we could not find any references for some of our parameters then we "Estimated" them (i.e., we chose an arbitrary value for the simulations).*

Variable	Value	Description	Reference
Δt	1 minute	Temporal time-step	Estimated
T	28 days	Simulation time length	Estimated
$R_{\max}$	$10\mu m$	Maximal radius of any cell	[242, 193]
F^{rep}	$0.45 - 0.9 \times 10 mg/(\mu m \cdot min^2)$	Repulsion spring stiffness	[22, 232]
F^{adh}	$0 - 0.12 \times 10 mg/(\mu m \cdot min^2)$	Cell-cell adhesion spring stiffness	[22, 232]
η	$1 \times 10 mg/(\mu m \cdot min)$	Medium viscosity	[243]
C_1^{mat}	18 hours	Baseline maturation age for the first cell	[242, 193]
N_{neigh}	10	Overcrowding threshold	Estimated
$\mathbf{S}_{cl}$	$0.01 \times 10 mg/min^2$	Cell-non-fibre adhesion coefficient	Estimated
$\mathbf{S}_{cF}$	$0 - 1.8 \times 10 mg/min^2$	Cell-fibre adhesion coefficient	Estimated
β_F	1.5	Non-dimensional degradation coefficient for fibre ECM due to the tumour	[245, 246, 247]
β_l	2	Non-dimensional degradation coefficient	[245, 246, 247]

Continued on next page

Table 4.1 – continued from previous page

Variable	Value	Description	Reference
		for non-fibre ECM due to the tumour	
R	$30 - 50\mu m$	Sensing radius	Estimated
Δx	$20\mu m$	Macro-scale spatial step-size	Estimated
δ	$20\mu m$	Size of the fibre micro-domain $\delta Y(x)$	Estimated
$\gamma_{\Delta x}$	$\Delta x/2$	Radius of the square neighbourhood $\mathbf{B}(x, \gamma_{\Delta x})$	Estimated
f_{max}	0.636	Maximum of micro-fibre density at any point	[245, 246, 247]

4.4 Results

For completeness of model description, in Figure 4.2 we show a diagrammatic description of the agent-based modelling of cells, the continuous modelling of the ECM and the connection of the two models at the specific stages of the numerical simulations. Here, we can also see the main stages of both models and the information that is required to share with each other.

In the context of the above described multi-scale hybrid framework, here we present some numerical simulations of the model, which highlight different migration cell patterns in various tissues with different levels of ECM fibres and different alignment levels. To this end, we start each simulation with a single cancer cell with well defined properties located at a point (x_1^0, x_2^0) (that will be defined for each simulations) of the computational domain $Y = [-1280\text{mm}, 1280\text{mm}] \times [-1280\text{mm}, 1280\text{mm}]$, and any alteration from this will be stated accordingly. Then, this single cancer cell is considered to be embedded within the following (scaled)

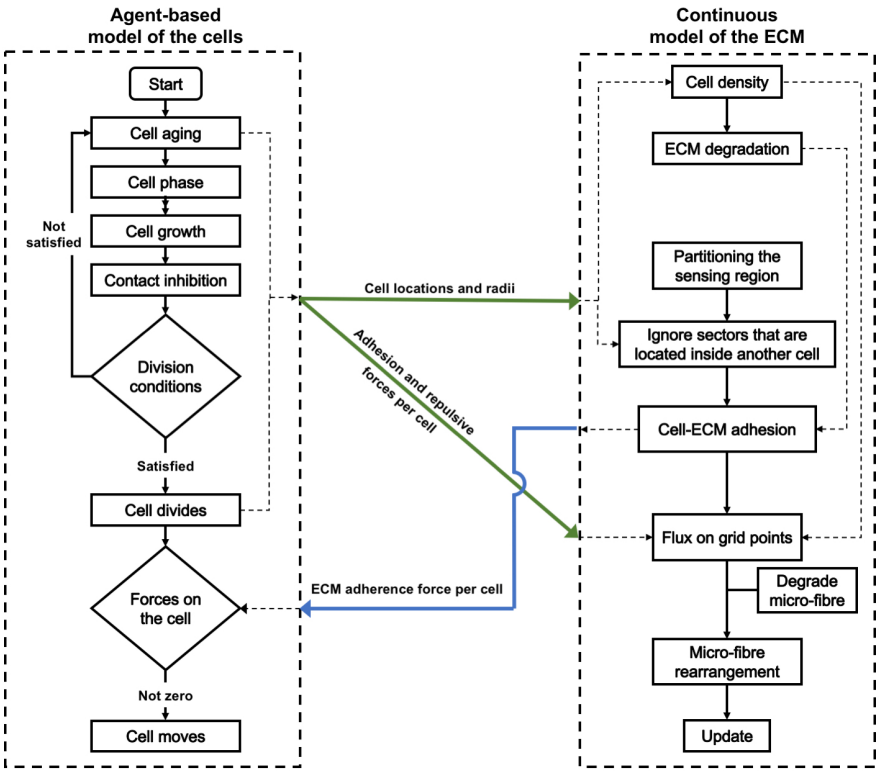

Figure 4.2: *Diagrammatic description of the agent-based modelling of cells, the continuous modelling of the ECM and the connection of the two models at the specific stages of the numerical simulations.*

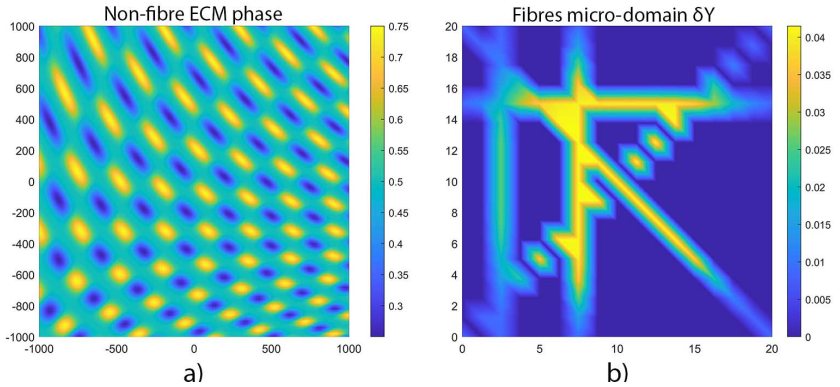

Figure 4.3: *Initial ECM conditions used for the numerical simulations. a) The macro-scale non-fibres ECM density. b) One aligned micro-fibres domain δY which is repeated for all macro-node x.*

non-fibre ECM environment [245, 246, 247, 265, 264]:

$$l(x,0) := \frac{1}{2} + \frac{1}{4}\sin\left(7\pi\frac{(x_1+1280)}{640}\frac{(x_2+1280)}{640}\right)^3 \cdot \sin\left(7\pi\frac{x_2+1280}{x_1+1280}\right),$$

which can be seen in Figure 4.3a) that is *in-silico* representation of the heterogeneous distribution of the non-fibre ECM. Note that this is a scaled version of the non-fibre ECM initial condition that we used in Chapter 2 and 3 that we chose for consistency. For illustrative purposes, in Figure 4.3 (as well as throughout the rest of this Section) we present the non-fibre ECM initial conditions only on the domain of $[-1000\text{mm}, 1000\text{mm}] \times [-1000\text{mm}, 1000\text{mm}]$. Moreover, for both Figures 4.3a)-b) (as well as for all other figures in this Section), the units of the x and y axes are in 'mm'. Finally to highlight the phase of each individual cell, we use five colours. Specifically, we colour the cells that are in the G1 phase white, those in the S phase yellow, those in the G2 phase orange, those in M phase red, and the ones that are both growth-arrested (due to contact inhibition) and in the M phase are coloured black in all simulations. Each simulation of this chapter is either finishes at the final time $T = 28$ days or when a cell reaches the boundary of the computational domain/tissue cube Y which results in shorter simulations. In these cases, we define

the final time T for each simulation.

To shed some light on the importance of ECM characteristics on cancer invasion, throughout this section we investigate numerically the type of cancer migration and invasion patterns obtained when we consider different cell sensing radii. We note here that the sensing radius is determined not only by the length of cell membrane protrusions called pseudopodia (which have lengths greater than $2\mu m$ [189, 138]), but also by the long-range cell sensing due to stress transmission via aligned ECM fibres (which allows cells to sense other cells up to $100\mu m$ away [166]). Throughout this study we investigate the impact of two sensing radii, $R = 30\mu m$ or $R = 50\mu m$, on tumour shape and invasion pattern. We also investigate the impact of different fibres to non-fibres ECM ratios (*i.e.,* $10\% : 90\%$, $20\% : 80\%$, or $30\% : 70\%$), different ECM fibre distribution (*i.e.,* random, aligned, or mixed), and different cell-cell and cell-ECM interaction strengths.

4.4.1 Simulations without Cell-ECM Adhesions in a Random Fibrous Environment

We start our numerical investigation of this hybrid multi-scale model by showing some baseline simulations for the case without cell-ECM adhesions, as we vary the fibre ECM density (i.e., $10 - 30\%$ fibres), for two different sensing radii: $R = 30\mu m$ in Figure 4.4, and $R = 50\mu m$ in Figure 4.5. By comparing the numerical results in Figures 4.4 and 4.5 we can conclude that in the absence of any cell-ECM adhesion, the tumour colonies have an almost circular shape, and they are stationary (*i.e.,* they do not move through the domain). Moreover, the larger cell sensing radius does not seem to have a significant impact on tumour structure.

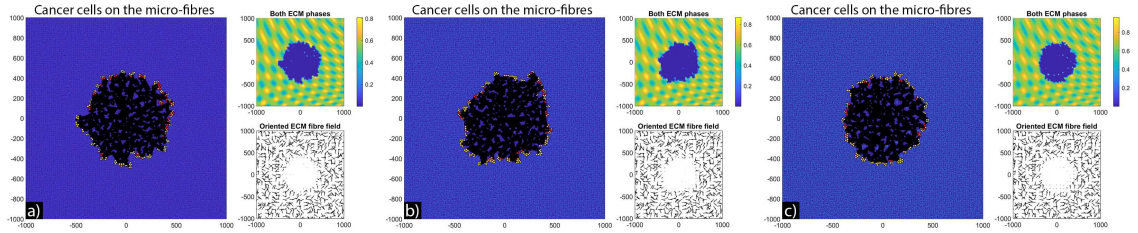

Figure 4.4: *Simulation results at final time $T = 28$ days with random fibres, sensing radius $R = 30\mu m$, repulsion $F^{rep} = 0.45 \times 10 mg/\mu m \cdot min^2$, cell-cell adhesion $F^{adh} = 0.12 \times 10 mg/\mu m \cdot min^2$, cell-non-fibre ECM adhesion $\mathbf{S}_{cl} = 0$, cell-fibre ECM adhesion $\mathbf{S}_{cF} = 0$ and with a) $10\% : 90\%$, b) $20\% : 80\%$, c) $30\% : 70\%$ fibres and non-fibres ECM ratios. For illustrative purposes, all oriented ECM fibre fields are coarsened four-fold. Initial cell position was: a)-c) (0,0).*

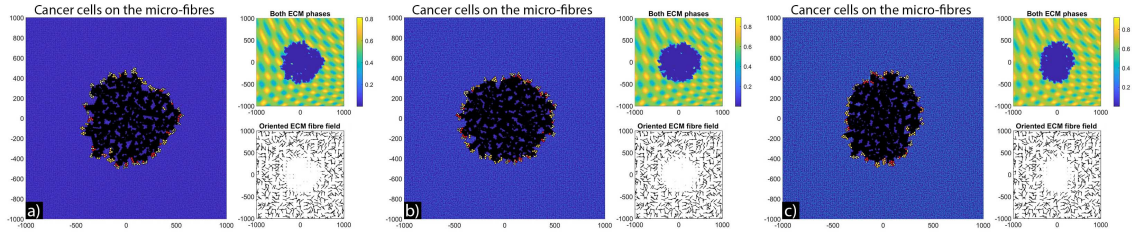

Figure 4.5: *Simulation results at final time $T = 28$ days with random fibres, sensing radius $R = 50\mu m$, repulsion $F^{rep} = 0.45 \times 10 mg/\mu m \cdot min^2$, cell-cell adhesion $F^{adh} = 0.12 \times 10 mg/\mu m \cdot min^2$, cell-non-fibre ECM adhesion $\mathbf{S}_{cl} = 0$, cell-fibre ECM adhesion $\mathbf{S}_{cF} = 0$ and with a) $10\% : 90\%$, b) $20\% : 80\%$, c) $30\% : 70\%$ fibres and non-fibres ECM ratios. For illustrative purposes, all oriented ECM fibre fields are coarsened four-fold. Initial cell position was: a)-c) (0,0).*

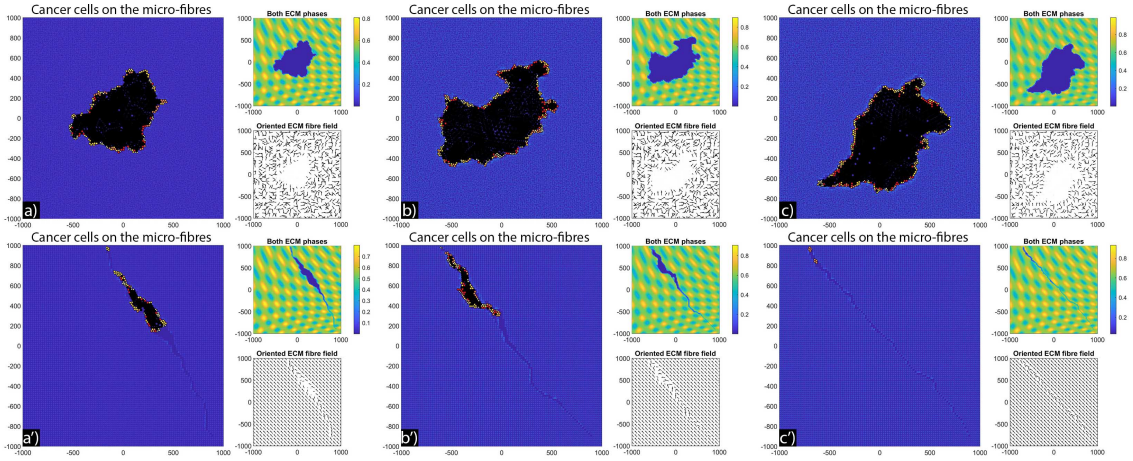

Figure 4.6: *Simulation results with random and aligned fibres, sensing radius* $R = 30\mu m$*, repulsion* $F^{rep} = 0.9 \times 10mg/\mu m \cdot min^2$*, cell-cell adhesion* $F^{adh} = 0.12 \times 10mg/\mu m \cdot min^2$*, cell-non-fibre ECM adhesion* $\mathbf{S}_{cl} = 0.01$*, cell-fibre ECM adhesion* $\mathbf{S}_{cF} = 1.8$ *and with a)-a')* $10\% : 90\%$*, b)-b')* $20\% : 80\%$*, c)-c')* $30\% : 70\%$ *fibres and non-fibres ECM ratios. In a),b),c) the fibre orientation field is set to be random and in a'),b'),c') it is set to be aligned. Moreover the final simulation times are a),b),c)* $T = 28$ *days, a')* $T = 14294$ *minutes, b')* $T = 10761$ *minutes and c')* $T = 4169$ *minutes. For illustrative purposes, all oriented ECM fibre fields are coarsened four-fold. Initial cell position was: a),b),c) (0,0), a'),b'),c') (900,-900).*

4.4.2 Simulations with Cell-ECM Adhesions in a Random Fibrous Environment

Next, we consider cell-ECM adhesion forces ($\mathbf{S}_{cl} = 0.01$, $\mathbf{S}_{cF} = 1.8$), and investigate again the effect of changes in fibre ECM density (i.e., $10 - 30\%$ fibres), for two different sensing radii: $R = 30\mu m$ in Figure 4.6, and $R = 50\mu m$ in Figure 4.7. Since now we consider cell-ECM interactions, in these two figures we also show model dynamics when the ECM environment is described by random fibres (sub-panels a)-c)) or by aligned fibres (sub-panels a')-c')).

First, we see that cell-ECM interactions can lead to irregular-shaped tumour aggregations as well as elongated tumour aggregations. The random fibres are associated with stationary cell aggregations (sub-panels a)-c)), while the aligned fibres are associated with moving cell aggregations (sub-panels a')-c')). The increase in

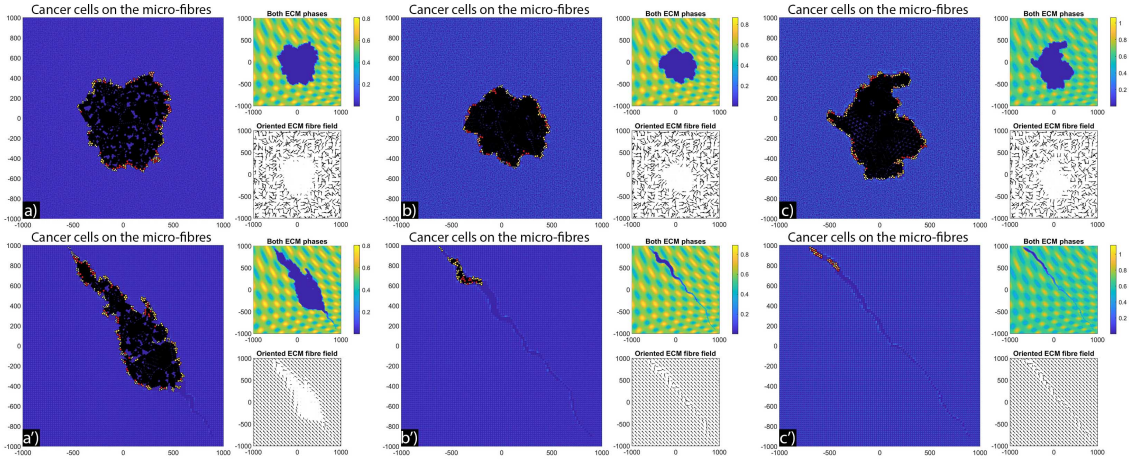

Figure 4.7: *Simulation results with random and aligned fibres, sensing radius* $R = 50\mu m$*, repulsion* $F^{rep} = 0.9 \times 10mg/\mu m \cdot min^2$*, cell-cell adhesion* $F^{adh} = 0.12 \times 10mg/\mu m \cdot min^2$*, cell-non-fibre ECM adhesion* $\mathbf{S}_{cl} = 0.01$*, cell-fibre ECM adhesion* $\mathbf{S}_{cF} = 1.8$ *and with a)-a')* $10\% : 90\%$*, b)-b')* $20\% : 80\%$*, c)-c')* $30\% : 70\%$ *fibres and non-fibres ECM ratios. In a),b),c) the fibre orientation field is set to be random and in a'),b'),c') it is set to be aligned. Moreover the final simulation times are a),b),c)* $T = 28$ *days, a')* $T = 28470$ *minutes, b')* $T = 9260$ *minutes and c')* $T = 6351$ *minutes. For illustrative purposes, all oriented ECM fibre fields are coarsened four-fold. Initial cell position was: a),b),c) (0,0), a'),b'),c') (900,-900).*

sensing region (from $R = 30$ in Figure 4.6 to $R = 50$ in Figure 4.7) leads to an important difference. Even though we have now introduced the cell-ECM adhesion, in a lower fibre ECM density ($10\% - 20\%$) the tumour still kept its more round shape due to the increase of the sensing region. One possible explanation for this is that by increasing the sensing region in a random ECM environment, the different forces that emerge from the fibre orientations, cancel each other out and so the cancer cells are not subject to a strong leading force.

Finally, the increase in cell sensing radius to $R = 50$ in an aligned fibrous environment, leads to a more compact tumour aggregation for the case of $10\% : 90\%$ fibres : non-fibres ECM ratios. For higher ratios, the tumour is extremely elongated and the sensing radius has almost no impact.

4.4.3 Decreasing the Cell-Cell Adhesion Strength

Previous simulations were performed with a relatively high cell-cell adhesion strength ($F^{\text{adh}} = 0.12$), which impacts the overall shape of tumour aggregations. Let us now decrease the cell-cell adhesion strength and consider $F^{\text{adh}} = 0.04$ (while keeping all other parameters as before). In Figure 4.8 and Figure 4.9 we can see that a decrease in cell-cell adhesion causes more irregularly-shaped tumour aggregations. This is counterbalanced a bit by an increase in the sensing radius to $R = 50$ which, as before, tends to favorise more round-shaped tumour aggregations.

4.4.4 Decreasing the Cell-Fibre ECM Adhesion Strength

Since the previous simulations had low cell-cell adhesion but high cell-fibre ECM adhesion, next we investigate tumour invasion patterns when we lower the cell-fibre adhesion strength to $\mathbf{S}_{cF} = 1.2$ (while keeping $F^{\text{adh}} = 0.04$). In Figure 4.10 and Figure 4.11 we see that lowering cell-fibre adhesion leads to a highly-irregular tumour shape, especially for the case of $30\% : 70\%$ fibres to non-fibres ECM ratios.

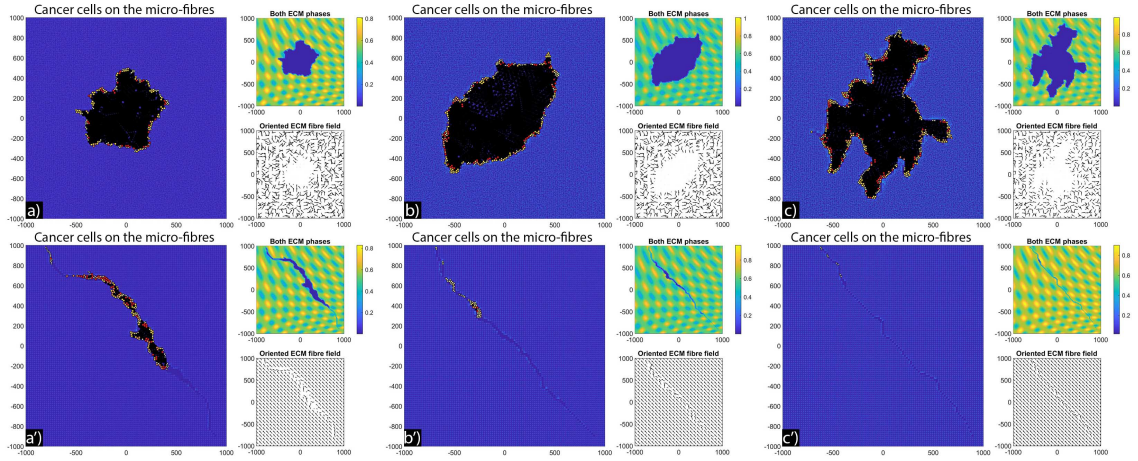

Figure 4.8: *Simulation results with random and aligned fibres, sensing radius* $R = 30\mu m$*, repulsion* $F^{rep} = 0.9 \times 10mg/\mu m \cdot min^2$*, cell-cell adhesion* $F^{adh} = 0.04 \times 10mg/\mu m \cdot min^2$*, cell-non-fibre ECM adhesion* $\mathbf{S}_{cl} = 0.01$*, cell-fibre ECM adhesion* $\mathbf{S}_{cF} = 1.8$ *and with a)-a')* $10\% : 90\%$*, b)-b')* $20\% : 80\%$*, c)-c')* $30\% : 70\%$ *fibres and non-fibres ECM ratios. In a),b),c) the fibre orientation field is set to be random and in a'),b'),c') it is set to be aligned. Moreover the final simulation times are a),b),c)* $T = 28$ *days, a')* $T = 11860$ *minutes, b')* $T = 6822$ *minutes and c')* $T = 3378$ *minutes. For illustrative purposes, all oriented ECM fibre fields are coarsened four-fold. Initial cell position was: a),b),c) (0,0), a'),b'),c') (900,-900).*

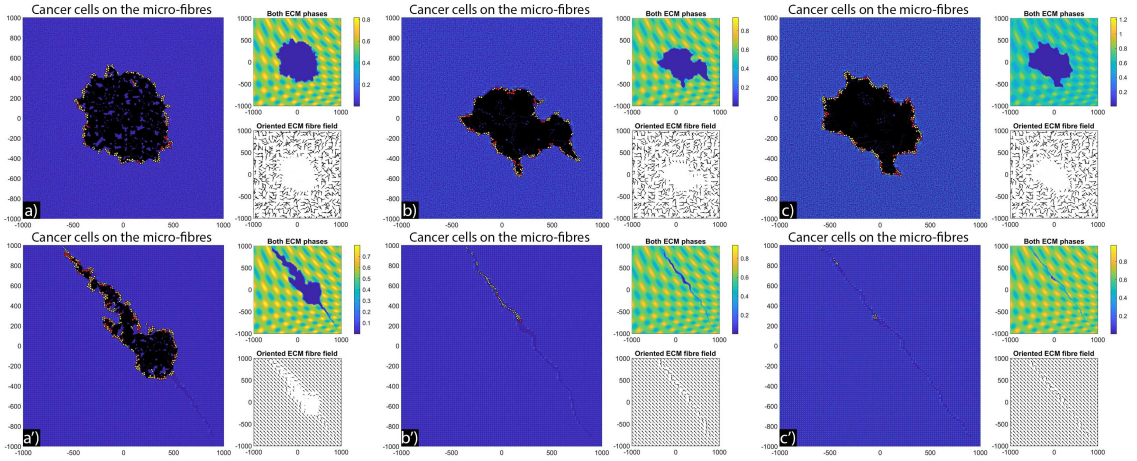

Figure 4.9: *Simulation results with random and aligned fibres, sensing radius* $R = 50\mu m$*, repulsion* $F^{rep} = 0.9 \times 10mg/\mu m \cdot min^2$*, cell-cell adhesion* $F^{dh} = 0.04 \times 10mg/\mu m \cdot min^2$*, cell-non-fibre ECM adhesion* $\mathbf{S}_{cl} = 0.01$*, cell-fibre ECM adhesion* $\mathbf{S}_{cF} = 1.8$ *and with a)-a')* $10\% : 90\%$*, b)-b')* $20\% : 80\%$*, c)-c')* $30\% : 70\%$ *fibres and non-fibres ECM ratios. In a),b),c) the fibre orientation field is set to be random and in a'),b'),c') it is set to be aligned. Moreover the final simulation times are a),b),c)* $T = 28$ *days, a')* $T = 21400$ *minutes, b')* $T = 6551$ *minutes and c')* $T = 4305$ *minutes. For illustrative purposes, all oriented ECM fibre fields are coarsened four-fold. Initial cell position was: a),b),c) (0,0), a'),b'),c') (900,-900).*

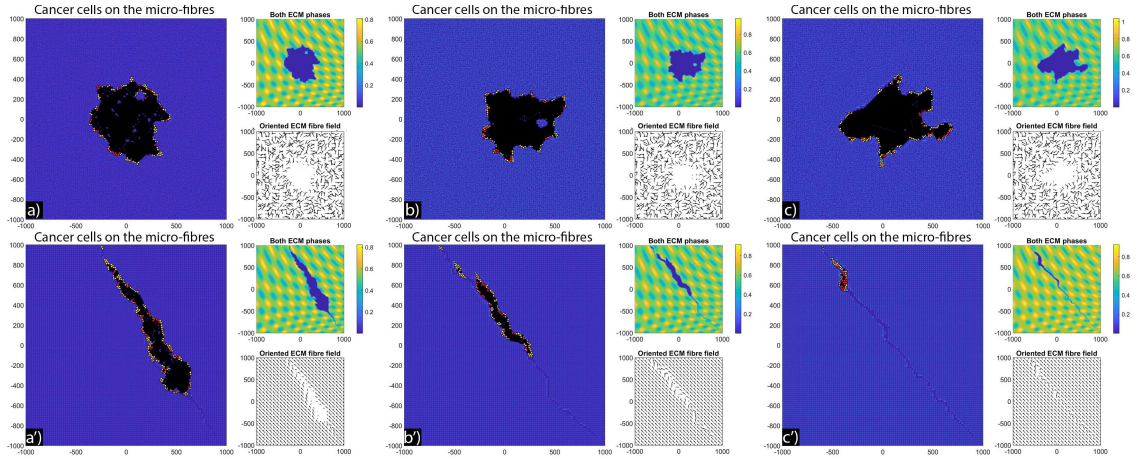

Figure 4.10: *Simulation results with random and aligned fibres, sensing radius* $R = 30\mu m$*, repulsion* $F^{rep} = 0.75 \times 10mg/\mu m \cdot min^2$*, cell-cell adhesion* $F^{adh} = 0.04 \times 10mg/\mu m \cdot min^2$*, cell-non-fibre ECM adhesion* $\mathbf{S}_{cl} = 0.01$*, cell-fibre ECM adhesion* $\mathbf{S}_{cF} = 1.2$ *and with a)-a')* $10\% : 90\%$*, b)-b')* $20\% : 80\%$*, c)-c')* $30\% : 70\%$ *fibres and non-fibres ECM ratios. In a),b),c) the fibre orientation field is set to be random and in a'),b'),c') it is set to be aligned. Moreover the final simulation times are a),b),c)* $T = 28$ *days, a')* $T = 20183$ *minutes, b')* $T = 12268$ *minutes and c')* $T = 7589$ *minutes. For illustrative purposes, all oriented ECM fibre fields are coarsened four-fold. Initial cell position was: a),b),c) (0,0), a'),b'),c') (900,-900).*

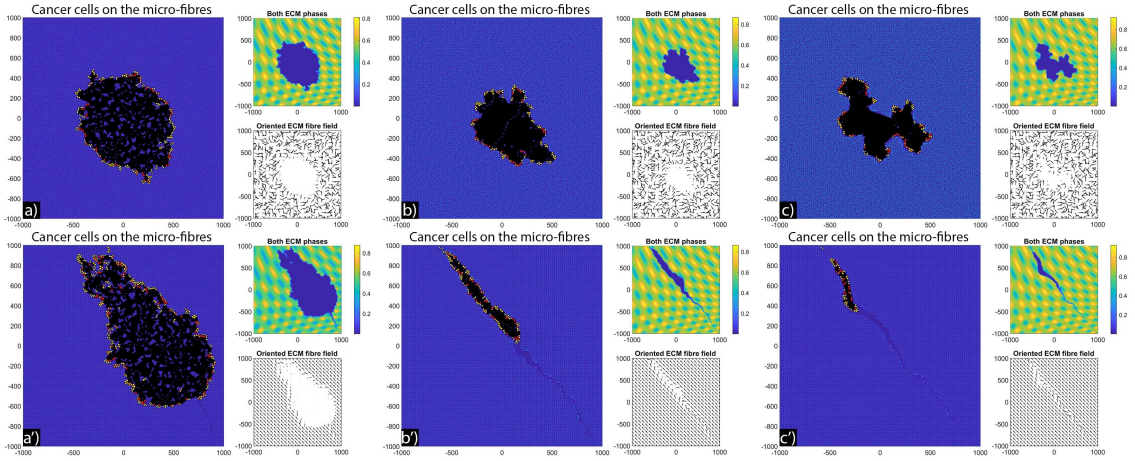

Figure 4.11: *Simulation results with random and aligned fibres, sensing radius* $R = 50\mu m$*, repulsion* $F^{rep} = 0.75 \times 10mg/\mu m \cdot min^2$*, cell-cell adhesion* $F^{adh} = 0.04 \times 10mg/\mu m \cdot min^2$*, cell-non-fibre ECM adhesion* $\mathbf{S}_{cl} = 0.01$*, cell-fibre ECM adhesion* $\mathbf{S}_{cF} = 1.2$ *and with a)-a')* $10\% : 90\%$*, b)-b')* $20\% : 80\%$*, c)-c')* $30\% : 70\%$ *fibres and non-fibres ECM ratios. In a),b),c) the fibre orientation field is set to be random and in a'),b'),c') it is set to be aligned. Moreover the final simulation times are a),b),c)* $T = 28$ *days, a')* $T = 37517$ *minutes, b')* $T = 14220$ *minutes and c')* $T = 9982$ *minutes. For illustrative purposes, all oriented ECM fibre fields are coarsened four-fold. Initial cell position was: a),b),c) (0,0), a'),b'),c') (900,-900).*

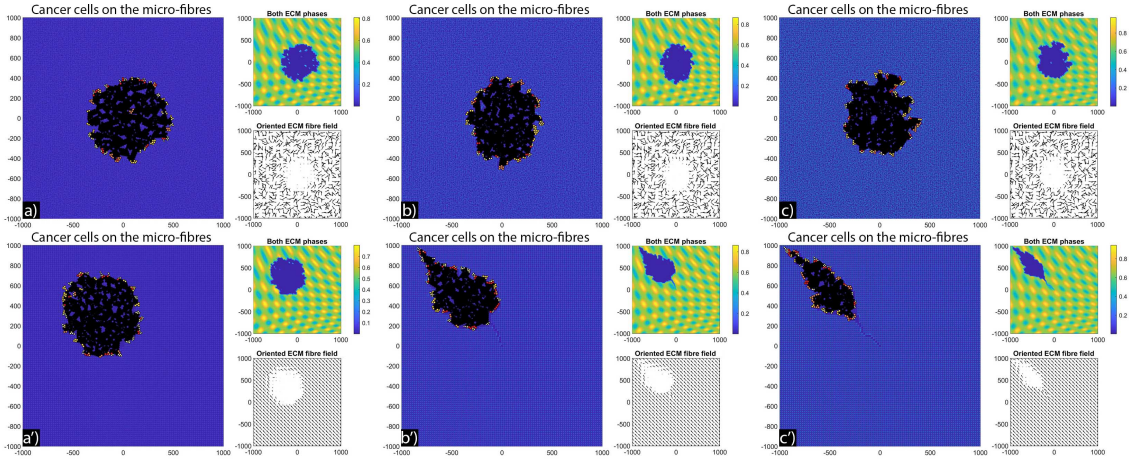

Figure 4.12: *Simulation results with random and aligned fibres, sensing radius* $R = 30\mu m$*, repulsion* $F^{rep} = 0.5 \times 10mg/\mu m \cdot min^2$*, cell-cell adhesion* $F^{adh} = 0.12 \times 10mg/\mu m \cdot min^2$*, cell-non-fibre ECM adhesion* $\mathbf{S}_{cl} = 0.01$*, cell-fibre ECM adhesion* $\mathbf{S}_{cF} = 0.3$ *and with a)-a')* $10\% : 90\%$*, b)-b')* $20\% : 80\%$*, c)-c')* $30\% : 70\%$ *fibres and non-fibres ECM ratios. In a),b),c) the fibre orientation field is set to be random and in a'),b'),c') it is set to be aligned. Moreover the final simulation times are a),a'),b),c)* $T = 28$ *days, b')* $T = 34707$ *minutes and c')* $T = 25801$ *minutes. For illustrative purposes, all oriented ECM fibre fields are coarsened four-fold. Initial cell position was: a)-c') (0,0).*

Consider now an even lower cell-ECM adhesion strength, $\mathbf{S}_{cF} = 0.3$, and at the same time a lower cell repulsion $F^{\text{rep}} = 0.5$. In Figures 4.12 and 4.13 we see that tumour aggregations have recovered their circular shape when the ECM fibres are distributed randomly, and have either circular or slightly elongated structures when the ECM fibres are aligned.

We emphasise that the simulations in sub-panels b')-c') in the above figures were ran for shorter times, since for longer times the cells leave the computational domain Y.

4.4.5 Different Tissues with Different Fibre Orientations

Finally, we investigate numerically what happens with tumour shape and its invasion pattern when the ECM domain is formed of patches of random and aligned fibres, corresponding to different types of tissues (see the discussion in the Introduction).

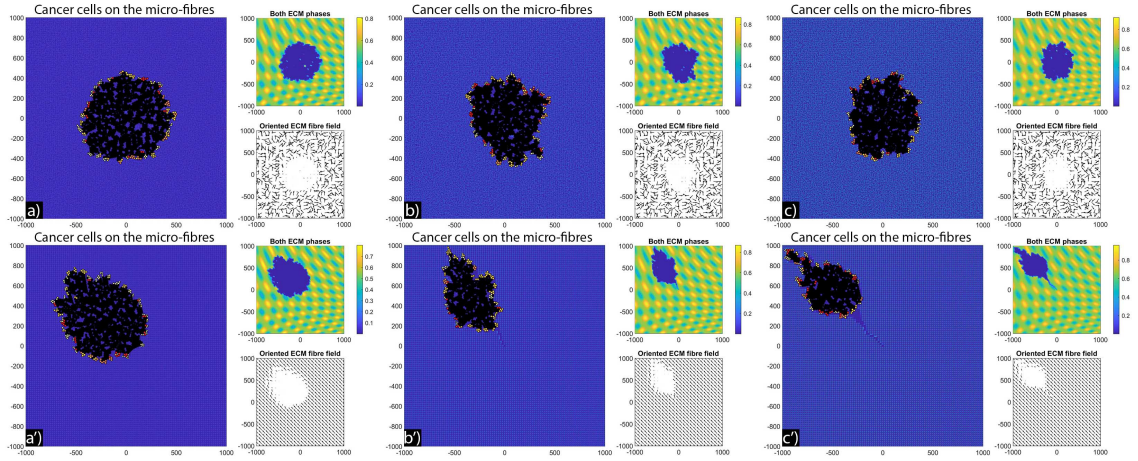

Figure 4.13: *Simulation results with random and aligned fibres, sensing radius* $R = 50\mu m$*, repulsion* $F^{rep} = 0.5 \times 10 mg/\mu m \cdot min^2$*, cell-cell adhesion* $F^{adh} = 0.12 \times 10 mg/\mu m \cdot min^2$*, cell-non-fibre ECM adhesion* $\mathbf{S}_{cl} = 0.01$*, cell-fibre ECM adhesion* $\mathbf{S}_{cF} = 0.3$ *and with a)-a')* $10\% : 90\%$*, b)-b')* $20\% : 80\%$*, c)-c')* $30\% : 70\%$ *fibres and non-fibres ECM ratios. In a),b),c) the fibre orientation field is set to be random and in a'),b'),c') it is set to be aligned. Moreover the final simulation times are a),a'),b),c)* $T = 28$ *days, b')* $T = 31873$ *minutes and c')* $T = 31506$ *minutes. For illustrative purposes, all oriented ECM fibre fields are coarsened four-fold. Initial cell position was: a)-c') (0,0).*

For this we start with a cluster of cells (*e.g.*, 19 cells, for illustration purposes) instead of just one cell. Moreover, we consider here again the parameter values used for the results in Figures 4.6c)-c)', namely: $R = 30\mu m$, $F^{\text{rep}} = 0.9$, $F^{\text{adh}} = 0.12$, $\mathbf{S}_{cl} = 0.01$, $\mathbf{S}_{cF} = 1.8$, and 30% : 70% fibres and non-fibres ECM ratios. In Figure 4.14 we present six scenarios corresponding to different regions of random and aligned ECM fibres. In sub-panels a)-c) we plot the distribution of cancer cells and the ECM degradation pattern at a single time snapshot (*i.e.*, a) $T = 5283$min, b) $T = 4601$min, c) $T = 9518$min). In panels d)-f) we plot the distribution of cancer cells and the ECM degradation patterns at three different times ($T = 9500$min, $T = 15000$min, $T = 20000$min), to illustrate the time-evolution of the system.

The simulations in Figure 4.14 show that the initial position of the cluster of tumour cells, together with the ECM alignment in that region, influences the direction of migration of these cells. In sub-panels a)-b) the cells migrate in the direction of fibre alignment, while in sub-panel c) the cells migrate along the boundary between two regions with opposite alignment. A similar migration pattern is observed in sub-panel d). Finally, in sub-panels e) and f) we observe that when the original tumour cell cluster is positioned in an area surrounded by different ECM alignment, the tumour tends to stay in that area and to very slowly invade the neighbouring tissues (with different ECM orientations). All these different tumour invasive patterns are consistent with the experimental results in [56, 219], which showed that aligned collagen fibres perpendicular to tumour boundary are associated with tumour invasion along those fibres, and the experiments in [219] which showed that aligned collagen fibres parallel to tumour boundary impede invasion.

4.5 Discussion

The composition and structural characteristics of the extracellular matrix (ECM) are known to vary widely among different tissues [175], and this has a significant impact

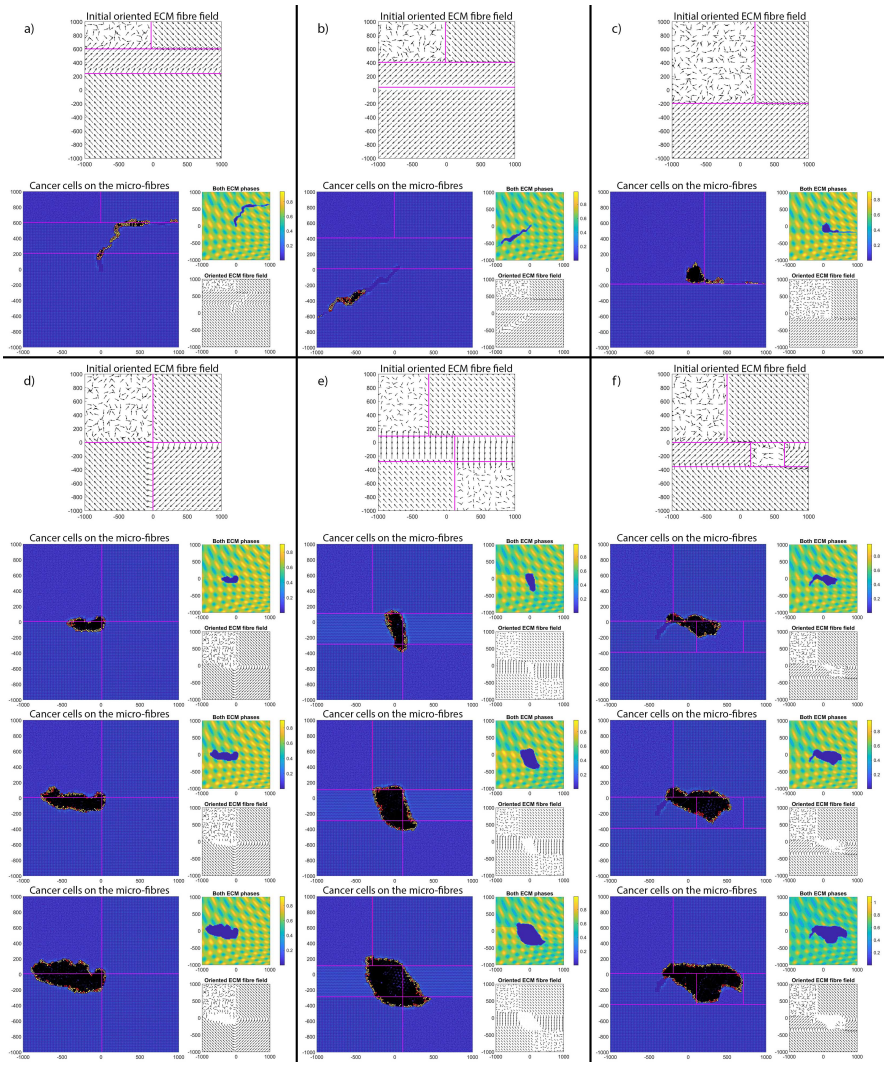

Figure 4.14: *Simulation results with different aligned fibre structures, sensing radius* $R = 30\mu m$*, repulsion* $F^{rep} = 0.9 \times 10mg/\mu m \cdot min^2$*, cell-cell adhesion* $F^{adh} = 0.12 \times 10mg/\mu m \cdot min^2$*, cell-non-fibre ECM adhesion* $\mathbf{S}_{cl} = 0.01$*, cell-fibre ECM adhesion* $\mathbf{S}_{cF} = 1.8$ *and with* $30\% : 70\%$ *fibres and non-fibres ECM ratios. In the first row of each panel a)-f), we present the four-fold coarsened initial oriented ECM fibre field and the purple lines represent the dividing lines between the regions with different tissue alignments. In panel a) we plot a single result at time* $T = 5283$ *minutes, in b) at time* $T = 4601$ *minutes and in c) at time* $T = 9518$*. In panels d)-f) we plot the results at three different times to illustrate the evolution of the tumour, specifically, we use* $T = 9500$*,* $T = 15000$*,* $T = 20000$ *minutes, respectively. The oriented ECM fibres fields are coarsened four-fold for illustration purposes. Initial center of cell cluster position was: a)-e) (0,0), f) (-400,-200).*

on the evolution of cancer. Since there is an increasing need for understanding the spatio-temporal changes in ECM and their roles in cancer progression, in this study we introduced a new multi-scale hybrid mathematical model for cell-cell and cell-ECM interactions, and used it to investigate numerically the impact of ECM fibre orientation and fibre density on cancer cell invasion patterns. To this end, we varied a number of parameters associated with the cell-cell interactions (e.g., cell sensing radius R, cell-cell adhesion stiffness F^{adh}, cell-cell repulsion stiffness F^{rep}), and parameters associated with cell-ECM interactions (i.e., cell-fibre adhesion coefficient $\mathbf{S}_{cF}$, and cell-non-fibre adhesion coefficient $\mathbf{S}_{cl}$), as well as we varied the random or aligned distribution of fibres. This enables us to explore their impact on the formation of cell aggregations and their collective dynamics.

Through numerical simulations, we tested a variety of scenarios: from the impact of smaller/larger cell sensing radius on tumour aggregations, to the impact of random vs. aligned fibres on the migration and invasion of cancer cells into nearby tissues, the role of different fibre orientation in the neighbourhood of initial tumour, and the roles of cell-cell and cell-ECM strengths on the shape of solid tumours. We summarise all these numerical results in Table 4.2 (for the case $R = 30\mu m$) and Table 4.3 (for the case $R = 50\mu m$). By comparing the 3^{rd} column (Description) with the 10^{th} column (Fibre orientation) it is clear that a random ECM fibre distribution leads to stationary tumour aggregations, while an oriented fibre distribution leads to moving tumour aggregations. These numerical results are consistent with experimental results showing that oriented collagen fibres direct tumour invasion, with the alignment of collagen fibres coinciding with the cell invasive direction [97, 56]. Moreover, our numerical results in Figure 4.14 showed that collagen fibres that are relatively parallel to tumour boundary (and create a capsule-like orientation) can limit tumour invasion. These results are consistent with a recent note by Friedl [79], as well as the experiments in [219], about to the importance of ECM orientation relative to the tumour (see also Figure 1 in [79]).

The results in Figure 4.14 suggest that if we could know the orientation of collagen fibres surrounding the tumour (which may be spanning different tissues with different ECM structures) we could predict the fast or slow evolution of the solid tumour, as well as potential cell migration directions. Since collagen can be easily visualised in standard histopathology slides through second harmonic generation microscopy [56] or via multiphoton tomography [283], such predictions on the evolution of tumours might help treatment decisions, *e.g.*, by deciding to resect more surrounding tissue if the imaging shows collagen fibres aligned perpendicular to tumour boundary in a certain area, or by deciding to preserve more surrounding tissue if the imaging shows collagen fibres parallel to tumour boundary. Intraoperative visualisation of tumour microenvironment, including collagen alignment in resected tissues [262], could be further combined with mathematical simulations in 2D (and even in 3D, although this is expected to carry a considerably higher computational cost) to improve such treatment decisions.

Finally, our numerical simulations suggest that the sensing radius R (determined by the length of membrane protrusions called pseudopodia [189, 138], as well as by the long-range sensing due to stress transmission via aligned ECM fibres [166]) impacts the shape of tumour colonies in an aligned fibrous ECM environment with relatively low ratios of fibres to non-fibres. More precisely, when the ECM ratio of fibres to non-fibres is $10\% : 90\%$, larger R leads to more compact tumor cell colonies (compare with the cluster invasion pattern in [80]). For higher fibres : non-fibres ratios this sensing radius has almost no impact, the tumour being extremely elongated as the cells move quickly along the collagen fibres (compare with the strands and files patterns in [80]).

Overall, this study not only confirmed some of the previous experimental results on the importance of alignement of ECM collagen fibres on tumour invasion [56, 219], but also proposed new hypotheses on the biological mechanisms involved in the shape of the tumour colonies (e.g., the roles of sensing radius vs. fibres to non-fibres

ratios; the roles of sensing radius vs. cell-cell and cell-ECM mechanical forces). Moreover, this multi-scale hybrid modelling, which incorporates ECM remodelling and fibre rearrangement in the direction of cell travelling (via cell flux $\mathcal{F}(x,t)$), can be further applied to understand various other fibrotic diseases characterised by ECM remodelling [58].

Table 4.2: *Summary of numerical results obtained for a cell sensing radius of* $R = 30\mu m$.

Figure	**Tumour Type**	**Description**	R	F^{adh}	$\mathbf{S}_{cl}$	$\mathbf{S}_{cF}$	F^{rep}	**Fibre ratio**	**Fibre orientation**
Figure 4.4a)	circular	stationary	30	0.12	0	0	0.45	10%	random
Figure 4.4b)	circular	stationary	30	0.12	0	0	0.45	20%	random
Figure 4.4c)	circular	stationary	30	0.12	0	0	0.45	30%	random
Figure 4.6a)	irregular	stationary	30	0.12	0.01	1.8	0.9	10%	random
Figure 4.6a')	elongated	moving	30	0.12	0.01	1.8	0.9	10%	oriented
Figure 4.6b)	irregular	stationary	30	0.12	0.01	1.8	0.9	20%	random
Figure 4.6b')	elongated	moving	30	0.12	0.01	1.8	0.9	20%	oriented
Figure 4.6c)	irregular	stationary	30	0.12	0.01	1.8	0.9	30%	random
Figure 4.6c')	elongated	moving	30	0.12	0.01	1.8	0.9	30%	oriented
Figure 4.8a)	circular	stationary	30	0.04	0.01	1.8	0.9	10%	random
Figure 4.8a')	elongated	moving	30	0.04	0.01	1.8	0.9	10%	oriented
Figure 4.8b)	irregular	stationary	30	0.04	0.01	1.8	0.9	20%	random
Figure 4.8b')	elongated	moving	30	0.04	0.01	1.8	0.9	20%	oriented
Figure 4.8c)	irregular	stationary	30	0.04	0.01	1.8	0.9	30%	random
Figure 4.8c')	elongated	moving	30	0.04	0.01	1.8	0.9	30%	oriented
Figure 4.10a)	circular	stationary	30	0.04	0.01	1.2	0.75	10%	random
Figure 4.10a')	elongated	moving	30	0.04	0.01	1.2	0.75	10%	oriented
Figure 4.10b)	circular	stationary	30	0.04	0.01	1.2	0.75	20%	random
Figure 4.10b')	elongated	moving	30	0.04	0.01	1.2	0.75	20%	oriented
Figure 4.10c)	irregular	stationary	30	0.04	0.01	1.2	0.75	30%	random
Figure 4.10c')	elongated	moving	30	0.04	0.01	1.2	0.75	30%	oriented
Figure 4.12a)	circular	stationary	30	0.12	0.01	0.3	0.5	10%	random
Figure 4.12a')	circular	moving	30	0.12	0.01	0.3	0.5	10%	oriented
Figure 4.12b)	circular	stationary	30	0.12	0.01	0.3	0.5	20%	random
Figure 4.12b')	elongated	moving	30	0.12	0.01	0.3	0.5	20%	oriented
Figure 4.12c	circular	stationary	30	0.12	0.01	0.3	0.5	30%	random
Figure 4.12c')	elongated	moving	30	0.12	0.01	0.3	0.5	30%	oriented

Table 4.3: *Summary of numerical results obtained for a cell sensing radius of* $R = 50\mu m$.

Figure	**Tumour Type**	**Description**	R	F^{adh}	$\mathbf{S}_{cl}$	$\mathbf{S}_{cF}$	F^{rep}	**Fibre ratio**	**Fibre orientation**
Figure 4.5a)	circular	stationary	50	0.12	0	0	0.45	10%	random
Figure 4.5b)	circular	stationary	50	0.12	0	0	0.45	20%	random
Figure 4.5c)	circular	stationary	50	0.12	0	0	0.45	30%	random
Figure 4.7a)	circular	stationary	50	0.12	0.01	1.8	0.9	10%	random
Figure 4.7a')	elongated	moving	50	0.12	0.01	1.8	0.9	10%	oriented
Figure 4.7b)	circular	stationary	50	0.12	0.01	1.8	0.9	20%	random
Figure 4.7b')	elongated	moving	50	0.12	0.01	1.8	0.9	20%	oriented
Figure 4.7c)	irregular	stationary	50	0.12	0.01	1.8	0.9	30%	random
Figure 4.7c')	elongated	moving	50	0.12	0.01	1.8	0.9	30%	oriented
Figure 4.9a)	circular	stationary	50	0.04	0.01	1.8	0.9	10%	random
Figure 4.9a')	elongated	moving	50	0.04	0.01	1.8	0.9	10%	oriented
Figure 4.9b)	irregular	stationary	50	0.04	0.01	1.8	0.9	20%	random
Figure 4.9b')	elongated	moving	50	0.04	0.01	1.8	0.9	20%	oriented
Figure 4.9c)	irregular	stationary	50	0.04	0.01	1.8	0.9	30%	random
Figure 4.9c')	elongated	moving	50	0.04	0.01	1.8	0.9	30%	oriented
Figure 4.11a)	circular	stationary	50	0.04	0.01	1.2	0.75	10%	random
Figure 4.11a')	elongated	moving	50	0.04	0.01	1.2	0.75	10%	oriented
Figure 4.11b)	irregular	stationary	50	0.04	0.01	1.2	0.75	20%	random
Figure 4.11b')	elongated	moving	50	0.04	0.01	1.2	0.75	20%	oriented
Figure 4.11c)	irregular	stationary	50	0.04	0.01	1.2	0.75	30%	random
Figure 4.11c')	elongated	moving	50	0.04	0.01	1.2	0.75	30%	oriented
Figure 4.13a)	circular	stationary	50	0.12	0.01	0.3	0.5	10%	random
Figure 4.13a')	circular	moving	50	0.12	0.01	0.3	0.5	10%	oriented
Figure 4.13b)	circular	stationary	50	0.12	0.01	0.3	0.5	20%	random
Figure 4.13b')	elongated	moving	50	0.12	0.01	0.3	0.5	20%	oriented
Figure 4.13c)	circular	stationary	50	0.12	0.01	0.3	0.5	30%	random
Figure 4.13c')	elongated	moving	50	0.12	0.01	0.3	0.5	30%	oriented

Chapter 5

Mathematical Modelling of Glioblastomas Invasion within the Brain: a 3D Multi-Scale Moving-Boundary Approach

Aims and Novelty: In this chapter, we extend our multi-scale moving boundary framework from 2D (described in Chapters 2 and 3) to 3D and use it to numerically simulate brain tumours. To do this, we also use T1 weighted and DTI images that ultimately allows us to investigate explicitly the role of brain micro-fibres in 3D invading brain tumours.

5.1 Introduction

Although so far, the presented models focused on generic tumours within a 2-dimensional environment, it is also important to consider specific type of tumours and their evolution within a 3D environment. These models can help connect mathematical models to real-world examples of tumour progression, for instance via pa-

rameter fitting or determining how different components/aspects of the modelling approach affect the overall tumour dynamics.

One of the most invasive and aggressive type of brain tumour is the glioblastoma multiforme, a type of tumour that we have restricted knowledge of since experimental approaches on the brain are limited. However, one important aspect of the brain that can be obtained experimentally, via MRI and DTI scans, is its structure which also plays a vital role in tumour progression.

Hence, in this chapter, we model glioblastoma invasion within a 3D fibrous brain environment to investigate the effects of brain micro-fibres as well as both T1 weighted and DTI scans on the overall tumour progression. To that end, we extend the general 2D multi-scale moving-boundary modelling framework introduced in Chapters 2 and 3 to a 3D one and apply it to model the glioblastoma invasion. The content of this chapter has been thoroughly discussed and presented in our recent publication [266].

5.2 Multi-Scale Modelling of the Tumour Dynamics

To model the evolution of glioblastomas within a 3-dimensional brain, we employ the multi-scale moving boundary framework that we introduced in the previous chapters, but here, we model the tumours in the absence of macrophages. To account for the brain's structure, we aim to use 3D T1 weighted and DTI scans that ultimately influence the migration of the cancer cells as well as affect both micro-scale dynamics. Hence, here we aim to explore the impact of the brain structure on the interlinked macro-scale and micro-scale tumour dynamics.

5.2.1 Macro-Scale Dynamics

Since in this work we extend the 2-dimensional (2D) modelling framework introduced in Chapter 2 and 3, we begin by revisiting briefly some of the key features of this framework and by giving a few useful notations. First, we denote by $\Omega(t)$ the expanding 3-dimensional (3D) tumour region that progresses over the time interval $[0,T]$ within a maximal tissue cube $Y \subset \mathbb{R}^N$ with $N = 3$, *i.e.,* $\Omega(t) \subset Y$, $\forall t \in [0,T]$; see also Figure 5.1 for a 3D illustration. Then at any macro-scale spatio-temporal point $(x,t) \in Y \times [0,T]$ we consider a cancer cell population $c(x,t)$ that is placed within and interacts with a two-phase ECM: the non-fibre $l(x,t)$ and fibre $F(x,t)$ ECM phases [245, 247, 246, 265, 264]. On the one hand, the fibre ECM phase accounts for all major fibrous proteins such as collagen and fibronectin, whose micro-scale distribution induces the spatial orientation of the ECM fibres. Hence, the macro-scale spatio-temporal distribution of the ECM fibres is represented by an oriented vector field $\theta_f(x,t)$ that describes their spatial bias, as well as by $F(x,t) := \|\theta_f(x,t)\|$ which denote the amount of fibres at a macro-scale point (x,t) [245, 247, 246, 265, 264] (for further details on these two quantities, we refer the reader to Section 2.2.2). On the other hand, in the non-fibre ECM phase we bundle together every other ECM constituent such as non-fibrous proteins (for example amyloid fibrils), enzymes, polysaccharides and extracellular Ca^{2+} ions [245, 247, 246, 265, 264]. Furthermore, we incorporate the structure of the brain by extracting data from DTI and T1 weighted brain scans, and then using this data to parametrise the model. Specifically, we denote by $\mathbb{D}_{Water}(x)$ the water diffusion tensor that is induced by the DTI scan. Also, we denote by $w(x)$ the white matter density and by $g(x)$ the grey matter density, both of which are extracted from the T1 weighted image. Finally, to facilitate the description of the model and to make the mathematical notations more compact, we denote by $\mathbf{u}$ the global tumour vector which at each (x,t) is given by

$$\mathbf{u} := (c(x,t), l(x,t), F(x,t))^{\intercal},$$

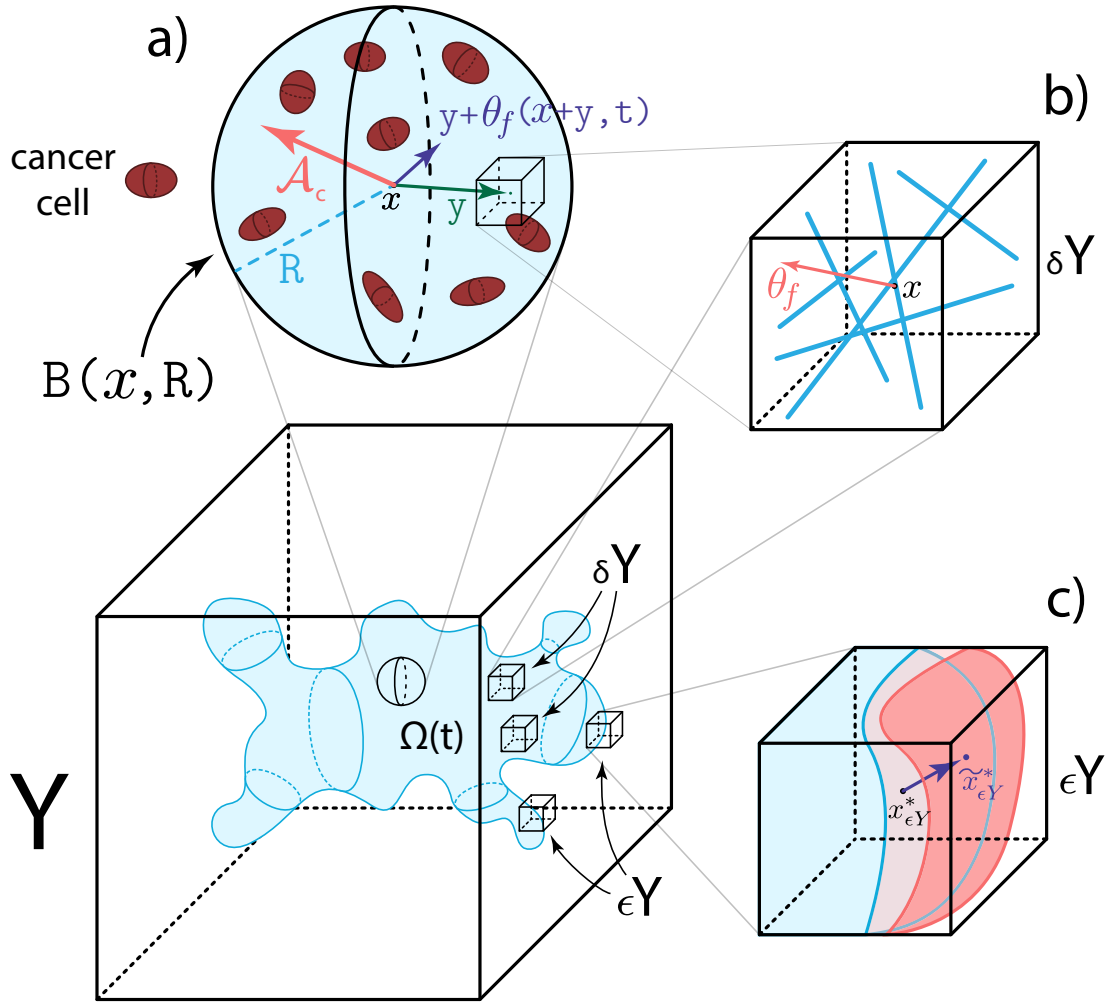

Figure 5.1: *Schematics of the multi-scale model. a) Illustration of the sensing region* $\mathbf{B}(x, R)$*, the two vectors* y *and* $y + \theta_f(y + x, t)$ *and the overall travelling direction* $\mathcal{A}_c$*. b) An example of a fibre micro-domain* $\delta Y(x)$ *containing fibres (blue lines) that induces an overall orientation* $\theta_f(x, t)$ *for* $\delta Y(x)$*. c) An example of a boundary micro-domain* $\epsilon Y(x)$ *where the blue volume represents the tumour volume at the current time-step with boundary point* x *and the red volume represents the evolved tumour at next time-step with shifted boundary point* $x^*_{\epsilon Y}$*.*

With this notation, the total space occupied by the macroscopic tissue is denoted by $\rho(\mathbf{u})$ and is defined as

$$\rho(\mathbf{u}) := c(x,t) + l(x,t) + F(x,t).$$

Cancer cell population dynamics

To describe the spatio-temporal evolution of the cancer cell population $c(x,t)$, we first assume a logistic-type growth with rate μ as in Chapters 2 and 3 [145, 146, 275, 245, 247, 246, 265, 264]. For the movement of this cell population, we use the structure of the brain by taking into account both the T1 weighted and DTI scans (from the IXI Dataset [1]), as well as the various adhesion mediated processes [49, 55, 115, 210, 292, 297]. Hence, the spatio-temporal dynamics of the cancer cell population is described by

$$\frac{\partial c}{\partial t} = \underbrace{\nabla\nabla : \big[\mathbb{D}_T(x)c\big]}_{\substack{\text{fully anisotropic}\\ \text{diffusion}}} - \underbrace{\nabla\cdot\big[c\mathcal{A}_c(x,t,\mathbf{u},\theta_f)\big]}_{\text{adhesion processes}} + \underbrace{\mu c\big[1-\rho(\mathbf{u})\big]^+}_{\substack{\text{logistic-type}\\ \text{proliferation}}}. \tag{5.1}$$

Here, the operator $\nabla\nabla$: denotes the full second order derivative [75], *i.e.,* it is defined as

$$\nabla\nabla : \big[\mathbb{D}_T(x)c\big] := \sum_{i,j=1}^{N} \frac{\partial}{\partial x_i}\frac{\partial}{\partial x_j}\Big(\mathbb{D}_{i,j}c\Big), \qquad N=3,$$

with $\mathbb{D}_{i,j}$ denoting the components of the tumour diffusion tensor $\mathbb{D}_T$. Since classical diffusion models with constant coefficient cannot capture any directional cues, as those provided by the DTI data, in Eq. (5.1) we use a tensor model (involving a fully anisotropic diffusion term) that is able to incorporate the anisotropic nature of the cancer cell movement. These tensor models were proposed in [20, 21, 18, 19] and have been used to mathematically model the gliomas within the brain; see for instance [75, 116, 202]. The main idea of this approach is to use the measured water diffusivity in the structured, fibrous brain environment characterised by a symmetric

water diffusion tensor [196]

$$\mathbb{D}_{Water}(x) = \begin{bmatrix} d_{xx}(x) & d_{xy}(x) & d_{xz}(x) \\ d_{xy}(x) & d_{yy}(x) & d_{yz}(x) \\ d_{xz}(x) & d_{yz}(x) & d_{zz}(x) \end{bmatrix}, \tag{5.2}$$

and appropriately construct a macroscopic diffusion tensor for the cancer cell population. Since this water tensor (5.2) is naturally symmetric (due to the DTI scans) [196], it can be diagonalised. Denoting its eigenvalues by $\lambda_1(x) \geq \cdots \geq \lambda_N(x)$ and the associated eigenvectors by $\phi_1(x), \cdots \phi_N(x)$, with $N = 3$, we follow [108, 178, 202] and construct the 3D tumour diffusion tensor as

$$\begin{aligned} \mathbb{D}_T(x) := D_c\, D_{WG}(x) \Bigg[& \left(r + (1-r) \left(\frac{\coth k(x)}{k(x)} - \frac{1}{k(x)^2} \right) \right) I_3 \\ & + (1-r) \left(1 - \frac{3 \coth k(x)}{k(x)} + \frac{3}{k(x)^2} \right) \phi_1(x) \phi_1^{\intercal}(x) \Bigg]. \end{aligned} \tag{5.3}$$

Here, $D_c > 0$ is the diffusion coefficient, $r \in [0, 1]$ specifies the degree of isotropic diffusion, I_3 denotes the 3×3 identity matrix, $k(x)$ is given by

$$k(x) := \mathcal{K}_{FA} FA(x),$$

with $\mathcal{K}_{FA} \geq 0$ being a proportionality constant measuring the sensitivity of the cells to the environments' direction, and $FA(x)$ denotes the *fractional anisotropy index* [95] given by

$$FA(x) := \sqrt{\frac{(\lambda_1 - \lambda_2)^2 + (\lambda_2 - \lambda_3)^2 + (\lambda_1 - \lambda_3)^2}{2(\lambda_1^2 + \lambda_2^2 + \lambda_3^2)}}.$$

Finally, it is well known that the malignant glioma cells positioned in the white matter exercise quicker motility than those situated in the grey matter [51, 133, 251, 267]. To account for this effect, in (5.3), we use a regulator term $D_{WG}(\cdot)$ that

is given by

$$D_{WG}(x) = a + (1-a)\Big(\big(D_G\, g(x) + w(x)\big) * \psi_\rho\Big)(x), \tag{5.4}$$

where $0 \leq D_G \leq 1$ is the grey matter regulator coefficient, $*$ is the convolution operator [64], $\psi_\rho := \psi(x)/\rho^N$ denotes the standard mollifier defined in Appendix A.2 and $g(x)$ and $w(x)$ are the grey and white matter densities provided by the T1 weighted image (following an image segmentation process). Finally, $0 \leq a \leq 1$ is a parameter that distinguishes between different cases (see Section 5.5).

In addition, as in the previous chapters, the movement of the cancer cells is further biased by various adhesion mediated process [49, 55, 115, 210, 292, 297]. Due to the increasing evidence that gliomas induce a fibrous environment within the brain [88, 93, 125, 186, 209, 212, 221, 226, 285, 284, 305], in (5.1) we model the overall adhesion process using a non-local flux term that was introduced in [245] (see also Sections 2.3.1 and 3.2.1 as well as [17, 70, 81, 206, 247, 246, 265, 264] for similar terms). Specifically, we explore the adhesive interactions of the cancer cells at $x \in \Omega(t)$ with other neighbouring cancer cells, with the distribution of the non-fibre ECM phase [84, 90, 91, 119] as well as with the oriented fibre ECM phase [294, 295], all located within a sensing region $\mathbf{B}(x, R)$ of radius $R > 0$. For this, we define the non-local flux term as

$$\begin{aligned}\mathcal{A}_c(x,t,\mathbf{u},\theta_f) := \frac{1}{R}\int\limits_{\mathbf{B}(0,R)} \mathcal{K}(y)\Big[n(y)\big(\mathbf{S}_{cc}c(x+y,t) + \mathbf{S}_{cl}l(x+y,t)\big) \\ + \widehat{n}(y,\theta_f(x+y,t))\mathbf{S}_{cF}F(x+y,t)\Big]\big[1-\rho(\mathbf{u}(x+y,t))\big]^+\, dy.\end{aligned} \tag{5.5}$$

Although each term and notation has already been introduced in previous chapters, here, for completeness, we redefine them as well. Hence, in (5.5) $\mathbf{S}_{cc}$, $\mathbf{S}_{cl}$, $\mathbf{S}_{cF} > 0$ are the strengths of the cell-cell, cell-non-fibre ECM and cell-fibre ECM adhesions, respectively and while we take both $\mathbf{S}_{cl}$ and $\mathbf{S}_{cF}$ as positive constants, we consider the

emergence of strong and stable cell-cell adhesion bonds to be positively correlated with the level of extracellular Ca^{+2} ions (one of the non-fibre ECM component) [94, 109]. Hence, following the approach in Chapters 2 and 3 as well as [245, 246, 247, 265, 264], we describe the cell-cell adhesion strength by

$$\mathbf{S}_{cc}(x,t) := \mathbf{S}_{min} + (\mathbf{S}_{max} - \mathbf{S}_{min}) \exp\left[1 - \frac{1}{1-(1-l(x,t))^2}\right],$$

where $S_{min} > 0$ and $S_{max} > 0$ are the minimum and maximum levels of Ca^{+2} ions. Furthermore, in (5.5) we denote by $n(\cdot)$ and $\widehat{n}(\cdot,\cdot)$ the unit radial vector and the unit radial vector biased by the oriented ECM fibres [245, 246, 247, 265, 264] defined by

$$n(y) := \begin{cases} \dfrac{y}{\parallel y \parallel_2} & \text{if } y \in \mathbf{B}(0,R) \setminus \{0\}, \\ 0 & \text{if } y = 0, \end{cases}$$

$$\widehat{n}(y, \theta_f(x+y)) := \begin{cases} \dfrac{y + \theta_f(x+y,t)}{\parallel y + \theta_f(x+y,t) \parallel_2} & \text{if } y \in \mathbf{B}(0,R) \setminus \{0\}, \\ 0 & \text{if } y = 0 \text{ or } y = \theta_f(x+y,t), \end{cases}$$

respectively (for details on the fibre orientation θ_f see Section 2.2.2). Also, to account for the gradual weakening of all adhesion bonds as we move away from the centre point x within the sensing region $\mathbf{B}(x,t)$ in (5.5), we use a radially symmetric kernel $\mathcal{K}(\cdot)$ [265, 264] given by

$$\mathcal{K}(y) = \psi\Big(\frac{y}{R}\Big), \qquad \forall y \in \mathbf{B}(0,R),$$

where $\psi(\cdot)$ is the standard mollifier. Finally, in (5.5) a limiting term $[1-\rho(\mathbf{u})]^+ := \max(0, 1-\rho(\mathbf{u}))$ is used to prevent the contribution of overcrowded regions to cell migration [81]. For a schematic of this adhesion process, we refer the reader to Figure 5.1a).

Two phase ECM macro-scale dynamics

In addition to the cancer cell population, the rest of the macro-scale tumour dynamics are described by the two-phase ECM. Here, both fibres and non-fibres ECM phases are assumed to be simply described by a degradation term due to the cancer cell population. Hence, per unit time, their dynamics is governed by

$$\begin{aligned} \frac{\partial F}{\partial t} &= -\beta_F c F, \\ \frac{\partial l}{\partial t} &= -\beta_l c l, \end{aligned} \tag{5.6}$$

where $\beta_F > 0$ and $\beta_l > 0$ are the degradation rates of the fibre and non-fibre ECM phases, respectively.

The complete macro-dynamics

In summary, equations (5.1) for cancer cells dynamics and (5.6) for the two-phase ECM dynamics lead to the following non-dimensional PDE system describing the evolution of tumour at macro-scale:

$$\begin{aligned} \frac{\partial c}{\partial t} &= \nabla\nabla : \big[\mathbb{D}_T(x)c\big] - \nabla \cdot \big[c\mathcal{A}_c(x,t,\mathbf{u},\theta_f)\big] + \mu c\big[1-\rho(\mathbf{u})\big], \\ \frac{\partial F}{\partial t} &= -\beta_F c F, \\ \frac{\partial l}{\partial t} &= -\beta_l c l. \end{aligned} \tag{5.7}$$

To complete the macro-scale model description, we consider zero-flux boundary conditions and appropriate initial conditions (for instance the ones given in Section 5.5).

5.2.2 Micro-Scale Processes and the Double Feedback Loop

As we have mentioned it before, the cancer invasion process is genuinely a multi-scale phenomenon, and so several micro-scale processes are closely linked to the macro-scale dynamics [293]. Identically to Chapters 2 and 3, here, we consider

two of these micro-processes, namely the rearrangement of the ECM fibres micro-constituents [245] and the cell-scale proteolytic processes that occur at the leading edge of the tumour [279]. Although the description of both micro-scale dynamics follows identical steps as before, for completeness, in the following, we give a brief outline of them.

Two-scale representation and dynamics of fibres

Since the underlying mathematics that describes the emerging *fibres bottom-up* link remains the same as in previous chapters, *i.e.,* we utilise the micro-scale fibre distribution $f(z,t)$ within a fibre micro-domain $\delta Y(x)$ analogously to Section 2.2.2 to calculate the amount of ECM fibres $F(x,t)$ and their bias $\theta_f(x,t)$, we refer the reader to Section 2.2.2 for details on these calculations. Also, a 3D illustration of a micro-domain $\delta Y(x)$ and its corresponding macro-scale orientation $\theta_f(x,t)$ can be seen in Figure 5.1b).

As opposed to Chapters 2 and 3, here we do not consider the presence of macrophages that naturally influence the fibre rearrangement process (*i.e.,* the *fibres top-down link*), and so we need to adjust the equations accordingly. Since here we consider one cell population, only the spatial movement of the cancer cells trigger a rearrangement of ECM fibres micro-constituents on each micro-domain $\delta Y(x)$ (enabled by the secretion of matrix-degrading enzymes that can break down various ECM proteins). Hence, using the fact that the fully anisotropic diffusion term can be rewritten as $\nabla\nabla : \left[\mathbb{D}_T(x)c\right] = \nabla\cdot[\mathbb{D}_T(x)\nabla c + c\nabla\cdot\mathbb{D}_T(x)]$, the fibre rearrangement process is kicked off by the cancer cell spatial flux

$$\mathcal{F}_c(x,t) := \mathbb{D}_T(x)\nabla c + c\nabla\cdot\mathbb{D}_T(x) - c\mathcal{A}_c(x,t,\mathbf{u},\theta_f), \tag{5.8}$$

which is generated by the tumour macro-dynamics (5.7). Then, at any spatio-temporal point $(x,t) \in \Omega(t)\times[0,T]$ this flux (5.8) gets naturally balanced in a

weighted fashion by the macro-scale ECM fibre orientation $\theta_f(\cdot,\cdot)$, resulting in a *rearrangement flux*

$$r(\delta Y(x),t) := \omega(x,t)\mathcal{F}_c(x,t) + (1-\omega(x,t))\theta_f(x,t), \tag{5.9}$$

with $\omega(x,t) := c(x,t)/(c(x,t)+F(x,t))$, that acts uniformly upon the micro-fibre distribution on each micro-domain $\delta Y(x)$. Ultimately, this macro-scale rearrangement vector (5.9) induces a micro-scale reallocation vector $\nu_{\delta Y(x)}(z,t)$ (see Section 2.3.2 for details), enabling us to appropriately calculate the new position z^* of any micro-node $z \in \delta Y(x)$ as

$$z^* := z + \nu_{\delta Y(x)}(z,t). \tag{5.10}$$

For further details on the micro-fibre rearrangement process, we refer the reader to Section 2.2.2 and for illustration of the two links see Figure 2.5.

MDE micro-dynamics and its links

To explore the second micro-scale process that occurs along the invasive edge of the tumour, we use the same approach as in Sections 2.2.2 and 3.2.2. Hence, we consider a bundle of overlapping cubic of micro-domains $\{\epsilon Y\}_{\epsilon Y \in \mathcal{P}(t)}$, with $\epsilon > 0$ being the size of each micro-domain ϵY, which allows us to decompose the overall MDE micro-process, transpiring on $\bigcup_{\epsilon Y \in \mathcal{P}(t)} \epsilon Y$, into a union of proteolytic micro-dynamics occurring on each ϵY; see also Figure 5.1c). Then, as before, denoting the spatio-temporal distribution of the MDEs by $m(y,\tau)$ at any micro-point $(y,\tau) \in \epsilon Y \times [0,\Delta t]$, we observe that the cancer cell population, located within an appropriately chosen distance $\gamma_h > 0$ from $y \in \epsilon Y$, induce a source $h(y,\tau)$ of MDEs

which can be mathematically described via a non-local term

$$h(y,\tau) = \begin{cases} \dfrac{\int\limits_{\mathbf{B}(y,\gamma_h)\cap\Omega(t_0)} c(x,t_0+\tau)\,dy}{\lambda(\mathbf{B}(y,\gamma_h)\cap\Omega(t_0))} & y \in \epsilon Y \cap \Omega(t_0), \\ \\ 0 & y \notin \epsilon Y \setminus (\Omega(t_0) + \{z \in Y \mid \|z\|_2 < \rho\}), \end{cases} \tag{5.11}$$

where $0 < \rho < \gamma_h$ is a small mollification range and $\mathbf{B}(y,\gamma_h)$ denotes the $\|\cdot\|_\infty$ ball of radius γ_h centred at a micro-node y. Since again, the calculation of this micro-scale MDE source (5.11) directly involves the macro-scale cancer cell population $c(\cdot,\cdot)$, we observe a naturally arising *MDE top-down* link that connects the macro-scale to the MDE micro-scale. Then, we can use the same MDE micro-dynamics on each ϵY defined in (2.15) as well as use the same procedure, detailed in Section 2.2.2, to acquire the movement direction and magnitude of a tumour boundary point $x^*_{\epsilon Y}$ within the peritumoral area covered by the associated boundary micro-domain ϵY. Ultimately as before, this causes a boundary movement, and as a consequence we obtain a new evolved tumour macro-domain $\Omega(t_0 + \Delta t)$, the link of which we refer to as the *MDE bottom-up link*. For illustration of the boundary movement we refer the reader to Figure 5.1c), for further details of the MDE micro dynamics see Section 2.2.2 and for illustration of the two links see Figure 2.5.

5.3 Numerical Approach

In this section, we aim to give a description of the numerical approach that we use to solve the macro-scale dynamics (5.7), and for details on the numerical approach used for the MDE micro-scale dynamics we refer the reader to Chapter 2. Here, we use the method of lines approach to discretise the macro-scale tumour dynamics (5.7) first in space, and then, for the resulting system of ODEs, we employ a non-local predictor-corrector scheme [245]. In this context, we carry out the spatial discretisation on a

uniform grid, where both spatial operators (fully anisotropic diffusion and adhesion) are accurately approximated in a convolution-driven fashion. First, we note that the fully anisotropic diffusion term can be split into two parts

$$\nabla\nabla : \big[\mathbb{D}_T(x)c\big] = \underbrace{\nabla \cdot \big[\mathbb{D}_T(x)\nabla c\big]}_{\text{diffusive}} + \underbrace{\nabla \cdot \big[c\nabla \cdot \mathbb{D}_T(x)\big]}_{\text{advective}}, \tag{5.12}$$

which enables us to use a combination of two appropriate distinct schemes for an accurate approximation. While for the diffusive part in (5.12), we use the *symmetric finite difference* scheme [76, 85], for the combination of the advective (5.12) and adhesion operators (5.5) (*i.e.,* $\nabla \cdot \big[c\big(\mathcal{A}_c(x,t,\mathbf{u},\theta_f) + \nabla \cdot \mathbb{D}_T(x)\big)\big]$) we use the standard *first-order upwind* finite difference scheme which ensures positivity and helps avoiding spurious oscillations in the solution. Finally, to approximate the adhesion integral $\mathcal{A}_c(x,t,\mathbf{u},\theta_f)$, we consider an analogous approach to Chapter 2, but instead of N_s well-placed barycentric points b_{S_ν}, here, we use N_s random points located within the sensing region $\mathbf{B}(0,R)$ and sums of discrete-convolutions.

To facilitate the narrative, we first introduce some basic notations. For our purposes, it is adequate to discretise the computational domain $Y \in \mathbb{R}^3$ uniformly in each direction of step-size Δx, allowing us to represent the discretisation of Y by the macro-spatial nodes $\{x_i, x_j, x_k\}_{i,j,k=1,\dots,N}$, with $N = \text{length}(Y)/\Delta x + 1$. Besides, at any time-step n we denote the three-dimensional tumour vector by $\mathbf{u}^n = [c^n, F^n, l^n]^\intercal$ and the adhesion integral by $\mathcal{A}_c^n$ allowing us to rewrite the macro-scale dynamics (5.7) as:

$$\frac{\partial \mathbf{u}}{\partial t} = \nabla \cdot \big[\mathcal{D}(x)\nabla \mathbf{u}\big] - \nabla \cdot \mathcal{F}(\mathbf{u}) + \mathcal{S}(\mathbf{u}), \tag{5.13}$$

with

$$\mathcal{D}(x) := \begin{bmatrix} \mathbb{D}_T(x) \\ 0 \\ 0 \end{bmatrix}, \qquad \mathcal{F}(\mathbf{u}) := \begin{bmatrix} c\Big(\mathcal{A}_c(x,t,\mathbf{u},\theta_f) - \nabla\cdot\mathbb{D}_T(x)\Big) \\ 0 \\ 0 \end{bmatrix},$$

$$\mathcal{S}(\mathbf{u}) := \begin{bmatrix} \mu c(1-\rho(\mathbf{u})) \\ -\beta_F cF \\ -\beta_l cl \end{bmatrix}.$$

5.3.1 Diffusion operator: $\nabla\cdot[\mathcal{D}(x)\nabla\mathbf{u}]$

To approximate the anisotropic diffusion operator ($\nabla\cdot[\mathcal{D}(x)\nabla\mathbf{u}]$) in (5.13), we follow [76, 85] and use the symmetric finite difference scheme as well as present its convolutional form. As before, we aim to split the tumour domain and diffusion operator into two parts (interior and boundary) so that we can use two different computational technique that ultimately reduces the computational time. For this, we use the indicator functions $\mathcal{I}_B(\cdot,\cdot)$ and $\mathcal{I}_{In}(\cdot,\cdot)$ introduced in (2.34) and (2.35), respectively. Hence, at any spatial node (i,j,k) at time-step n, the spatial diffusion operator $\nabla\cdot[\mathcal{D}(x)\nabla\mathbf{u}]$ operator can be equivalently represented as

$$\big(\nabla\cdot[\mathcal{D}\nabla\mathbf{u}]\big)^n_{i,j,k} := \begin{cases} \big(\nabla\cdot[\mathcal{D}\nabla\mathbf{u}]^{In}\big)^n_{i,j,k} & \text{if } \mathcal{I}^n_{In}(i,j,k)=1, \\ \big(\nabla\cdot[\mathcal{D}\nabla\mathbf{u}]^{B}\big)^n_{i,j,k} & \text{if } \mathcal{I}^n_{B}(i,j,k)=1, \\ 0 & \text{otherwise.} \end{cases} \tag{5.14}$$

In this context, the symmetric finite difference scheme [76, 85] goes as follows. First, we need to approximate the tumour gradients at the centre points (see Figure 5.2a) for visual representation) that we do by

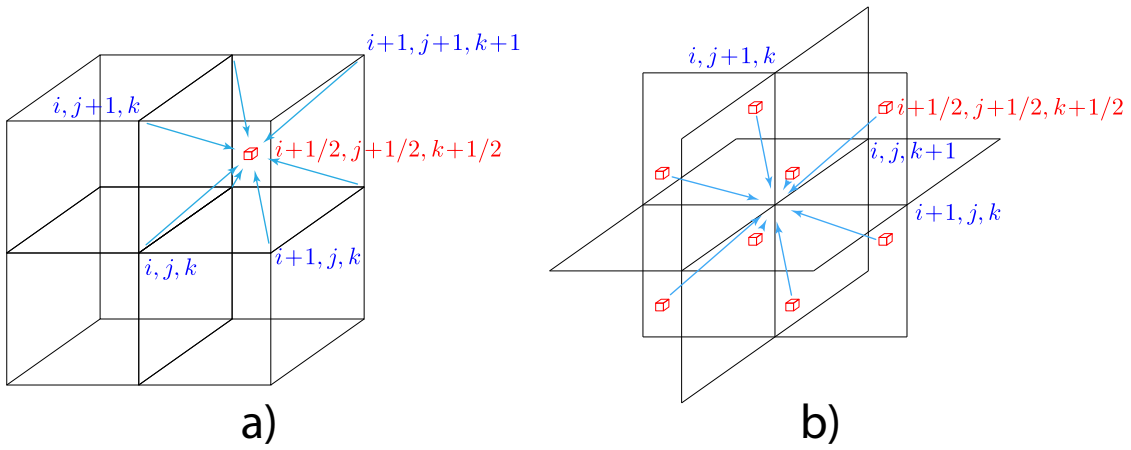

Figure 5.2: *Illustration of a) the approximation of the gradient at one of the center point* $(i+1/2, j+1/2, k+1/2)$*, b) the approximation of the divergence using the* 8 *center points* $(i \pm 1/2, j \pm 1/2, k \pm 1/2)$*.*

$$
\begin{aligned}
(\mathbf{u}_x)^n_{i+\frac{1}{2},j+\frac{1}{2},k+\frac{1}{2}} =& \frac{1}{2\Delta x}\big(\mathbf{u}^n_{i+1,j+1,k+1} + \mathbf{u}^n_{i+1,j,k+1} + \mathbf{u}^n_{i+1,j+1,k} + \mathbf{u}^n_{i+1,j,k} \\
& - \mathbf{u}^n_{i,j+1,k+1} - \mathbf{u}^n_{i,j,k+1} - \mathbf{u}^n_{i,j+1,k} - \mathbf{u}^n_{i,j,k}\big), \\
(\mathbf{u}_y)^n_{i+\frac{1}{2},j+\frac{1}{2},k+\frac{1}{2}} =& \frac{1}{2\Delta x}\big(\mathbf{u}^n_{i+1,j+1,k+1} + \mathbf{u}^n_{i,j+1,k+1} + \mathbf{u}^n_{i+1,j+1,k} + \mathbf{u}^n_{i,j+1,k} \\
& - \mathbf{u}^n_{i+1,j,k+1} - \mathbf{u}^n_{i,j,k+1} - \mathbf{u}^n_{i+1,j,k} - \mathbf{u}^n_{i,j,k}\big), \\
(\mathbf{u}_z)^n_{i+\frac{1}{2},j+\frac{1}{2},k+\frac{1}{2}} =& \frac{1}{2\Delta x}\big(\mathbf{u}^n_{i+1,j+1,k+1} + \mathbf{u}^n_{i,j+1,k+1} + \mathbf{u}^n_{i+1,j,k+1} + \mathbf{u}^n_{i,j,k+1} \\
& - \mathbf{u}^n_{i+1,j+1,k} - \mathbf{u}^n_{i,j+1,k} - \mathbf{u}^n_{i+1,j,k} - \mathbf{u}^n_{i,j,k}\big),
\end{aligned}
\tag{5.15}
$$

and similarly for each $(\mathbf{u}_x)^n_{i\pm1/2,j\pm1/2,k\pm1/2}$, $(\mathbf{u}_y)^n_{i\pm1/2,j1/2,k\pm1/2}$ and $(\mathbf{u}_z)^n_{i\pm1/2,j\pm1/2,k\pm1/2}$. Then since our aim is to use convolution for interior nodes, we note that these gradients (5.15) can be equivalently represented by discrete convolutions, *i.e.,*

$$
(\mathbf{u}_x)^n = \frac{\mathbf{u}^n * \mathcal{K}^x_{\pm\frac{1}{2},\pm\frac{1}{2},\pm\frac{1}{2}}}{2\Delta x}, \quad (\mathbf{u}_y)^n = \frac{\mathbf{u}^n * \mathcal{K}^y_{\pm\frac{1}{2},\pm\frac{1}{2},\pm\frac{1}{2}}}{2\Delta x}, \quad (\mathbf{u}_z)^n = \frac{\mathbf{u}^n * \mathcal{K}^z_{\pm\frac{1}{2},\pm\frac{1}{2},\pm\frac{1}{2}}}{2\Delta x},
\tag{5.16}
$$

where each $(3 \times 3 \times 3)$ matrix $\mathcal{K}^x_{\pm1/2,\pm\frac{1}{2},\pm1/2}$, $\mathcal{K}^y_{\pm1/2,\pm1/2,\pm1/2}$ and $\mathcal{K}^z_{\pm1/2,\pm1/2,\pm1/2}$ is appropriately constructed, using the usual representation (5.15) of the scheme. The next step is to also approximate each component $(d,p) \in Q \times Q$, with $Q := \{x, y, z\}$,

of the diffusion tensor $\mathcal{D}$, that is represented here by the symmetric 3×3 matrix

$$\mathcal{D} = \begin{bmatrix} \mathcal{D}^{x,x} & \mathcal{D}^{x,y} & \mathcal{D}^{x,z} \\ \mathcal{D}^{y,x} & \mathcal{D}^{y,y} & \mathcal{D}^{y,z} \\ \mathcal{D}^{z,x} & \mathcal{D}^{z,y} & \mathcal{D}^{z,z} \end{bmatrix},$$

at the centre points which we do via the midpoint rule. Therefore, considering an arbitrary entry (d, p) these centre points are approximated by

$$\begin{aligned} (\mathcal{D}_{\text{mid}})^{d,p}_{i+\frac{1}{2},j+\frac{1}{2},k+\frac{1}{2}} =& \frac{1}{8}\big(\mathcal{D}^{d,p}_{i+1,j+1,k+1} + \mathcal{D}^{d,p}_{i,j+1,k+1} + \mathcal{D}^{d,p}_{i+1,j,k+1} + \mathcal{D}^{d,p}_{i,j,k+1} \\ &+ \mathcal{D}^{d,p}_{i+1,j+1,k} + \mathcal{D}^{d,p}_{i,j+1,k} + \mathcal{D}^{d,p}_{i+1,j,k} + \mathcal{D}^{d,p}_{i,j,k}\big), \end{aligned} \tag{5.17}$$

and similarly for the remainder $(\mathcal{D}_{\text{mid}})^{d,p}_{i\pm1/2,j\pm1/2,k\pm1/2}$. On the other hand, such approximation can also be written by using discrete convolutions, hence we can approximate each entry of $\mathcal{D}_{\text{mid}}$ at the centre points by

$$(\mathcal{D}_{\text{mid}})^{d,p} = \frac{\mathcal{D}^{d,p} * \mathcal{K}^{\mathcal{D}}_{\pm\frac{1}{2},\pm\frac{1}{2},\pm\frac{1}{2}}}{8}, \tag{5.18}$$

where again we can appropriately construct the $3 \times 3 \times 3$ matrices $\mathcal{K}^{\mathcal{D}}_{\pm1/2,\pm1/2,\pm1/2}$, by using the usual formula for the midpoint rule. The final step in the scheme is to define the flux ($\mathcal{F}_{\mathcal{D}} := \mathcal{D}(x)\nabla u$) at these center points by

$$\big(\mathcal{F}_{\mathcal{D}}\big)^{n}_{i\pm\frac{1}{2},j\pm\frac{1}{2},k\pm\frac{1}{2}} = (\mathcal{D}_{\text{mid}})_{i\pm\frac{1}{2},j\pm\frac{1}{2},k\pm\frac{1}{2}} \cdot \begin{bmatrix} (\mathbf{u}_x)^n_{i\pm\frac{1}{2},j\pm\frac{1}{2},k\pm\frac{1}{2}} \\ (\mathbf{u}_y)^n_{i\pm\frac{1}{2},j\pm\frac{1}{2},k\pm\frac{1}{2}} \\ (\mathbf{u}_z)^n_{i\pm\frac{1}{2},j\pm\frac{1}{2},k\pm\frac{1}{2}} \end{bmatrix} \tag{5.19}$$

where we note that each $(\mathcal{D}_{\text{mid}})_{i\pm1/2,j\pm1/2,k\pm1/2}$ is a 3×3 matrix, which ultimately allows us to approximate the divergence of the flux with the usual central difference formula. Consequently, the approximation of the diffusion term at any boundary

node, using the non-convolutional forms (5.15) and (5.17), is given by

$$\begin{aligned}\left(\nabla\cdot[\mathcal{D}\nabla\mathbf{u}]^B\right)^n_{i,j,k} =& \frac{1}{2\Delta x}\left(\sum_{m,n\in W}\left(\mathcal{F}^x_{\mathcal{D}}\right)^n_{i+\frac{1}{2},j+m,k+n} - \sum_{m,n\in W}\left(\mathcal{F}^x_{\mathcal{D}}\right)^n_{i-\frac{1}{2},j+m,k+n}\right)\\ & \frac{1}{2\Delta x}\left(\sum_{l,n\in W}\left(\mathcal{F}^y_{\mathcal{D}}\right)^n_{i+l,j+\frac{1}{2},k+n} - \sum_{l,n\in W}\left(\mathcal{F}^y_{\mathcal{D}}\right)^n_{i+l,j-\frac{1}{2},k+n}\right)\\ & \frac{1}{2\Delta x}\left(\sum_{l,m\in W}\left(\mathcal{F}^z_{\mathcal{D}}\right)^n_{i+l,j+m,k+m} - \sum_{l,m\in W}\left(\mathcal{F}^z_{\mathcal{D}}\right)^n_{i+l,j+m,k-m}\right)\end{aligned} \tag{5.20}$$

where the set of numbers is defined as $W := \{+1/2, -1/2\}$ and $\mathcal{F}^x_{\mathcal{D}}$, $\mathcal{F}^y_{\mathcal{D}}$ and $\mathcal{F}^z_{\mathcal{D}}$ denotes the x, y and z component of the flux (5.19), respectively. The involved center points in (5.20) are illustrated in Figure 5.2b. However, since (5.20) is the approximation of the anisotropic diffusion at the boundary nodes, it is inevitable to use ghost/outside nodes during the calculations. Since these are outside of the tumour domain $\Omega(t_n)$ we need to approximate their values, that we do by symmetrically reflect the values of the interior nodes to these ghost node in a node by node fashion. In some cases, due to the possibly irregular tumour domain, such values may not be uniquely defined since two different boundary nodes can use the value of the same ghost point, however because of the reflection this value may be different for the two boundary nodes. Hence, for the boundary points we cannot use universal operators (convolution) and we need to approximate the diffusion with the usual form (5.20) in a node by node fashion. On the other hand, for interior nodes we do not have such restriction since the approximation of the diffusion at these nodes involves only known values and so here it is appropriate to use convolution (universal operator). Therefore, for all interior nodes, the convolutional form of the

symmetric finite difference scheme (5.20), using (5.16) and (5.18), is given by

$$\begin{aligned}\left(\nabla\cdot[\mathcal{D}\nabla\mathbf{u}]^{In}\right)^n &= \frac{1}{2\Delta x}\sum_{\substack{l,m,n\in W\\ d,p\in Q}}\left((\mathbf{u}_p)^n\circ(\mathcal{D}_{\text{mid}})^{d,p}\cdot(-1)^q\right)\\ &= \frac{1}{2\Delta x}\sum_{\substack{l,m,n\in W\\ d,p\in Q}}\left[\left(\frac{\mathbf{u}^n * \mathcal{K}^p_{+l,+m,+n}}{2\Delta x}\right)\circ\left(\frac{\mathcal{D}^{d,p} * \mathcal{K}^{\mathcal{D}}_{\pm\frac{1}{2},\pm\frac{1}{2},\pm\frac{1}{2}}}{8}\right)\cdot(-1)^q\right],\end{aligned} \tag{5.21}$$

where $\circ$ is the Hadamard product [87] and q is defined as

$$q := \begin{cases} 0 & \text{if } (d,l)=\left(x,+\frac{1}{2}\right)\vee(d,m)=\left(y,+\frac{1}{2}\right)\vee(d,n)=\left(z,+\frac{1}{2}\right),\\ 1 & \text{otherwise.}\end{cases}$$

5.3.2 Adhesion-advective operator: $\nabla\cdot\mathcal{F}(\mathbf{u})$

To approximate the second spatial operator that describes cell movement $\nabla\cdot\mathcal{F}(\mathbf{u})$, we simply use the first order upwind scheme which helps avoiding spurious oscillations and guarantees positivity. Once more, we split the domain and spatial operator into two parts (interior and boundary) using the indicator functions $\mathcal{I}_B(\cdot,\cdot)$ and $\mathcal{I}_{In}(\cdot,\cdot)$ defined in (2.34) and (2.35), respectively. Hence, we note that the spatial operator can be rewritten as:

$$\left(\nabla\cdot\mathcal{F}(\mathbf{u})\right)^n_{i,j,k} := \begin{cases}\left(\nabla\cdot\mathcal{F}(\mathbf{u})^{In}\right)^n_{i,j,k} & \text{if } \mathcal{I}^n_{In}(i,j,k)=1,\\ \left(\nabla\cdot\mathcal{F}(\mathbf{u})^{B}\right)^n_{i,j,k} & \text{if } \mathcal{I}^n_{B}(i,j,k)=1,\\ 0 & \text{otherwise,}\end{cases} \tag{5.22}$$

and as before, we aim to use a convolutional form for the interior nodes and the standard (non-convolutional) form for the boundary nodes. In this context, for any

boundary point (i,j,k) the spatial operator $\nabla \cdot \mathcal{F}(\mathbf{u})^B$ is approximated by

$$\begin{aligned}\left(\nabla \cdot \mathcal{F}(\mathbf{u})^B\right)^n_{i,j,k} = \frac{1}{\Delta x}\Bigg(& (a_x^+)_{i,j,k}\left(\mathcal{F}^x_{i,j,k} - \mathcal{F}^x_{i-1,j,k}\right) + (a_x^-)_{i,j,k}\left(\mathcal{F}^x_{i+1,j,k} - \mathcal{F}^x_{i,j,k}\right) \\ & (a_y^+)_{i,j,k}\left(\mathcal{F}^y_{i,j,k} - \mathcal{F}^y_{i,j-1,k}\right) + (a_y^-)_{i,j,k}\left(\mathcal{F}^y_{i,j+1,k} - \mathcal{F}^y_{i,j,k}\right) \\ & (a_z^+)_{i,j,k}\left(\mathcal{F}^z_{i,j,k} - \mathcal{F}^z_{i,j,k-1}\right) + (a_x^-)_{i,j,k}\left(\mathcal{F}^z_{i,j,k+1} - \mathcal{F}^z_{i,j,k}\right)\Bigg),\end{aligned} \tag{5.23}$$

where a^+ and a^- are defined as

$$a^+ := \max(\mathcal{F}(\mathbf{u}), 0), \qquad a^- := \min(\mathcal{F}(\mathbf{u}), 0), \tag{5.24}$$

and so $a_x^\pm$, $a_y^\pm$, $a_y^\pm$ are the x, y and z components as well as $\mathcal{F}^x$, $\mathcal{F}^y$ and $\mathcal{F}^z$ are the x, y and z components of the vector field $\mathcal{F}$, respectively. Within the formula defined in (5.23), we may need to use the value of outside/ghost nodes, that as before, we approximate by symmetrically reflecting the value of the interior nodes to these outside nodes in a node by node fashion.

On the other hand, we can observe that (5.23) can be written as sums of convolutions for any interior node (i,j,k) (since we only use nodes that are located within the tumour domain $\Omega(t_n)$, and so their values are known):

$$\left(\nabla \cdot \mathcal{F}(\mathbf{u})^{In}\right)^n = \frac{1}{\Delta x}\left(\sum_{d\in Q} a_d^+ \circ \left(\mathcal{F}^d * \mathcal{K}_d^+\right) + a_d^- \circ \left(\mathcal{F}^d * \mathcal{K}_d^-\right)\right), \tag{5.25}$$

where $Q := \{x, y, z\}$ and each $\mathcal{K}$ is defined as

$$\mathcal{K}_x^+ := [0, 1, -1], \qquad \mathcal{K}_x^- := [1, -1, 0], \qquad \mathcal{K}_y^+ := (\mathcal{K}_x^+)^\intercal, \qquad \mathcal{K}_y^- := (\mathcal{K}_x^-)^\intercal,$$

$$\mathcal{K}_z^+ := \left[\left[\begin{array}{c} 0 \\ 1 \\ -1 \end{array}\right]\right], \qquad \mathcal{K}_z^- := \left[\left[\begin{array}{c} 1 \\ -1 \\ 0 \end{array}\right]\right],$$

where we note that $\mathcal{K}_z^\pm$ are (1x1x3) matrices. This completes the description of the convolution driven upwind scheme that is used for the approximation of the spatial operator $\nabla \cdot \mathcal{F}(\mathbf{u})$.

5.3.3 Adhesion integral: $\mathcal{A}_c(x, t, \mathbf{u}, \theta_f)$

To model the various adhesion processes (cell-cell, cell-non-fibre ECM and cell-fibre ECM), that take place within the sensing region $x+\mathbf{B}(0, R)$, we employed an integral form (5.5) in the macro-scale dynamics (5.13). To numerically approximate this integral, we use a quasi-random sequence of $N_s = P^3$ points p_ν, with $\nu = 1, \ldots, N_s$ and $P = \lceil 2R/\Delta x \rceil + 1$. Here, these off-grid quasi-random points are similar and play the same role as the off-grid barycentres $b_{S_{(\cdot)}}$ used in previous chapters, however, their position within the sensing region $\mathbf{B}(0, R)$ are different. Hence, considering the minimal cubic region of macro-nodes $\{y^x_{l,m,n}\}_{l,m,n=1,\ldots,P}$ that covers the entire sensing region $\mathbf{B}(0, R)$, we note that these quasi-random points p_ν are positioned such that each macro-scale cube, defined by

$$S_\nu := [y^x_{l,m,n}, y^x_{l+1,m,n}] \times [y^x_{l,m,n}, y^x_{l,m+1,n}] \times [y^x_{l,m,n}, y^x_{l,m,n+1}]$$

contains exactly one of these quasi-random points, *i.e.*, $p_\nu \in S_\nu$ whose position is generated uniformly. Then, this enables us to approximate the adhesion integral (5.5) as the sum of the integrals of the step functions associated with each cube S_ν. Furthermore, we observe that these cubes S_ν are on-grid cubes, and so we know the

values of the cancer cell density, both ECM components and the fibre orientations at the corner points, which we can utilise to approximate the values at the quasi-random points p_ν by using bi-linear shape functions. Thus, each value, at point p_ν, is approximated by a convex combination of the on-grid neighbouring points, *i.e.,* by the corners of S_ν, with uniquely determined weights β_ν^r, $r = 1, \ldots, 8$. Hence, here we approximate the value of each step function by the value at its associated random point p_ν.

Since we seek to use convolutions, we need to construct N_s different matrices (one for each cube S_ν), using the uniquely determined weights β_ν^r. Considering an arbitrary cube S_ν, its associated matrix $\widetilde{\mathcal{K}}_{\mathcal{A}}^\nu$ entries are defined as

$$(\widetilde{\mathcal{K}}_{\mathcal{A}}^\nu)_{w_1,w_2,w_3} := \begin{cases} \beta_\nu^1 & \text{if } (w_1,w_2,w_3) = (P-l, P-m, P-n), \\ \beta_\nu^2 & \text{if } (w_1,w_2,w_3) = (P-l-1, P-m, P-n), \\ \beta_\nu^3 & \text{if } (w_1,w_2,w_3) = (P-l, P-m-1, P-n), \\ \beta_\nu^4 & \text{if } (w_1,w_2,w_3) = (P-l, P-m, P-n-1), \\ \beta_\nu^5 & \text{if } (w_1,w_2,w_3) = (P-l-1, P-m-1, P-n), \\ \beta_\nu^6 & \text{if } (w_1,w_2,w_3) = (P-l-1, P-m, P-n-1), \\ \beta_\nu^7 & \text{if } (w_1,w_2,w_3) = (P-l, P-m-1, P-n-1), \\ \beta_\nu^8 & \text{if } (w_1,w_2,w_3) = (P-l-1, P-m-1, P-n-1), \\ 0 & \text{otherwise.} \end{cases}$$

This allow us to approximate the adhesion integral $\mathcal{A}_c$, defined in (5.5), at any time-step n as

$$\mathcal{A}_c^n = \sum_{\nu \in P_{in}} (\mathcal{A}_c)_\nu^n$$

where the set P_{in} contains the indices whose associated quasi-random point is located

within the sensing region $\mathbf{B}(0,R)$ and $(\mathcal{A}_c)^n_\nu$ is given by

$$(\mathcal{A}_c)^n_\nu = \frac{K(p_\nu)}{R}\Bigg[\left(n_\nu \widetilde{\mathcal{K}}^\nu_{\mathcal{A}}\right) * \left(\left(\mathbf{S}_{cc}c^n + \mathbf{S}_{cl}l^n\right) \circ \left(1-\rho(\mathbf{u}^n)\right)^+\right) + \left(\widehat{n}_\nu \widetilde{\mathcal{K}}^\nu_{\mathcal{A}}\right) * \left(\mathbf{S}_{cF}F^n\right) \circ \left(1-\rho(\mathbf{u}^n)\right)^+\Bigg)\Bigg].$$

5.4 Parameter Values

In Table 5.1, we summarise the parameter values that will be used in the presented numerical simulations in the upcoming section.

Table 5.1: *Parameter set used for the numerical simulations in this chapter. If we could not find any references for some of our parameters then we "Estimated" them (i.e., we chose an arbitrary value for the simulations).*

Variable	Value	Description	Reference
D_c	1.25×10^{-4}	Diffusion coeff. for the cancer cell population	[202]
D_G	0.25	Grey matter regulator coefficient	Estimated
r	0.1	Degree of randomised turning	[202]
a	0	Model switching parameter	Estimated
$\mathcal{K}_{FA}$	100	Cell's sensitivity to the directional information	[202]
$\mathbf{S}_{max}$	0.5	Cell-cell adhesion coeff.	[245]
$\mathbf{S}_{min}$	0.01	Minimum level of cell-cell adhesion	[265]
$\mathbf{S}_{cl}$	0.01	Cell-non-fibre adhesion coeff.	[245]
$\mathbf{S}_{cF}$	0.3	Cell-fibre adhesion coeff.	[70]
μ	0.25	Proliferation coeff. for cancer cell population	[70]
β_F	1.5	Degradation coeff. of the fibre ECM	[264]
β_l	3.0	Degradation coeff. of the non-fibre ECM	[264]
β	0.8	Optimal tissue environment controller	[279]

Continued on next page

Table 5.1 – continued from previous page

Variable	Value	Description	Reference
R	0.15	Sensing radius	[245]
f_{max}	0.636	Maximum of micro-fibre density at any point	[245]
Δx	0.03125	Macro-scale spatial step-size	[279]
ϵ	0.0625	Size of a boundary micro-domain $\epsilon Y(x)$	[279]
δ	0.03125	Size of a fibre micro-domain $\delta Y(x)$	[245]
N_s	450	Number of random points used for the approximation of the adhesion integral $\mathcal{A}_c$	Estimated
Δt	10^{-3}	Macro-scale temporal step size	Estimated
$\Delta \tau$	10^{-4}	MDE micro-scale temporal step size	Estimated

5.5 Computational Results: Numerical Simulations in 3D

For the numerical simulations presented in this paper, we consider the tissue cube $Y = [0,4] \times [0,4] \times [0,4]$ with the following initial condition for the cancer cells

$$c(x,0) = \frac{1}{2} \exp\left(\frac{- \parallel x \parallel_2^2}{0.02}\right) \cdot \chi_{\mathbf{B}((2,2,2),0.25)},$$

and for the non-fibre ECM phase, the initial condition $l(x,0)$ is acquired by appropriately scaling the T1 weighted image via a normalising constant. Current DTI scans do not provide suitable resolution to determine the underlying micro-fibre distributions, and so here, we describe the initial micro-fibre distribution within a micro-domain $\delta Y(x)$ as follows. When the macro-scale point x that corresponds to the micro-domain $\delta Y(x)$ is located in the grey matter, then within $\delta Y(x)$ we randomly draw straight lines until the ratio between the points that belong and

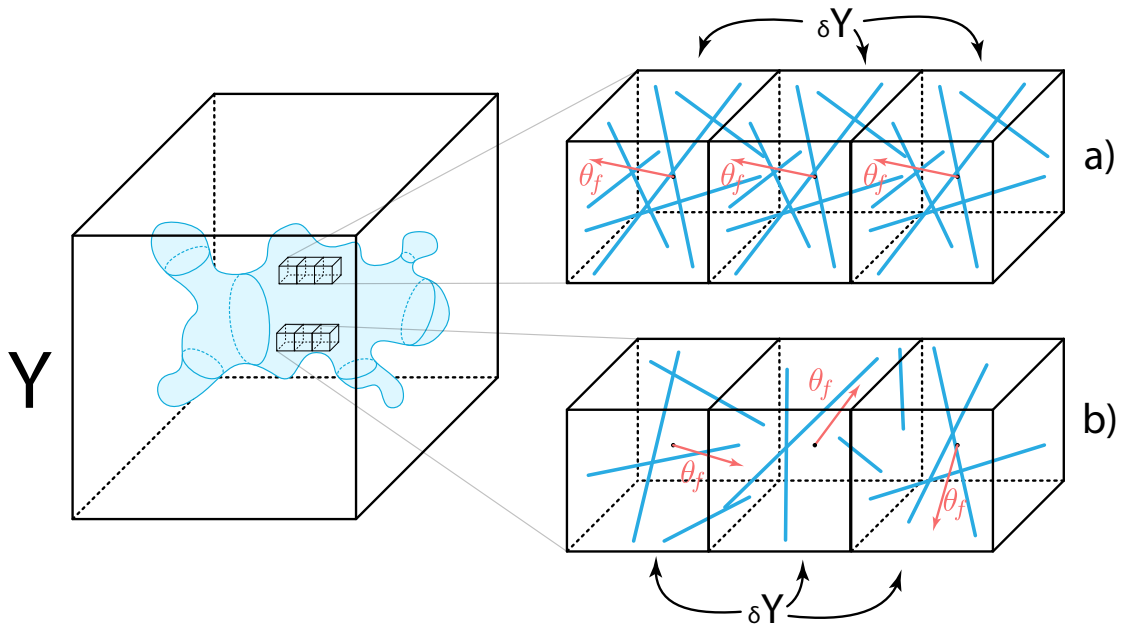

Figure 5.3: *Schematics of the initial condition of the micro-fibres (blue lines) within a micro-domain $\delta Y(x)$ of orientation $\theta_f(x,t)$ located in the a) white matter and in the b) grey matter.*

the points that do not belong to the collection of lines is about 35% : 65%. On the other hand, when the point x is located within the white matter, we use a set of predefined lines with the same point ratio (35% : 65%), ultimately achieving a random orientation within the grey matter and an aligned orientation within the white matter [225]. Finally, the grey matter's fibre density is assumed to be $1/D_G$ times smaller than the density in the white matter [225]. A schematics of this initial condition for the micro-fibres can be seen in Figure 5.3. Hence, we also incorporate the information about the white and grey matter tracks provided by the T1 weighted image into our micro-scale fibre distribution.

5.5.1 Numerical Simulations in 3D

Here, we present the 3D numerical solutions of the multi-scale model described above, for the parameter values listed in Table 5.1 in Appendix 5.4 (any alteration

from these values will be stated accordingly). To display the advanced tumours at time $50\Delta t$, we show four panels for each simulation results. In the first three panels we show the three classical cross-section planes *i.e.,* the coronal plane (the head of the subject is viewed from behind), the axial plane (the head of the subject is viewed from above) and the sagittal plane (the head of the subject is viewed from the left). In the last panel of each simulation we show the 3D image of the brain with the embedded tumour alongside the 3D tumour in isolation.

The three Figures shown below investigate tumour evolution when the initial tumour starts in different regions of the brain. To present the simulations, we divide each result into four panels: coronal, axial, sagittal and 3D view. Within each coronal, axial and sagittal views, we show the tumour embedded within the brain on the left, the cancer cell density on the top-right and the ECM density on the bottom-right. In the 3D view (the most right panel in each results) we show the cross-section of the whole brain with the tumour on the bottom-left corner and on the top-right corner we show the isolated tumour.

In Figure 5.4 we present three distinct cases obtained by varying different parameters that appear in the tumour diffusion tensor $\mathbb{D}_T(x)$ defined in (5.3). In Figure 5.4 a) we assume that the tensor $\mathbb{D}_T(x)$ depends on the white-grey matter and for that purpose we set $r = 1$ in (5.3) and $a = 0$ in (5.4); this results in isotropic tumour diffusion. In Figure 5.4 b) we use the DTI data (i.e., there is no a-priory assumption about the preferential direction for cell movement in white matter) and thus we set $a = 1$ in (5.4) (with $r = 0.1$, as in Table 5.1); this results in an anisotropic diffusion that does not depend explicitly on the white-grey matter. In Figure 5.4 c) we use both DTI data and the white-grey matter dependency (i.e., $r = 0.1$ and $a = 0$), with the baseline parameters from Table 5.1. Here, it is worth mentioning that even though we do not use the T1 weighted image to obtain functions $w(x)$ and $g(x)$ that appear in D_{WG} (as $D_{WG} = 1$ in Figure 5.4 b), since $a = 1$) we still use the T1 weighted image to initialise the micro-scale non-fibre initial density as well as the

initial micro-scale fibre distributions as described above.

In all these simulations shown in Figure 5.4, we place the small initial tumour in the middle-right part of the brain, and we show the results of the three cases at time $50\Delta t$ where we observe significant tumour morphology changes across the three cases. By comparing Figure 5.4 a) to b) and Figure 5.4 b) to c), we see that when we include the white-grey matter dependency function D_{WG} within the tumour diffusion tensor it leads to a more advanced tumour. On the other hand, comparing Figure 5.4 a) to c) shows that including the DTI data, which creates an anisotropic tumour diffusion term, leads to a slight reduction in tumour spread. Furthermore, in all three cases, we can notice that the advancing tumour tends to mostly follow the white matter tracks and usually avoids the invasion of tissues located in the grey matter. This invasion resulted in the degradation (and rearrangement) of the ECM that we can see in the bottom-right of each panel (coronal, axial and sagittal) which enabled the tumour to further expand into the surrounding tissues.

In Figure 5.5 we keep the same three cases as in Figure 5.4, *i.e.,* Figure 5.5 a) only white-grey matter dependency, Figure 5.5 b) only DTI data and Figure 5.5 c) both. However, here we place the initial tumour in the front-right part of the brain and show the results of tumour invasion at the final time $50\Delta t$. Due to the initial position of the tumour, we can see a tumour that is growing away from the skull towards the centre of the brain as well as it is mainly following the white matter. This creates a highly heterogeneous elongated tumour with many branching outgrowths. On the other hand, in Figure 5.5 we only see slight differences between the three cases. This contradicts the results from Figure 5.4 and suggests that both the DTI data and white-grey matter dependency may not always be decisive factor in tumour morphology.

Similarly to Figure 5.4 and Figure 5.5, in Figure 5.6 we keep the same three cases (Figure 5.6 a) only white-grey matter dependency, Figure 5.6 b) only DTI data and Figure 5.6 c) both) while we place the initial tumour mass in the middle

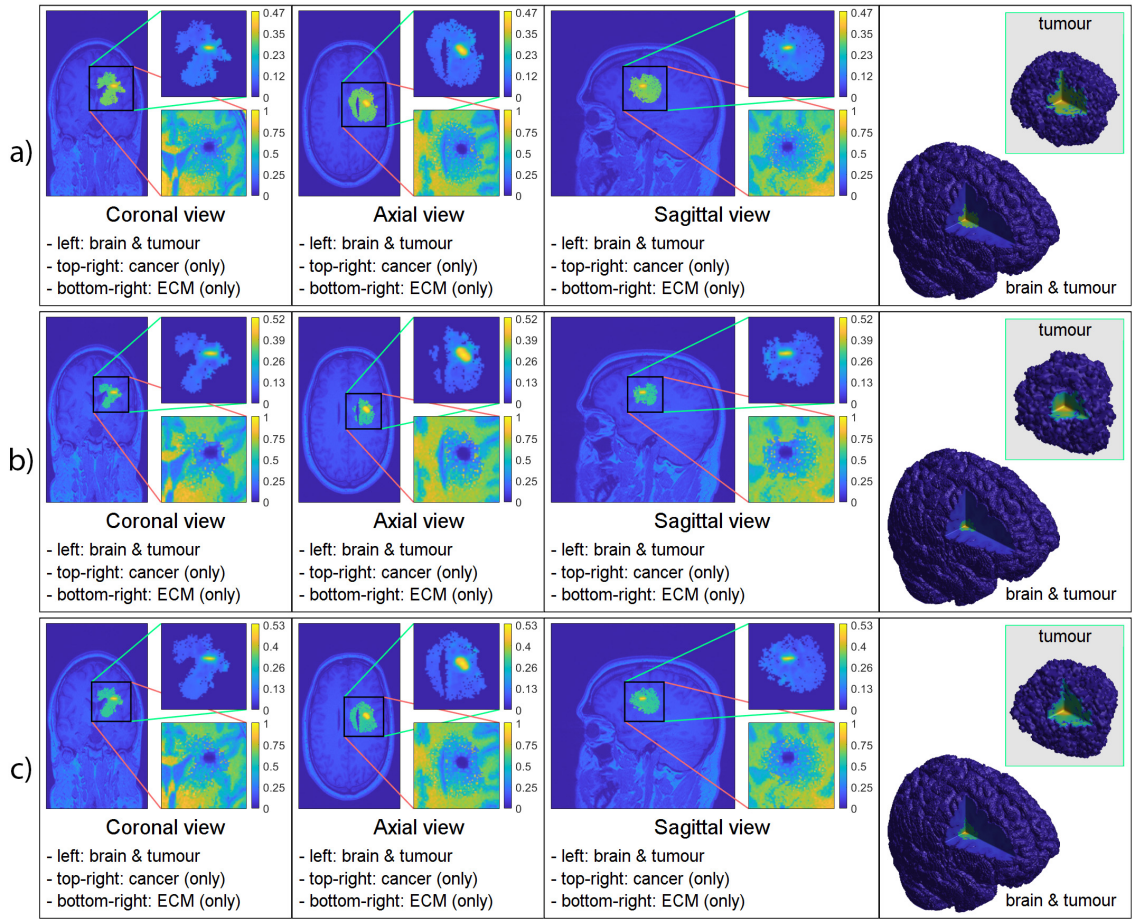

Figure 5.4: *3D computer simulation results a) with only white-grey matter dependency ($r = 1$), b) with only DTI data used ($D_G = 1$) c) with both white-grey matter dependency and DTI data incorporated. To present the simulations, we divide each result into four panels: coronal, axial, sagittal and 3D view. Within each coronal, axial and sagittal views, we show the tumour embedded within the brain on the left, the cancer cell density on the top-right and the ECM density on the bottom-right. In the 3D view (the most right panel in each results) we show the cross-section of the whole brain with the tumour on the bottom-left corner and on the top-right corner we show the isolated tumour.*

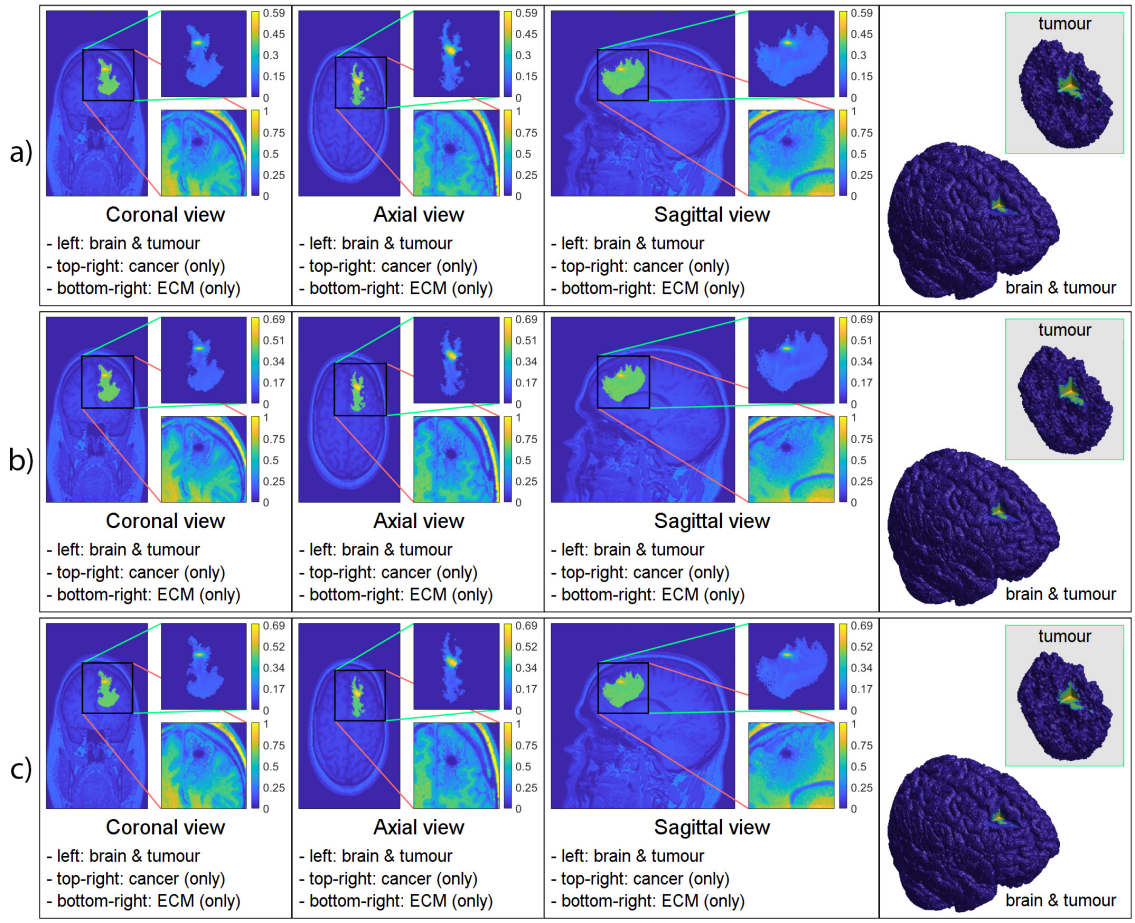

Figure 5.5: *3D computer simulation results a) with only white-grey matter dependency ($r = 1$), b) with only DTI data used ($D_G = 1$) c) with both white-grey matter dependency and DTI data incorporated. To represent the simulation results, we use the same format as in Figure 5.4.*

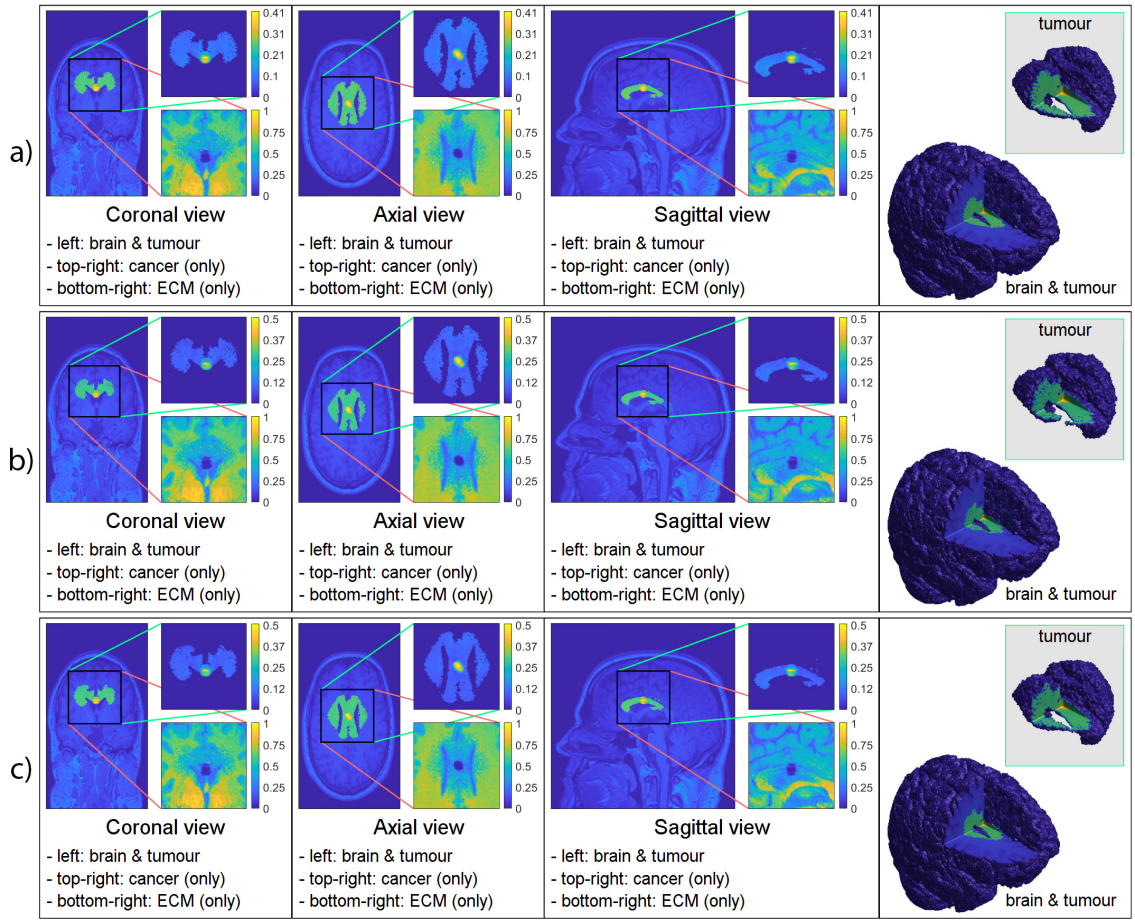

Figure 5.6: *3D computer simulation results a) with only white-grey matter dependency ($r = 1$), b) with only DTI data used ($D_G = 1$) c) with both white-grey matter dependency and DTI data incorporated. To represent the simulation results, we use the same format as in Figure 5.4.*

of the brain and present the results at time $50\Delta t$. As a consequence of the initial location, we see a "butterfly" shaped tumour that branched to both the left and right side of the brain with some asymmetry. Also, as in Figure 5.5 we can see that all three cases are quite similar, and so the additional information provided by both the DTI data and white-grey matter dependency seems to be unnecessary for this initial condition. However, we must note that the initial conditions (fibre and non-fibre ECM) still uses the information provided by the T1 weighted image, and so here, we only investigate the effect of changing the diffusion tensor.

As we mentioned, we see significant differences between the three cases only in Figure 5.4. This either indicates that the anisotropic diffusion tensor provides valuable information only in certain cases or that the initial micro-fibre density differs from the one that produced the DTI scan (*i.e.,* the actual distribution). Since we use an artificial micro-fibre structure that does not depend on the DTI scan which also aid the movement of the cancer cell population via the adhesion integral $\mathcal{A}_c(\cdot,\cdot,\cdot,\cdot)$ defined in (5.5), it is possible that in this specific case the micro-scale fibre distribution introduced a significantly different travelling direction than the DTI data, resulting in discrepancies between the simulations. However, due to the resolution of current DTI scans, it is not possible to construct a unique fibre distribution within a micro-domain $\delta Y(x)$. Hence, to genuinely capture the underlying brain structures that we can use within a mathematical model, our results suggest that DTI scans with their present resolution may not be sufficient, and one might need to look into either obtaining better resolution DTI scans or combine this with the strength of different technologies such as magnetic resonance elastography. Nonetheless, this exceeds the current scope of this work and requires further investigation.

5.6 Discussion

In this chapter, we have further extended the 2D multi-scale moving-boundary framework previously introduced in Chapters 2 and 3 as well as in [279, 245], by developing it to 3D and applying it to the study of glioma invasion within the brain. Since experiments are limited within the brain, we focused on incorporating DTI and T1 weighted scans into our framework to provide insights into the structure of the brain, the tumour, and the surrounding tissue.

The original framework developed in [279, 245] modelled a generic tumour in a 2D setting, and so to model gliomas within a 3D brain, we extended this modelling approach by considering the structural information provided by both DTI and T1

weighted scans. We used both DTI and T1 weighted scans to construct the tumour diffusion tensor $\mathbb{D}_T(x)$ defined in (5.3), which resulted in a fully anisotropic diffusion term. While the T1 weighted image can give different diffusion rates based on whether the cancer cells are located in the white or grey matter, the DTI data is used to incorporate the underlying brain structure and to give higher diffusion rates along specific directions based on how the measured water molecules behaved within the brain. The T1 weighted image, which provided the white-grey matter densities, were also used in our initial conditions for both ECM phases. Hence, the initial density of the non-fibre ECM phase was taken as a normalised version of the T1 weighted image, and the initial condition of the micro-fibre distribution and magnitude were also considered to be dependent on the white-grey matter structure. Furthermore, as the available DTI scans lack the adequate resolution required to construct more appropriate micro-fibre distributions, in this chapter we considered a simple case where we set the fibre distributions to be either random or oriented based on whether they are positioned in the grey or white matter, respectively.

Therefore, compared to other previous 3D models such as those in [75, 116, 202], here we can explicitly capture the underlying tissue structure changes via the micro-fibre rearrangement process and trace how the boundary of the tumour changes over time. Moreover, the cancer cells' movement is not only influenced by the T1 weighted and DTI scans (through an anisotropic diffusion term) but also biased by crucial non-local adhesions such as cell-cell and cell-fibre ECM adhesion the latter of which is naturally interconnected to the tissue structural changes. Hence, our model presents a novel approach that can incorporate several vital processes for tumour development and have not been available in other previous models. This allowed us to produce exciting and valuable results/outcomes which provide further insights into the overall tumour development process.

To that end, we used this new 3D model to explore the effects of the anisotropic diffusion term for the cancer cell population. Our numerical simulations in Figure 5.4

showed that including an anisotropic diffusion term may lead to significant changes in the overall tumour morphology. However, it seems that these changes depend on the position of the tumour inside the brain, as Figures 5.5 and 5.6 do not exhibit changes consistent to the ones observed between the three sub-panels of Figure 5.4. This may be the result of the underlying brain structure and its microscopic fibre representation, which seems to take a leading role in influencing cancer-invasion patterns through the underlying cell-adhesion process (see Eq. (5.5)), overshadowing this way the diffusion process. More precisely, the simplified fibre representation might not be sufficient for Figure 5.4, where the initial tumour was positioned in the right-middle part of the brain. However, this fibre representation might be enough for Figure 5.5 (with tumour positioned in the front-right of the brain) and for Figure 5.6 (with tumour positioned in the middle of the brain), where we did not see significant morphological differences between the three sub-panels considered in each of these figures.

To conclude this chapter, we mention that further investigation is needed to determine whether these changes in tumour invasion patterns are caused by the lack of directional information on the fibre micro-scale level or an anisotropic diffusive cell motility is necessary to better represent the invasion process. A feasible approach would also be to use a new imaging technology called magnetic resonance elastography, but this is beyond the scope of this thesis. Nonetheless, these results are not only interesting and important from a mathematical modelling point of view but from a medical one as well. For instance, we showed how different model parameters change the evolution of the tumour boundary, this being a vital and desired information in any clinical/medical decision-making process. Such a model with tuned parameters (to specific patients) could help, for example, decide the optimal amount of tissue to resect so that the chance of survival is maximised.

Finally, as our simulations are able to reproduce known tumour patterns of growth seen clinically, future experiments will be refined by MRI data collected

prospectively from glioma patients and also incorporate the effects of their radiotherapy and chemotherapy treatments.

Chapter 6

Conclusion and Discussion

The main purpose of this thesis is to further develop and propose new extensions of a multi-scale moving boundary modelling framework initially introduced in [245, 279] with the aim to investigate tumour invasion patterns and how tumour aggregations respond to different TME compositions, tissue scenarios and cell properties. For this, we used both fully continuous and hybrid mathematical modelling frameworks that enabled a comprehensive insight into the underlying relationships and how these affect the overall tumour development process. On the one hand, the fully continuous multi-scale moving boundary framework was based on the one initially introduced in [279] to account for the proteolytic processes occurring at the leading edge of the tumour and later expanded in [245] to account for the fibrous structure of the ECM. Hence, here, both the tumour macro-scale (tissue-scale) and the two micro-scale (cell-scale) dynamics were modelled using continuous approaches (for example, coupled system of partial differential equations) which are ultimately interlinked though a double feedback loop. On the other hand, in the hybrid multi-scale framework, we used an agent-based lattice free method to model the cancer cells population that was based on the model derived in [27, 128, 135] as well as used the continuous multi-scale two-phase ECM which was developed in [245] (that we also used for our continuous framework). Thus, here, we have a feedback loop

between the micro-fibre structure and the cancer cell population as well as several communication channels between the discrete and continuous frameworks.

In Chapter 2, we built upon the multi-scale moving boundary framework [245, 279] to investigate how the directional movement of the M2-like macrophages affect the overall tumour progression and morphology. To that end, we considered a tumour macro-scale dynamics that consist of two cell populations (cancer cell and M2 TAMs) and two ECM phases (fibre and non-fibre) and which is interlinked to both fibre and MDE micro-scales. To model the macro-scale dynamics of the M2 TAMs population, we considered their motility to be given by a mixture of random and directed movements, where the latter was described by the combination of self, ECM fibre and cancer cell (non-local) adhesions. The rest of the M2 TAMs dynamics consisted of a fibre and cancer dependent proliferation term, a linear death term and an influx term which aimed to model a constant M2 TAMs supply on the outer tumour boundary. Furthermore, we considered a few effects of these M2-like macrophages exerted on the rest of the dynamics such as cancer-macrophage adhesion and the regularisation of cancer cell proliferation. Due to their ability to secrete MDEs, both cell populations naturally contribute to the proteolytic processes taking place at the leading edge of the tumour, and so this *MDE top-down* link is modelled via an emerging source of the MDEs on the micro-scale. Consequently, this results in a degradation of the peritumoral ECM within a cell-scale neighbourhood of the tumour that ultimately leads to an expanded tumour macro-scale domain which we refer to as the *MDE bottom-up* link. On the other hand, the second feedback loop arise from the redistribution of the ECM fibres micro-constituents initiated by the movement of both cell populations. Hence, here, the spatial fluxes (generated by the cancer cell and M2 TAMs populations) trigger a rearrangement of the ECM fibres micro-constituents which is called the *fibre top-down* link. As a consequence, the rearranged micro-fibre distribution changes the macro-scale density and orientation of the fibres ECM which is referred to as the *fibre bottom-up* link.

Therefore, in this chapter, we addressed the lack of knowledge about the effects of the directional movement of the M2 TAMs on the overall tumour development, and so we used this extended model to investigate some hypotheses on tumour spread connected to the M2 TAMs population. First, we explored whether the various M2 TAMs adhesions can significantly enhance tumour spread individually, and concluded that although none of them are capable of increasing it alone, they do introduce a few changes in tumour morphology. However, we showed that utilising all these different adhesion terms within the M2 TAMs equation at once, leads to an increase in tumour spread. Then, we shifted our attention to the fibre ECM phase and studied how its density and the M2 TAMs-fibre ECM adhesion strength affect the tumour development. Here, the numerical simulations suggested that reduced fibre density decreased tumour spread and that the M2-fibre adhesion played only a minor role and did not influence tumour progression notably. Finally, we also investigated the effects of the underlying ECM fibre structure by considering unstructured, random oriented fibres which revealed a dramatically reduced tumour spread but it did not propose any new properties.

Building on Chapter 2, in Chapter 3, we extended our multi-scale modelling framework and also incorporated the pro-inflammatory M1-like macrophages as well as the nutrients, to study multiple properties of a possible re-polarisation based treatment strategy. Hence, the macro-scale dynamics included three cell populations (cancer, M1 and M2 TAMs), two ECM phases (fibres and non-fibres ECM) and the nutrients, most of which influence both micro-scale dynamics (fibre and MDE micro-scales). On the one hand, to model both macrophage phenotypes, we considered their movement to be described by a combination of random motility given by a diffusion term with non-constant coefficient, and directed movement described by a non-local adhesion term. The rest of the TAMs dynamics consisted of a cancer, fibre and nutrient dependent proliferation term, a nutrient dependent death term, a nutrient dependent polarisation and a re-polarisation terms. Moreover, we also

considered the nutrients to influence the cancer cell population via the proliferation as well as death terms, latter of which is affected by the M1-like macrophages as well. Since M1-like macrophages also secrete various MDEs, they also contribute to the degradation of the two ECM phases on both macro- and micro-scales, which we incorporated into this model accordingly.

Using this extended model allowed us to study whether a re-polarisation (M1↔M2) based treatment strategy is temporal, spatial and/or nutrient dependent. First, we studied the spatial dependency of the re-polarisation for which we considered the re-polarisation domain $\Omega_p(t, R_p)$ with various radii R_p. Here, our numerical results suggested that although tumour spread does not seem to be highly affected by the re-polarisation, tumour spread can be dramatically reduced especially in the case of $R_p = 0$, *i.e.,* when we re-polarise M2 TAMs within the whole tumour domain. Then, we also explored the temporal aspect of the re-polarisation by varying the start time parameter t_p, where our numerical simulations suggested that although the most optimal time to start the re-polarisation is as early as possible, even for later times the tumour mass can be significantly reduced. Finally, we also explored whether these results were impacted by the nutrients, and so we presented the same numerical results in the absence of nutrients. Here, we noticed changes within the distribution of the three cell population, suggesting that the varying level of nutrients within the different tumour regions induce more heterogeneous cell populations, that might be of great importance for other models that use the information of how cell populations are distributed within a region (for example tumour region). However, the fundamental results of the spatial and temporal dependencies achieved previously (in the presence of nutrients) remained unchanged. All these results were consistent for three tumour types (that differ in MDE secretion rate) and within three ECM environment (controlled by the parameter β).

Furthermore, in Chapter 4, we developed a hybrid multi-scale model that enabled us to investigate the emerging shape of tumour aggregations and their migration

types. On the one hand, we described the cancer cell population with a discrete *Multi-Cell Lattice-Free* model that allowed us to assign different properties for each individual cells such as position, radius and age as well as track the forces that act on each cell, for instance, repulsion, cell-cell adhesion and cell-ECM adhesion forces. Hence, the migration of these cells is biased by both the neighbouring cells and ECM fibre structure that ultimately drives the overall movement of tumour aggregations and in some cases leads to non-stationary tumours. On the other hand, we used the same continuous *multi-scale two-phase* ECM that we used in Chapters 2 and 3 which enabled us to model various ECM structures and how these affect tumour aggregations. As before, since cancer cells are capable of degrading and rearranging the ECM, we modelled the interaction with the same feedback loop that we described and used in Chapters 2 and 3. Hence, the movement of cancer cells naturally trigger a rearrangement of micro-fibres (fibres top-down link) which in turn, changes the macro-scale ECM structure (fibres bottom-up link) and consequently influence cell migration. To provide sufficient communication between the two frameworks, we ensured that connections between the two are established at stages where one require any information from the other.

Using numerical simulations of this hybrid model, we tested a number of scenarios which provided further insights into the different processes and cell properties that can significantly impact the overall tumour shape. Specifically, we have demonstrated that our hybrid model is capable of creating both stationary tumours in the case of random ECM micro-fibre distribution and moving tumour aggregations when we consider an aligned fibre distributions which are consistent with experimental results. Another interesting property of our model is the ability to produce fibre aggregations at the tumour boundary with a capsule-like orientation that can ultimately limit tumour invasion which are also consistent with biological experiments. We suggested that using some existing technology for visualising collagen could potentially aid treatment decisions since this could be used to predict the speed of

tumour in a patient specific environment. Hence, for example, such visualisations can aid in deciding how much of the surrounding tissue should be removed which could be further combined with mathematical simulations to improve predictions. Finally, we identified some key parameters and their combinations that can impact tumour shape such as sensing radius and ratio of fibres and non-fibre ECM as well as we carried out an extensive set of simulations with different parameter values to show different tumour behaviours.

Finally in Chapter 5, we extended our 2D continuous multi-scale moving boundary framework to a 3D one and applied to a specific type of brain tumour, *i.e.,* glioblastomas to study the role of brain micro-fibres. Hence, the model consisted of a macro-scale dynamics, including a cancer cell population and a two-phase ECM as well as the two micro-scale dynamics (fibres and MDE). While we kept the underlying principles of the two-micro scale dynamics, on the macro-scale, we incorporated 3D T1 weighted and DTI scans to describe the movement of the cancer cells (via an anisotropic diffusion term) in addition to the adhesion-mediated one.

Using numerical simulations of this extended 3D model, we explored how the anisotropic diffusion term affects the cancer cell motility and the way brain micro-fibres influence the 3D invading tumour. Our numerical results showed that including an anisotropic diffusion term for specific micro-fibre distributions may lead to significant changes in the overall tumour morphology, while in other cases this effect may be smaller or neglectable and may be dependent on the initial position of the tumour. We argued that this may be caused by the underlying brain structure and its microscopic fibre representation, which seems to take the primary role in affecting cancer-invasion patterns through the underlying cell-adhesion process that ultimately overshadows the diffusion process. Hence, our simplified initial condition for the ECM fibres might not be adequate in some cases.

6.1 Possible Extensions and Future Works

Looking forward, there are several ways to extend this multi-scale modelling framework. First, as it was already mentioned, macrophages are also present in the tumour stroma because they arrive to the sites through the vasculature as an immune response. Since in Chapters 2 and 3 we only studied the effects of macrophages located within the tumour, this could be extended by also incorporating peritumoral macrophages. This aspect may be of great importance, for example, because of the accumulated non-aligned ECM at the tumour boundary which is known to limit tumour progression (that we also demonstrated in Chapter 4). Since macrophages are capable of secreting MDEs, and so breaking down ECM components, they may degrade these accumulated "collagen fibre walls" and as a consequence they free the cancer cells, leading to faster tumour spread. However, a higher M1 TAMs density in the peritumoral regions could also result in a reduced tumour spread and even fully stop tumour progression since the M1 phenotype has the ability to kill cancer cells, and so they could potentially kill them before they invade further into the surrounding tissues.

Another type of cell that can change the micro-scale structure of the ECM is called the fibroblasts. While these cells can highly remodel their surrounding ECM, they can also secrete significant amounts of collagen along their long axis, thereby creating a more aligned ECM [38, 211, 235] which are vital in many biological processes such as wound healing. However, these properties can also be critical in tumour development since they can penetrate those collagen fibre walls (mentioned in the previous point) and set the cancer cells free, resulting in faster tumour spread. Besides, by producing aligned collagen fibre bundles, fibroblasts could also create an aligned pathway of fibres toward vasculatures which would increase the probability of metastasis as well [187]. Hence, incorporating these type of cells could also be of great significance and could lead to further insights and knowledge about tumour development.

In addition to these two previous points, one could further extend this modelling framework by introducing a network of blood vessels along with vascular endothelial growth factors to model the evolution of the tumour vasculature and its effect on the tumour development. This network could also be used as the supply for the macrophage population (since at the moment the supply of macrophages is modelled via a constant influx on the boundary), which would create further heterogeneity within the various cell populations.

Finally, different therapy options could be incorporated into this multi-scale framework. On the one hand, drug and chemotherapy deliveries could be added that naturally follow the non-fibre ECM phase and investigate the effects of these treatments on the proteolytic processes and how they affect the spread and mass of the tumour. On the other hand, one can add a macrophage-mediated drug delivery treatment option since macrophages are abundant in the TME and are known to penetrate the tumour effectively. Hence, macrophages could be used to deliver various drugs into each layer of the tumour, potentially leading to further advancements in the fight against cancer.

Appendix A

Appendix

A.1 Definition of the Outer Boundary

Let $x \in \partial\Omega(t)$. Then, $x \in \partial\Omega_o(t)$ if and only if there exists $\phi_x : [0, \infty) \to \mathbb{R}^d$ such that the following four properties hold true simultaneously:

$$
\begin{aligned}
&1) \quad \phi_x(0) = x, \\
&2) \quad \phi_x(s) \neq x, \quad \forall s \in (0, \infty), \\
&3) \quad Im\phi_x \setminus \{x\} \subset \complement\Omega(t), \\
&4) \quad \lim_{s \to \infty} dist(\phi(s), \partial\Omega(t)) = \infty,
\end{aligned}
$$

where $\forall\, s \in (0, \infty)$, we have $dist(\phi(s), \partial\Omega(t)) := \inf_{z \in \partial\Omega(t)} \parallel \phi(s) - z \parallel_2$ and represents the Euclidean distance from $\phi(s)$ to $\partial\Omega(t)$.

A.2 Standard Mollifier (The Compact Support Function)

The smooth compact support function $\psi : \mathbb{R}^d \to \mathbb{R}_+$ used for the construction of standard mollifiers used in this paper is defined as usual by

$$\psi(x) := \begin{cases} \dfrac{\exp\left(\dfrac{1}{\| x \|_2^2 - 1}\right)}{\int\limits_{\mathbf{B}(0,1)} \exp\left(\dfrac{1}{\| z \|_2^2 - 1}\right) dz} & \text{if } x \in \mathbf{B}(0,1), \\ 0 & \text{if } x \notin \mathbf{B}(0,1). \end{cases} \tag{A.1}$$

A.3 Hadamard Product and Frobenius Inner Products

The Hadamard product of two square matrices A and B of the same dimensions, is the matrix entry-wise product that is defined by

$$(A \circ B)_{i,j} = A_{i,j} \cdot B_{i,j},$$

which we use to derive our numerical scheme.

The Frobenius norm of an n by m matrix A, is the square root of the sum of all elements of A i.e.

$$\sum(A) := \mathrm{Tr}\big(A^H A\big),$$

where A^H is the conjugate transpose.

A.4 Definition of the Re-Polarisation Domain: $\Omega_p(t, R_p)$

Here, we define the re-polarisation domain used in (3.12), which allows us to investigate the spatial dependency of a re-polarisation strategy. Hence, let us define this new domain by

$$\Omega_p(t, R_p) := \{x \in \Omega(t), x_B \in \partial\Omega_o(t) | \parallel x - x_B \parallel_2 \geq R_p\} \subset \Omega(t),$$

where $R_p > 0$ is a constant and $\partial\Omega_o(t)$ is the outer tumour boundary, defined in Appendix A.1. Again, this new domain is illustrated in Fig. 3.2.

A.5 Vectors Induced by the ZSWENO Scheme

Here, for completeness we define the vectors used for the discrete convolutions in (3.45) and (3.49). Let us start with the vectors that were induced by the ENO fluxes (3.43) and (3.44). Hence, first the vectors $\widetilde{\mathcal{K}}^{\pm}_{k,+}$ with $k = 0, \ldots, 2$ are given by

$$\widetilde{\mathcal{K}}^{+}_{0,+} = \begin{bmatrix} 0 \\ 0 \\ 0 \\ \frac{11}{6} \\ -\frac{7}{6} \\ \frac{1}{3} \\ 0 \end{bmatrix}, \ \widetilde{\mathcal{K}}^{+}_{1,+} = \begin{bmatrix} 0 \\ 0 \\ \frac{1}{3} \\ \frac{5}{6} \\ -\frac{1}{6} \\ 0 \\ 0 \end{bmatrix}, \ \widetilde{\mathcal{K}}^{+}_{2,+} = \begin{bmatrix} 0 \\ -\frac{1}{6} \\ \frac{5}{6} \\ \frac{1}{3} \\ 0 \\ 0 \\ 0 \end{bmatrix}, \ \widetilde{\mathcal{K}}^{-}_{0,+} = \begin{bmatrix} \frac{1}{3} \\ -\frac{7}{6} \\ \frac{11}{6} \\ 0 \\ 0 \\ 0 \\ 0 \end{bmatrix}, \ \widetilde{\mathcal{K}}^{-}_{1,+} = \begin{bmatrix} 0 \\ -\frac{1}{6} \\ \frac{5}{6} \\ \frac{1}{3} \\ 0 \\ 0 \\ 0 \end{bmatrix}, \ \widetilde{\mathcal{K}}^{-}_{2,+} = \begin{bmatrix} 0 \\ 0 \\ \frac{1}{3} \\ \frac{5}{6} \\ -\frac{1}{6} \\ 0 \\ 0 \end{bmatrix}.$$

Similarly, the vectors $\widetilde{\mathcal{K}}^{\pm}_{k,-}$ with $k = 0, \ldots, 2$ are given by

$$\widetilde{\mathcal{K}}^{+}_{0,-}=\begin{bmatrix} 0 \\ 0 \\ 0 \\ 0 \\ \frac{11}{6} \\ -\frac{7}{6} \\ \frac{1}{3} \end{bmatrix},\ \widetilde{\mathcal{K}}^{+}_{1,-}=\begin{bmatrix} 0 \\ 0 \\ 0 \\ \frac{1}{3} \\ \frac{5}{6} \\ -\frac{1}{6} \\ 0 \end{bmatrix},\ \widetilde{\mathcal{K}}^{+}_{2,-}=\begin{bmatrix} 0 \\ 0 \\ -\frac{1}{6} \\ \frac{5}{6} \\ \frac{1}{3} \\ 0 \\ 0 \end{bmatrix},\ \widetilde{\mathcal{K}}^{-}_{0,-}=\begin{bmatrix} 0 \\ \frac{1}{3} \\ -\frac{7}{6} \\ \frac{11}{6} \\ 0 \\ 0 \\ 0 \end{bmatrix},\ \widetilde{\mathcal{K}}^{-}_{1,-}=\begin{bmatrix} 0 \\ 0 \\ -\frac{1}{6} \\ \frac{5}{6} \\ \frac{1}{3} \\ 0 \\ 0 \end{bmatrix},\ \widetilde{\mathcal{K}}^{-}_{2,-}=\begin{bmatrix} 0 \\ 0 \\ 0 \\ \frac{1}{3} \\ \frac{5}{6} \\ -\frac{1}{6} \\ 0 \end{bmatrix}.$$

Then, the other vectors induced by the smoothness indicators (3.47) and (3.48) are $\overline{\mathcal{K}}^{\pm}_{k,+}$ and $\overline{\mathcal{K}}^{\pm}_{k,-}$ which were used in the convolutional form (3.49). First, $\overline{\mathcal{K}}^{\pm}_{k,+}$ are defined by

$$\overline{\mathcal{K}}^{+}_{0,+}=\begin{bmatrix} 0 \\ 0 \\ 0 \\ 3 \\ -4 \\ 1 \\ 0 \end{bmatrix},\ \overline{\mathcal{K}}^{+}_{1,+}=\begin{bmatrix} 0 \\ 0 \\ -1 \\ 0 \\ 1 \\ 0 \\ 0 \end{bmatrix},\ \overline{\mathcal{K}}^{+}_{2,+}=\begin{bmatrix} 0 \\ 1 \\ -4 \\ 3 \\ 0 \\ 0 \\ 0 \end{bmatrix},\ \overline{\mathcal{K}}^{-}_{0,+}=\begin{bmatrix} 1 \\ -4 \\ 3 \\ 0 \\ 0 \\ 0 \\ 0 \end{bmatrix},\ \overline{\mathcal{K}}^{-}_{1,+}=\begin{bmatrix} 0 \\ 1 \\ 0 \\ -1 \\ 0 \\ 0 \\ 0 \end{bmatrix},\ \overline{\mathcal{K}}^{-}_{2,+}=\begin{bmatrix} 0 \\ 0 \\ 3 \\ -4 \\ 1 \\ 0 \\ 0 \end{bmatrix},$$

and similarly $\overline{\mathcal{K}}^{\pm}_{k,-}$ are given by

$$\overline{\mathcal{K}}^{+}_{0,-}=\begin{bmatrix}0\\0\\0\\0\\3\\-4\\1\end{bmatrix},\ \overline{\mathcal{K}}^{+}_{1,-}=\begin{bmatrix}0\\0\\0\\-1\\0\\1\\0\end{bmatrix},\ \overline{\mathcal{K}}^{+}_{2,-}=\begin{bmatrix}0\\0\\1\\-4\\3\\0\\0\end{bmatrix},\ \overline{\mathcal{K}}^{-}_{0,-}=\begin{bmatrix}0\\1\\-4\\3\\0\\0\\0\end{bmatrix},\ \overline{\mathcal{K}}^{-}_{1,-}=\begin{bmatrix}0\\0\\1\\0\\-1\\0\\0\end{bmatrix},\ \overline{\mathcal{K}}^{-}_{2,-}=\begin{bmatrix}0\\0\\0\\3\\-4\\1\\0\end{bmatrix},$$

Bibliography

[1] Ixi dataset – information extraction from images URL `http://brain-development.org/ixi-dataset`

[2] Adlerz, K.M., Aranda-Espinoza, H., Hayenga, H.N.: Substrate elasticity regulates the behavior of human monocyte-derived macrophages. European Biophysics Journal **45**(4), 301–309 (2016). DOI 10.1007/s00249-015-1096-8

[3] Afik, R., Zigmond, E., Vugman, M., Klepfish, M., Shimshoni, E., Pasmanik-Chor, M., Shenoy, A., Bassat, E., Halpern, Z., Geiger, T., Sagi, I., Varol, C.: Tumor macrophages are pivotal constructors of tumor collagenous matrix. The Journal of Experimental Medicine **213**(11), 2315–2331 (2016). DOI 10.1084/jem.20151193

[4] Alberts, B., Johnson, A., Lewis, J., Raff, M., Roberts, K., Walter, P.: Molecular biology of the cell. Garland Science, New York (2002)

[5] Alfonso, J.C.L., Köhn-Luque, A., Stylianopoulos, T., Feuerhake, F., Deutsch, A., Hatzikirou, H.: Why one-size-fits-all vaso-modulatory interventions fail to control glioma invasion: in silico insights **6**(1). DOI 10.1038/srep37283

[6] Allena, R., Scianna, M., Preziosi, L.: A cellular potts model of single cell migration in presence of durotaxis. Mathematical Biosciences **275**, 57–70 (2016). DOI 10.1016/j.mbs.2016.02.011

[7] Alsisi, A., Eftimie, R., Trucu, D.: Non-local multiscale approaches for tumour-oncolytic viruses interactions **1**(3), 249–273. DOI 10.5206/mase/10773

[8] Alzahrani, T., Eftimie, R., Trucu, D.: Multiscale modelling of cancer response to oncolytic viral therapy **310**, 76–95. DOI 10.1016/j.mbs.2018.12.018

[9] Andasari, V., Gerisch, A., Lolas, G., South, A., Chaplain, M.A.J.: Mathematical modeling of cancer cell invasion of tissue: biological insight from mathematical analysis and computational simulation. J. Math. Biol. **63**(1), 141–171 (2011)

[10] Andasari, V., Roper, R.T., Swat, M.H., Chaplain, M.A.J.: Integrating intracellular dynamics using CompuCell3d and bionetsolver: Applications to multiscale modelling of cancer cell growth and invasion **7**(3), e33726. DOI 10.1371/journal.pone.0033726

[11] Anderson, A., Chaplain, M., Newman, E., Steele, R., Thompson, A.: Mathematical modelling of tumour invasion and metastasis. J. Theorl. Medic. **2**, 129–154 (2000)

[12] Anderson, A.R., Hassanein, M., Branch, K.M., Lu, J., Lobdell, N.A., Maier, J., Basanta, D., Weidow, B., Narasanna, A., Arteaga, C.L., Reynolds, A.B., Quaranta, V., Estrada, L., Weaver, A.M.: Microenvironmental independence associated with tumor progression. Cancer Res **69**(22), 8797–8806 (2009). DOI 10.1158/0008-5472.CAN-09-0437

[13] Anderson, A.R.A.: A hybrid mathematical model of solid tumour invasion: the importance of cell adhesion **22**(2), 163–186. DOI 10.1093/imammb/dqi005

[14] Anderson, A.R.A.: A hybrid mathematical model of solid tumour invasion: the importance of cell adhesion. Math. Medic. Biol. **22**, 163–186 (2005)

[15] Araujo, R.: A history of the study of solid tumour growth: the contribution of mathematical modelling **66**(5), 1039–1091. DOI 10.1016/j.bulm.2003.11.002

[16] Aristorena, M., Gallardo-Vara, E., Vicen, M., de Las Casas-Engel, M., Ojeda-Fernandez, L., Nieto, C., Blanco, F.J., Valbuena-Diez, A.C., Botella, L.M., Nachtigal, P., Corbi, A.L., Colmenares, M., Bernabeu, C.: Mmp-12, secreted by pro-inflammatory macrophages, targets endoglin in human macrophages and endothelial cells. International Journal of Molecular Sciences **20**(12) (2019). DOI 10.3390/ijms20123107

[17] Armstrong, N.J., Painter, K.J., Sherratt, J.A.: A continuum approach to modelling cell-cell adhesion. J. Theor. Biol. **243**(1), 98–113 (2006)

[18] Basser, P., Mattiello, J., Lebihan, D.: Estimation of the effective self-diffusion tensor from the NMR spin echo **103**(3), 247–254. DOI 10.1006/jmrb.1994.1037

[19] Basser, P., Mattiello, J., LeBihan, D.: MR diffusion tensor spectroscopy and imaging **66**(1), 259–267. DOI 10.1016/s0006-3495(94)80775-1

[20] Basser, P., Mattiello, J., LeBihan, D.: Diagonal and off-diagonal components of the self-diffusion tensor:their relation to and estimation from the nmr spin-echo signal. 11th Society of Magnetic Resonance in Medicine Meeting 1222 (1992)

[21] Basser, P., Mattiello, J., Robert, T., LeBihan, D.: Diffusion tensor echo-planar imaging of human brain. In: Proceedings of the SMRM 584 (1993)

[22] Baumgartner, W., Drenckhahn, D.: Transmembrane cooperative linkage in cellular adhesion. Eur J Cell Biol. **81**(3), 161–8 (2002). DOI 10.1078/0171-9335-00233

[23] Beatty, G., Chiorean, E., Fishman, M., Saboury, B., Teitelbaum, U., Sun, W., Huhn, R., Song, W., Li, D., Sharp, L., *et al.*: CD40 agonists alter tumor

stroma and show efficacy against pancreatic carcinoma in mice and humans **331**, 1612–1616

[24] Becker, M., Müller, C., De Bastiani, M., Klamt, F.: The prognostic impact of tumor-associated macrophages and intra-tumoral apoptosis in non-small cell lung cancer. Histology and histopathology **29** (2013). DOI 10.14670/HH-29.21

[25] Behrens, J., Mareel, M.M., Roy, F.M.V., Birchmeier, W.: Dissecting tumor cell invasion: Epithelial cells acquire invasive properties after the loss of uvomorulin-mediated cell-cell adhesion. J Cell Biol **108**(6), 2435–2447 (1989). DOI 10.1083/jcb.108.6.2435

[26] Berrier, A.L., Yamada, K.M.: Cell-matrix adhesion. J Cell Physiol **213**(3), 565–573 (2007). DOI 10.1002/jcp.21237

[27] Berrouet, C., Dorilas, N., Rejniak, K.A., Tuncer, N.: Comparison of drug inhibitory effects (IC_{50}) in monolayer and spheroid cultures. Bulletin of Mathematical Biology **82**(6), 68 (2020). DOI 10.1007/s11538-020-00746-7

[28] Bhagavathula, N., Hanosh, A.W., Nerusu, K.C., Appelman, H., Chakrabarty, S., Varani, J.: Regulation of e-cadherin and β-catenin by Ca^{2+} in colon carcinoma is dependent on calcium-sensing receptor expression and function. Int J Cancer **121**, 1455–1462 (2007). DOI 10.1002/ijc.22858

[29] Bitsouni, V., Chaplain, M., Eftimie, R.: Mathematical modelling of cancer invasion: The multiple roles of tgf-β pathway on tumour proliferation and cell adhesion. Math Mod Meth Appl S **27**(10), 1929–1962 (2017)

[30] Blankenstein, T., Qin, Z.H., Uberla, K., Müller, W., Rosen, H., Volk, H.D., Diamantstein, T.: Tumor suppression after tumor cell-targeted tumor necrosis factor alpha gene transfer. The Journal of Experimental Medicine **173**(5), 1047–1052 (1991). DOI 10.1084/jem.173.5.1047

[31] Bray, D.: Cell movements. Garland Pub

[32] den Breems, N.Y., Eftimie, R.: The re-polarisation of m2 and m1 macrophages and its role on cancer outcomes **390**, 23–39. DOI 10.1016/j.jtbi.2015.10.034

[33] Brodbelt, A., Greenberg, D., Winters, T., Williams, M., Vernon, S., Collins, V.P.: Glioblastoma in england: 2007–2011 **51**(4), 533–542. DOI 10.1016/j.ejca.2014.12.014

[34] Brown, L.F., Berse, B., Jackman, R.W., Tognazzi, K., Manseau, E.J., Dvorak, H.F., Senger, D.R.: Increased expression of vascular permeability factor (vascular endothelial growth factor) and its receptors in kidney and bladder carcinomas. **143**, 1255–1262

[35] Burri, S.H., Gondi, V., Brown, P.D., Mehta, M.P.: The evolving role of tumor treating fields in managing glioblastoma **41**(2), 191–196. DOI 10.1097/coc.0000000000000395

[36] Byrne, H., Chaplain, M.: Growth of nonnecrotic tumors in the presence and absence of inhibitors **130**(2), 151–181. DOI 10.1016/0025-5564(94)00117-3

[37] Byrne, H., Chaplain, M., Pettet, G., Mcelwain, D.L.S.: A mathematical model of trophoblast invasion. Appl. Math. Lett. **14**(8), 1005–1010 (2001)

[38] Canty, E.G., Lu, Y., Meadows, R.S., Shaw, M.K., Holmes, D.F., Kadler, K.E.: Coalignment of plasma membrane channels and protrusions (fibripositors) specifies the parallelism of tendon **165**(4), 553–563. DOI 10.1083/jcb.200312071

[39] Caro, G.D., Cortese, N., Castino, G.F., Grizzi, F., Gavazzi, F., Ridolfi, C., Capretti, G., Mineri, R., Todoric, J., Zerbi, A., Allavena, P., Mantovani, A., Marchesi, F.: Dual prognostic significance of tumour-associated macrophages

in human pancreatic adenocarcinoma treated or untreated with chemotherapy. Gut **65**(10), 1710–1720 (2015). DOI 10.1136/gutjnl-2015-309193

[40] Cassetta, L., Fragkogianni, S., Sims, A.H., Swierczak, A., Forrester, L.M., Zhang, H., Soong, D.Y., Cotechini, T., Anur, P., Lin, E.Y., Fidanza, A., Lopez-Yrigoyen, M., Millar, M.R., Urman, A., Ai, Z., Spellman, P.T., Hwang, E.S., Dixon, J.M., Wiechmann, L., Coussens, L.M., Smith, H.O., Pollard, J.W.: Human tumor-associated macrophage and monocyte transcriptional landscapes reveal cancer-specific reprogramming, biomarkers, and therapeutic targets. Cancer Cell **35**(4), 588–602.e10 (2019). DOI 10.1016/j.ccell.2019.02.009

[41] Cassetta, L., Noy, R., Swierczak, A., Sugano, G., Smith, H., Wiechmann, L., Pollard, J.W.: Isolation of mouse and human tumor-associated macrophages. In: Advances in Experimental Medicine and Biology, pp. 211–229. Springer International Publishing (2016). DOI 10.1007/978-3-319-26666-4_12

[42] Cavallaro, U., Christofori, G.: Cell adhesion in tumor invasion and metastasis: loss of the glue is not enough. Biochimica et Biophysica Acta (BBA) - Reviews on Cancer **1552**(1), 39–45 (2001). DOI 10.1016/S0304-419X(01)00038-5

[43] Chamseddine, I.M., Frieboes, H.B., Kokkolaras, M.: Design optimization of tumor vasculature-bound nanoparticles **8**(1). DOI 10.1038/s41598-018-35675-y

[44] Chamseddine, I.M., Rejniak, K.A.: Hybrid modeling frameworks of tumor development and treatment. Wiley Interdisciplinary Reviews: Systems Biology and Medicine **12**, e1461 (2020). DOI 10.1002/wsbm.1461

[45] Chaplain, M., Lachowicz, M., Szymanska, Z., Wrzosek, D.: Mathematical modelling of cancer invasion: The importance of cell-cell adhesion and cell-matrix adhesion. Math. Model. Meth. Appl. Sci. **21**(4), 719–743 (2011)

[46] Chaplain, M., Lolas, G.: Mathematical modelling of cancer cell invasion of tissue: the role of the urokinase plasminogen activation system. Math. Model. Meth. Appl. Sci. **15**(11), 1685–1734 (2005)

[47] Chaplain, M.A.J., Lolas, G.: Mathematical modelling of cancer invasion of tissue: Dynamic heterogeneity. Netw Heterog Media **1**(3), 399–439 (2006). DOI 10.3934/nhm.2006.1.399

[48] Chauviere, A., Hillen, T., Preziosi, L.: Modeling cell movement in anisotropic and heterogeneous network tissues. Netw Heterog Media **2**(2), 333–357 (2007)

[49] Chen, Q., Zhang, X.H.F., Massagué, J.: Macrophage binding to receptor VCAM-1 transmits survival signals in breast cancer cells that invade the lungs. Cancer Cell **20**(4), 538–549 (2011). DOI 10.1016/j.ccr.2011.08.025

[50] Cheung, Y., Azeloglu, E., Shiovitz, D., Costa, K., Seliktar, D., Sia, S.: Microscale control of stiffness in a cell-adhesive substrate using microfluidics-based lithography. Angewandte Chemie International Edition **48**(39), 7188–7192 (2009). DOI 10.1002/anie.200900807

[51] Chicoine, M.R., Silbergeld, D.L.: Assessment of brain tumor cell motility in vivo and in vitro **82**(4), 615–622. DOI 10.3171/jns.1995.82.4.0615

[52] Chitu, V., Yeung, Y., Yu, W., Nandi, S., Stanley, E.: Measurement of macrophage growth and differentiation. Current Protocols in Immunology **Chapter 14** (2011)

[53] Clatz, O., Sermesant, M., Bondiau, P.Y., Delingette, H., Warfield, S., Malandain, G., Ayache, N.: Realistic simulation of the 3-d growth of brain tumors in MR images coupling diffusion with biomechanical deformation **24**(10), 1334–1346. DOI 10.1109/tmi.2005.857217

[54] Cobzas, D., Mosayebi, P., Murtha, A., Jagersand, M.: Tumor invasion margin on the riemannian space of brain fibers. In: Medical Image Computing and Computer-Assisted Intervention – MICCAI 2009, pp. 531–539. Springer Berlin Heidelberg. DOI 10.1007/978-3-642-04271-3_65

[55] Condeelis, J., Pollard, J.W.: Macrophages: Obligate partners for tumor cell migration, invasion, and metastasis. Cell **124**(2), 263–266 (2006). DOI 10.1016/j.cell.2006.01.007

[56] Conklin, M., Eickhoff, J., Riching, K., Pehlke, C., Eliceiri, K., Provenzano, P., Friedl, A., Keely, P.: Aligned collagen is a prognostic signature for survival in human breast carcinoma **178**(3), 1221–1232

[57] Cooper, G.: The cell : a molecular approach. ASM Press Sinauer Associates, Washington, D.C. Sunderland, Mass (2000)

[58] Cox, T.R., Erler, J.T.: Remodeling and homeostasis of the extracellular matrix: implications for fibrotic diseases and cancer. Disease Models and Mechanisms **4**(2), 165–178 (2011)

[59] Cristini, V., Lowengrub, J.: Multiscale Modeling of Cancer: An Integrated Experimental and Mathematical Modeling Approach. Cambridge (2010)

[60] Cui, K., Ardell, C.L., Podolnikova, N.P., Yakubenko, V.P.: Distinct migratory properties of m1, m2, and resident macrophages are regulated by αdβ2 and αmβ2 integrin-mediated adhesion. Frontiers in Immunology **9** (2018). DOI 10.3389/fimmu.2018.02650

[61] Cui, Y.L., Li, H.K., Zhou, H.Y., Zhang, T., Li, Q.: Correlations of tumor-associated macrophage subtypes with liver metastases of colorectal cancer. Asian Pacific Journal of Cancer Prevention **14**(2), 1003–1007 (2013). DOI 10.7314/apjcp.2013.14.2.1003

[62] Cunningham, J.J., Brown, J.S., Gatenby, R.A., Staňková, K.: Optimal control to develop therapeutic strategies for metastatic castrate resistant prostate cancer **459**, 67–78. DOI 10.1016/j.jtbi.2018.09.022

[63] Dallon, J.C., Sherratt, J.A., Maini, P.K.: Mathematical modelling of extracellular matrix dynamics using discrete cells: Fiber orientation and tissue regeneration. Journal of Theoretical Biology **199**(4), 449–471 (1999). DOI 10.1006/jtbi.1999.0971

[64] Damelin, S.B., Miller, W.J.: The Mathematics of Signal Processing. Cambridge University Press (2011). DOI 10.1017/cbo9781139003896

[65] Davis, M.: Glioblastoma: Overview of disease and treatment **20**(5), S2–S8. DOI 10.1188/16.cjon.s1.2-8

[66] Davis, M.J., Tsang, T.M., Qiu, Y., Dayrit, J.K., Freij, J.B., Huffnagle, G.B., Olszewski, M.A.: Macrophage m1/m2 polarization dynamically adapts to changes in cytokine microenvironments in cryptococcus neoformans infection. mBio **4**(3) (2013). DOI 10.1128/mbio.00264-13

[67] Deakin, N.E., Chaplain, M.A.J.: Mathematical modelling of cancer cell invasion: the role of membrane-bound matrix metalloproteinases. Front. Oncol. **3**(70), 1–9 (2013)

[68] Deisboeck, T.S., Wang, Z., Macklin, P., Cristini, V.: Multiscale cancer modeling. Annu. Rev. Biomed. Eng. **13**, 127–155 (2011)

[69] DOLLERY, C., LIBBY, P.: Atherosclerosis and proteinase activation. Cardiovascular Research **69**(3), 625–635 (2006). DOI 10.1016/j.cardiores.2005.11.003

[70] Domschke, P., Trucu, D., Gerisch, A., Chaplain, M.: Mathematical modelling of cancer invasion: Implications of cell adhesion variability for tumour infiltrative growth patterns. J. Theor. Biol. **361**, 41–60 (2014)

[71] Domschke, P., Trucu, D., Gerisch, A., Chaplain, M.A.J.: Structured models of cell migration incorporating membrane reactions. submitted to Journal of Mathematical Biology (2016)

[72] Dutta, P., Sarkissyan, M., Paico, K., Wu, Y., Vadgama, J.V.: Mcp-1 is overexpressed in triple-negative breast cancers and drives cancer invasiveness and metastasis. Breast Cancer Research and Treatment **170**(3), 477–486 (2018). DOI 10.1007/s10549-018-4760-8

[73] Ebata, H., Moriyama, K., Kuboki, T., Kidoaki, S.: General cellular durotaxis induced with cell-scale heterogeneity of matrix-elasticity. Biomaterials **230**, 119647 (2020). DOI 10.1016/j.biomaterials.2019.119647

[74] Eftimie, R., Bramson, J.L., Earn, D.J.: Modeling anti-tumor th1 and th2 immunity in the rejection of melanoma **265**(3), 467–480. DOI 10.1016/j.jtbi.2010.04.030

[75] Engwer, C., Hillen, T., Knappitsch, M., Surulescu, C.: Glioma follow white matter tracts: a multiscale DTI-based model **71**(3), 551–582. DOI 10.1007/s00285-014-0822-7

[76] van Es, B., Koren, B., de Blank, H.J.: Finite-difference schemes for anisotropic diffusion **272**, 526–549. DOI 10.1016/j.jcp.2014.04.046

[77] Filipe, E., Chitty, J., Cox, T.: Charting the unexplored extracellular matrix in cancer. International Journal of Experimental Pathology **99**, 58–76 (2018)

[78] Flier, J.S., Underhill, L.H., Dvorak, H.F.: Tumors: Wounds that do not heal **315**(26), 1650–1659. DOI 10.1056/nejm198612253152606

[79] Friedl, P.: Rethinking research into metastasis **8**, e53511

[80] Friedl, P., Alexander, S.: Cancer invasion and the microenvironment: Plasticity and reciprocity. Cell **147**, 992–1009 (2011)

[81] Gerisch, A., Chaplain, M.: Mathematical modelling of cancer cell invasion of tissue: Local and non-local models and the effect of adhesion. J. Theor. Biol. **250**, 684–704 (2008)

[82] Gerisch, A., Chaplain, M.A.J.: Robust numerical methods for taxis–diffusion–reaction systems: Applications to biomedical problems. Math Comput Model **43**(1–2), 49–75 (2006). DOI 10.1016/j.mcm.2004.05.016

[83] Ghaffarizadeh, A., Heiland, R., Friedman, S.H., Mumenthaler, S.M., Macklin, P.: PhysiCell: An open source physics-based cell simulator for 3-d multicellular systems **14**(2), e1005991. DOI 10.1371/journal.pcbi.1005991

[84] Ghosh, S., Salot, S., Sengupta, S., Navalkar, A., Ghosh, D., Jacob, R., Das, S., Kumar, R., Jha, N.N., Sahay, S., Mehra, S., Mohite, G.M., Ghosh, S.K., Kombrabail, M., Krishnamoorthy, G., Chaudhari, P., Maji, S.K.: p53 amyloid formation leading to its loss of function: implications in cancer pathogenesis. Cell Death & Differentiation **24**(10), 1784–1798 (2017). DOI 10.1038/cdd.2017.105

[85] Günter, S., Yu, Q., Krüger, J., Lackner, K.: Modelling of heat transport in magnetised plasmas using non-aligned coordinates **209**(1), 354–370. DOI 10.1016/j.jcp.2005.03.021

[86] Gobin, E., Bagwell, K., Wagner, J., Mysona, D., Sandirasegarane, S., Smith, N., Bai, S., Sharma, A., Schleifer, R., She, J.X.: A pan-cancer perspective of matrix metalloproteases (MMP) gene expression profile and their diagnostic/prognostic potential. BMC Cancer **19**(1) (2019). DOI 10.1186/s12885-019-5768-0

[87] Golub, G.H., van Loan, C.F.: Matrix Computations, fourth edn. JHU Press (2013). URL `http://www.cs.cornell.edu/cv/GVL4/golubandvanloan.htm`

[88] Gondi, C.S., Lakka, S.S., Yanamandra, N., Olivero, W.C., Dinh, D.H., Gujrati, M., Tung, C.H., Weissleder, R., Rao, J.S.: Adenovirus-mediated expression of antisense urokinase plasminogen activator receptor and antisense cathepsin b inhibits tumor growth, invasion, and angiogenesis in gliomas **64**(12), 4069–4077. DOI 10.1158/0008-5472.can-04-1243

[89] Goswami, K.K., Ghosh, T., Ghosh, S., Sarkar, M., Bose, A., Baral, R.: Tumor promoting role of anti-tumor macrophages in tumor microenvironment. Cellular Immunology **316**, 1–10 (2017). DOI 10.1016/j.cellimm.2017.04.005

[90] Gras, S.L.: Chapter 6 - surface- and solution-based assembly of amyloid fibrils for biomedical and nanotechnology applications. In: R.J. Koopmans (ed.) Engineering Aspects of Self-Organizing Materials, *Advances in Chemical Engineering*, vol. 35, pp. 161 – 209. Academic Press (2009). DOI 10.1016/S0065-2377(08)00206-8

[91] Gras, S.L., Tickler, A.K., Squires, A.M., Devlin, G.L., Horton, M.A., Dobson, C.M., MacPhee, C.E.: Functionalised amyloid fibrils for roles in cell adhesion. Biomaterials **29**(11), 1553 – 1562 (2008). DOI 10.1016/j.biomaterials.2007.11.028

[92] Green, C., Liu, T., Montel, V., Hsiao, G., Lester, R., Subramaniam, S., Gonias, S., Klemke, R.: Chemoattractant signalling between tumour cells and macrophages regulates cancer cell migration, metastasis and neovascularisation. PLoS ONE **4**(8), e6713 (2009)

[93] Gregorio, I., Braghetta, P., Bonaldo, P., Cescon, M.: Collagen VI in healthy and diseased nervous system **11**(6), dmm032946. DOI 10.1242/dmm.032946

[94] Gu, Z., Liu, F., Tonkova, E.A., Lee, S.Y., Tschumperlin, D.J., Brenner, M.B., Ginsberg, M.H.: Soft matrix is a natural stimulator for cellular in-

vasiveness. Molecular Biology of the Cell **25**(4), 457–469 (2014). DOI 10.1091/mbc.e13-05-0260

[95] Hagmann, P., Jonasson, L., Maeder, P., Thiran, J.P., Wedeen, V.J., Meuli, R.: Understanding diffusion MR imaging techniques: From scalar diffusion-weighted imaging to diffusion tensor imaging and beyond **26**(suppl_1), S205–S223. DOI 10.1148/rg.26si065510

[96] Hallam, S.L., Candido, J., Coutinho, R., Maniati, E., Thompson, R.G., van Rooijen, N., Hagemann, T., Gribben, J.G.: Manipulating tumor associated macrophages (TAM) in a mouse model of b-cell non-hodgkin lymphoma (NHL). Blood **118**(21), 1657–1657 (2011). DOI 10.1182/blood.v118.21.1657.1657

[97] Han, W., Chen, S., Yuan, W., Fan, Q., Tian, J., Wang, X., Chen, L., Zhang, X., Wei, W., Liu, R., Qu, J., Jiao, Y., Austin, R., Liu, L.: Oriented collagen fibres direct tumour cell intravasation **113**(40), 11208–11213

[98] Hanahan, D., Weinberg, R.A.: The hallmarks of cancer. Cell **100**, 57–70 (2000)

[99] Hanahan, D., Weinberg, R.A.: Hallmarks of cancer: The next generation. Cell **144**(5), 646–674 (2011). DOI 10.1016/j.cell.2011.02.013

[100] Hatoum, A., Mohammed, R., Zakieh, O.: The unique invasiveness of glioblastoma and possible drug targets on extracellular matrix **Volume 11**, 1843–1855. DOI 10.2147/cmar.s186142

[101] Hayenga, H.N., Adlerz, K., Aranda-Espinoza, H.: Substrate stiffness regulates the behavior of human monocyte-derived macrophages. Biophysical Journal **108**(2), 306a–307a (2015). DOI 10.1016/j.bpj.2014.11.1667

[102] He, X., Lee, B., Jiang, Y.: Cell-ECM interactions in tumor invasion. In: Advances in Experimental Medicine and Biology, pp. 73–91. Springer International Publishing. DOI 10.1007/978-3-319-42023-3_4

[103] Hedbrant, A., Wijkander, J., Seidal, T., Delbro, D., Erlandsson, A.: Macrophages of m1 phenotype have properties that influence lung cancer cell progression. Tumor Biology **36**(11), 8715–8725 (2015). DOI 10.1007/s13277-015-3630-9

[104] Henke, E., Nandigama, R., Ergün, S.: Extracellular matrix in the tumor microenvironment and its impact on cancer therapy **6**. DOI 10.3389/fmolb.2019.00160

[105] Heusinkveld, M., van der Burg, S.H.: Identification and manipulation of tumor associated macrophages in human cancers **9**(1). DOI 10.1186/1479-5876-9-216

[106] Hillen, T.: M5 mesoscopic and macroscopic models for mesenchymal motion. Journal of Mathematical Biology **53**(4), 585–616 (2006). DOI 10.1007/s00285-006-0017-y

[107] Hillen, T., Hinow, P., Wang, Z.: Mathematical analysis of a kinetic model for cell movement in network tissues. Discrete and continuous dynamical systems **14**(3), 1055–1080 (2010)

[108] Hillen, T., Painter, K.J., Swan, A.C., Murtha, A.D.: Moments of von mises and fisher distributions and applications **14**(3), 673–694. DOI 10.3934/mbe.2017038

[109] Hofer, A.M., Curci, S., Doble, M.A., Brown, E.M., Soybel, D.I.: Intercellular communication mediated by the extracellular calcium-sensing receptor. Nat Cell Biol **2**(7), 392–398 (2000). DOI 10.1038/35017020

[110] Hong, C.R., Bogle, G., Wang, J., Patel, K., Pruijn, F.B., Wilson, W.R., Hicks, K.O.: Bystander effects of hypoxia-activated prodrugs: Agent-based modeling using three dimensional cell cultures **9**. DOI 10.3389/fphar.2018.01013

[111] Horn, R.A., Johnson, C.R.: Topics in matrix analysis. Cambridge University Press (1991). DOI 10.1017/cbo9780511840371

[112] Hsu, T.H., Kao, Y.L., Lin, W.L., Xiao, J.L., Kuo, P.L., Wu, C.W., Liao, W.Y., Lee, C.H.: The migration speed of cancer cells influenced by macrophages and myofibroblasts co-cultured in a microfluidic chip. Integr. Biol. **4**(2), 177–182 (2012). DOI 10.1039/c2ib00112h

[113] Hu, H.L., Bai, H.S., Pan, H.X.: Correlation between TAMs and proliferation and invasion of type i endometrial carcinoma. Asian Pacific Journal of Tropical Medicine **8**(8), 643–650 (2015). DOI 10.1016/j.apjtm.2015.07.009

[114] Huang, W.C., Sala-Newby, G.B., Susana, A., Johnson, J.L., Newby, A.C.: Classical macrophage activation up-regulates several matrix metalloproteinases through mitogen activated protein kinases and nuclear factor-kb. PLOS ONE **7**(8), 1–14 (2012). DOI 10.1371/journal.pone.0042507

[115] Huda, S., Weigelin, B., Wolf, K., Tretiakov, K.V., Polev, K., Wilk, G., Iwasa, M., Emami, F.S., Narojczyk, J.W., Banaszak, M., Soh, S., Pilans, D., Vahid, A., Makurath, M., Friedl, P., Borisy, G.G., Kandere-Grzybowska, K., Grzybowski, B.A.: Lévy-like movement patterns of metastatic cancer cells revealed in microfabricated systems and implicated in vivo. Nature communications **9**(1), 4539–4539 (2018). DOI 10.1038/s41467-018-06563-w

[116] Hunt, A., Surulescu, C.: A multiscale modeling approach to glioma invasion with therapy **45**(1-2), 221–240. DOI 10.1007/s10013-016-0223-x

[117] Hynes, R.O., Naba, A.: Overview of the matrisome–an inventory of extracellular matrix constituents and functions. Cold Spring Harbor Perspectives in Biology **4**(a004903), 16 (2012). DOI 10.1101/cshperspect.a004903

[118] Isenberg, B.C., DiMilla, P.A., Walker, M., Kim, S., Wong, J.Y.: Vascular smooth muscle cell durotaxis depends on substrate stiffness gradient strength. Biophysical Journal **97**(5), 1313–1322 (2009). DOI 10.1016/j.bpj.2009.06.021

[119] Jacob, R.S., George, E., Singh, P.K., Salot, S., Anoop, A., Jha, N.N., Sen, S., Maji, S.K.: Cell adhesion on amyloid fibrils lacking integrin recognition motif. Journal of Biological Chemistry **291**(10), 5278–5298 (2016). DOI 10.1074/jbc.m115.678177

[120] Jagiella, N., Müller, B., Müller, M., Vignon-Clementel, I.E., Drasdo, D.: Inferring growth control mechanisms in growing multi-cellular spheroids of NSCLC cells from spatial-temporal image data **12**(2), e1004412. DOI 10.1371/journal.pcbi.1004412

[121] Jbabdi, S., Mandonnet, E., Duffau, H., Capelle, L., Swanson, K.R., Pélégrini-Issac, M., Guillevin, R., Benali, H.: Simulation of anisotropic growth of low-grade gliomas using diffusion tensor imaging **54**(3), 616–624. DOI 10.1002/mrm.20625

[122] Jenkins, S.J., Ruckerl, D., Cook, P.C., Jones, L.H., Finkelman, F.D., van Rooijen, N., MacDonald, A.S., Allen, J.E.: Local macrophage proliferation, rather than recruitment from the blood, is a signature of TH2 inflammation. Science **332**(6035), 1284–1288 (2011). DOI 10.1126/science.1204351

[123] Jiang, G.S., Shu, C.W.: Efficient implementation of weighted ENO schemes. Journal of Computational Physics **126**(1), 202–228 (1996). DOI 10.1006/jcph.1996.0130

[124] Jiang, Y., Pjesivac-Grbovic, J., Cantrell, C., Freyer, J.P.: A multiscale model for avascular tumor growth **89**(6), 3884–3894. DOI 10.1529/biophysj.105.060640

[125] Kalinin, V.: Cell – extracellular matrix interaction in glioma growth. in silico model **17**(4). DOI 10.1515/jib-2020-0027

[126] Kansal, A., Torquato, S., Chiocca, E., Deisboeck, T.: Emergence of a subpopulation in a computational model of tumor growth **207**(3), 431–441. DOI 10.1006/jtbi.2000.2186

[127] Karolak, A., Agrawal, S., Lee, S., Rejniak, K.A.: Single-cell-based in silico models: A tool for dissecting tumor heterogeneity. In: Encyclopedia of Biomedical Engineering, pp. 130–143. Elsevier. DOI 10.1016/b978-0-12-801238-3.64117-x

[128] Karolak, A., Poonja, S., Rejniak, K.A.: Morphophenotypic classification of tumor organoids as an indicator of drug exposure and penetration potential. PLOS Computational Biology **15**(7), e1007214 (2019). DOI 10.1371/journal.pcbi.1007214

[129] Kawanishi, J., Kato, J., Sasaki, K., Fujii, S., Watanabe, N., Niitsu, Y.: Loss of e-cadherin-dependent cell-cell adhesion due to mutation of the beta-catenin gene in a human cancer cell line, hsc-39. Molecular and Cellular Biology **15**(3), 1175–1181 (1995)

[130] Ke, X., Chen, C., Song, Y., Cai, Q., Li, J., Tang, Y., Han, X., Qu, W., Chen, A., Wang, H., Xu, G., Liu, D.: Hypoxia modifies the polarization of macrophages and their inflammatory microenvironment, and inhibits malignant behavior in cancer cells DOI 10.3892/ol.2019.10956

[131] Kelley, C.T.: Solving Nonlinear Equations with Newton's Method. Society for Industrial and Applied Mathematics (2003). DOI 10.1137/1.9780898718898

[132] Kelly, P., Davison, R., Bliss, E., McGee, J.: Macrophages in human breast disease: a quantitative immunohistochemical study. British Journal of Cancer **57**(2), 174–177 (1988). DOI 10.1038/bjc.1988.36

[133] Kelly, P.J., Hunt, C.: The limited value of cytoreductive surgery in elderly patients with malignant gliomas. **34**, 62–6; discussion 66–7

[134] Kim, D., Kwon, J.H.: A high-order accurate hybrid scheme using a central flux scheme and a WENO scheme for compressible flowfield analysis. Journal of Computational Physics **210**(2), 554–583 (2005). DOI 10.1016/j.jcp.2005.04.023

[135] Kim, M., Reed, D., Rejniak, K.A.: The formation of tight tumor clusters affects the efficacy of cell cycle inhibitors: A hybrid model study. Journal of Theoretical Biology **352**, 31–50 (2014). DOI 10.1016/j.jtbi.2014.02.027

[136] Kim, S.H., Debnath, J., Mostov, K., Park, S., Hunt, C.A.: A computational approach to resolve cell level contributions to early glandular epithelial cancer progression **3**(1). DOI 10.1186/1752-0509-3-122

[137] Kim, Y., Lee, S., Kim, Y.S., Lawler, S., Gho, Y.S., Kim, Y.K., Hwang, H.J.: Regulation of th1/th2 cells in asthma development: a mathematical model. **10**, 1095–1133. DOI 10.3934/mbe.2013.10.1095

[138] Klemke, R.: Trespassing cancer cells: 'fingerprinting' invasive protrusions reveals metastatic culprits **24**(5), 662–669

[139] Klopfenstein, Q., Truntzer, C., Vincent, J., Ghiringhelli, F.: Cell lines and immune classification of glioblastoma define patient's prognosis **120**(8), 806–814. DOI 10.1038/s41416-019-0404-y

[140] Knoll, D., Keyes, D.: Jacobian-free newton–krylov methods: a survey of approaches and applications. Journal of Computational Physics **193**(2), 357–397 (2004). DOI 10.1016/j.jcp.2003.08.010

[141] Knútsdóttir, H., Pálsson, E., Edelstein-Keshet, L.: Mathematical model of macrophage-facilitated breast cancer cells invasion. J. Theor. Biol. **357**(184-199) (2014)

[142] Kogan, Y., Agur, Z., Elishmereni, M.: A mathematical model for the immunotherapeutic control of the th1/th2 imbalance in melanoma **18**(4), 1017–1030. DOI 10.3934/dcdsb.2013.18.1017

[143] Konukoglu, E., Clatz, O., Bondiau, P.Y., Delingette, H., Ayache, N.: Extrapolating glioma invasion margin in brain magnetic resonance images: Suggesting new irradiation margins **14**(2), 111–125. DOI 10.1016/j.media.2009.11.005

[144] Kuzmin, D.: On the design of general-purpose flux limiters for finite element schemes. i. scalar convection. Journal of Computational Physics **219**(2), 513–531 (2006). DOI 10.1016/j.jcp.2006.03.034

[145] Laird, A.K.: Dynamics of tumour growth. British Journal of Cancer **13**(3), 490–502 (1964). DOI 10.1038/bjc.1964.55

[146] Laird, A.K.: Dynamics of tumour growth: Comparison of growth rates and extrapolation of growth curve to one cell. British Journal of Cancer **19**(2), 278–291 (1965). DOI 10.1038/bjc.1965.32

[147] Lamagna, C., Aurrand-Lions, M., Imhof, B.A.: Dual role of macrophages in tumor growth and angiogenesis. Journal of Leukocyte Biology **80**(4), 705–713 (2006). DOI 10.1189/jlb.1105656

[148] Lee, S., Ju, K., Jeon, H., Jeong, E., Lee, Y., Kim, C., Park, H., Han, S., Kang, H.: Regulation of tumour progression by programmed necrosis **2018**, 3537471

[149] Lee, W., Lim, S., Kim, Y.: The role of myosin II in glioma invasion: A mathematical model **12**(2), e0171312. DOI 10.1371/journal.pone.0171312

[150] Lee, Y.S., Song, S.J., Hong, H.K., Oh, B.Y., Lee, W.Y., Cho, Y.B.: The FBW7-MCL-1 axis is key in m1 and m2 macrophage-related colon cancer cell progression: validating the immunotherapeutic value of targeting PI3kγ. Experimental & Molecular Medicine **52**(5), 815–831 (2020). DOI 10.1038/s12276-020-0436-7

[151] Li, J., Xie, Y., Wang, X., Li, F., Li, S., Li, M., Peng, H., Yang, L., Liu, C., Pang, L., Zou, H., Zhao, J., Qi, Y., Cao, Y., Hu, J.: Prognostic impact of tumor-associated macrophage infiltration in esophageal cancer: a meta-analysis. Future Oncology **15**(19), 2303–2317 (2019). DOI 10.2217/fon-2018-0669

[152] Liang, T., Zhang, R., Liu, X., Ding, Q., Wu, S., Li, C., Lin, Y., Ye, Y., Zhong, Z., Zhou, M.: Recent advances in macrophage-mediated drug delivery systems. International Journal of Nanomedicine **Volume 16**, 2703–2714. DOI 10.2147/ijn.s298159

[153] Liao, M.C., Van Nostrand, W.E.: Degradation of soluble and fibrillar amyloid $\beta-$protein by matrix metalloproteinase (mt1-mmp) in vitro. Biochemistry **49**(6), 1127–1136 (2010). DOI 10.1021/bi901994d

[154] Lien, F.S., Leschziner, M.A.: Upstream monotonic interpolation for scalar transport with application to complex turbulent flows. International Journal for Numerical Methods in Fluids **19**(6), 527–548 (1994). DOI 10.1002/fld.1650190606

[155] Liguori, M., Solinas, G., Germano, G., Mantovani, A., Allavena, P.: Tumor-associated macrophages as incessant builders and destroyers of the cancer stroma. Cancers **3**(4), 3740–3761 (2011). DOI 10.3390/cancers3043740

[156] Lin, E.Y., Nguyen, A.V., Russell, R.G., Pollard, J.W.: Colony-stimulating factor 1 promotes progression of mammary tumors to malignancy **193**(6), 727–740. DOI 10.1084/jem.193.6.727

[157] Liu, H., Yang, L., Qi, M., Zhang, J.: NFAT1 enhances the effects of tumor-associated macrophages on promoting malignant melanoma growth and metastasis. Bioscience Reports **38**(6) (2018). DOI 10.1042/bsr20181604

[158] Liu, J.Y., Peng, C., Yang, G.F., Hu, W.Q., Yang, X.J., Huang, C.Q., Xiong, B., Li, Y.: Distribution pattern of tumour associated macrophages predicts the prognosis of gastric cancer. Oncotarget **8**(54), 92757–92769 (2017)

[159] Liu, X.D., Osher, S., Chan, T.: Weighted essentially non-oscillatory schemes. Journal of Computational Physics **115**(1), 200–212 (1994). DOI 10.1006/jcph.1994.1187

[160] Lo, C.M., Wang, H.B., Dembo, M., li Wang, Y.: Cell movement is guided by the rigidity of the substrate. Biophysical Journal **79**(1), 144–152 (2000). DOI 10.1016/s0006-3495(00)76279-5

[161] Lodish, H., Berk, A., Zipursky, S.: Tumor cells and the onset of cancer. Molecular Cell Biology **4**, Section 24.1 (2000)

[162] Louis, D.N., Ohgaki, H., Wiestler, O.D., Cavenee, W.K., Burger, P.C., Jouvet, A., Scheithauer, B.W., Kleihues, P.: The 2007 WHO classification of tumours of the central nervous system **114**(2), 97–109. DOI 10.1007/s00401-007-0243-4

[163] Louzoun, Y., Xue, C., Lesinski, G.B., Friedman, A.: A mathematical model for pancreatic cancer growth and treatments **351**, 74–82. DOI 10.1016/j.jtbi.2014.02.028

[164] Lu, P., Takai, K., Weaver, V.M., Werb, Z.: Extracellular matrix degradation and remodeling in development and disease. Cold Spring Harb Perspect Biol. **3**(12) (2011). DOI 10.1101/cshperspect.a005058

[165] Ma, J., Liu, L., Che, G., Yu, N., Dai, F., You, Z.: The m1 form of tumor-associated macrophages in non-small cell lung cancer is positively associated with survival time. BMC Cancer **10**(1) (2010). DOI 10.1186/1471-2407-10-112

[166] Ma, X., Schickel, M., Stevenson, M., Sarang-Sieminski, A., Gooch, K., Ghadiali, S., Hart, R.: Fibres in the extracellular matrix enable long-range stress transmission between cells **104**, 1410–1418

[167] Macklin, P., Edgerton, M.E., Thompson, A.M., Cristini, V.: Patient-calibrated agent-based modelling of ductal carcinoma in situ (DCIS): From microscopic measurements to macroscopic predictions of clinical progression **301**, 122–140. DOI 10.1016/j.jtbi.2012.02.002

[168] Macklin, P., McDougall, S., Anderson, A.R.A., Chaplain, M.A.J., Cristini, V., Lowengrub, J.: Multiscale modelling and nonlinear simulation of vascular tumour growth **58**(4-5), 765–798. DOI 10.1007/s00285-008-0216-9

[169] Macklin, P., McDougall, S., Anderson, A.R.A., Chaplain, M.A.J., Cristini, V., Lowengrub, J.: Multiscale modelling and nonlinear simulation of vascular tumour growth. J. Math. Biol. **58**, 765–798 (2009)

[170] MacMicking, J., wen Xie, Q., Nathan, C.: NITRIC OXIDE AND MACROPHAGE FUNCTION. Annual Review of Immunology **15**(1), 323–350 (1997). DOI 10.1146/annurev.immunol.15.1.323

[171] Madsen, D., Bugge, T.: The soure of matrix-degrading enzymes in human cancer: problems of research reproducibility and possible solutions. J. Cell Biol. **209**(2), 195–198 (2015)

[172] Madsen, D., Leonard, D., Masedunskas, A., Moyer, A., Jürgensen, H., Peters, D., Amornphimoltham, P., Selvaraj, A., Yamada, S., Brenner, D., Burgdorf, S., Engelholm, L., Behrendt, N., Holmbeck, K., Weigert, R., Bugge, T.: M2-like macrophages are responsible for collagen degradation through a mannose receptor-mediated pathway. Journal of Cell Biology **202**(6), 951 –966 (2013)

[173] Madsen, D.H., Jürgensen, H.J., Siersbæk, M.S., Kuczek, D.E., Cloud, L.G., Liu, S., Behrendt, N., Grøntved, L., Weigert, R., Bugge, T.H.: Tumor-associated macrophages derived from circulating inflammatory monocytes degrade collagen through cellular uptake. Cell Reports **21**(13), 3662–3671 (2017). DOI 10.1016/j.celrep.2017.12.011

[174] Mahlbacher, G., Curtis, L., Lowengrub, J., Frieboes, H.: Mathematical modelling of tumour-associated macrophage interactions with the cancer microenvironment. J. Immunother. Cancer **6**(10) (2018)

[175] Malandrino, A., Mak, M., Kamm, R., Moeendarbary, E.: Complex mechanics of the heterogeneous extracellular matrix in cancer **21**, 25–34

[176] Mantovani, A., Marchesi, F., Malesci, A., Laghi, L., Allavena, P.: Tumour-associated macrophages as treatment targets in oncology. Nature Reviews Clinical Oncology **14**(7), 399–416 (2017). DOI 10.1038/nrclinonc.2016.217

[177] Mantzaris, N.V., Webb, S., Othmer, H.G.: Mathematical modeling of tumor-induced angiogenesis **49**(2). DOI 10.1007/s00285-003-0262-2

[178] Mardia, K.V.: Directional statistics. J. Wiley

[179] McBride, W.: Phenotype and functions of intratumoral macrophages. Biochimica et Biophysica Acta (BBA) - Reviews on Cancer **865**(1), 27–41 (1986). DOI 10.1016/0304-419x(86)90011-9

[180] McDougall, S., Dallon, J., Sherratt, J., Maini, P.: Fibroblast migration and collagen deposition during dermal wound healing: mathematical modelling and clinical implications. Philosophical Transactions of the Royal Society A: Mathematical, Physical and Engineering Sciences **364**(1843), 1385–1405 (2006). DOI 10.1098/rsta.2006.1773

[181] Mehrabi, M., Amini, F., Mehrabi, S.: Active role of the necrotic zone in desensitisation of hypoxic macrophages and regulation of CSC-fate: a hypothesis **8**, 235

[182] Meneceur, S., Linge, A., Meinhardt, M., Hering, S., Löck, S., Bütof, R., Krex, D., Schackert, G., Temme, A., Baumann, M., Krause, M., von Neubeck, C.: Establishment and characterisation of heterotopic patient-derived xenografts for glioblastoma **12**(4), 871. DOI 10.3390/cancers12040871

[183] Metzcar, J., Wang, Y., Heiland, R., Macklin, P.: A review of cell-based computational modeling in cancer biology (3), 1–13. DOI 10.1200/cci.18.00069

[184] Mierke, C.T.: The biomechanical properties of 3d extracellular matrices and embedded cells regulate the invasiveness of cancer cells. Cell Biochemistry and Biophysics **61**(2), 217–236 (2011). DOI 10.1007/s12013-011-9193-5

[185] Milotti, E., Chignola, R.: Emergent properties of tumor microenvironment in a real-life model of multicell tumor spheroids **5**(11), e13942. DOI 10.1371/journal.pone.0013942

[186] Mohanam, S.: Biological significance of the expression of urokinase-type plasminogen activator receptors (uPARs) in brain tumors **4**(1-3), d178. DOI 10.2741/mohanam

[187] Monteran, L., Erez, N.: The dark side of fibroblasts: Cancer-associated fibroblasts as mediators of immunosuppression in the tumor microenvironment **10**. DOI 10.3389/fimmu.2019.01835

[188] Murdoch, C., Giannoudis, A., Lewis, C.E.: Mechanisms regulating the recruitment of macrophages into hypoxic areas of tumors and other ischemic tissues. Blood **104**(8), 2224–2234 (2004). DOI 10.1182/blood-2004-03-1109

[189] Murphy, D., Courtneidge, S.: The 'ins' and 'outs' of podosomes and invadopodia: characteristics, formation and function **12**(7), 413–426

[190] Nabeshima, K., Inoue, T., Shimao, Y., Sameshima, T.: Matrix metalloproteinases in tumor invasion: Role for cell migration **52**(4), 255–264. DOI 10.1046/j.1440-1827.2002.01343.x

[191] Nagase, H., Visse, R., Murphy, G.: Structure and function of matrix metalloproteinases and TIMPs. Cardiovascular Research **69**(3), 562–573 (2006). DOI 10.1016/j.cardiores.2005.12.002

[192] Nathan, C.F.: Secretory products of macrophages. Journal of Clinical Investigation **79**(2), 319–326 (1987). DOI 10.1172/jci112815

[193] NCI: NCI-60 human tumor cell lines screen [internet]. on line (2015). URL `https://dtp.cancer.gov/discovery_development/nci-60/`

[194] Newby, A.C.: Metalloproteinase expression in monocytes and macrophages and its relationship to atherosclerotic plaque instability. Arteriosclerosis, Thrombosis, and Vascular Biology **28**(12), 2108–2114 (2008). DOI 10.1161/atvbaha.108.173898

[195] O'Byrne, K.J., Koukourakis, M.I., Giatromanolaki, A., Cox, G., Turley, H., Steward, W.P., Gatter, K., Langrish, V.: Vascular endothelial growth factor,

platelet-derived endothelial cell growth factor and angiogenesis in non-small-cell lung cancer **82**(8), 1427–1432. DOI 10.1054/bjoc.1999.1129

[196] O'Donnell, L.J., Westin, C.F.: An introduction to diffusion tensor image analysis **22**(2), 185–196. DOI 10.1016/j.nec.2010.12.004

[197] Ohri, C.M., Shikotra, A., Green, R.H., Waller, D.A., Bradding, P.: Macrophages within NSCLC tumour islets are predominantly of a cytotoxic m1 phenotype associated with extended survival. European Respiratory Journal **33**(1), 118–126 (2009). DOI 10.1183/09031936.00065708

[198] Owen, M.R., Byrne, H.M., Lewis, C.E.: Mathematical modelling of the use of macrophages as vehicles for drug delivery to hypoxic tumour sites. Journal of Theoretical Biology **226**(4), 377–391 (2004). DOI 10.1016/j.jtbi.2003.09.004

[199] Owen, M.R., Sherratt, J.A.: Pattern formation and spatiotemporal irregularity in a model for macrophage–tumour interactions. Journal of Theoretical Biology **189**(1), 63–80 (1997). DOI 10.1006/jtbi.1997.0494

[200] Owen, M.R., Sherratt, J.A.: Modelling the macrophage invasion of tumours: effects on growth and composition. IMA journal of mathematics applied in medicine and biology **15**, 165–185 (1998)

[201] Page, C.L., Marineau, A., Bonza, P.K., Rahimi, K., Cyr, L., Labouba, I., Madore, J., Delvoye, N., Mes-Masson, A.M., Provencher, D.M., Cailhier, J.F.: BTN3a2 expression in epithelial ovarian cancer is associated with higher tumor infiltrating t cells and a better prognosis **7**(6), e38541. DOI 10.1371/journal.pone.0038541

[202] Painter, K., Hillen, T.: Mathematical modelling of glioma growth: The use of diffusion tensor imaging (DTI) data to predict the anisotropic pathways of cancer invasion **323**, 25–39. DOI 10.1016/j.jtbi.2013.01.014

[203] Painter, K.J.: Modelling cell migration strategies in the extracellular matrix. Journal of Mathematical Biology **58**(4), 511 (2008). DOI 10.1007/s00285-008-0217-8

[204] Pantano, F., Berti, P., Guida, F.M., Perrone, G., Vincenzi, B., Amato, M.M.C., Righi, D., Dell'Aquila, E., Graziano, F., Catalano, V., Caricato, M., Rizzo, S., Muda, A.O., Russo, A., Tonini, G., Santini, D.: The role of macrophages polarization in predicting prognosis of radically resected gastric cancer patients. Journal of Cellular and Molecular Medicine **17**(11), 1415–1421 (2013). DOI 10.1111/jcmm.12109

[205] Pastuszak-Lewandoska, D., Domańska-Senderowska, D., Antczak, A., Kordiak, J., Górski, P., Czarnecka, K.H., Migdalska-Sek, M., Nawrot, E., Kiszałkiewicz, J.M., Brzeziańska-Lasota, E.: The expression levels of IL-4/IL-13/STAT6 signaling pathway genes and SOCS3 could help to differentiate the histopathological subtypes of non-small cell lung carcinoma. Molecular Diagnosis & Therapy **22**(5), 621–629 (2018). DOI 10.1007/s40291-018-0355-7

[206] Peng, L., Trucu, D., Lin, P., Thompson, A., Chaplain, M.A.J.: A multiscale mathematical model of tumour invasive growth. Bull. Math. Biol. **79**(3), 389–429 (2017)

[207] Pérez-Velázquez, J., Gevertz, J.L., Karolak, A., Rejniak, K.A.: Microenvironmental niches and sanctuaries: A route to acquired resistance. In: Advances in Experimental Medicine and Biology, pp. 149–164. Springer International Publishing. DOI 10.1007/978-3-319-42023-3_8

[208] Pérez-Velázquez, J., Rejniak, K.A.: Drug-induced resistance in micrometastases: Analysis of spatio-temporal cell linages. Frontiers in Physiology **11**, 319 (2020). DOI 10.3389/fphys.2020.00319

[209] Persson, M., Nedergaard, M.K., Brandt-Larsen, M., Skovgaard, D., Jorgensen, J.T., Michaelsen, S.R., Madsen, J., Lassen, U., Poulsen, H.S., Kjaer, A.: Urokinase-type plasminogen activator receptor as a potential PET biomarker in glioblastoma **57**(2), 272–278. DOI 10.2967/jnumed.115.161703

[210] Petrie, R.J., Doyle, A.D., Yamada, K.M.: Random versus directionally persistent cell migration. Nature Reviews Molecular Cell Biology **10**(8), 538–549 (2009). DOI 10.1038/nrm2729

[211] Petroll, W.M., Ma, L., Jester, J.V.: Direct correlation of collagen matrix deformation with focal adhesion dynamics in living corneal fibroblasts **116**(8), 1481–1491. DOI 10.1242/jcs.00357

[212] Pointer, K.B., Clark, P.A., Schroeder, A.B., Salamat, M.S., Eliceiri, K.W., Kuo, J.S.: Association of collagen architecture with glioblastoma patient survival **126**(6), 1812–1821. DOI 10.3171/2016.6.jns152797

[213] Poleszczuk, J., Hahnfeldt, P., Enderling, H.: Evolution and phenotypic selection of cancer stem cells **11**(3), e1004025. DOI 10.1371/journal.pcbi.1004025

[214] Pollard, J.W.: Tumour-educated macrophages promote tumour progression and metastasis. Nature Reviews Cancer **4**(1), 71–78 (2004). DOI 10.1038/nrc1256

[215] Poplawski, N.J., Shirinifard, A., Agero, U., Gens, J.S., Swat, M., Glazier, J.A.: Front instabilities and invasiveness of simulated 3d avascular tumors **5**(5), e10641. DOI 10.1371/journal.pone.0010641

[216] Preusser, M., de Ribaupierre, S., Wöhrer, A., Erridge, S.C., Hegi, M., Weller, M., Stupp, R.: Current concepts and management of glioblastoma **70**(1), 9–21. DOI 10.1002/ana.22425

[217] Preziosi, L., Tosin, A.: Multiphase modelling of tumour growth and extracellular matrix interaction: mathematical tools and applications. J. Math. Biol. **58**, 625–656 (2009)

[218] Pries, A.R., Secomb, T.W.: Making microvascular networks work: Angiogenesis, remodeling, and pruning **29**(6), 446–455. DOI 10.1152/physiol.00012.2014

[219] Provenzano, P., Inman, D., Eliceiri, K., Trier, S., P.J.Keely: Contact guidance mediated three-dimensional cell migration is regulated by Rho/ROCK-dependent matrix reorganisation **95**, 5374–5384

[220] Provenzano, P.P., Inman, D.R., Eliceiri, K.W., Keely, P.J.: Matrix density-induced mechanoregulation of breast cell phenotype, signaling and gene expression through a fak-erk linkage. Oncogene **28**(49), 4326–4343 (2009). DOI 10.1038/onc.2009.299

[221] Pullen, N., Pickford, A., Perry, M., Jaworski, D., Loveson, K., Arthur, D., Holliday, J., Meter, T.V., Peckham, R., Younas, W., Briggs, S., MacDonald, S., Butterfield, T., Constantinou, M., Fillmore, H.: Current insights into matrix metalloproteinases and glioma progression: transcending the degradation boundary **Volume 5**, 13–30. DOI 10.2147/mnm.s105123

[222] Qiong-wen, Z., Lei, L., Chang-yang, G., Hua-shan, S., Yun-hui, Z., Xiaoze, W., Yu-wei, Z., Yu-quan, W.: Prognostic significance of tumor-associated macrophages in solid tumor: A meta-analysis of the literature. PLoS ONE **7**(12), e50946 (2012). DOI 10.1371/journal.pone.0050946

[223] Qiu, S.Q., Waaijer, S.J., Zwager, M.C., de Vries, E.G., van der Vegt, B., Schröder, C.P.: Tumor-associated macrophages in breast cancer: Innocent bystander or important player? Cancer Treatment Reviews **70**, 178–189 (2018). DOI 10.1016/j.ctrv.2018.08.010

[224] Raab, M., Swift, J., Dingal, P.D.P., Shah, P., Shin, J.W., Discher, D.E.: Crawling from soft to stiff matrix polarizes the cytoskeleton and phosphoregulates myosin-II heavy chain. The Journal of Cell Biology **199**(4), 669–683 (2012). DOI 10.1083/jcb.201205056

[225] Raffelt, D.A., Tournier, J.D., Smith, R.E., Vaughan, D.N., Jackson, G., Ridgway, G.R., Connelly, A.: Investigating white matter fibre density and morphology using fixel-based analysis **144**, 58–73. DOI 10.1016/j.neuroimage.2016.09.029

[226] Ramachandran, R.K., Sørensen, M.D., Aaberg-Jessen, C., Hermansen, S.K., Kristensen, B.W.: Expression and prognostic impact of matrix metalloproteinase-2 (MMP-2) in astrocytomas **12**(2), e0172234. DOI 10.1371/journal.pone.0172234

[227] Rambaran, R.N., Serpell, L.C.: Amyloid fibrils: abnormal protein assembly **2**(3), 112–117. DOI 10.4161/pri.2.3.7488

[228] Rath, B., Klameth, L., Plangger, A., Hochmair, M., Ulsperger, E., Huk, I., Zeillinger, R., Hamilton, G.: Expression of proteolytic enzymes by small cell lung cancer circulating tumor cell lines. Cancers **11**(1), 114 (2019). DOI 10.3390/cancers11010114

[229] Redente, E., Orlicky, D., Bouchard, R., Malkinson, A.: Tumour signalling to the bone marrow changes the phenotype of monocytes and pulmonary macrophages during urethane-induced primary lung tumorigenesis in A/J mice. Americ. J. Pathol. **170**(2), 693–708 (2007)

[230] Reinhart-King, C.A., Dembo, M., Hammer, D.A.: The dynamics and mechanics of endothelial cell spreading. Biophysical Journal **89**(1), 676–689 (2005). DOI 10.1529/biophysj.104.054320

[231] Rejniak, K.A., Anderson, A.R.A.: Hybrid models of tumor growth **3**(1), 115–125. DOI 10.1002/wsbm.102

[232] Rejniak, K.A., Dillon, R.H.: A single cell-based model of the ductal tumour microarchitecture. Computational and Mathematical Methods in Medicine **8**(1), 51–69 (2007)

[233] Rejniak, K.A., Quaranta, V., Anderson, A.R.A.: Computational investigation of intrinsic and extrinsic mechanisms underlying the formation of carcinoma **29**(1), 67–84. DOI 10.1093/imammb/dqq021

[234] da Rocha, R.F., Bastiani, M.A.D., Klamt, F.: Bioinformatics approach to evaluate differential gene expression of m1/m2 macrophage phenotypes and antioxidant genes in atherosclerosis. Cell Biochemistry and Biophysics **70**(2), 831–839 (2014). DOI 10.1007/s12013-014-9987-3

[235] Rouillard, A.D., Holmes, J.W.: Mechanical regulation of fibroblast migration and collagen remodelling in healing myocardial infarcts **590**(18), 4585–4602. DOI 10.1113/jphysiol.2012.229484

[236] Rusanov, V.: The calculation of the interaction of non-stationary shock waves and obstacles. USSR Computational Mathematics and Mathematical Physics **1**(2), 304–320 (1962). DOI 10.1016/0041-5553(62)90062-9

[237] Saez, A., Ghibaudo, M., Buguin, A., Silberzan, P., Ladoux, B.: Rigidity-driven growth and migration of epithelial cells on microstructured anisotropic substrates. Proceedings of the National Academy of Sciences **104**(20), 8281–8286 (2007). DOI 10.1073/pnas.0702259104

[238] Sakagami, H., Kishino, K., Amano, O., Kanda, Y., Kunii, S., Yokote, Y., Oizumi, H., Oizumi, T.: Cell death induced by nutritional starvation in mouse macrophage-like raw264.7 cells, **29**(1), 343–347

[239] Schaller, G., Meyer-Hermann, M.: Continuum versus discrete model: a comparison for multicellular tumour spheroids. Philosophical Transactions of the Royal Society A: Mathematical, Physical and Engineering Sciences **364**(1843), 1443–1464 (2006). DOI 10.1098/rsta.2006.1780

[240] Scott, J.G., Fletcher, A.G., Anderson, A.R.A., Maini, P.K.: Spatial metrics of tumour vascular organisation predict radiation efficacy in a computational model **12**(1), e1004712. DOI 10.1371/journal.pcbi.1004712

[241] Scribner, E., Saut, O., Province, P., Bag, A., Colin, T., Fathallah-Shaykh, H.M.: Effects of anti-angiogenesis on glioblastoma growth and migration: Model to clinical predictions **9**(12), e115018. DOI 10.1371/journal.pone.0115018

[242] Shashni, B., Ariyasu, S., Takeda, R., Suzuki, T., Shiina, S., Akimoto, K., Maeda, T., Aikawa, N., Abe, R., Osaki, T., Itoh, N., Aoki, S.: Size-based differentiation of cancer and normal cells by a particle size analyzer assisted by a cell-recognition pc software. Biol Pharm Bull **4**(41), 487–503 (2018)

[243] Shimolina, L., Izquierdo, M., Lopez-Duarte, I., Bull, J., Shirmanova, M., Klapshina, L., Zagaynova, E., Kuimova, M.: Imaging tumor microscopic viscosity in vivo using molecular rotors. Sci Rep. **7**, 41097 (2017). DOI 10.1038/srep41097

[244] Shirinifard, A., Gens, J.S., Zaitlen, B.L., Popławski, N.J., Swat, M., Glazier, J.A.: 3d multi-cell simulation of tumor growth and angiogenesis **4**(10), e7190. DOI 10.1371/journal.pone.0007190

[245] Shuttleworth, R., Trucu, D.: Multiscale modelling of fibres dynamics and cell adhesion within moving boundary cancer invasion. Bulletin of Mathematical Biology (2019). DOI 10.1007/s11538-019-00598-w

[246] Shuttleworth, R., Trucu, D.: Cell-scale degradation of peritumoural extracellular matrix fibre network and its role within tissue-scale cancer invasion. Bulletin of Mathematical Biology **82**(6), 65 (2020). DOI 10.1007/s11538-020-00732-z

[247] Shuttleworth, R., Trucu, D.: Multiscale dynamics of a heterotypic cancer cell population within a fibrous extracellular matrix. Journal of Theoretical Biology **486**, 110040 (2020). DOI 10.1016/j.jtbi.2019.110040

[248] Sica, A., Bronte, V.: Altered macrophage differentiation and immune dysfunction in tumor development. Journal of Clinical Investigation **117**(5), 1155–1166 (2007). DOI 10.1172/jci31422

[249] Sica, A., Larghi, P., Mancino, A., Rubino, L., Porta, C., Totaro, M.G., Rimoldi, M., Biswas, S.K., Allavena, P., Mantovani, A.: Macrophage polarization in tumour progression. Seminars in Cancer Biology **18**(5), 349–355 (2008). DOI 10.1016/j.semcancer.2008.03.004

[250] Siemann, D.W., Horsman, M.R.: Modulation of the tumor vasculature and oxygenation to improve therapy **153**, 107–124. DOI 10.1016/j.pharmthera.2015.06.006

[251] Silbergeld, D.L., Chicoine, M.R.: Isolation and characterization of human malignant glioma cells from histologically normal brain **86**(3), 525–531. DOI 10.3171/jns.1997.86.3.0525

[252] Sottoriva, A., Spiteri, I., Piccirillo, S.G.M., Touloumis, A., Collins, V.P., Marioni, J.C., Curtis, C., Watts, C., Tavare, S.: Intratumor heterogeneity in human glioblastoma reflects cancer evolutionary dynamics **110**(10), 4009–4014. DOI 10.1073/pnas.1219747110

[253] Sporn, M.: The war on cancer. Lancet **347**, 1377–1381 (1996)

[254] Springer, N.L., Fischbach, C.: Biomaterials approaches to modeling macrophage–extracellular matrix interactions in the tumor microenvironment. Current Opinion in Biotechnology **40**, 16–23 (2016). DOI 10.1016/j.copbio.2016.02.003

[255] Steinkamp, M.P., Winner, K.K., Davies, S., Muller, C., Zhang, Y., Hoffman, R.M., Shirinifard, A., Moses, M., Jiang, Y., Wilson, B.S.: Ovarian tumor attachment, invasion, and vascularization reflect unique microenvironments in the peritoneum: Insights from xenograft and mathematical models **3**. DOI 10.3389/fonc.2013.00097

[256] Stéphanou, A., Lesart, A., Deverchère, J., Juhem, A., Popov, A., Estève, F.: How tumour-induced vascular changes alter angiogenesis: Insights from a computational model **419**, 211–226. DOI 10.1016/j.jtbi.2017.02.018

[257] Stix, B., Kähne, T., Sletten, K., Raynes, J., Roessner, A., Röcken, C.: Proteolysis of aa amyloid fibril proteins by matrix metalloproteinases-1, -2, and -3. The American Journal of Pathology **159**(2), 561 – 570 (2001). DOI 10.1016/S0002-9440(10)61727-0

[258] Stolarska, M.A., Kim, Y., Othmer, H.G.: Multi-scale models of cell and tissue dynamics. Philos. Trans. A. Math. Phys. Eng. Sci. **367**(1902), 3525–3553 (2009)

[259] Strachan, D.C., Ruffell, B., Oei, Y., Bissell, M.J., Coussens, L.M., Pryer, N., Daniel, D.: CSF1r inhibition delays cervical and mammary tumor growth in murine models by attenuating the turnover of tumor-associated macrophages and enhancing infiltration by CD8 t cells. OncoImmunology **2**(12), e26968 (2013). DOI 10.4161/onci.26968

[260] Suarez, C., Maglietti, F., Colonna, M., Breitburd, K., Marshall, G.: Mathematical modeling of human glioma growth based on brain topological struc-

tures: Study of two clinical cases **7**(6), e39616. DOI 10.1371/journal.pone.0039616

[261] Sumimoto, R., Hirai, T., Fujita, M., Murakami, H., Otake, Y., Huang, C.L.: M2 tumor-associated macrophages promote tumour progression in non-small-cell lung cancer. Exp Ther Med **18**(6), 4490–4498 (2019)

[262] Sun, Y., You, S., Tu, H., Jr., D.S., Chaney, E., Marjanovic, M., Li, J., Barkalifa, R., Wang, J., Higham, A., Luckey, N., Cradock, K., Liu, Z., Boppart, S.: Intraoperative visualisation of the tumour microenvironment and quantification of extracellular vesicles by label-free nonlinear imaging **4**, eaau5603

[263] Suveges, S., Chamseddine, I., Rejniak, K.A., Eftimie, R., Trucu, D.: Collective cell migration in a fibrous environment: A hybrid multiscale modelling approach **7**. DOI 10.3389/fams.2021.680029

[264] Suveges, S., Eftimie, R., Trucu, D.: Re-polarisation of macrophages within a multi-scale moving boundary tumour invasion model pp. 1–50. arXiv:2103.03384

[265] Suveges, S., Eftimie, R., Trucu, D.: Directionality of macrophages movement in tumour invasion: A multiscale moving-boundary approach. Bulletin of Mathematical Biology **82**(12) (2020). DOI 10.1007/s11538-020-00819-7

[266] Suveges, S., Hossain-Ibrahim, K., Steele, J.D., Eftimie, R., Trucu, D.: Mathematical modelling of glioblastomas invasion within the brain: A 3d multi-scale moving-boundary approach **9**(18), 2214. DOI 10.3390/math9182214

[267] Swanson, K.R., Alvord, E.C., Murray, J.D.: A quantitative model for differential motility of gliomas in grey and white matter **33**(5), 317–329. DOI 10.1046/j.1365-2184.2000.00177.x

[268] Swanson, K.R., Rockne, R.C., Claridge, J., Chaplain, M.A., Alvord, E.C., Anderson, A.R.: Quantifying the role of angiogenesis in malignant progression of gliomas: In silico modeling integrates imaging and histology **71**(24), 7366–7375. DOI 10.1158/0008-5472.can-11-1399

[269] Swanson, K.R., Rostomily, R.C., Alvord, E.C.: A mathematical modelling tool for predicting survival of individual patients following resection of glioblastoma: a proof of principle **98**(1), 113–119. DOI 10.1038/sj.bjc.6604125

[270] Syková, E., Nicholson, C.: Diffusion in brain extracellular space **88**(4), 1277–1340. DOI 10.1152/physrev.00027.2007

[271] Szabó, A., Merks, R.M.H.: Blood vessel tortuosity selects against evolution of aggressive tumor cells in confined tissue environments: A modeling approach **13**(7), e1005635. DOI 10.1371/journal.pcbi.1005635

[272] Szymańska, Z., Morales-Rodrigo, C., Lachowicz, M., Chaplain, M.A.J.: Mathematical modelling of cancer invasion of tissue: the role and effect of nonlocal interactions. Math Mod Meth Appl S **19**(2), 257–281 (2009)

[273] Tan, H.Y., Wang, N., Li, S., Hong, M., Wang, X., Feng, Y.: The reactive oxygen species in macrophage polarization: Reflecting its dual role in progression and treatment of human diseases. Oxidative Medicine and Cellular Longevity **2016**, 1–16 (2016). DOI 10.1155/2016/2795090

[274] Tang, J., Enderling, H., Becker-Weimann, S., Pham, C., Polyzos, A., Chen, C.Y., Costes, S.V.: Phenotypic transition maps of 3d breast acini obtained by imaging-guided agent-based modeling **3**(4), 408. DOI 10.1039/c0ib00092b

[275] Tjorve, K.M.C., Tjorve, E.: The use of gompertz models in growth analyses, and new gompertz-model approach: An addition to the unified-richards family. PLOS ONE **12**(6), 1–17 (2017)

[276] Todd, J.R., Ryall, K.A., Vyse, S., Wong, J.P., Natrajan, R.C., Yuan, Y., Tan, A.C., Huang, P.H.: Systematic analysis of tumour cell-extracellular matrix adhesion identifies independent prognostic factors in breast cancer **7**(39), 62939–62953. DOI 10.18632/oncotarget.11307

[277] Toi, M., Inada, K., Hoshina, S., Suzuki, H., Kondo, S., Tominaga, T.: Vascular endothelial growth factor and platelet-derived endothelial cell growth factor are frequently coexpressed in highly vascularized human breast cancer. **1**(9), 961–964

[278] Trichet, L., Digabel, J.L., Hawkins, R.J., Vedula, S.R.K., Gupta, M., Ribrault, C., Hersen, P., Voituriez, R., Ladoux, B.: Evidence of a large-scale mechanosensing mechanism for cellular adaptation to substrate stiffness. Proceedings of the National Academy of Sciences **109**(18), 6933–6938 (2012). DOI 10.1073/pnas.1117810109

[279] Trucu, D., Lin, P., Chaplain, M.A.J., Wang, Y.: A multiscale moving boundary model arising in cancer invasion. Multiscale Model. Simul. **11**(1), 309–335 (2013)

[280] Turner, S., Sherratt, J.: Intercellular adhesion and cancer invasion: A discrete simulation using the extended potts model. J. Theor. Biol. **216**(1), 85–100 (2002)

[281] Tymoszuk, P., Evens, H., Marzola, V., Wachowicz, K., Wasmer, M.H., Datta, S., Müller-Holzner, E., Fiegl, H., Böck, G., van Rooijen, N., Theurl, I., Doppler, W.: In situ proliferation contributes to accumulation of tumour-associated macrophages in spontaneous mammary tumors **44**(8), 2247–2262

[282] Tyson, J.J., Novak, B.: Temporal organization of the cell cycle. Current Biology **18**(17), R759–R768 (2008). DOI 10.1016/j.cub.2008.07.001

[283] Uchugonova, A., Zhao, M., Weinigel, M., Zhang, Y., Bouvet, M., Hoffman, R., König, K.: Multiphoton tomography visualises collagen fibres in the tumour microenvironment that maintain cancer-cell anchorage and shape **114**(1), 99–102

[284] Veeravalli, K.K., Ponnala, S., Chetty, C., Tsung, A.J., Gujrati, M., Rao, J.S.: Integrin $\alpha 9\beta 1$-mediated cell migration in glioblastoma via SSAT and kir4.2 potassium channel pathway **24**(1), 272–281. DOI 10.1016/j.cellsig.2011.09.011

[285] Veeravalli, K.K., Rao, J.S.: MMP-9 and uPAR regulated glioma cell migration **6**(6), 509–512. DOI 10.4161/cam.21673

[286] Vinogradov, S., Warren, G., Wei, X.: Macrophages associated with tumours as potential targets and therapeutic intermediates. Nanomedicine **9**(5), 695–707 (2014)

[287] Visse, R., Nagase, H.: Matrix metalloproteinases and tissue inhibitors of metalloproteinases: structure function and biochemistry. Circ Res **92**, 827–839 (2003). DOI 10.1161/01.RES.0000070112.80711.3D

[288] Wang, X., Jiang, J., Wu, C.: Prognostic significance of tumor-associated macrophage infiltration in gastric cancer: a meta-analysis. Genetics and Molecular Research **15**(4) (2016). DOI 10.4238/gmr15049040

[289] Wang, Y., Yang, T., Ma, Y., Halade, G.V., Zhang, J., Lindsey, M.L., Jin, Y.F.: Mathematical modeling and stability analysis of macrophage activation in left ventricular remodeling post-myocardial infarction **13**(Suppl 6), S21. DOI 10.1186/1471-2164-13-s6-s21

[290] Webb, S.D., Owen, M.R., Byrne, H.M., Murdoch, C., Lewis, C.E.: Macrophage-based anti-cancer therapy: Modelling different modes of tumour

targeting. Bulletin of Mathematical Biology **69**(5), 1747–1776 (2007). DOI 10.1007/s11538-006-9189-2

[291] Wei, C., Yang, C., Wang, S., Shi, D., Zhang, C., Lin, X., Liu, Q., Dou, R., Xiong, B.: Crosstalk between cancer cells and tumor associated macrophages is required for mesenchymal circulating tumor cell-mediated colorectal cancer metastasis. Molecular Cancer **18**(1), 64 (2019). DOI 10.1186/s12943-019-0976-4

[292] Weiger, M.C., Vedham, V., Stuelten, C.H., Shou, K., Herrera, M., Sato, M., Losert, W., Parent, C.A.: Real-time motion analysis reveals cell directionality as an indicator of breast cancer progression. PLOS ONE **8**(3), 1–12 (2013). DOI 10.1371/journal.pone.0058859

[293] Weinberg, R.A.: The Biology of Cancer. Garland Science, New York (2006)

[294] Wolf, K., Alexander, S., Schacht, V., Coussens, L., Andrian, U., Rheenen, J., Deryugina, E., Friedl, P.: Collagen-based cell migration models in vitro and in vivo. Semin Cell Dev Biol **20**, 931–41 (2009). DOI 10.1016/j.semcdb.2009.08.005

[295] Wolf, K., Friedl, P.: Extracellular matrix determinants of proteolytic and non-proteolytic cell migration. Tren. Cel. Biol. **21**(12), 736–744 (2011)

[296] Wu, P., Wu, D., Zhao, L., Huang, L., Chen, G., Shen, G., Huang, J., Chai, Y.: Inverse role of distinct subsets and distribution of macrophage in lung cancer prognosis: a meta-analysis. Oncotarget **7**(26), 40451–40460 (2016). DOI 10.18632/oncotarget.9625

[297] Wu, P.H., Giri, A., Sun, S.X., Wirtz, D.: Three-dimensional cell migration does not follow a random walk. Proceedings of the National Academy of Sciences **111**(11), 3949–3954 (2014). DOI 10.1073/pnas.1318967111

[298] Wullkopf, L., West, A.K.V., Leijnse, N., Cox, T.R., Madsen, C.D., Oddershede, L.B., Erler, J.T.: Cancer cells' ability to mechanically adjust to extracellular matrix stiffness correlates with their invasive potential. Molecular biology of the cell **29**(20), 2378–2385 (2018). DOI 10.1091/mbc.E18-05-0319

[299] Xuan, W., Qu, Q., Zheng, B., Xiong, S., Fan, G.H.: The chemotaxis of m1 and m2 macrophages is regulated by different chemokines. Journal of Leukocyte Biology **97**(1), 61–69 (2014). DOI 10.1189/jlb.1a0314-170r

[300] Yamaguchi, H., Pixley, F., Condeelis, J.: Invadopodia and podosomes in tumor invasion. European Journal of Cell Biology **85**(3-4), 213–218 (2006). DOI 10.1016/j.ejcb.2005.10.004

[301] Yamaguchi, H., Wyckoff, J., Condeelis, J.: Cell migration in tumors. Current Opinion in Cell Biology **17**(5), 559–564 (2005). DOI 10.1016/j.ceb.2005.08.002

[302] Yan, H., Romero-López, M., Benitez, L.I., Di, K., Frieboes, H.B., Hughes, C.C., Bota, D.A., Lowengrub, J.S.: 3d mathematical modeling of glioblastoma suggests that transdifferentiated vascular endothelial cells mediate resistance to current standard-of-care therapy **77**(15), 4171–4184. DOI 10.1158/0008-5472.can-16-3094

[303] Yin, S., Huang, J., Li, Z., Zhang, J., Luo, J., Lu, C., Xu, H., Xu, H.: The prognostic and clinicopathological significance of tumor-associated macrophages in patients with gastric cancer: A meta-analysis. PLOS ONE **12**(1), e0170042 (2017). DOI 10.1371/journal.pone.0170042

[304] Yosida, K.: Functional Analysis, 6th edn. Springer-Verlag (1980)

[305] Young, N., Pearl, D.K., Brocklyn, J.R.V.: Sphingosine-1-phosphate regulates glioblastoma cell invasiveness through the urokinase plasminogen activator system and CCN1/cyr61 **7**(1), 23–32. DOI 10.1158/1541-7786.mcr-08-0061

[306] Yu, M., Guan, R., Hong, W., Zhou, Y., Lin, Y., Jin, H., Hou, B., Jian, Z.: Prognostic value of tumor-associated macrophages in pancreatic cancer: a meta-analysis. Cancer Management and Research **Volume 11**, 4041–4058 (2019). DOI 10.2147/cmar.s196951

[307] Yuan, X., Zhang, J., Li, D., Mao, Y., Mo, F., Du, W., Ma, X.: Prognostic significance of tumor-associated macrophages in ovarian cancer: A meta-analysis. Gynecologic Oncology **147**(1), 181–187 (2017). DOI 10.1016/j.ygyno.2017.07.007

[308] Zhang, M., He, Y., Sun, X., Li, Q., Wang, W., Zhao, A., Di, W.: A high m1/m2 ratio of tumor-associated macrophages is associated with extended survival in ovarian cancer patients **7**(1). DOI 10.1186/1757-2215-7-19

[309] Zhang, M., Xi, N. (eds.): Nanomedicine. Jenny Stanford Publishing (2019). DOI 10.1201/9780429065767

[310] Zhang, S., Shu, C.W.: A new smoothness indicator for the WENO schemes and its effect on the convergence to steady state solutions. Journal of Scientific Computing **31**(1-2), 273–305 (2006). DOI 10.1007/s10915-006-9111-y

[311] Zhao, X., Qu, J., Sun, Y., Wang, J., Liu, X., Wang, F., Zhang, H., Wang, W., Ma, X., Gao, X., Zhang, S.: Prognostic significance of tumor-associated macrophages in breast cancer: a meta-analysis of the literature. Oncotarget **8**(18), 30576–30586 (2017). DOI 10.18632/oncotarget.15736